
Ultracold atoms in adjustable arrays of optical microtraps

Ultrakalte Atome in frei konfigurierbaren optischen Mikrofallenregistern

Zur Erlangung des Grades eines Doktors der Naturwissenschaften (Dr. rer. nat.)

genehmigte Dissertation von Martin Raphael Sturm aus Berlin

Tag der Einreichung: 10. April 2018, Tag der Prüfung: 28. Mai 2018

Darmstadt – D 17

1. Gutachten: Prof. Dr. Reinhold Walser

2. Gutachten: Prof. Dr. Gerhard Birkl



TECHNISCHE
UNIVERSITÄT
DARMSTADT

Fachbereich Physik
Institut für Angewandte Physik
Theoretische Quantendynamik

Ultracold atoms in adjustable arrays of optical microtraps
Ultrakalte Atome in frei konfigurierbaren optischen Mikrofallenregistern

Genehmigte Dissertation von Martin Raphael Sturm aus Berlin

1. Gutachten: Prof. Dr. Reinhold Walser
2. Gutachten: Prof. Dr. Gerhard Birkl

Tag der Einreichung: 10. April 2018

Tag der Prüfung: 28. Mai 2018

Darmstadt – D 17

Bitte zitieren Sie dieses Dokument als:

URN: urn:nbn:de:tuda-tuprints-74658

URL: <http://tuprints.ulb.tu-darmstadt.de/7465>

Dieses Dokument wird bereitgestellt von tuprints,

E-Publishing-Service der TU Darmstadt

<http://tuprints.ulb.tu-darmstadt.de>

tuprints@ulb.tu-darmstadt.de



Die Veröffentlichung steht unter folgender Creative Commons Lizenz:

Namensnennung – Keine kommerzielle Nutzung – Weitergabe unter gleichen Bedingungen

CC BY-NC-SA 4.0 International

<https://creativecommons.org/licenses/by-nc-sa/4.0/>

Zusammenfassung

Ultrakalte Atome in optischen Gittern ermöglichen die experimentelle Untersuchung von Quantenvielteilchensystemen. Dabei sind die Atome in hohem Maße von der Umgebung isoliert und alle relevanten Systemparameter sind kontrollierbar. Dies sind ideale Voraussetzungen für die Quantensimulation von grundlegenden Gittermodellen. Allerdings schränkt die Tatsache, dass die Atome durch stehende Wellen interferierender Laserstrahlen gefangen werden, die möglichen Fallenanordnungen auf reguläre Gitter ein und erschwert die Einzelplatzkontrolle.

In der vorliegenden Dissertation wird eine alternative experimentelle Plattform untersucht. Dabei wird die Kombination aus einem Mikrolinsenregister und einem räumlichen Lichtmodulator genutzt, um ein zweidimensionales Mikrofallenregister für ultrakalte Atome zu erzeugen. Dieser Ansatz ermöglicht viele unterschiedliche Fallenanordnungen und eine umfangreiche Einzelplatzkontrolle.

Die Umsetzbarkeit der beschriebenen experimentellen Plattform wird im Rahmen dieser Arbeit wie folgt untersucht: Erstens wird mithilfe eines detaillierten Modells des optischen Systems das Lichtfeld simuliert, welches die Mikrofallen erzeugt. Die so berechnete Intensitätsverteilung ist proportional zum optischen Dipolpotenzial für die Atome. Zweitens werden ausgehend von diesen Simulationsergebnissen die Hubbard-Parameter für mehrere Alkali-Isotope numerisch berechnet und analytisch genähert. Die Resultate zeigen, dass das stark korrelierte Regime des Bose-Hubbard-Modells bei hinreichend großen Tunnelraten erreicht werden kann. Weiterhin wird der Einfluss von Fluktuationen der Fallenparameter untersucht. Drittens werden zwei Ansätze für die Präparation von Zuständen mit niedriger Entropie betrachtet. Diese starten von einem Bose-Einstein-Kondensat beziehungsweise einem Register deterministisch geladener, isolierter Fallen. In beiden Fällen wird die Fallentiefe adiabatisch geändert, um das System in das angestrebte Regime des Bose-Hubbard-Modells zu überführen. Eine Analyse der dabei auftretenden rampeninduzierten Anregungen und externen Heizprozesse zeigt, dass beide Ansätze experimentell umsetzbar sind.

Um das Potenzial der beschriebenen Plattform zu demonstrieren, werden zwei Anwendungen beschrieben. Das erste System besteht aus zwei schwach gekoppelten Ringgittern. Die Tunneldynamik von ultrakalten Atomen zwischen diesen Ringen weist, abhängig von der Wechselwirkungsstärke, mehrere Phänomene auf: kollabierende und wiederkehrende Josephson-Oszillationen, wechselwirkungsinduziertes Self-Trapping und Tunnelresonanzen. Die zweite untersuchte Anwendung ist die Implementierung eines Schemas für einen universellen Quantencomputer, welches auf zeitkontinuierlichen Quantum-Walks von wechselwirkenden Teilchen basiert. Dabei werden die Informationen in der Position von atomaren Wellenpaketen, die sich auf einem planaren Graphen aus Mikrofallen bewegen, kodiert. Die Details von experimentellen Umsetzungen der beschriebenen Anwendungen werden, basierend auf den Ergebnissen der vorhergehenden Kapitel, diskutiert.

Abstract

Ultracold atoms in optical lattices are a powerful platform for the study of quantum many-body physics. The combination of a high degree of isolation from the environment and external control over all relevant parameters makes these systems ideal candidates for the quantum simulation of fundamental lattice models. However, since the atoms are trapped in standing waves of interfering laser beams, the available trap geometries are constrained to regular lattices and single-site control is limited.

In this thesis, an alternative experimental platform is investigated. Here, the combination of a microlens array and a spatial light modulator is used to provide a two-dimensional optical microtrap array for ultracold atoms. This setup allows for versatile trap geometries and comprehensive single-site control.

The experimental feasibility of the described platform is investigated in the following way. First, the light field generating the microtrap array is simulated using a detailed model of the optical setup. The computed intensity distribution is proportional to the optical dipole potential for the atoms. Second, the simulation results are used to obtain the Hubbard parameters for multiple alkalis from numerical calculations as well as approximative analytical methods. It is shown that the strongly correlated regimes of the Bose-Hubbard model can be reached at sufficiently large tunneling rates. In addition, the impact of fluctuations in the trap parameters is investigated. Third, two approaches are considered for the preparation of low-entropy many-body states. On the one hand, a loading scheme is investigated which starts from a Bose-Einstein condensate and is used in optical lattice experiments. Here, the depth of the microtrap array is increased adiabatically. On the other hand, an array of isolated traps, which is initialized with one atom per site in the respective motional ground state, is considered as starting point. The itinerant regime of the Hubbard model is accessed by an adiabatic decrease of the trap depth. An analysis of ramp-induced excitations and external heating processes shows the feasibility of both approaches.

Demonstrating the potential of the investigated platform, two applications are described. On the one hand, the tunneling dynamics of ultracold atoms between weakly coupled ring lattices is analyzed. Controlled by the interaction strength, multiple phenomena can be observed: Josephson oscillations exhibiting collapse and revival, interaction-induced self-trapping, and tunneling resonances. On the other hand, the implementation of a scheme for universal quantum computing based on time-continuous quantum walks of interacting particles is proposed. Here, the information is encoded into the position of atomic wave packets moving through a planar graph which is built from optical microtraps and implements a quantum circuit. Details of an experimental implementation are discussed for both applications using the results derived in the preceding parts of this thesis.

Contents

1	Introduction	1
I	Fundamentals	3
2	Fundamentals of ultracold atoms	5
2.1	Atom-light interaction	5
2.1.1	Two-level atom	7
2.1.2	Alkali atoms	10
2.2	Atom-atom interaction	12
2.2.1	Two-particle scattering	13
2.2.2	Pseudo potential	15
2.3	Cold dilute gases	15
3	Ultracold atoms in optical lattices	17
3.1	Single-particle wave functions in periodic potentials	17
3.2	Bose-Hubbard model	18
3.2.1	Derivation of the Bose-Hubbard model	18
3.2.2	Weak interaction limit	20
3.2.3	Strong interaction limit	23
3.2.4	Phase diagram	24
3.3	Overview of research directions	26
II	Feasibility	27
4	Optical trapping potential	29
4.1	Generation of optical microtraps	29
4.1.1	Micro lens arrays	29
4.1.2	Alternative techniques	30
4.2	Simulation methods for optical systems	31
4.2.1	Geometrical optics	31
4.2.2	Scalar diffraction theory	31
4.2.3	Vector diffraction theory	32
4.3	Simulation of the light field	34
4.3.1	Optical system	34
4.3.2	Simulation results and measurements	35
4.3.3	Diffraction-limited optical system	37
4.3.4	Polarization effects	38
4.4	Parametrization of the intensity distribution	40

5	Hubbard parameters	43
5.1	Periodic potentials	43
5.1.1	MLA-based optical potential	43
5.1.2	Band structure	45
5.1.3	Wannier functions and Hubbard parameters	48
5.2	Closed-form expressions for the Hubbard parameters	50
5.2.1	Interaction strength	50
5.2.2	Tunneling parameter	51
5.3	Non-periodic potentials	56
5.3.1	Maximally localized low-energy functions	56
5.3.2	Effects from fluctuations of the optical potential	58
5.3.3	Validity of approximations for the optical potential	60
6	State preparation	61
6.1	Loading from a Bose-Einstein condensate	61
6.1.1	Initial state	61
6.1.2	Loading sequence	62
6.1.3	Final state	63
6.2	Loading from the atomic limit	65
6.2.1	Rapid adiabatic parameter ramps	65
6.2.2	Cold atoms in optical microtraps	67
6.2.3	Realistic experimental setting	71
6.2.4	Rapid adiabatic loading of a Mott insulator	73
6.2.5	Limits on scalability	80
6.2.6	Transfer to a Bose-Einstein condensate	80
III	Applications	81
7	Tunneling dynamics between coupled ring lattices	83
7.1	Hamilton operator and two-mode approximation	83
7.2	Tunneling dynamics	84
7.2.1	Josephson oscillations	85
7.2.2	Collapse and revival	86
7.2.3	High-order tunneling and self-trapping	88
7.2.4	Many-body resonances	89
7.3	Experimental considerations	92
8	Quantum computing with continuous-time quantum walks	93
8.1	Childs-Gosset-Webb scheme	93
8.2	Modified scheme with time-dependent control	95
8.3	Computational basis states	96
8.3.1	Gaussian wave packets	97
8.3.2	Wave packet preparation	98
8.3.3	Wave packet compression	100
8.4	Gate fidelity	101
8.4.1	Effects from finite momentum widths	102
8.4.2	Effects from parameter fluctuations	103
8.5	Scalability	105
9	Conclusion and outlook	107

IV	Appendices	109
A	Properties of relevant isotopes	111
B	Representations of the many-body state	113
	B.1 Number-state representation	113
	B.2 Phase-state representation	115
	B.3 Phase-coherent-state representation	117
C	Two-dimensional Gaussian lattices	119
	C.1 Square lattice	119
	C.2 Triangular lattice	120
	C.3 Honeycomb lattice	121
D	Variational calculation for the two-dimensional Gaussian well	123
E	Details of the instanton calculation	125
F	Thermodynamics of the Mott insulator	129
G	Minimization of the adiabatic error measures	133
H	Solving the Bose-Hubbard model numerically	135
	H.1 Matrix representation of the Hamilton operator	135
	H.2 Diagonalization of the Hamilton matrix	137
	H.3 Solution of the time-dependent Schrödinger equation	137
I	Two-mode approximation	139
J	Scattering on graphs	141
	J.1 One-qubit gates	141
	J.2 Two-qubit gates	142
	Bibliography	143

Chapter 1

Introduction

Cold dilute gases have been in the focus of research in atomic, molecular, and optical physics for the last three decades. The main reason for this interest is that these systems provide a clean and controllable platform for studying quantum many-body physics. The required external control is exerted by electromagnetic fields, most prominently lasers, which are used to cool dilute gases to submillikelvin temperatures. For the development of these techniques [1–3] in the 1980’s, Steven Chu, Claude N. Cohen-Tannoudji, and William D. Phillips received the Nobel prize in 1997. The combination of laser and evaporative cooling allowed for a breakthrough in 1995, i. e. the production of Bose-Einstein condensates (BECs) in dilute gases of alkali atoms [4, 5]. For this, Eric A. Cornell, Wolfgang Ketterle, and Carl E. Wieman were awarded the Nobel prize in 2001 [6, 7]. Bose-Einstein condensation is a quantum statistical phenomenon, which manifests as the macroscopic population of the ground state in a system of identical bosonic particles. Satyendranath Bose and Albert Einstein predicted this effect in the 1920’s [8–10]. Later it was identified as an explanation for the superfluidity in liquid ^4He .

Starting from the first BEC experiments, the field of ultracold gases has expanded and diversified significantly. On the one hand, more and more species, including molecules [11] and fermionic atoms [12], have been cooled to very low temperatures. On the other hand, cold dilute gases have been loaded into optical lattices [13–16]. The latter are generated by standing-wave laser fields providing regular grids of dipole traps. In this potential landscape, the motion of the atoms is restricted to tunneling between adjacent sites. Therefore, the ratio of interaction energy to kinetic energy is significantly increased, which induces strong correlations. In addition, the lattice structure of the external potential allows for the implementation of the Hubbard model, a fundamental model from condensed matter physics. The experimental breakthrough for optical lattice experiments was the observation of the quantum phase transition from a superfluid to a Mott insulator in 2001 [14]. From this point onwards the field developed rapidly [15, 16].

Optical lattice experiments implement quantum many-body models in a clean and controllable way. In addition, a large toolbox of measurement techniques allows accessing a wide range of observables. For these reasons, optical lattices are considered as a promising platform for quantum simulation, a concept introduced by Feynman [17]. It is based on the observation that the simulation of a quantum many-body system with classical computers is hindered by the exponential growth of the Hilbert space, whereas the simulation using another controllable quantum system, the quantum simulator, is efficient. The prime example for an effect that can be analyzed with optical lattice quantum simulators is high T_c superconductivity [18].

In this thesis, an experimental platform is investigated, which constitutes an alternative to optical lattices for the study of many-body physics with ultracold atoms. This platform utilizes a microlens array to generate an array of light spots in its focal plane, which is demagnified using an objective with a high numerical aperture. The resulting optical microtraps have spacings below $2\ \mu\text{m}$, which allows for inter-trap tunneling.

In contrast to optical lattice experiments, the array geometry is not limited to regular lattices. In addition, a spatial light modulator can be used to control the illumination of each lenslet and thus the depth of each microtrap individually. The considered setup offers a new approach to the experimental study of itinerant quantum many-body systems in arbitrary periodic and non-periodic two-dimensional microtrap arrays with comprehensive single-site control over the trap parameters. This thesis provides a theoretical feasibility analysis for the described setup and proposals for applications.

Part I provides a brief introduction to the fields of ultracold atoms and optical lattices. This serves two purposes. On the one hand, those readers who are unfamiliar with the field are provided with basic knowledge and references for further reading. On the other hand, the notations required for later chapters are introduced. In **chapter 2**, the physics of ultracold atoms is reviewed. The main topics in this chapter are the motion of atoms in a coherent light field and the interaction of atoms in a cold dilute gas. In **chapter 3**, an introduction to the field of optical lattices is provided. The focus is on the many-body physics of the Bose-Hubbard model and its phase diagram. In addition, an overview of current research directions is given.

In part II, the feasibility of the considered experimental approach is investigated. First, the light field generated by the optical setup is simulated in **chapter 4** and the results are validated by a comparison to measurements performed in the research group of Gerhard Birkl. The obtained intensity distribution is proportional to the optical dipole potential experienced by the atoms. Second, in **chapter 5**, the parameters of the Bose-Hubbard model are determined for multiple alkali species using the optical potentials computed in chapter 4. Third, in **chapter 6**, the preparation of ultracold atoms in optical microtrap arrays is investigated. Two approaches are considered, which start either from a BEC in a wide trap or a deterministically loaded array of isolated traps.

In part III, two applications for the considered setup are analyzed. First, the tunneling dynamics of ultracold atoms between two coupled ring lattices is investigated in **chapter 7**. Depending on the interaction strength, multiple regimes are identified: collective oscillations exhibiting collapse and revival, self-trapping, and tunneling resonances. The former mimic Josephson oscillations between superconductors. For the prediction of this effect [19], Brian D. Josephson was awarded the Nobel prize in 1973. In **chapter 8**, the implementation of a scheme for universal quantum computation using continuous-time quantum walks of interacting particles [20] is discussed. Finally, in **chapter 9**, the results of this thesis are discussed, and an outlook is provided.

Parts of this thesis are or will be published as articles in scientific journals:

M. R. Sturm, M. Schlosser, R. Walser, and G. Birkl

"Quantum simulators by design: Many-body physics in reconfigurable arrays of tunnel-coupled traps"

Phys. Rev. A **95**, 063625 (2017)

Based on chapters 4, 5, and 7.

M. R. Sturm, M. Schlosser, G. Birkl, and R. Walser

"Rapid loading of a Mott insulator from arrays of non-condensed atoms"

Submitted to Phys. Rev. A

Based on section 6.2.

M. R. Sturm, M. Schlosser, G. Birkl, and R. Walser

"Quantum computation with continuous-time quantum walks of ultracold atoms"

In preparation

Based on chapter 8.

Part I

Fundamentals

Chapter 2

Fundamentals of ultracold atoms

In this chapter, the physics of ultracold atoms is summarized to introduce the basic concepts and notations needed for this thesis. In section 2.1, the interaction of atoms with light is discussed. This topic is of special interest since coherent light fields are used for the cooling and trapping of atoms. Thereafter, atom-atom interactions in the ultracold regime will be the topic of section 2.2. Summarizing the results of these two sections, the many-body Hamilton operator of interacting ultracold atoms in an optical potential is formulated in section 2.3 using the language of second quantization.

2.1 Atom-light interaction

The interaction of matter with electromagnetic radiation is a complex topic [21]. A full description using the theory of quantum electrodynamics is a formidable task. However, for the scope of this thesis, it is sufficient to restrict one's attention to a regime for which the theoretical description can be simplified significantly. The matter under consideration is a cold dilute gas of neutral atoms which move with relative velocities much smaller than the speed of light. These atoms interact with an electromagnetic field produced by one or several lasers that operate in the visible or near-infrared regime. The intensity and frequency of this field are sufficiently low such that the atoms are not ionized and higher order processes from quantum electrodynamics (e.g. pair creation) can be neglected. This situation allows treating the atoms' center-of-mass motion with non-relativistic quantum mechanics. At first, the discussion is restricted to the case of a single atom. Many-body effects and atom-atom interactions will be the topics of later sections. The atomic part of the system's Hamilton operator can be written as the sum of the atom's kinetic and internal electronic energy

$$\hat{H}_a = \frac{\hat{\mathbf{p}}^2}{2m} + \hat{H}_e, \quad (2.1)$$

with the atomic mass m , the atom's center-of-mass momentum $\hat{\mathbf{p}}$, and the internal electronic Hamilton operator \hat{H}_e . The Hilbert space for the atomic degrees of freedom has a product structure $\mathcal{H}_a = \mathcal{H}_{\text{com}} \otimes \mathcal{H}_e$, with the center-of-mass part \mathcal{H}_{com} and the internal electronic part \mathcal{H}_e . The former is the Hilbert space of a particle moving in three-dimensional space. The latter is spanned by the atom's electronic eigenstates $\{|i\rangle : i \in \mathcal{I}\}$. Since the atom is initially in its internal ground state and the electromagnetic field drives excitations only to a few excited bound states, the relevant part of the Hilbert space \mathcal{H}_e is low-dimensional. Using the states $|i\rangle$ and the corresponding energies $\hbar\omega_i$ the atom's internal Hamilton operator can be expressed in the following way

$$\hat{H}_e = \sum_{i \in \mathcal{I}} \hbar\omega_i |i\rangle\langle i|. \quad (2.2)$$

Turning to the electromagnetic field, it is worth noting that it consists of two parts, the Coulomb field generated by a static configuration of the atom's electrons and nucleus and a purely transverse radiation field. The former vanishes outside the extent of the atom and its energy is already included in \hat{H}_e . The Hamilton operator corresponding to the energy of the latter can be expressed using a mode decomposition

$$\hat{H}_r = \sum_{j \in \mathcal{M}} \hbar \omega_j \hat{a}_j^\dagger \hat{a}_j \quad (2.3)$$

with the set \mathcal{M} of the radiation field's modes, the j^{th} mode annihilation operator \hat{a}_j , and the respective angular frequency ω_j . The Hilbert space \mathcal{H}_r of the radiation field is the product of Fock spaces for the modes in \mathcal{M} . The total Hilbert space of the atom and the radiation field is given by $\mathcal{H} = \mathcal{H}_a \otimes \mathcal{H}_r$.

The interaction between the transverse electromagnetic field and the atom gives rise to the third part of the system's Hamilton operator \hat{H}_i . This part can be significantly simplified because the spatial variation of the transverse electromagnetic field happens on scales of its wavelength (> 100 nm), which is much larger than the extent of the atom that is typically a few Bohr radii ($a_0 \approx 0.05$ nm). Therefore, the long-wavelength or dipole approximation [22] can be applied. Here, the respective part of the Hamilton operator takes the form

$$\hat{H}_i = -\hat{\mathbf{d}} \cdot \hat{\mathbf{E}}_\perp(\mathbf{r}), \quad \hat{\mathbf{d}} = \sum_i q_i \hat{\mathbf{r}}_i, \quad (2.4)$$

with the atomic constituents' charges q_i and positions $\hat{\mathbf{r}}_i$, the atomic dipole moment $\hat{\mathbf{d}}$, and the transverse electromagnetic field operator $\hat{\mathbf{E}}_\perp$ evaluated at the atom's center-of-mass position \mathbf{r} .

The electromagnetic field produced by a laser has the property that a few of its modes contain many photons whereas the remaining modes are practically unoccupied. In addition, the thermal occupation of radiation modes is negligible in the relevant frequency range at room temperature. These facts allow approximating the field by the combination of a classical external field \mathbf{E}_c and the vacuum field. It is worth mentioning that if the occupied modes are in a coherent state, then this substitution is exact [21, 23].

For the following considerations, the radiation field's state is not of interest. Therefore, a partial trace over its degrees of freedom is performed. Thus, the atomic subsystem needs to be described with a density operator $\hat{\rho}$ representing a mixed state instead of a state vector $|\psi\rangle$. The partial trace in conjunction with the Born-Markov approximation yields a master equation in Lindblad form (cf. [24, 25])

$$\partial_t \hat{\rho} = -\frac{i}{\hbar} [\hat{H}_a - \hat{\mathbf{d}} \cdot \mathbf{E}_c, \hat{\rho}] + \mathcal{L}(\hat{\rho}), \quad (2.5)$$

for the atomic density operator $\hat{\rho}$. The first term on the right-hand side of equation (2.5) corresponds to the right-hand side of the Liouville-von Neumann equation for an atom interacting with a classical external field. In contrast, the operator-valued Lindblad function $\mathcal{L}(\hat{\rho})$ in the second term, stems from the interaction of the atom with the vacuum modes of the quantized electromagnetic field and incorporates the process of spontaneous emission (cf. Wigner-Weisskopf theory [26]) as well as the Lamb shift [27]. In the next subsection, solutions to equation (2.5) are discussed for a two-level atom interacting with a monochromatic light field. This simple example facilitates the understanding of the basic mechanisms for the control of atoms with light.

2.1.1 Two-level atom

In this subsection, it is assumed that only two electronic states of the atom are relevant. One of which is the ground state $|g\rangle$ and the other one is an excited state $|e\rangle$. The monochromatic external electric field is given by

$$\mathbf{E}_c(\mathbf{r}, t) = \mathcal{E}(\mathbf{r})e^{-i\omega t} + \mathcal{E}^*(\mathbf{r})e^{i\omega t}, \quad (2.6)$$

with complex amplitude \mathcal{E} and angular frequency ω . To have a compact notation, the spatial dependence is suppressed in the following. Further, it is assumed that the atom is fixed in position or equivalently has infinite mass. This allows disregarding the external degrees of freedom simplifying the analysis significantly. In later parts of this chapter, this restriction is lifted and the forces acting on the atom are analyzed. To derive explicit equations of motion for the atom's density operator $\hat{\rho}$, it is advantageous to express \hat{H}_e and $\hat{\mathbf{d}}$ using the basis $\{|g\rangle, |e\rangle\}$, which yields

$$\hat{H}_e = \hbar\omega_g |g\rangle\langle g| + \hbar\omega_e |e\rangle\langle e|, \quad \hat{\mathbf{d}} = \mathbf{d}_{eg} |e\rangle\langle g| + \mathbf{d}_{ge} |g\rangle\langle e|. \quad (2.7)$$

Here, the dipole matrix elements $\mathbf{d}_{ij} = \langle i|\hat{\mathbf{d}}|j\rangle$ are introduced. The energies of the atomic levels determine the transition frequency $\omega_{eg} = \omega_e - \omega_g$. The next step is to derive the equations of motion for the components of the atomic density matrix $\rho_{ij} = \langle i|\hat{\rho}|j\rangle$. Before these equations are given explicitly, it is convenient to apply a further simplification. If the monochromatic field is not too far detuned from the atomic transition $|\Delta| = |\omega - \omega_{eg}| \ll \omega_{eg}$, ω and not too strong $\Omega = \mathbf{d}_{eg} \cdot \mathcal{E}/\hbar \ll \omega$, then rapidly oscillating terms in the master equation can be neglected [28]. This is the so-called rotating wave approximation. Here, the detuning Δ between the angular frequencies of the laser ω and the atomic transition ω_{eg} , as well as the Rabi frequency Ω are introduced. In a suitable co-rotating interaction picture, the equations of motion for the components of the density matrix are time independent [21]

$$\partial_t \rho_{ee} = -\Gamma \rho_{ee} + i\Omega^* \rho_{ge} - i\Omega \rho_{eg}, \quad (2.8)$$

$$\partial_t \rho_{gg} = \Gamma \rho_{ee} - i\Omega^* \rho_{ge} + i\Omega \rho_{eg}, \quad (2.9)$$

$$\partial_t \rho_{eg} = -(\Gamma/2 - i\Delta) \rho_{eg} - i\Omega^* (\rho_{ee} - \rho_{gg}), \quad (2.10)$$

$$\partial_t \rho_{ge} = -(\Gamma/2 + i\Delta) \rho_{ge} + i\Omega (\rho_{ee} - \rho_{gg}). \quad (2.11)$$

Here, Γ denotes the decay rate of the excited state due to spontaneous emission. The solutions to these equations have the form of oscillations which damp on the time scale of Γ^{-1} . These oscillations are general feature of driven two-level systems. They are called Rabi oscillations in honor of Isidor I. Rabi who investigated them in the context of nuclear magnetic resonance [29] and received the Nobel prize in 1944. The stationary solution to the system of equations given above is

$$\rho_{ee}^{\text{stat}} = \frac{1}{2} \frac{s(\Delta)}{1 + s(\Delta)}, \quad \rho_{eg}^{\text{stat}} = \frac{i\Gamma - 2\Delta}{4\Omega} \frac{s(\Delta)}{1 + s(\Delta)}, \quad s(\Delta) = \frac{2|\Omega|^2}{\Delta^2 + \Gamma^2/4}, \quad (2.12)$$

with the saturation parameter s . The remaining components of the density matrix can be determined from the relations $\rho_{gg} = 1 - \rho_{ee}$ and $\rho_{ge} = \rho_{eg}^*$.

External degrees of freedom

In this part, the force that the light field exerts on the atom is investigated (cf. [30]). To do so, the atom's external degrees of freedom, i. e. its position, needs to be included in the theoretical description. For this, it is convenient to work in the basis

$$\mathcal{B} = \{|\mathbf{r}\rangle \otimes |i\rangle : \mathbf{r} \in \mathbb{R}^3, i \in \mathcal{I}\} \quad (2.13)$$

with the atom's center-of-mass position vector \mathbf{r} and its internal state's coordinate i . The mechanical effect of light on the atom is described by the force operator $\hat{\mathbf{F}}$. Using Heisenberg's equation of motion for the atomic momentum operator, the Force operator can be computed in the following way

$$\hat{\mathbf{F}} = \partial_t \hat{\mathbf{p}} = \frac{i}{\hbar} [\hat{H}, \hat{\mathbf{p}}] = \frac{i}{\hbar} [\hat{H}_i, \hat{\mathbf{p}}]. \quad (2.14)$$

The quantity of interest is the expectation value of the force $\mathbf{F} = \text{Tr}\{\hat{\mathbf{F}}\hat{\rho}\}$. Here, $\hat{\rho}$ is the density operator of the total system consisting of the atom and the radiation field. Partial traces can be executed subsequently. Therefore, the partial trace over the radiation field's degrees of freedom can be executed first, this yields $\mathbf{F} = \text{Tr}_a\{\text{Tr}_r\{\hat{\mathbf{F}}\hat{\rho}\}\} = \text{Tr}_a\{\hat{\mathbf{F}}\hat{\rho}\}$. Here, $\hat{\rho}$ is the reduced density operator of the atomic system. However, in contrast to the previous discussion the full atomic Hilbert space is considered including the atom's external degrees of freedom. The trace can be computed explicitly using the basis \mathcal{B} [31, 32] yielding

$$\mathbf{F} = \text{Tr}_a\{\hat{\mathbf{F}}\hat{\rho}\} \approx \rho_{eg}\hbar\nabla\Omega^* + \rho_{ge}\hbar\nabla\Omega. \quad (2.15)$$

Here, it is assumed that the atomic wave function is strongly localized around the atomic center off mass and that its extent is small compared to the spatial variation of the electric field. In order to allow for a physical interpretation, the complex Rabi frequency is split into amplitude and phase $\Omega = |\Omega|e^{i\phi}$. Using this expression, equation (2.15) can be rewritten in the following way

$$\mathbf{F} = 2\hbar|\Omega|^2 \text{Im}\left(\frac{\rho_{eg}}{\Omega^*}\right)\nabla\phi + \hbar \text{Re}\left(\frac{\rho_{eg}}{\Omega^*}\right)\nabla|\Omega|^2. \quad (2.16)$$

The first term on the right-hand side is called dissipative force and is connected to the radiation pressure. It points in the direction of $\nabla\phi$ and therefore in the direction of the field's local wave vector \mathbf{k} . The second term is called reactive or dipole force and it acts in the direction of $\nabla|\Omega|^2 \propto \nabla I$ with $I = 2\epsilon_0 c |\mathcal{E}|^2$ denoting the light field's intensity. The dipole force stems from the interaction of the atom's induced dipole moment with the gradient of the electric field.

To proceed with the calculation of the force, the density matrix elements need to be determined. For this task, it is necessary to elaborate on the different timescales of the system's dynamics. On the one hand, the internal time-evolution relaxes on a timescale of Γ^{-1} as mentioned earlier. On the other hand, the external dynamics take place on a timescale of \hbar/E_r . The recoil energy $E_r = \hbar^2\mathbf{k}^2/(2m)$ is the kinetic energy the atom gains in its initial center-of-mass reference frame by absorbing a photon with wave vector \mathbf{k} . For most allowed transitions the internal dynamics are much faster than the external dynamics, i. e. $\Gamma^{-1} \ll \hbar/E_r$. Therefore, the stationary solution given in equation (2.12) can be used to evaluate the expression for \mathbf{F} in equation (2.16). Before this substitution can be applied to obtain explicit expressions for the mean force, the Doppler shift due to the atom's center-of-mass velocity \mathbf{v} in the laboratory's frame of reference needs to be

considered. This can be taken into account by the substitution $\Delta \rightarrow \Delta - \mathbf{k} \cdot \mathbf{v}$. Using these considerations, important special cases are discussed in the following.

Radiation pressure

The light field is assumed to be a plane wave resulting in the Rabi frequency $\Omega(\mathbf{r}) = \Omega_0 e^{i\mathbf{k}\mathbf{r}}$. Note that the dipole force vanishes since $\nabla |\Omega(\mathbf{r})|^2 = 0$. The dissipative force on the atom can be expressed using equations (2.16) and (2.12)

$$\mathbf{F} = \hbar \mathbf{k} \frac{\Gamma}{2} \frac{s(\Delta - \mathbf{k} \cdot \mathbf{v})}{1 + s(\Delta - \mathbf{k} \cdot \mathbf{v})} = \hbar \mathbf{k} \Gamma_{\text{sc}}. \quad (2.17)$$

In the above equation the photon scattering rate $\Gamma_{\text{sc}} = \Gamma s / (2 + 2s)$ is introduced. Equation (2.17) allows for an intuitive interpretation of the dissipative force. It is the rate of the atom's momentum change and it is given by the momentum of one photon $\hbar \mathbf{k}$ times the rate of scattering events Γ_{sc} . This force causes the so called radiation pressure. The following two limits can be distinguished. For a strong driving field $\Omega_0 \gg \Gamma$, $|\Delta - \mathbf{k} \cdot \mathbf{v}|$ the atomic transition is saturated $s \gg 1$ and the mean force on the atom is given by $\mathbf{F} = \hbar \mathbf{k} \Gamma / 2$. The opposite limit $s \ll 1$ yields

$$\mathbf{F} = \hbar \mathbf{k} \frac{\Gamma}{2} \frac{2|\Omega_0|^2}{(\Delta - \mathbf{k} \cdot \mathbf{v})^2 + \Gamma^2/4}. \quad (2.18)$$

Doppler cooling

The dissipative force can be used to cool atoms, which can be seen by expanding equation (2.18) to first order in $\mathbf{k} \cdot \mathbf{v}$

$$\mathbf{F} = \hbar \mathbf{k} \frac{\Gamma |\Omega_0|^2}{\Gamma^2/4 + \Delta^2} \left(1 + \frac{2\Delta}{\Gamma^2/4 + \Delta^2} \mathbf{k} \cdot \mathbf{v} \right). \quad (2.19)$$

The force consists of a velocity-independent part and a part that is proportional to the velocity. By applying two plane waves with orthogonal polarizations, equal intensities, and wave vectors \mathbf{k} and $-\mathbf{k}$ respectively, the velocity-independent part cancels out yielding

$$\mathbf{F} = \frac{4\hbar \mathbf{k}^2 \Gamma |\Omega_0|^2 \Delta}{(\Gamma^2/4 + \Delta^2)^2} v_k \mathbf{e}_k = \beta v_k \mathbf{e}_k, \quad (2.20)$$

with the unit vector in \mathbf{k} -direction \mathbf{e}_k and $v_k = \mathbf{e}_k \cdot \mathbf{v}$. From $\Delta < 0$ follows $\beta < 0$ and therefore an effective damping of the atomic movement along the direction of the wave vector. By adding analog beam pairs for the other spatial directions, atoms can be cooled efficiently. This procedure is called Doppler cooling and is one example of several techniques to cool neutral atoms using laser light [1–3, 33]. In order to reach quantum degeneracy in atomic gases, these techniques are combined with evaporative cooling [34, 35].

Optical dipole traps

Second, the light field is assumed to be strongly red detuned from the atomic resonance, i. e. $|\Delta| \gg \Omega, \Gamma, |\mathbf{k} \cdot \mathbf{v}|$. In this limit, the dissipative and the dipole Force are given by

$$\mathbf{F}_{\text{dis}} = \frac{\hbar |\Omega|^2 \Gamma}{\Delta^2} \nabla \phi, \quad \mathbf{F}_{\text{dip}} = -\frac{\hbar}{\Delta} \nabla |\Omega|^2. \quad (2.21)$$

The above expressions show that the dipole force dominates for large Δ and that this force is conservative, i. e. it is the negative gradient of a potential

$$V(\mathbf{r}) = \frac{\hbar}{\Delta} |\Omega(\mathbf{r})|^2 = \frac{3\pi c^2}{2\omega_{eg}^3} \frac{\Gamma}{\Delta} I(\mathbf{r}), \quad (2.22)$$

Here, the spatial dependency of Ω and I , which was suppressed in the preceding calculations, is reintroduced. The potential V is denoted optical dipole potential [36] and can be used to trap atoms. The remainder of this thesis is mainly concerned with this regime of atom-light interaction. It is worth noting that the above expression can also be obtained by treating the \hat{H}_{int} as a perturbation to the bare atomic Hamilton operator \hat{H}_a and computing the corresponding energy shift.

2.1.2 Alkali atoms

The discussion in the preceding subsection is limited to two-level atoms. A generalization to multi-level atoms and multiple laser fields is straightforward [37]. The purpose of this subsection is to apply these results to the electronic structure of real atoms. The discussion is limited to alkali metals because these elements are most relevant for cold-atom experiments. The reason for this lies in the combination of a simple hydrogen-like electronic structure and closed optical transitions in a convenient spectral range. This allows for straightforward implementations of laser-based cooling and trapping techniques.

Alkali atoms have one valence electron outside filled shells. The latter are very stable and therefore not relevant for the atom-light interaction. Thus, for the scope of this work, alkali atoms are described as effective single-electron systems. The electronic state is specified by $|n, ((L, S), J, I), F, m_F\rangle$, with the valence electron's principle, spin, and orbital angular momentum quantum numbers n, L, S . The electron's total angular momentum with quantum number J is the sum of its spin and orbital angular momentum. Whereas, the atom's total angular momentum with quantum number F is the sum of the angular momenta of the valence electron and the nucleus. The quantum number of the latter is denoted by I . Finally, m_F is the projection of the atom's total angular momentum onto the quantization axis. States that coincide with regard to the quantum numbers n, L , and J have similar energies that lie within the range given by the respective hyperfine splitting $\hbar\Delta_{\text{hfs}}$. The hyperfine splittings are much smaller than the energy differences between states that differ in n, L , or J . Further, in the absence of an external electromagnetic field, states that differ only in the quantum number m_F have the same energy.

The remainder of this thesis focuses on the trapping of ground state atoms with light fields that are far red detuned with respect to the lowest energetic optical transitions. The species considered in this thesis, ${}^7\text{Li}$, ${}^{23}\text{Na}$, ${}^{41}\text{K}$, and ${}^{87}\text{Rb}$, have a nuclear angular momentum of $I = 3/2$. The relevant part of the level structure for these isotopes is shown in figure 2.1.

In order to compute the optical potential and the scattering rate for a state in the $n^2S_{1/2}$ manifold, it is necessary to consider the contributions from all states in the $n^2P_{1/2}$ and $n^2P_{3/2}$ manifolds. The corresponding optical transitions are summarized as D1 and

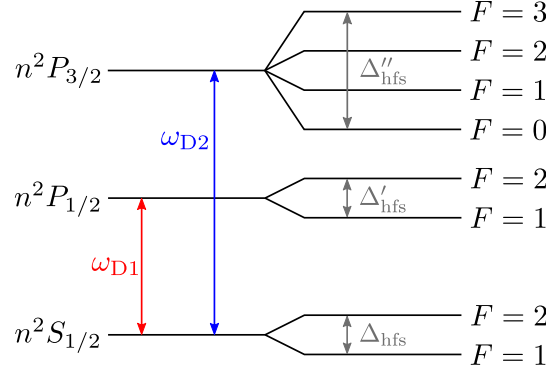


Figure 2.1: Level scheme of alkali atoms with nuclear angular momentum of $I = 3/2$, e. g. ${}^7\text{Li}$, ${}^{23}\text{Na}$, ${}^{41}\text{K}$, and ${}^{87}\text{Rb}$.

D2 lines respectively. Due to the strong detuning of the light field from the atomic transitions, the rotating wave approximation used in the preceding subsection cannot be applied. Neglecting saturation effects, the expressions for the optical potential and the scattering rate are given by [36, 38]

$$V(\mathbf{r}) = \sum_e \frac{|\langle e | \hat{\mathbf{d}} \cdot \boldsymbol{\mathcal{E}}(\mathbf{r}) | g \rangle|^2}{\hbar} \left(\frac{1}{\omega - \omega_{eg}} - \frac{1}{\omega + \omega_{eg}} \right), \quad (2.23)$$

$$\Gamma_{\text{sc}}(\mathbf{r}) = \sum_e \Gamma_{n'J'nJ} \frac{|\langle e | \hat{\mathbf{d}} \cdot \boldsymbol{\mathcal{E}}(\mathbf{r}) | g \rangle|^2}{\hbar^2} \left(\frac{1}{\omega - \omega_{eg}} - \frac{1}{\omega + \omega_{eg}} \right)^2. \quad (2.24)$$

Here, the transition frequencies ω_{eg} and decay rates $\Gamma_{n'J'nJ}$ for the excited and ground states

$$|e\rangle = |n', ((L', S'), J', I'), F', m'_F\rangle, \quad |g\rangle = |n, ((L, S), J, I), F, m_F\rangle, \quad (2.25)$$

are introduced. It is worth noting that the terms containing $\omega + \omega_{eg}$ in equations (2.23) and (2.24) correspond to off-resonant contributions that were neglected in the rotating wave approximation.

It remains to determine the matrix elements $\langle e | \hat{\mathbf{d}} \cdot \boldsymbol{\mathcal{E}}(\mathbf{r}) | g \rangle$. For this task it is convenient to decompose the electric field using the spherical basis

$$\boldsymbol{\mathcal{E}}(\mathbf{r}) = \sum_{q=-1}^1 \mathcal{E}^q(\mathbf{r}) \mathbf{e}_q, \quad \mathbf{e}_{\pm 1} = \mp \frac{1}{\sqrt{2}} (\mathbf{e}_x \pm i \mathbf{e}_y), \quad \mathbf{e}_0 = \mathbf{e}_z, \quad (2.26)$$

because this basis captures the symmetry of the problem and facilitates the application of the Wigner-Eckert theorem [39–41]. In combination with the fact that the dipole operator commutes with the nuclear angular momentum and the electron spin, this allows expressing the dipole matrix elements in the following form [41]

$$\langle e | \hat{\mathbf{d}} \cdot \mathbf{e}_q | g \rangle = C_{eg}^q \langle n' J' || \hat{\mathbf{d}} || n J \rangle. \quad (2.27)$$

Here, C_{eg}^q is a purely geometric factor that includes all angular momentum conservation and selection rules. It is given by

$$C_{eg}^q = (-1)^{2F' - m'_F + I' + J + 1} \sqrt{(2F' + 1)(2F + 1)} \begin{Bmatrix} J' & 1 & J \\ F & I' & F' \end{Bmatrix} \begin{pmatrix} F' & 1 & F \\ -m'_F & q & m_F \end{pmatrix}. \quad (2.28)$$

The second factor in equation 2.27 is called reduced dipole matrix element and quantifies the transition strength of the respective line. It is related to the transition frequency $\omega_{n'J'nJ}$, the decay rate $\Gamma_{n'J'nJ}$, and the oscillator strength $f_{n'J'nJ}$ [41]

$$\langle n', J' | \hat{d} | n, J \rangle = (-1)^{J+\max(J, J')} \sqrt{2J'+1} \sqrt{\frac{3\pi\epsilon_0 \hbar c^3 \Gamma_{n'J'nJ}}{\omega_{n'J'nJ}^3}}, \quad (2.29)$$

$$= (-1)^{J+\max(J, J')} \sqrt{2J'+1} \sqrt{\frac{3e^2 \hbar f_{n'J'nJ}}{2m_e \omega_{n'J'nJ}}}. \quad (2.30)$$

Here, the electron mass m_e and the elementary charge e are introduced. The quantities $\omega_{n'J'nJ}$, $\Gamma_{n'J'nJ}$, and $f_{n'J'nJ}$ can be measured precisely and are tabulated in the atomic spectra database of the National Institute of Standards and Technology [42]. In appendix A, the corresponding values for the isotopes ^7Li , ^{23}Na , ^{41}K , and ^{87}Rb are provided.

If the light's detuning is much larger than Δ_{hfs} , Δ'_{hfs} , and Δ''_{hfs} , then the hyperfine structure is not resolved and the calculations simplify significantly. For linearly polarized light the optical potential and the scattering rate are given by [36]

$$V(\mathbf{r}) = \frac{\pi c^2}{2} I(\mathbf{r}) \left[\frac{\Gamma_{D1}}{\omega_{D1}^3} \left(\frac{1}{\omega - \omega_{D1}} - \frac{1}{\omega + \omega_{D1}} \right) + \frac{2\Gamma_{D2}}{\omega_{D2}^3} \left(\frac{1}{\omega - \omega_{D2}} - \frac{1}{\omega + \omega_{D2}} \right) \right], \quad (2.31)$$

$$\Gamma_{\text{sc}}(\mathbf{r}) = \frac{\pi c^2 \omega^3}{2\hbar} I(\mathbf{r}) \left[\frac{\Gamma_{D1}^2}{\omega_{D1}^6} \left(\frac{1}{\omega - \omega_{D1}} - \frac{1}{\omega + \omega_{D1}} \right)^2 + \frac{2\Gamma_{D2}^2}{\omega_{D2}^6} \left(\frac{1}{\omega - \omega_{D2}} - \frac{1}{\omega + \omega_{D2}} \right)^2 \right]. \quad (2.32)$$

2.2 Atom-atom interaction

In this section, atom-atom interactions in dilute cold gases are discussed briefly. For a more detailed presentation, the reader is referred to [34, 35, 43–45]. The typical densities of the considered gases range from 10^{12} to 10^{15} cm^{-3} , which results in average atom separations between $0.1 \mu\text{m}$ and $1 \mu\text{m}$. The interaction potential between two atoms that are separated by the distance $r > 1 \text{ nm}$ is given by the van der Waals potential

$$U_{\text{vdW}}(r) = -\frac{\hbar}{m} \frac{r_0^4}{r^6}, \quad (2.33)$$

with the atomic mass m and the range of the van der Waals force $r_0 \approx (1 - 10) \text{ nm}$. Since the average distance between atoms is much larger than the range of the interaction potential, only two-body interactions, i. e. binary collisions, are relevant. The considered gases are very cold with typical temperatures below $1 \mu\text{K}$, which implies that the relative momenta between the atoms are small. This fact can be quantified using the relation $kr_0 \ll 1$ with k being the relative wavenumber between two colliding atoms. Therefore, only the low-energy limit of scattering theory needs to be considered. In the next subsection, it is shown that this simplifies the analysis considerably since all the information about the atomic interaction can be expressed with a single quantity, the s -wave scattering length a_s .

2.2.1 Two-particle scattering

In this section, scattering theory [46] is reviewed in order to analyze binary low-energetic collisions. Consider the elastic scattering of two spinless, distinguishable, non-relativistic particles that interact via a rotationally symmetric short range potential $U(r)$. It is convenient to change from the position coordinates of the two atoms, \mathbf{r}_1 and \mathbf{r}_2 , to center-of-mass and relative coordinates

$$\mathbf{R} = \frac{m_1 \mathbf{r}_1 + m_2 \mathbf{r}_2}{m_1 + m_2}, \quad \mathbf{r} = \mathbf{r}_1 - \mathbf{r}_2, \quad (2.34)$$

with the masses of the particles m_1 and m_2 . The system's wave function separates with respect to these coordinates

$$\Psi(\mathbf{R}, \mathbf{r}) = \psi_{\text{com}}(\mathbf{R})\psi_{\text{rel}}(\mathbf{r}) \quad (2.35)$$

On the one hand, the center-of-mass part of the wave function ψ_{com} reduces to a constant prefactor if the center-of-mass reference frame is chosen. On the other hand, the part of the wave function describing the relative motion ψ_{rel} can be decomposed into momentum components ψ_k . If the z -axis is chosen in the direction of the incident relative momentum, then ψ_k can be expressed as the sum

$$\psi_k(r, \theta) = e^{ikr \cos \theta} + \psi_{\text{sc}}(r, \theta), \quad (2.36)$$

of an incident plane wave $e^{ikr \cos \theta}$ and a scattered wave ψ_{sc} . The aim of time-independent scattering theory is to determine the asymptotic expression of ψ_{sc} for large r . Starting point for this analysis is the Schrödinger equation

$$\left[-\frac{\hbar^2}{2\mu} \left(\partial_r^2 + \frac{2}{r} \partial_r + \frac{1}{r^2 \sin \theta} \partial_\theta \sin \theta \partial_\theta \right) + U(r) \right] \psi_k(r, \theta) = E_k \psi_k(r, \theta) \quad (2.37)$$

with the reduced mass $\mu = m_1 m_2 / (m_1 + m_2)$. From the above equation, it follows that ψ_k separates into a radial and an angular part. The eigenfunctions of the angular part are Legendre polynomials P_l . This fact is used in the partial wave expansion

$$\psi_k(r, \theta) = \sum_{l=0}^{\infty} A_l R_{kl}(r) P_l(\cos \theta). \quad (2.38)$$

The radial part R_{kl} obeys the radial Schrödinger equation

$$\left[-\frac{\hbar^2}{2\mu} \left(\frac{d^2}{dr^2} + \frac{2}{r} \frac{d}{dr} \right) + U_{\text{rot}}(r) + U(r) \right] R_{kl}(r) = E_k R_{kl}(r) \quad (2.39)$$

with the effective rotational potential

$$U_{\text{rot}}(r) = \frac{\hbar^2 l(l+1)}{2\mu r^2}, \quad (2.40)$$

creating the centrifugal barrier. For short range potentials or potentials that drop off sufficiently fast, R_{kl} satisfies the free radial Schrödinger equation with $U(r) = U_{\text{rot}}(r) = 0$ for $r \rightarrow \infty$. The solution of this equation is a linear combination of Bessel and Neumann functions [47]. For $kr \rightarrow \infty$ their asymptotic form can be used yielding

$$R_{kl}(r) \xrightarrow{r \rightarrow \infty} \frac{1}{kr} \sin(kr - l\pi/2 + \delta_l), \quad (2.41)$$

with the phase shifts δ_l containing all the information about the scattered wave. In the same limit, the scattered wave can be written as

$$\psi_{\text{sc}}(r, \theta) \xrightarrow{r \rightarrow \infty} f(\theta) \frac{e^{ikr}}{r}, \quad (2.42)$$

with the scattering amplitude f . The relation between the scattering amplitude and the phase shifts can be established using the partial wave expansion of the incident wave together with equations (2.36), (2.38) and (2.41) yielding

$$f(\theta) = \sum_{l=0}^{\infty} (2l+1) f_l P_l(\cos \theta), \quad f_l = \frac{e^{2i\delta_l} - 1}{2ik}. \quad (2.43)$$

For power law potentials of the type $U(r) = -C_s/r^s$ with $s \geq 2$ the k -dependence of the partial scattering amplitudes f_l can be computed in the limit $k \rightarrow 0$ [44]:

$$f_l \sim \begin{cases} k^{2l} & \text{for } l < \frac{s-3}{2}, \\ k^{s-3} & \text{for } l \geq \frac{s-3}{2}. \end{cases} \quad (2.44)$$

Therefore, for $s > 3$ all f_l with $l > 0$ are negligible in the limit $k \rightarrow 0$. This includes, as a special case, the van der Waals potential given in equation (2.33). Therefore, the low-momentum limit of the scattering wave function of two colliding alkali atoms is given by

$$\lim_{k \rightarrow 0} \psi_k(r, \theta) = 1 - \frac{a_s}{r}, \quad (2.45)$$

implicitly defining the s -wave scattering length a_s . The quantities scattering amplitude f , differential scattering cross section $\frac{d\sigma}{d\Omega}$, and total cross section σ are given by

$$f(\theta) = -a_s, \quad \frac{d\sigma}{d\Omega} = |f(\theta)|^2 = a_s^2, \quad \sigma = \int_0^{2\pi} \int_0^{\pi} |f(\theta)|^2 d\theta d\phi = 4\pi a_s^2. \quad (2.46)$$

The above expressions show that in the low-energy limit elastic two-particle scattering is entirely determined by the s -wave scattering length. In appendix A, the scattering lengths of the isotopes ${}^7\text{Li}$, ${}^{23}\text{Na}$, ${}^{41}\text{K}$, and ${}^{87}\text{Rb}$ in the $F = 1$ and $m_F = -1$ state are provided. It is worth noting that a_s can be tuned by applying an external magnetic field using a Feshbach resonance [48]. In this way, the non-interacting limit $a_s \rightarrow 0$ and the unitary limit $a_s \rightarrow \infty$ can be realized.

Until this point, it was assumed that the colliding particles are distinguishable. This is the case if the atoms are in distinct internal states or belong to different species. If the particles are identical bosons or fermions, then the two-particle wave function is symmetric respectively antisymmetric with respect to particle permutations. This results in symmetric respectively antisymmetric scattering amplitudes f_+ and f_- given by

$$f_{\pm}(\theta) = f(\theta) \pm f(\pi - \theta). \quad (2.47)$$

The above expression implies that identical fermions behave as free particles in the low-energy limit.

2.2.2 Pseudo potential

In the preceding subsection, it is shown that the collisional properties of a cold and dilute atomic gas are fully described by the respective s -wave scattering length. In particular, two interaction potentials that result in the same scattering length are indistinguishable in this regime. This leads to the idea to replace the complicated and possibly unknown real interaction potential by a simpler one that reproduces the same physics in the low-energy limit. This idea is called the method of pseudopotentials [49–51] and was introduced by Fermi [52]. In this work, ultracold identical bosons are considered for which s -wave scattering is dominant. In this case, the pseudopotential is given by [51]

$$U(\mathbf{r})\psi(\mathbf{r}) = \frac{4\pi\hbar^2 a_s}{m} \delta(\mathbf{r}) \partial_r(r\psi(\mathbf{r})). \quad (2.48)$$

For functions ψ that are less singular than $1/r$, this expression simplifies to

$$U(\mathbf{r}) = \frac{4\pi\hbar^2 a_s}{m} \delta(\mathbf{r}). \quad (2.49)$$

It is worth noting that the method of pseudopotentials was formulated in a mathematically rigorous way in [53] for arbitrary dimensions and all partial waves.

2.3 Cold dilute gases

In this section, the many-body physics of cold, interacting, bosonic atoms trapped in an optical dipole potential is formulated using the results of the preceding sections. For this task it is convenient to use the formalism of second quantization. The general form of the Hamilton operator for a system of identical bosons trapped in an external potential V and interacting via a two-body potential U is given by

$$\begin{aligned} \hat{H} = & \int \hat{\Psi}^\dagger(\mathbf{r}) \left[-\frac{\hbar^2}{2m} \nabla^2 + V(\mathbf{r}) \right] \hat{\Psi}(\mathbf{r}) d^3r \\ & + \frac{1}{2} \iint \hat{\Psi}^\dagger(\mathbf{r}) \hat{\Psi}^\dagger(\mathbf{r}') U(\mathbf{r}, \mathbf{r}') \hat{\Psi}(\mathbf{r}') \hat{\Psi}(\mathbf{r}) d^3r d^3r'. \end{aligned} \quad (2.50)$$

The field operator $\hat{\Psi}(\mathbf{r})$ annihilates a particle at position \mathbf{r} and obeys the commutation relations

$$[\hat{\Psi}(\mathbf{r}), \hat{\Psi}^\dagger(\mathbf{r}')] = \delta(\mathbf{r} - \mathbf{r}'), \quad [\hat{\Psi}(\mathbf{r}), \hat{\Psi}(\mathbf{r}')] = 0. \quad (2.51)$$

In the considered case, the external potential is the optical dipole potential produced by a coherent light field which is far detuned from the relevant atomic transitions (cf. section 2.1). As discussed in subsection 2.2.2, the two-body interaction potential can be substituted with the pseudo potential

$$U(\mathbf{r}, \mathbf{r}') = \frac{4\pi a_s \hbar^2}{m} \delta(\mathbf{r} - \mathbf{r}'). \quad (2.52)$$

This allows simplifying equation (2.50) to

$$\begin{aligned} \hat{H} = & \int \hat{\Psi}^\dagger(\mathbf{r}) \left[-\frac{\hbar^2}{2m} \nabla^2 + V(\mathbf{r}) \right] \hat{\Psi}(\mathbf{r}) d^3r \\ & + \frac{2\pi a_s \hbar^2}{m} \int \hat{\Psi}^\dagger(\mathbf{r}) \hat{\Psi}^\dagger(\mathbf{r}) \hat{\Psi}(\mathbf{r}) \hat{\Psi}(\mathbf{r}) d^3r. \end{aligned} \quad (2.53)$$

The above Hamilton operator is used as starting point for the discussion of many-body physics in the following chapters.

Chapter 3

Ultracold atoms in optical lattices

In this section, the physics of ultracold atoms in optical lattices is reviewed. This serves two purposes: First, the concepts, methods, and notations which are fundamental for the following chapters are introduced. Second, the success as well as the limitations of optical lattice experiments serve as motivation and guideline for this thesis.

In the preceding chapter, the physics of ultracold gases is discussed. One of the reasons why this field has attracted considerable interest is that it allows implementing clean and controllable systems. These can be used to demonstrate and isolate fundamental physical effects. This fact is exemplified by the demonstration of Bose-Einstein condensation [4, 5]. For this, weakly interacting ultracold gases provide an ideal platform, since the quantum statistical effect causing Bose-Einstein condensation is not overshadowed by interaction effects as it is the case in liquid Helium [54]. However, other many-body phenomena of interest require interactions that cause strong correlations between the particles. There are two approaches to implement this regime with ultracold atoms. First, the interaction strength can be increased by using Feshbach resonances [48]. Second, the importance of the interactions can be increased by decreasing other energy scales in the system. The latter approach is used in optical lattice experiments [15, 16]. Here, standing waves of far-detuned laser light are used to imprint a periodic potential onto the atoms. The optical lattice strongly decreases the system's kinetic energy since the atoms' motion is restricted to tunneling between the potential wells. This approach has the additional advantage that it allows studying many-body phenomena in lattices which are fundamental to solid-state physics.

This chapter is organized in the following way. In section 3.1, the single-particle physics in a periodic potential is discussed. Here, the concepts of band structure, as well as Bloch and Wannier functions, are introduced. Based on this description the many-body physics of ultracold atoms in optical lattices is investigated in section 3.2. It is shown that under certain conditions the considered system implements the Hubbard model, which was introduced by John Hubbard [55] to describe strongly correlated electrons in solids. This model is investigated for different parameter regimes, and its phase diagram is explored. In section 3.3, an overview of the research directions in the field of optical lattices is given.

3.1 Single-particle wave functions in periodic potentials

Consider an atom of mass m in an optical dipole potential V . The time independent Schrödinger equation in position representation is given by

$$\left(-\frac{\hbar^2}{2m}\Delta + V(\mathbf{r})\right)\psi_\lambda(\mathbf{r}) = E_\lambda\psi_\lambda(\mathbf{r}). \quad (3.1)$$

The wave functions ψ_λ and eigenenergies E_λ are associated to a tuple of quantum numbers λ that characterizes the corresponding state of the system.

In the following V is assumed to be a D -dimensional lattice potential, i. e.

$$V(\mathbf{r} + \mathbf{R}) = V(\mathbf{r}) \quad \forall \mathbf{R} \in \mathcal{G} \quad (3.2)$$

with the set of lattice vectors $\mathcal{G} = \{n_1 \mathbf{a}_1 + \dots + n_D \mathbf{a}_D : n_i \in \mathbb{Z}\}$ and the primitive lattice vectors \mathbf{a}_i . For this kind of potentials the system's energy eigenstates are Bloch waves [56]

$$\psi_{\mathbf{k}}^n(\mathbf{r}) = e^{i\mathbf{k}\mathbf{r}} u_{\mathbf{k}}^n(\mathbf{r}), \quad u_{\mathbf{k}}^n(\mathbf{r} + \mathbf{R}) = u_{\mathbf{k}}^n(\mathbf{r}), \quad (3.3)$$

with the wave vector \mathbf{k} in the first Brillouin zone, the band index n , and the corresponding energy $E_n(\mathbf{k})$. The periodicity of the functions $u_{\mathbf{k}}^n$ implies that they are delocalized. For deep potentials the atoms are tightly confined to the regions around the minima of V . In this case, it is advantageous to use a description based on wave functions that are localized on lattice sites. These are called Wannier functions [57] and are defined by

$$w_i^n(\mathbf{r}) = \frac{\Upsilon}{(2\pi)^D} \int_{\text{BZ}} e^{-i\mathbf{k}\mathbf{R}_i} \psi_{\mathbf{k}}^n(\mathbf{r}) d^D k, \quad \psi_{\mathbf{k}}^n(\mathbf{r}) = \sum_i w_i^n(\mathbf{r}) e^{i\mathbf{k}\mathbf{R}_i}. \quad (3.4)$$

In the above equations $\mathbf{R}_i \in \mathcal{G}$ is the position of the i^{th} lattice site, Υ is the volume of the primitive cell, and BZ denotes the first Brillouin zone. In [58], the analytic properties of Wannier functions are investigated and it is shown that they are exponentially localized around the corresponding lattice site. However, this is only the case for isolated energy bands, if the energy bands form composite groups the situation is more complicated. For this case maximally localized, generalized Wannier functions were introduced in [59]. It is worth noting that these functions can always be chosen real [59, 60].

3.2 Bose-Hubbard model

Based on the concepts of the preceding section, the many-body physics of ultracold bosonic atoms in periodic optical potentials is discussed in this section. In subsection 3.2.1, it is shown that under certain conditions the considered system implements the Bose-Hubbard model. In the subsections 3.2.2 and 3.2.3, the weak and strong interaction limit of the Bose-Hubbard model are investigated and in subsection 3.2.4 the model's phase diagram is explored.

3.2.1 Derivation of the Bose-Hubbard model

The idea to use ultracold atoms in optical lattices to implement the Bose-Hubbard model was introduced in [13]. In the following, the derivation and validity of this model are discussed. The starting point is the Hamilton operator for interacting ultracold atoms in an optical potential which is given in equation (2.50). The first step is to expand the field operator using the Wannier functions of the periodic optical potential

$$\hat{\Psi}(\mathbf{r}) = \sum_{n,i} \hat{a}_i^n w_i^n(\mathbf{r}). \quad (3.5)$$

Here, \hat{a}_i^n is the annihilation operator corresponding to the Wannier function w_i^n . This expansion is valid if the atom's energy is sufficiently low such that the contribution of unbound states is negligible.

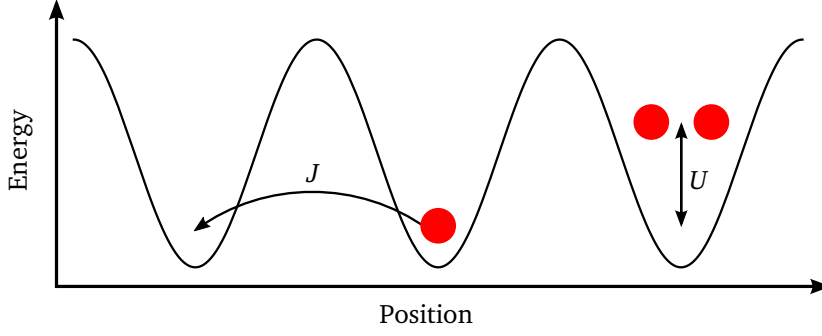


Figure 3.1: Schematic representation of the basic processes occurring in the Bose-Hubbard model. Tunneling between adjacent sites is connected to the energy scale J , whereas the on-site interaction of atoms is quantified by the energy U .

By inserting equation (3.5) into equation (2.50) the system's Hamilton operator can be written in the following form

$$\hat{H} = \sum_{n,i} \epsilon_i^n \hat{a}_i^{n\dagger} \hat{a}_i^n - \sum_n \sum_{i \neq j} J_{ij}^n \hat{a}_i^{m\dagger} \hat{a}_j^n + \frac{1}{2} \sum_{mnop} \sum_{ijkl} U_{ijkl}^{mnop} \hat{a}_i^{m\dagger} \hat{a}_j^{m\dagger} \hat{a}_k^o \hat{a}_l^p, \quad (3.6)$$

with the on-site energies ϵ_i^n , tunneling parameters J_{ij}^n , and interaction strengths U_{ijkl}^{mnop} defined by

$$\epsilon_i^n = \int w_i^n(\mathbf{r}) \left[-\frac{\hbar^2}{2m} \nabla^2 + V(\mathbf{r}) \right] w_i^n(\mathbf{r}) d^3r, \quad (3.7)$$

$$J_{ij}^n = - \int w_i^n(\mathbf{r}) \left[-\frac{\hbar^2}{2m} \nabla^2 + V(\mathbf{r}) \right] w_j^n(\mathbf{r}) d^3r, \quad (3.8)$$

$$U_{ijkl}^{mnop} = \frac{4\pi a_s \hbar^2}{m} \int w_i^m(\mathbf{r}) w_j^n(\mathbf{r}) w_k^o(\mathbf{r}) w_l^p(\mathbf{r}) d^3r. \quad (3.9)$$

For sufficiently low temperatures, deep lattice potentials, and weak interactions the contribution of all bands except for the lowest one can be neglected. Further, for deep optical potentials the Wannier functions are tightly localized around the minima of the potential. Therefore, the on-site interaction and the nearest-neighbor tunneling processes dominate. If a homogeneous system is considered, then the energy origin can be shifted in order to set the on-site energy of the lowest band to zero. This leads to the Hamilton operator of the Bose-Hubbard model [61]

$$\hat{H} = -J \sum_{\langle i,j \rangle} (\hat{a}_i^\dagger \hat{a}_j + \hat{a}_j^\dagger \hat{a}_i) + \frac{U}{2} \sum_i \hat{a}_i^\dagger \hat{a}_i^\dagger \hat{a}_i \hat{a}_i. \quad (3.10)$$

Here, J is the tunneling parameter between adjacent sites and U is the on-site interaction energy (cf. figure 3.1). The notation $\langle ij \rangle$ indicates that the summation is performed over nearest-neighbor pairs only. For the lowest band, J is always positive whereas the sign of U depends on the sign of the s -wave scattering length a_s . $U > 0$ corresponds to on-site repulsion whereas $U < 0$ corresponds to attraction. Quantitative investigations on the validity of the Bose-Hubbard model for ultracold atoms in optical lattices are performed in [62–68].

3.2.2 Weak interaction limit

In the regime of weak interactions, the contribution of tunneling to the system's total energy is dominant. Therefore, in order to investigate this regime, it is reasonable to diagonalize the corresponding part of the Hamilton operator

$$\hat{H}_J = -J \sum_{\langle i,j \rangle} (\hat{a}_i^\dagger \hat{a}_j + \hat{a}_j^\dagger \hat{a}_i). \quad (3.11)$$

This is achieved by introducing operators $\hat{c}_\mathbf{k}$ that annihilate a particle with a given lattice momentum \mathbf{k}

$$\hat{a}_i = \frac{1}{\sqrt{M}} \sum_{\mathbf{k}} \hat{c}_\mathbf{k} e^{-i\mathbf{k}\mathbf{R}_i}, \quad \mathbf{k} \in \left\{ \sum_{i=1}^D \frac{z_i}{m} \mathbf{b}_i : z_i \in \mathbb{Z}, \frac{m}{2} < z_i \leq \frac{m}{2} \right\}, \quad (3.12)$$

with the basis vectors of the reciprocal lattice \mathbf{b}_i obeying $\mathbf{a}_i \cdot \mathbf{b}_j = 2\pi\delta_{ij}$. Here, a finite lattice with $M = m^d$ sites and periodic boundary conditions is assumed. The physics of the homogeneous infinite lattice is recovered in the limit $M \rightarrow \infty$. Inserting the expression given in equation (3.12) into the Hamilton operator yields

$$\hat{H} = \sum_{\mathbf{k}} \epsilon_{\mathbf{k}} \hat{c}_\mathbf{k}^\dagger \hat{c}_\mathbf{k} + \frac{U}{2M} \sum_{\mathbf{k}} \sum_{\mathbf{k}'} \sum_{\mathbf{k}''} \sum_{\mathbf{k}'''} \hat{c}_\mathbf{k}^\dagger \hat{c}_{\mathbf{k}'}^\dagger \hat{c}_{\mathbf{k}''} \hat{c}_{\mathbf{k}'''} \delta_{\mathbf{k}+\mathbf{k}', \mathbf{k}''+\mathbf{k}'''}. \quad (3.13)$$

For a D -dimensional cubic lattice the single particle energy $\epsilon_{\mathbf{k}}$ is given by

$$\epsilon_{\mathbf{k}} = -2J \sum_{i=1}^D \cos(k_i d), \quad (3.14)$$

with the i^{th} quasi momentum coordinate k_i and the lattice constant d . For $U = 0$, the Hamilton operator in equation (3.13) is diagonal and at $T = 0$ and $D \geq 2$ a condensate in the $\mathbf{k} = 0$ mode is formed. The corresponding many-body state is given by

$$|\psi\rangle = \frac{(\hat{c}_0^\dagger)^N}{\sqrt{N!}} |0\rangle. \quad (3.15)$$

If U has a small but finite value, then some particles leave the condensate while the large majority remains at $\mathbf{k} = 0$. In this situation, the operators \hat{c}_0 and \hat{c}_0^\dagger are only weakly non-commutative since $\langle \hat{c}_0^\dagger \hat{c}_0 \rangle \gg [\hat{c}_0, \hat{c}_0^\dagger]$. Therefore, they can be treated as c-numbers plus small operator-valued corrections, i. e.

$$\hat{c}_0 = e^{i\phi} \sqrt{N_0} + \delta\hat{c}_0, \quad (3.16)$$

with the number of particles in the condensate $N_0 = \langle \hat{c}_0^\dagger \hat{c}_0 \rangle$ and the phase ϕ . Without loss of generality, the latter is set to zero in the following. Equation (3.16) corresponds to a gauge transformation to a symmetry broken state. This ansatz was introduced by Bogoliubov in order to investigate the physics of superfluid helium [69]. Later it was successfully applied in the field of ultracold gases [34, 35]. The application to the Bose-Hubbard model that is discussed in this subsection is developed in [70].

It is worth noting that the smallness of $\delta\hat{c}_0$ implies that $\langle \hat{c}_0 \rangle \neq 0$. This is not compatible with a fixed total particle number. Therefore, a grand canonical ensemble is considered in the following. Here, the mean particle number $N = \langle \hat{N} \rangle$ is fixed by a chemical potential μ . The state of the system is obtained by minimizing $\langle \hat{H} - \mu \hat{N} \rangle$.

Using equations (3.13) and (3.16) one obtains, up to two second order in the fluctuations $\delta\hat{c}_0^{(\dagger)}$, the following expression

$$\begin{aligned}\hat{H} - \mu\hat{N} &= \left(\frac{U}{2}n_0 - zJ - \mu\right)N_0 + (Un_0 - zJ - \mu)\sqrt{N_0}(\delta\hat{c}_0 + \delta\hat{c}_0^\dagger) \\ &+ \sum_{\mathbf{k}}(\epsilon_{\mathbf{k}} - \mu)\hat{c}_{\mathbf{k}}^\dagger\hat{c}_{\mathbf{k}} + \frac{Un_0}{2}\sum_{\mathbf{k}}(4\hat{c}_{\mathbf{k}}^\dagger\hat{c}_{\mathbf{k}} + \hat{c}_{\mathbf{k}}\hat{c}_{-\mathbf{k}} + \hat{c}_{\mathbf{k}}^\dagger\hat{c}_{-\mathbf{k}}^\dagger),\end{aligned}\quad (3.17)$$

with the condensate density $n_0 = N_0/M$. At the energy minimum the contribution of the term linear in the fluctuations vanishes. This can be used to relate the chemical potential to the condensate density $\mu = Un_0 - zJ$ with the coordination number $z = 2D$. Using this relation, $\hat{H} - \mu\hat{N}$ can be expressed as a bilinear function of the momentum operators

$$\begin{aligned}\hat{H} - \mu\hat{N} &= -\frac{1}{2}Un_0N_0 - \frac{1}{2}\sum_{\mathbf{k}}(zJ + \epsilon_{\mathbf{k}} + Un_0) \\ &+ \frac{1}{2}\sum_{\mathbf{k}}(\hat{c}_{\mathbf{k}}^\dagger, \hat{c}_{-\mathbf{k}})\begin{pmatrix} \epsilon_{\mathbf{k}} + zJ + Un_0 & Un_0 \\ Un_0 & \epsilon_{\mathbf{k}} + zJ + Un_0 \end{pmatrix}\begin{pmatrix} \hat{c}_{\mathbf{k}} \\ \hat{c}_{-\mathbf{k}}^\dagger \end{pmatrix}.\end{aligned}\quad (3.18)$$

The above operator can be diagonalized by introducing new operators $\hat{b}_{\mathbf{k}}$ that are connected to $\hat{c}_{\mathbf{k}}$ via a Bogoliubov transformation

$$\begin{pmatrix} \hat{b}_{\mathbf{k}} \\ \hat{b}_{-\mathbf{k}}^\dagger \end{pmatrix} = \begin{pmatrix} u_{\mathbf{k}} & v_{\mathbf{k}} \\ v_{-\mathbf{k}}^* & u_{-\mathbf{k}}^* \end{pmatrix} \begin{pmatrix} \hat{c}_{\mathbf{k}} \\ \hat{c}_{-\mathbf{k}}^\dagger \end{pmatrix}.\quad (3.19)$$

In order to preserve the commutator relations, i. e. $[\hat{b}_{\mathbf{k}}, \hat{b}_{\mathbf{k}'}^\dagger] = \delta_{\mathbf{k}\mathbf{k}'}$, the coefficients $u_{\mathbf{k}}$ and $v_{\mathbf{k}}$ need to satisfy

$$|u_{\mathbf{k}}|^2 - |v_{\mathbf{k}}|^2 = 1.\quad (3.20)$$

A diagonalization of the expression in equation (3.18) corresponds to the matrix equation

$$\begin{pmatrix} u_{\mathbf{k}} & v_{\mathbf{k}} \\ v_{\mathbf{k}} & u_{\mathbf{k}} \end{pmatrix} \begin{pmatrix} \epsilon_{\mathbf{k}} + zJ + Un_0 & Un_0 \\ Un_0 & \epsilon_{\mathbf{k}} + zJ + Un_0 \end{pmatrix} \begin{pmatrix} u_{\mathbf{k}} & v_{\mathbf{k}} \\ v_{\mathbf{k}} & u_{\mathbf{k}} \end{pmatrix} = \begin{pmatrix} \hbar\omega_{\mathbf{k}} & 0 \\ 0 & \hbar\omega_{\mathbf{k}} \end{pmatrix},\quad (3.21)$$

with the energy $\hbar\omega_{\mathbf{k}}$. Here, it is assumed that $u_{\mathbf{k}}$ and $v_{\mathbf{k}}$ are real and $u_{\mathbf{k}} = u_{-\mathbf{k}}$, $v_{\mathbf{k}} = v_{-\mathbf{k}}$. This simplification will be justified by diagonalization the right-hand side of equation (3.18). The off-diagonal and diagonal parts of equation (3.21) yield the equations

$$(u_{\mathbf{k}}^2 + v_{\mathbf{k}}^2)Un_0 - 2u_{\mathbf{k}}v_{\mathbf{k}}(\epsilon_{\mathbf{k}} + zJ + Un_0) = 0,\quad (3.22)$$

$$(u_{\mathbf{k}}^2 + v_{\mathbf{k}}^2)(\epsilon_{\mathbf{k}} + zJ + Un_0) - (u_{\mathbf{k}}v_{\mathbf{k}} + u_{\mathbf{k}}v_{\mathbf{k}})Un_0 = \hbar\omega_{\mathbf{k}},\quad (3.23)$$

respectively. Using equations (3.22) and (3.20) the coefficients $u_{\mathbf{k}}$ and $v_{\mathbf{k}}$ can be determined to

$$u_{\mathbf{k}}^2 = \frac{\epsilon_{\mathbf{k}} + zJ + n_0U}{2\sqrt{(zJ + \epsilon_{\mathbf{k}})^2 + 2Un_0(zJ + \epsilon_{\mathbf{k}})}} + \frac{1}{2},\quad (3.24)$$

$$v_{\mathbf{k}}^2 = \frac{\epsilon_{\mathbf{k}} + zJ + n_0U}{2\sqrt{(zJ + \epsilon_{\mathbf{k}})^2 + 2Un_0(zJ + \epsilon_{\mathbf{k}})}} - \frac{1}{2}.\quad (3.25)$$

From the above expressions and equation (3.23), the energies $\hbar\omega_{\mathbf{k}}$ are derived

$$\hbar\omega_{\mathbf{k}} = \sqrt{(\epsilon_{\mathbf{k}} + zJ)^2 + 2Un_0(\epsilon_{\mathbf{k}} + zJ)}.\quad (3.26)$$

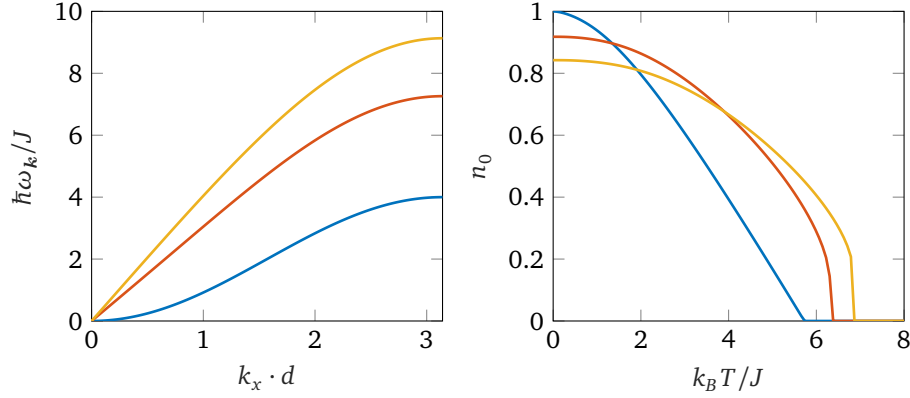


Figure 3.2: Bogoliubov approximation for the Bose-Hubbard model. The left figure shows the Bogoliubov dispersion relation $\hbar\omega_{\mathbf{k}}$ at $T = 0$ and $n = 1$ along the $\mathbf{k} = (k_x, k_y = 0, k_z = 0)$ line for a three-dimensional cubic lattice with $U/J = 0$ (blue line), $U/J = 5$ (red line), and $U/J = 10$ (yellow line). For the same parameters, the right figure shows the condensate fraction n_0 as a function of the temperature T . For the calculations, $M = 40^3$ was used.

It is worth noting that negative energy solution $-\hbar\omega_{\mathbf{k}}$ is disregarded because it is unphysical. The diagonal form of equation (3.18) is given by

$$\hat{H} - \mu\hat{N} = -\frac{1}{2}Un_0N_0 + \frac{1}{2}\sum_{\mathbf{k}}(\hbar\omega_{\mathbf{k}} - \epsilon_{\mathbf{k}} - zJ - Un_0) + \sum_{\mathbf{k}}\hbar\omega_{\mathbf{k}}\hat{b}_{\mathbf{k}}^\dagger\hat{b}_{\mathbf{k}}. \quad (3.27)$$

The operators $\hat{b}_{\mathbf{k}}$ are annihilation operators of excitations that can be interpreted as non-interacting quasi particles. The last remaining quantity that needs to be determined is the condensate density n_0 . For this the expression for the particle density $n = \langle\hat{N}\rangle/M$ can be used

$$n = n_0 + \frac{1}{M}\sum_{\mathbf{k}\neq\mathbf{0}}\langle\hat{c}_{\mathbf{k}}^\dagger\hat{c}_{\mathbf{k}}\rangle = n_0 + \frac{1}{M}\sum_{\mathbf{k}\neq\mathbf{0}}[(u_{\mathbf{k}}^2 + v_{\mathbf{k}}^2)\langle\hat{b}_{\mathbf{k}}^\dagger\hat{b}_{\mathbf{k}}\rangle + v_{\mathbf{k}}^2]. \quad (3.28)$$

Using the Bose-Einstein distribution for the non-interacting quasi particles

$$\langle\hat{b}_{\mathbf{k}}^\dagger\hat{b}_{\mathbf{k}}\rangle = \frac{1}{e^{\beta\hbar\omega_{\mathbf{k}}} - 1} \quad (3.29)$$

at the inverse temperature $\beta = 1/(k_B T)$ yields

$$n = n_0 + \frac{1}{M}\sum_{\mathbf{k}\neq\mathbf{0}}\left(\frac{\epsilon_{\mathbf{k}} + zJ + Un_0}{\hbar\omega_{\mathbf{k}}}\frac{1}{e^{\beta\hbar\omega_{\mathbf{k}}} - 1} + \frac{\epsilon_{\mathbf{k}} + zJ + Un_0 - \hbar\omega_{\mathbf{k}}}{2\hbar\omega_{\mathbf{k}}}\right). \quad (3.30)$$

The above equation can be solved numerically for a given density n and temperature T to determine n_0 .

The dispersion relation $\hbar\omega_{\mathbf{k}}$ and the condensate fraction n_0 are shown figure 3.2 for a three-dimensional cubic lattice and $n = 1$. It is worth noting that the system's excitation spectrum given in equation (3.26) is gapless in the thermodynamic limit, i. e. $N, M \rightarrow \infty$ with constant N/M . For small wave vectors $|\mathbf{k}|d \ll 1$ the dispersion relation $\hbar\omega_{\mathbf{k}}$ is linear. Therefore, the system satisfies Landau's criterion for superfluidity [34]. At a critical temperature a phase transition to a normal phase occurs [61].

3.2.3 Strong interaction limit

In the regime of strong interactions, the on-site repulsion of particles contributes the dominant part of the system's energy. The eigenstates of the corresponding part of the Hamiltonian operator

$$\hat{H}_U = \frac{U}{2} \sum_i \hat{a}_i^\dagger \hat{a}_i^\dagger \hat{a}_i \hat{a}_i \quad (3.31)$$

are products of local Fock states

$$|\mathbf{n}\rangle = \prod_{i=1}^M \frac{(\hat{a}_i^\dagger)^{n_i}}{\sqrt{n_i!}} |0\rangle, \quad \mathbf{n} \in \mathcal{N} = \left\{ (n_1, n_2, \dots, n_M) : \sum_{i=1}^M n_i = N \right\}. \quad (3.32)$$

It is worth noting that these states constitute an orthonormal basis of the Hilbert space. Therefore, they can be used for state representation. This is discussed in appendix B. The interaction energy corresponding to the state $|\mathbf{n}\rangle$ is given by

$$E_{\mathbf{n}} = \frac{U}{2} \sum_{i=1}^M n_i(n_i - 1). \quad (3.33)$$

Therefore, for $J = 0$ and commensurate filling, i. e. $N = \bar{n}M$ with $\bar{n} \in \mathbb{N}$, the system's ground state is the number state $|\bar{\mathbf{n}}\rangle$ with $\bar{n}_i = \bar{n}$. This state is separated by an energy gap of magnitude U from the lowest excited states. The latter are of the form

$$|p, q\rangle = \frac{\hat{a}_p^\dagger \hat{a}_q}{\sqrt{\bar{n}(\bar{n} + 1)}} |\bar{\mathbf{n}}\rangle. \quad (3.34)$$

Here, an excess particle and a hole is created at site p and q respectively. For small but finite tunneling parameters $J \ll U$ this qualitative picture remains valid. In this regime, quantitative results can be obtained by treating the tunneling part \hat{H}_J of the Hamiltonian operator with perturbation theory [71, 72]. This approach is used to compute a multitude of observables to high accuracy [73, 74]. As an example, the ground state energy

$$E = E^{(0)} + \Delta E^{(1)} + \Delta E^{(2)} + \mathcal{O}\left(\frac{J^3}{U^3}\right), \quad (3.35)$$

can be computed to second order in J/U

$$E^{(0)} = \langle \bar{\mathbf{n}} | \hat{H}_U | \bar{\mathbf{n}} \rangle = \frac{MU}{2} \bar{n}(\bar{n} - 1), \quad \Delta E^{(1)} = \langle \bar{\mathbf{n}} | \hat{H}_J | \bar{\mathbf{n}} \rangle = 0, \quad (3.36)$$

$$\Delta E^{(2)} = \sum_{\mathbf{n} \neq \bar{\mathbf{n}}} \frac{|\langle \mathbf{n} | \hat{H}_{\text{tun}} | \bar{\mathbf{n}} \rangle|^2}{E_{\bar{\mathbf{n}}} - E_{\mathbf{n}}} = -2 \sum_{\langle ij \rangle} \frac{|\langle j, i | \hat{a}_i^\dagger \hat{a}_j | \bar{\mathbf{n}} \rangle|^2}{U} = -zM \frac{J^2}{U} \bar{n}(\bar{n} + 1). \quad (3.37)$$

The phase corresponding to the situation analyzed in the preceding paragraph is called Mott insulator. Here, particle transport is strongly suppressed due to the on-site repulsion of the particles. Strictly speaking the Mott insulator exists only at $T = 0$, however, for low temperatures $k_B T \lesssim 0.2U$ the characteristic features survive. For higher temperatures, the Mott insulator melts into a normal phase [75].

3.2.4 Phase diagram

In the preceding subsections, two limits of the Bose-Hubbard model are discussed. For low temperatures and commensurable fillings, the system is either in the superfluid phase (weak interactions) or the Mott-insulator phase (strong interactions). In the intermediate regime, a quantum phase transition occurs. In this subsection, the phase diagram of the Bose-Hubbard model is investigated. For this task, the Gutzwiller approach [76–78] is used. Here, the system's state is approximated by a product state of the form

$$|\psi\rangle = \prod_{i=1}^M \sum_{n=0}^{n_{\max}} f_{n,i} \frac{\hat{a}_i^{\dagger n}}{\sqrt{n!}} |0\rangle, \quad (3.38)$$

with n_{\max} being a cutoff in the populations of sites. For $n_{\max} = N$ this ansatz is exact in the strong interaction limit since the number states defined in equation (3.32) are included as special cases in the above definition. However, for the weak interaction limit, the system's ground state is very different from a product state (cf. equation (3.15)). Therefore, it is remarkable that in the thermodynamic limit the Gutzwiller approach produces correct results for all local observables at $U = 0$ [79]. This raises the hope that the Gutzwiller approach yields reasonable results for all parameter regimes. It is worth noting that the Gutzwiller approach is equivalent to a mean field approximation [80] in which a local Hamilton operator is obtained by approximating the tunneling term in the following way

$$\hat{a}_i^{\dagger} \hat{a}_j \approx \hat{a}_i^{\dagger} \langle \hat{a}_j \rangle + \langle \hat{a}_i^{\dagger} \rangle \hat{a}_j - \langle \hat{a}_i^{\dagger} \rangle \langle \hat{a}_j \rangle. \quad (3.39)$$

The mean-field nature of the Gutzwiller approach implies that it is exact for $z \rightarrow \infty$. In fact, in [81, 82] it is shown that the Gutzwiller approach corresponds to the zeroth-order term in a hierarchy of inter-site correlations that yields a systematic expansion in $1/z$. Another refinement of the Gutzwiller approach based on a cluster expansion is developed in [83]. It is worth noting that the Gutzwiller approach can also be used to compute the system's time evolution [84, 85]. The equations of motion for the time-dependent parameters $f_{n,i}(t)$ can be derived by minimizing the functional

$$\langle \psi | i\hbar \partial_t - \hat{H} | \psi \rangle \quad (3.40)$$

with respect to $f_{n,i}^*(t)$. This is known as the Dirac-Frenkel variational principle.

Using the Gutzwiller approach the critical value u_c for the ratio U/J regarding the superfluid to Mott insulator transition at integer density \bar{n} can be predicted [78]. For a homogeneous system the coefficients of the ansatz in equation (3.38) do not depend on the site index i . Further, in the regime close to the transition point only the coefficients $f_{\bar{n}-1}$, $f_{\bar{n}}$ and $f_{\bar{n}+1}$ contribute. Using the normalization condition $\sum_n |f_n|^2 = 1$ and $\sum_n n |f_n|^2 = \bar{n}$ the state can be parametrized in the following way

$$|\psi\rangle = \prod_{i=1}^M \left(\epsilon \frac{\hat{a}_i^{\dagger \bar{n}-1}}{\sqrt{(\bar{n}-1)!}} + \sqrt{1-2\epsilon^2} \frac{\hat{a}_i^{\dagger \bar{n}}}{\sqrt{\bar{n}!}} + \epsilon \frac{\hat{a}_i^{\dagger \bar{n}+1}}{\sqrt{(\bar{n}+1)!}} \right) |0\rangle. \quad (3.41)$$

The coefficient ϵ can be determined by minimizing the energy

$$\langle \psi | \hat{H} | \psi \rangle = -zJM(\epsilon^2 - 2\epsilon^4) (\sqrt{\bar{n}} + \sqrt{\bar{n}+1})^2 + \frac{UM}{2} [\bar{n}(\bar{n}-1)2\epsilon^2] \quad (3.42)$$

yielding

$$\epsilon = \frac{1}{2} \sqrt{1 - (\sqrt{\bar{n}} - \sqrt{\bar{n}+1})^2 \frac{U}{zJ}}. \quad (3.43)$$

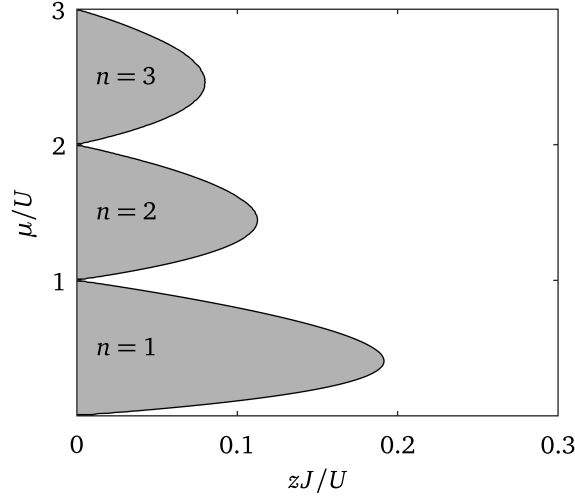


Figure 3.3: Mean field phase diagram of the Bose-Hubbard model at $T = 0$. The gray areas correspond to the Mott-insulator phases with density n . The white area is the superfluid phase.

The critical value for the phase transition is reached at $\epsilon = 0$, i. e. a number state is formed. This yields

$$u_c = z \left(\sqrt{\bar{n}} + \sqrt{\bar{n} + 1} \right)^2. \quad (3.44)$$

To determine the phase diagram of the Bose-Hubbard model, it is necessary to identify a quantity that distinguishes the superfluid and the Mott insulator phase. A possible choice is the local number variance $\delta^2 n_i = \langle \hat{n}_i^2 \rangle - \langle \hat{n}_i \rangle^2$. This quantity is zero in the Mott-insulator phase and larger than zero in the superfluid phase.

To map out the phase diagram, the amplitudes f_n need to be determined from a minimization of the functional

$$\langle \psi | \hat{H} - \mu \hat{N} | \psi \rangle = \frac{MU}{2} \sum_{n=0}^{n_{\max}} |f_n|^2 n(n-1) - MJ \left| \sum_{n=1}^{n_{\max}} f_{n-1}^* f_n \sqrt{n} \right|^2 - \mu M \sum_{n=0}^{n_{\max}} |f_n|^2 n \quad (3.45)$$

for all values of U , J , and μ . Here, a grand canonical ensemble with a chemical potential μ is considered. The local number variance is calculated from

$$\delta n^2 = \sum_{n=0}^{n_{\max}} |f_n|^2 n^2 - \left(\sum_{n=0}^{n_{\max}} |f_n|^2 n \right)^2. \quad (3.46)$$

The result of this calculation is shown in figure 3.3. Here, the gray regions are Mott-insulator phases with integer densities n and $\delta n^2 = 0$ whereas the white region is the superfluid phase with $\delta n^2 > 0$. From the phase diagram, the incompressibility of the Mott insulator phase can be observed, i. e. an increase in the chemical potential does not lead to a change in the particle number. This is a result of the energy gap in the excitation spectrum.

The system's behavior for non-zero temperature has been discussed in the preceding subsection for the weak and strong interaction limit separately. In the weak interaction regime, a phase transition to the normal phase occurs at a critical temperature, whereas in the strong interaction regime a crossover to the normal phase can be observed. Detailed studies of the finite-temperature phase diagram of the Bose-Hubbard model are performed in [75, 82, 86–89].

3.3 Overview of research directions

The proposal to implement the Bose-Hubbard model with ultracold atoms in optical lattices [13] and the experimental demonstration of the superfluid to Mott-insulator transition [14] attracted considerable interest and initiated a rapidly growing research field. The following list contains a selection of this field's research direction. For exhaustive overviews, the reader is referred to the following reviews [15, 16, 18, 90–93].

- **Single-site resolution**

The first experiments with ultracold atoms in optical lattices used time-of-flight measurements [14]. Though these measurements allow observing the superfluid to Mott-insulator transition, the accessible observables are limited. This triggered the interest in alternative measurement techniques. Most information about the physical system can be obtained from site-resolved measurements of the atom distribution. This approach was implemented for bosonic [94–96] and fermionic systems [97–103] allowing to access a variety of properties of the many-body system.

- **Exotic lattice geometries**

Besides cubic lattices also more exotic lattice geometries have been implemented in optical lattice experiments. Among these are superlattices [104–111], quasicrystals [112], kagome lattices [113, 114], checkerboard lattices [115, 116], and triangular and honeycomb lattices [117–122]. Notably, the honeycomb lattice geometry has attracted considerable interest for its connection to graphene and the Dirac cone in its band structure [123].

- **Artificial gauge fields**

One of the motivations for optical lattice experiments is to implement analogs of condensed matter systems. However, in contrast to electrons, ultracold atoms do not have a net charge which prohibits the direct implementation of phenomena based on the interactions with the electromagnetic gauge field. Therefore, techniques to implement artificial gauge fields have been developed [124–126], which allow studying analogs of topological effects in condensed matter systems and possibly the simulation high energy physics.

- **Disorder and localization**

In a seminal paper, Anderson [127] established the connection between disorder and localization in lattice systems. The considered model is equivalent to the Hubbard model with $U = 0$, which is called the tight-binding model. The question to what extent the connection between disorder and localization applies to interacting many-body systems is investigated intensively. Optical lattice experiments allow for the measurement of the atom distribution and the introduction of controllable disorder enabling the study of this question experimentally [128–138].

- **Antiferromagnetic order in the Fermi-Hubbard model**

The Fermi-Hubbard model is considered to be the simplest model to explain high T_c superconductivity [139]. However, the exploration of its phase diagram is very challenging, and many open questions are still unanswered. Optical lattice experiments with fermionic atoms may help to solve these questions. The challenge for these experiments is that the interesting part of the phase diagram is located at very low temperatures which have not been reached in state-of-the-art experiments. The first step in this direction is the observation of antiferromagnetic correlations which has been reported recently [140–146].

Part II

Feasibility

Chapter 4

Optical trapping potential

In this chapter, the light field, which generates the optical microtrap array, is investigated. The main task is to compute the intensity distribution, since it is directly proportional to the optical potential for the atoms (cf. section 2.1).

The chapter is organized in the following way. In section 4.1, the generation of optical microtraps with microlens arrays is discussed and compared to alternative techniques. Computational methods for light propagation are briefly reviewed in section 4.2. In section 4.3, results of measurements and simulations are presented for a specific setup. Based on this, a parametrization of the light field is given in section 4.4.

4.1 Generation of optical microtraps

In the following, the experimental implementation of optical microtraps for ultracold atoms is discussed. The focus is on a technique based on microlens arrays, which is presented in the following subsection. Thereafter, alternative techniques are reviewed, and advantages and disadvantages of the different approaches are compared.

4.1.1 Microlens arrays

Microlens arrays (MLAs) are arrays of lenses with typical diameters between 1 mm and 10 μm . Due to the wide range of applications, from light collection for CCD arrays to laser beam homogenization, these devices are commercially available with a large variety of parameters. If a collimated laser beam illuminates an MLA, then an array of light spots is generated in the MLA's focal plane. These spots can be used to trap atoms if the laser light is red detuned to the atomic transition (cf. section 2.1 and [147–149]).

To allow for sufficiently fast tunneling, the trap spacing needs to be in the order of 1 μm . Therefore, it is necessary to reimage and demagnify the intensity distribution in the MLA's focal plane. This can be done by a combination of an achromatic lens and a high numerical aperture (NA) objective. The demagnification achieved with this configuration is equal to the ratio of the components' focal lengths. The NA of the objective limits the size of the focal spots after demagnification. To minimize crosstalk between adjacent traps, the trap spacing should be larger than the trap size. Single-site resolved control over the traps can be added to the setup by using a spatial light modulator, which controls the illumination of each microlens individually. In addition, the tunneling strengths between the traps can be controlled by adding an identical setup for blue-detuned light. To confine the atoms in the direction of the optical axis, a light sheet is used. Figure 4.1 shows a scheme of the described setup.

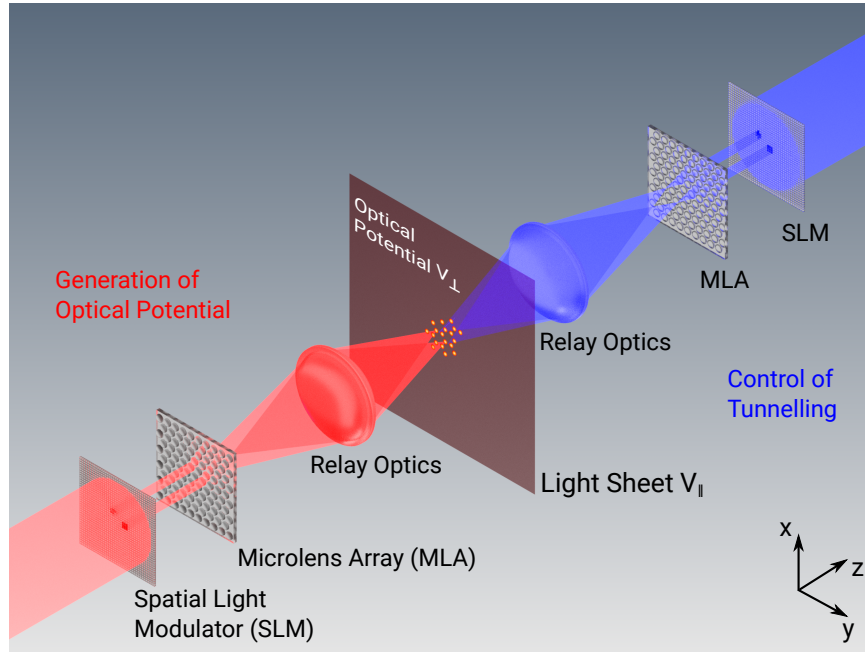


Figure 4.1: Scheme of the setup for the generation of an adjustable array of optical microtraps. The intensity profile of a red-detuned laser beam (from the bottom-left) is shaped by an SLM and used to illuminate an MLA. This setup generates an array of focal spots which is reimaged and demagnified by relay optics. This produces an optical microtrap array for the atoms. An identical setup for a blue-detuned laser beam (from the top-right) is used to control the tunneling between the traps individually. A light sheet adds additional confinement for the atoms along the direction of the optical axis. Figure courtesy of Malte Schlosser.

4.1.2 Alternative techniques

In this subsection, alternative techniques for the production of arrays of optical microtraps are discussed and compared to the MLA-based approach. Acousto-optic deflectors (AODs) can be used to split a laser beam into a beam array. The angles between the beamlets depend on the frequencies of the applied radio-frequency field whereas the corresponding amplitudes control the relative intensities. The beam array can be used as an array of optical microtraps for ultracold atomic gases. This was demonstrated for bosonic [150] and fermionic [151] species. In addition, these experiments varied the frequencies of the applied radio-frequency field in time to generate more flexible time-averaged potentials. AODs were also used in double-well [152, 153] and atom-assembly [154, 155] experiments. Compared to the MLA approach, the AOD technique is more restricted in terms of array geometries. To some extent, this can be overcome by time-averaged potentials. However, these introduce an additional source of heating [151].

Spatial light modulators (SLMs) allow for a spatially and temporally resolved modification of an incoming light field's amplitude or phase. The former can be achieved with digital micromirror devices (DMDs) whereas the latter is facilitated by liquid-crystal (LC) based devices. The most direct approach to generate optical microtraps is to image and demagnify the intensity distribution on a DMD [156]. Compared to the MLA based approach this allows implementing a wider variety of lattice geometries. However, the implementation of gray scales is much more limited.

Alternatively, the SLM can be used as a holographic phase [157] or amplitude [158] mask. This allows generating nearly arbitrary trap geometries and compensating wave-front aberrations of the used optical setup. However, the computation of the holograms is computationally expensive and often additional feedback loops are required. Further, the number of available pixel limits the achievable trap homogeneity and the system size.

4.2 Simulation methods for optical systems

In this section, the computation of the light field for a given optical setup is discussed. The methods which are introduced here are used in the subsequent section to determine the optical potential for the atoms. A standard problem of optics is to compute the action of an optical system on an incoming light field. For the exact solution, Maxwell's equations need to be solved for the corresponding boundary conditions. However, the solution of these equations is a formidable task, and approximative methods usually yield sufficiently accurate results. In the following subsections, the most commonly used approximations and their ranges of validity are discussed.

4.2.1 Geometrical optics

For many practical purposes, the wave character of light can be neglected, since its wavelength is usually much smaller than all other relevant length scales. The corresponding theory, which is derived from the short-wave asymptotics of Maxwell's equations, is called geometrical optics [159]. Within this theory, light propagation is described by rays along which the light field's energy is transported. Fermat's principle states that these rays are curves for which the line integral $S = \int_{\gamma} n ds$ is stationary. Here, γ is a curve connecting two points \mathbf{r}_1 and \mathbf{r}_2 and n is the index of refraction. For most optical systems the latter is a piecewise constant function of position. This implies that light rays are straight lines with a kink at the interface between two media. Snell's law of refraction determines the corresponding angles. Light propagation through an optical system can be simulated by constructing rays using the aforementioned rules. This method is called ray tracing. Since the computation of different rays is independent, the task of computing multiple rays can be parallelized allowing for efficient implementation on modern computers.

4.2.2 Scalar diffraction theory

Geometric optics neglects the wave character of light. Therefore, it does not allow for a comprehensive description of diffraction phenomena. However, especially close to the focus of an optical system, diffraction plays an important role. In the following, an efficient way to calculate diffraction effects, namely scalar diffraction theory [160, 161], is introduced. This allows computing the electric field at a point \mathbf{r} from the electric field given on a surface S . To derive this expression, several approximations are made: First, only monochromatic waves with an angular frequency ω are considered. Second, instead of the electric vector field a scalar field, i.e. one polarization component, is considered. The latter is only valid if the polarization components are uncoupled. The field can be written in the following form

$$\mathbf{E}(\mathbf{r}, t) = \mathcal{E}(\mathbf{r}) e^{-i\omega t} \mathbf{e}_p + \mathcal{E}^*(\mathbf{r}) e^{i\omega t} \mathbf{e}_p^*. \quad (4.1)$$

Third, in case of a finite aperture, boundary conditions need to be specified. There are two commonly used boundary conditions which were introduced by Kirchhoff and Sommerfeld respectively. Using either of these together with Green's theorem and Sommerfeld's

radiation condition, one arrives at an integral formula for the scalar positive frequency component of the electric field at the position \mathbf{r}

$$\mathcal{E}(\mathbf{r}) = -\frac{i}{\lambda} \int_S \frac{e^{ikr'}}{r'} K(\mathbf{r}, \boldsymbol{\sigma}) \mathcal{E}(\boldsymbol{\sigma}) d^2\sigma. \quad (4.2)$$

Here, S is a surface on which the electric field is known, $\boldsymbol{\sigma} \in S$, $r' = |\mathbf{r} - \boldsymbol{\sigma}|$, and $K(\mathbf{r}, \boldsymbol{\sigma})$ is the inclination factor, which depends on the chosen boundary conditions. A derivation of this formula can be found in [160, 161].

The numerical evaluation of the integral in equation (4.2) is computationally expensive. Therefore, additional approximations are frequently applied. Among these, the Fresnel approximation is arguably the most important. It is derived from the observation, that in most optical systems a principal axis of light propagation can be defined. This is called the optical axis and without loss of generality it is chosen to be the z axis. In addition, it is assumed that S lies in a plane at $z = 0$. Using Cartesian coordinates for $\mathbf{r} = (x, y, z)$ and $\boldsymbol{\sigma} = (x', y', 0)$ allows introducing the smallness parameters $|x - x'|/z \ll 1$ and $|y - y'|/z \ll 1$. The Fresnel approximation consists in expanding r in these parameters yielding

$$r = z \sqrt{1 + \frac{(x - x')^2}{z^2} + \frac{(y - y')^2}{z^2}} \approx z \left[1 + \frac{(x - x')^2}{2z^2} + \frac{(y - y')^2}{2z^2} \right]. \quad (4.3)$$

For the denominator in e^{ikr}/r the even stronger approximation $r \approx z$ is used. Together with the approximation $K \approx 1$ this yields

$$\mathcal{E}(x, y, z) = \frac{e^{ikz}}{i\lambda z} \iint \exp \left\{ \frac{i\pi}{\lambda z} [(x - x')^2 + (y - y')^2] \right\} \mathcal{E}(x', y', 0) dx' dy'. \quad (4.4)$$

A detailed discussion on the validity of this approximation can be found on pages 68 to 72 in [161]. Equation (4.4) can be interpreted either as a convolution of the initial electric field with the function $\exp[i\pi(x^2 + y^2)/(\lambda z)]$, or as multiplication with a quadratic phase and a subsequent Fourier transform. The former is called angular spectrum propagation and the latter is called Fresnel propagation. Both methods allow for the numerical calculation of the propagated electric field using the fast Fourier transform algorithm. Which of the two approaches is preferable depends on the Fresnel number $F = a^2/(\lambda z)$, with the aperture's linear dimension a . The angular spectrum propagator is used for large F whereas the Fresnel propagator is used for small F [162]. It is worth noting that in the far field $F \ll 1$, equation (4.4) can be simplified further by applying the Fraunhofer approximation [161]. However, this is not used for the calculations in the following sections.

4.2.3 Vector diffraction theory

To provide fast tunneling as well as single-site control, the waists of the desired traps need to be on the order of the light field's wavelength. Therefore, the focal plane of the MLA needs to be demagnified using an objective with a high NA. Scalar diffraction theory ceases to be valid for this kind of optical systems because close to the focal region the polarization components couple to each other. In [163], a vector diffraction theory for the electromagnetic field in the focal region of an optical system with a high NA is derived. It is a generalization of Debye's formulation [164] to vector fields which is valid if both the exit pupil's linear dimension and the distance between the observation point and the exit pupil (cf. figure 4.2) are much larger than the light field's wavelength λ .

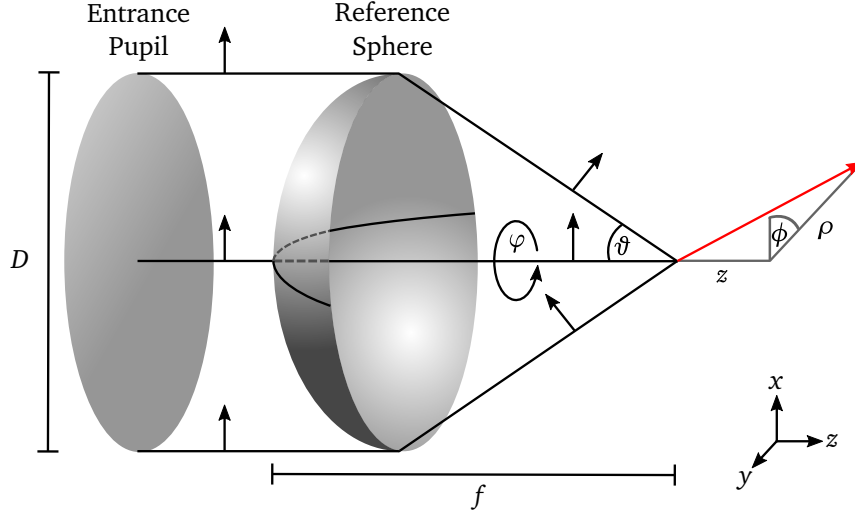


Figure 4.2: Schematic representation of the geometry for the Debye-Wolf vectorial diffraction integral. An incident electromagnetic wave passes through the optical system's entrance pupil with diameter D . The wavefront of the field is mapped onto a sphere in the region of the exit pupil. The focal plane is positioned at a distance f behind the exit pupil.

This condition is satisfied for the objectives that are considered in this work since these have diameters and focal lengths in the millimeter regime whereas $\lambda \approx 1 \mu\text{m}$.

The electric field's positive frequency component (cf. equation (2.6)) at a point in the focal region, which is specified by Cartesian coordinates x, y, z with respect to the Gaussian image point that obey $x^2 + y^2 + z^2 \ll f^2$, is given by

$$\mathcal{E}(x, y, z) = -\frac{i}{\lambda} \iint_S \frac{\mathbf{a}(s_x, s_y)}{s_z} e^{ik(s_x x + s_y y + s_z z)} ds_x ds_y. \quad (4.5)$$

Here, the light field's wave number $k = 2\pi/\lambda = \omega/c$, a unit vector $\mathbf{s} = (s_x, s_y, s_z)$ in direction of the local wave vector, the wavefront S at the exit pupil, and the system's focal length f are introduced. The strength factor $\mathbf{a}(s_x, s_y)$ is a complex vector field that encodes the strength and polarization of the incident electric field. It is worth mentioning that in contrast to Huygens principle the electric field in equation (4.5) is decomposed into plane and not into spherical waves.

In order to proceed, further assumptions are required, because both S and \mathbf{a} are generally unknown. In the following, it is assumed that the electric field incident at the optical system's entrance pupil is given by

$$\mathcal{E}_{\text{in}}(x_p, y_p) = A_x(x_p, y_p) \mathbf{e}_x + A_y(x_p, y_p) \mathbf{e}_y, \quad (4.6)$$

with unit vectors $\mathbf{e}_{x/y}$ in x and y direction, complex amplitudes $A_{x/y}$, and pupil coordinates (x_p, y_p) . Note that the above form of the electric field is only consistent if the amplitudes' phases are slowly varying since otherwise, a longitudinal polarization component emerges. For the following, it is assumed that the optical system is aberration free and obeys Abbe's sine condition

$$\frac{\sin \alpha}{\sin \alpha'} = \frac{\sin \beta}{\sin \beta'}, \quad (4.7)$$

with α and β being the angles between two arbitrary rays and the optical axis before

they enter the optical system. The primed quantities α' and β' are the respective angles of the same rays after passing the optical system. In this case, S is part of a sphere and geometrical consideration (cf. [165]) suggest the use of spherical coordinates

$$\mathbf{a}(\varphi, \vartheta) = f \sqrt{\cos \vartheta} [\tilde{A}_x(\varphi, \vartheta) \mathbf{b}_1 + \tilde{A}_y(\varphi, \vartheta) \mathbf{b}_2], \quad (4.8)$$

$$\tilde{A}_{x/y}(\varphi, \vartheta) = A_{x/y}(f \sin \vartheta \cos \varphi, f \sin \vartheta \sin \varphi). \quad (4.9)$$

Here, the angles φ and ϑ parameterizing S and the vectors

$$\mathbf{b}_1 = \begin{pmatrix} (\cos \vartheta - 1) \sin^2 \varphi - \cos \vartheta \\ (1 - \cos \vartheta) \sin \varphi \cos \varphi \\ \sin \vartheta \cos \varphi \end{pmatrix}, \quad \mathbf{b}_2 = \begin{pmatrix} (1 - \cos \vartheta) \sin \varphi \cos \varphi \\ (\cos \vartheta - 1) \cos^2 \varphi - \cos \vartheta \\ \sin \vartheta \sin \varphi \end{pmatrix}, \quad (4.10)$$

are introduced.

By changing to cylindrical image space coordinates $(x, y, z) \rightarrow (\rho, \phi, z)$, equation (4.5) can be rewritten to

$$\mathcal{E}(\rho, \phi, z) = \frac{if}{\lambda} \iint_{\Omega} \sqrt{\cos \vartheta} \sin \vartheta (\tilde{A}_x \mathbf{b}_1 + \tilde{A}_y \mathbf{b}_2) e^{ik\rho \sin \vartheta \cos(\varphi - \phi)} e^{ikz \cos \vartheta} d\varphi d\vartheta, \quad (4.11)$$

with the aperture's solid angle Ω . The geometry of the situation is shown in figure 4.2. Aberrations of the optical system can be included by introducing the factor $e^{i\Phi(\varphi, \vartheta)}$ with the wavefront error $\Phi(\varphi, \vartheta)$. The integral in equation (4.11) can be computed numerically. However, it can be more efficient to recast the integration to a Fourier transform and use fast Fourier transform algorithms to calculate the field [166].

4.3 Simulation of the light field

In this section, a specific optical setup is investigated. This setup was implemented and the resulting intensity distribution was measured in the research group of Gerhard Birkel by Jan-Niklas Schmidt under the supervision of Malte Schlosser [167].

The section is organized in the following way. First, in subsection 4.3.1 the details of the optical setup are specified. Second, in subsection 4.3.2 the results of optical simulations are compared with the measurements of the intensity distribution and the structure of the light field in the area of the optical system's image plane is investigated. Third, in subsection 4.3.3 an analog diffraction-limited optical system is simulated to determine the physical limits of the discussed approach. Finally, in subsection 4.3.4 polarization effects due to the high NA of the objective are investigated using vector diffraction theory.

4.3.1 Optical system

As described in subsection 4.1.1, the optical system consists of three parts: an MLA, an achromatic lens, and a high NA objective. In the considered case, the MLA (SÜSS MICROOPTICS 18-00013) is a square array of plano-convex lenslets made of fused silica. These have a diameter of 106 μm and a radius of curvature of 2.65 mm. The distance between the center of adjacent lenslets is 110 μm . The achromatic lens (THORLABS AC254-200-B) has an effective focal length of 200 mm and a diameter of 25.4 mm. Finally, the objective (THORLABS C330TME-B) is an aspheric lens with an effective focal length of 3.1 mm, a diameter of 5 mm, and $\text{NA} = 0.68$. The combination of the achromatic and the aspheric lens reimages the focal plane of the MLA and provides a demagnification by a factor of 64.5. A cross section of the optical system is shown in figure 4.3.

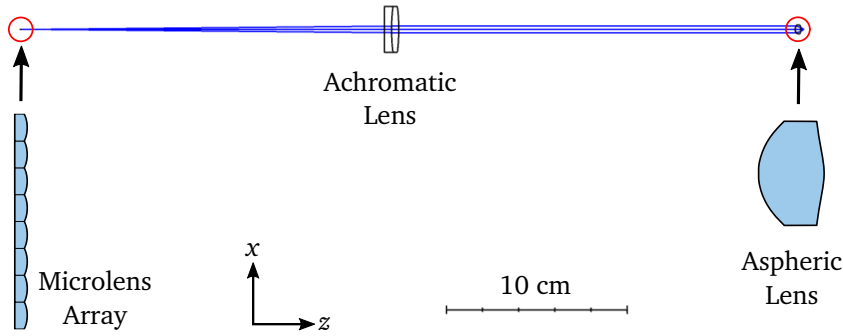


Figure 4.3: Cross section of the optical setup used to generate an array of optical microtraps.

4.3.2 Simulation results and measurements

In this subsection, the intensity distribution in the system's image plane is investigated using measurements and simulations of the optical system. The simulations are performed with the optical design software ZEMAX [168]. Here, the optical system described in the preceding subsection is implemented by specifying its surfaces and materials according to the information provided by the vendors. The light propagation is performed using scalar diffraction theory and the Fresnel approximation (cf. subsection 4.2.2). To compute the refraction at the interface between two media, the wavefront is converted into a ray pencil to which Snell's law is applied. Thereafter, the ray pencil is converted back into a wavefront. For the simulation, the considered incoming light field is a Gaussian laser beam which is focused on the MLA with a wavelength of $\lambda = 780 \text{ nm}$ and a waist of $w_0 = 6 \text{ mm}$. The MLA array is assumed to consist of 21×21 lenslets. In the setup used for the measurements there are two differences to the model used for the simulations: First, the exact waist of the incoming laser beam is not recorded. Second, the number of illuminated lenslets is 27×27 . However, both differences have a negligible effect on the central part of the intensity distribution on which the following discussion is focused.

The simulated two-dimensional intensity distribution

$$I(x, y, z = 0) = 2\epsilon_0 c |\mathcal{E}(x, y, z = 0)|^2 \quad (4.12)$$

in the image plane at $z = 0$ is shown in figure 4.4 (a). As expected, the intensity distribution consists of a square array of focal spots with a trap distance of $110 \mu\text{m}/64.5 = 1.7 \mu\text{m}$. The shape of the focal spots changes as a function of the distance to the optical axis. This is caused by aberrations from the aspherical lens as will be shown later. The corresponding measured intensity distribution is shown in figure 4.4 (b) and shows qualitative agreement with the simulation result.

To provide a more detailed comparison between the simulation and the measurement, the central part of a cut through the $y = 0$ line is shown in figure 4.4 (c). This shows quantitative agreement between the simulation result and the measurement. It is worth noting that the only free parameters are the overall amplitude of the intensity distribution and the position of the coordinate origin.

The simulation of the light field allows investigating the intensity distribution along the optical axis which would require much experimental work to measure. The simulated intensity distribution in the $y = 0$ plane is shown in figure 4.4 (d). Regular reoccurrences of the image plane can be observed along the z -axis. This phenomenon is called Talbot

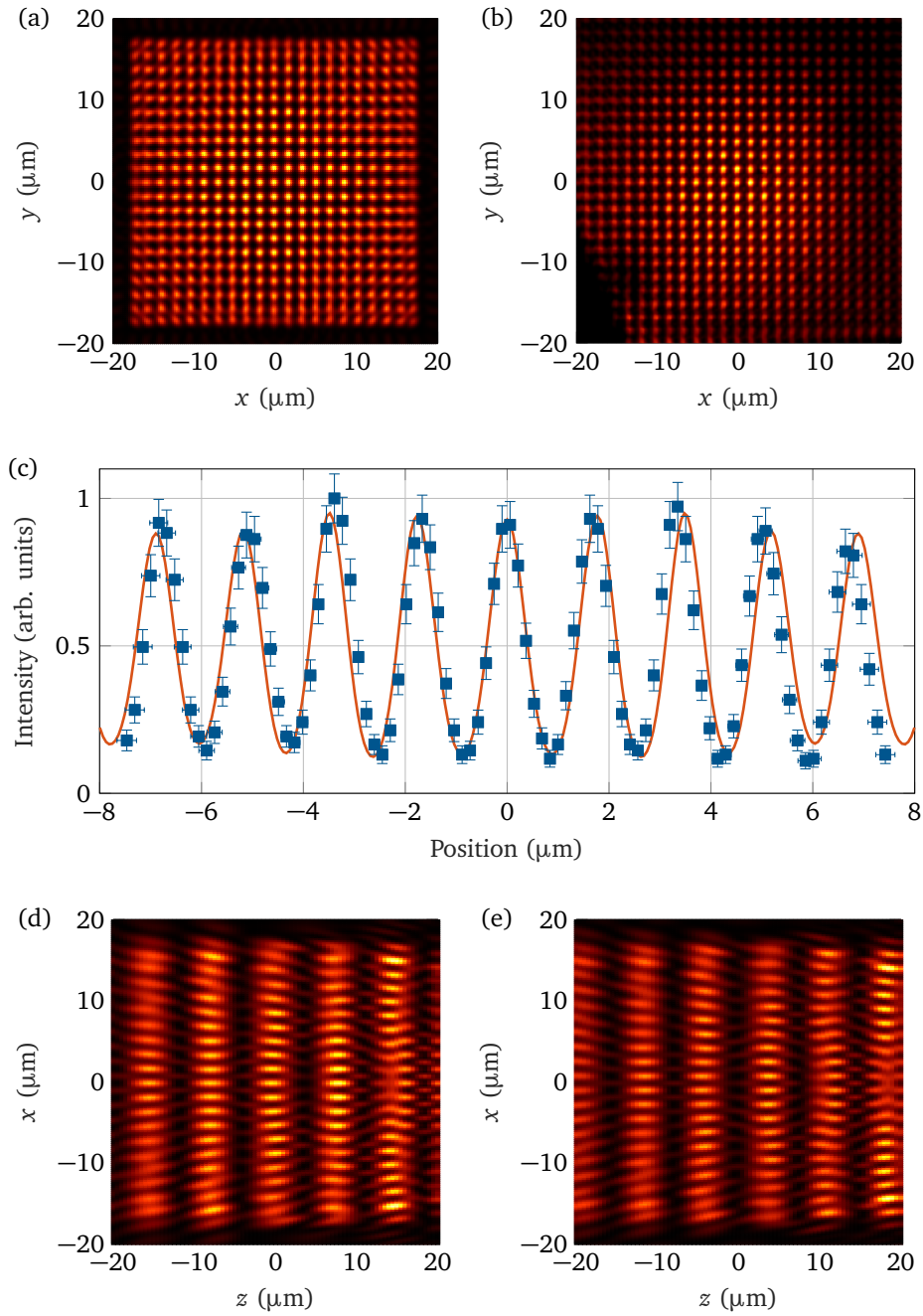


Figure 4.4: Simulated and measured intensity distributions $I(x, y, z)$ for the setup shown in figure 4.3. The incoming light field has a wavelength of $\lambda = 780$ nm. The simulated and measured intensity distributions in the image plane are shown in figure (a) and (b) respectively. (c) shows a cut along the $y = 0$ line of the central part of the intensity distributions shown in (a) and (b). The orange line is the result of the simulation, and the blue squares are the measurement results. The errorbars arise from shot noise of the detector and position calibration of the pixels. Simulated intensity distributions in the $y = 0$ plane (d) and in the $y = d/2$ plane (e) are shown. For the position of the image plane $z = 0$ is chosen.

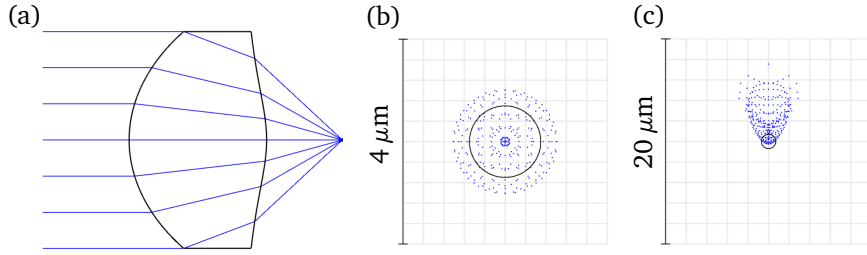


Figure 4.5: Aspheric lens used for demagnification. (a) 2D section of the lens and a pencil of axially parallel rays, (b) and (c) spot diagrams for field angles of 0° and 0.2° in y -direction. The y -coordinates of the intersection of the chief ray with the image plane are $0 \mu\text{m}$ and $11 \mu\text{m}$ for (a) and (b). The RMS spot radii are $0.6 \mu\text{m}$ for (a) and $3.2 \mu\text{m}$ for (b). These have been computed with respect to the chief ray's intersection point. The black circles represent the Airy disk. The ray tracing is performed for $\lambda = 780 \text{ nm}$.

effect [169–171]. The theoretically expected period for these reoccurrences

$$L_{\text{Talbot}} = \frac{\lambda}{1 - \sqrt{1 - \lambda^2/d^2}} \approx 7 \mu\text{m} \quad (4.13)$$

agrees well with the period observed in the simulation result. Further, for square-array geometries, additional arrays of traps shifted by $d/2$ along the x - and y -direction occur between the Talbot planes. This can be observed in the intensity distribution in the $y = d/2$ plane shown in 4.4 (e).

The main reason for the imperfections in the intensity distribution are aberrations caused by the aspheric lens. This fact can be demonstrated using ray tracing. For this, parallel ray fans illuminating the aspheric lens are considered (cf. figure 4.5 (a)). The spot diagram for the incident ray fan, which is parallel to the optical axis, is shown in figure 4.5 (b). The comparison between the size of the spot diagram and the airy disk (black circle) shows that for this ray fan the optical system operates close to the diffraction limit. However, if one considers a ray fan that encloses an angle of 0.2° with the optical axis (cf. figure 4.5 (c)), then the effect of geometric aberrations is visible. In this case, the dominant aberration is the coma which can be deduced from the tail-like shape of the spot diagram.

4.3.3 Diffraction-limited optical system

In the preceding subsection, it is shown that the observed deformation of the off-center focal spots is caused by aberrations stemming from the used aspheric lens. To provide a homogeneous trap quality, it is therefore necessary to replace the aspheric lens by a diffraction-limited objective. In this subsection, the resulting intensity distribution is investigated. For this, the aspheric lens is replaced in the simulation by a thin ideal lens with the same diameter and focal length. This results in a slightly reduced numerical aperture of 0.63. For the trapping of Rubidium atoms the wavelength $\lambda = 780 \text{ nm}$, considered in the preceding subsection, is not a suitable choice since it is close to an atomic transition. Therefore, the wavelength is changed to $\lambda = 1064 \text{ nm}$, which is strongly red-detuned to the relevant atomic transitions.

The resulting intensity distribution in the image plane is shown in figure 4.6 (a). In comparison to the intensity distributions shown in figure 4.4, the trap shapes are much more homogeneous. This impression is supported by figure 4.6 (b) showing a cut along

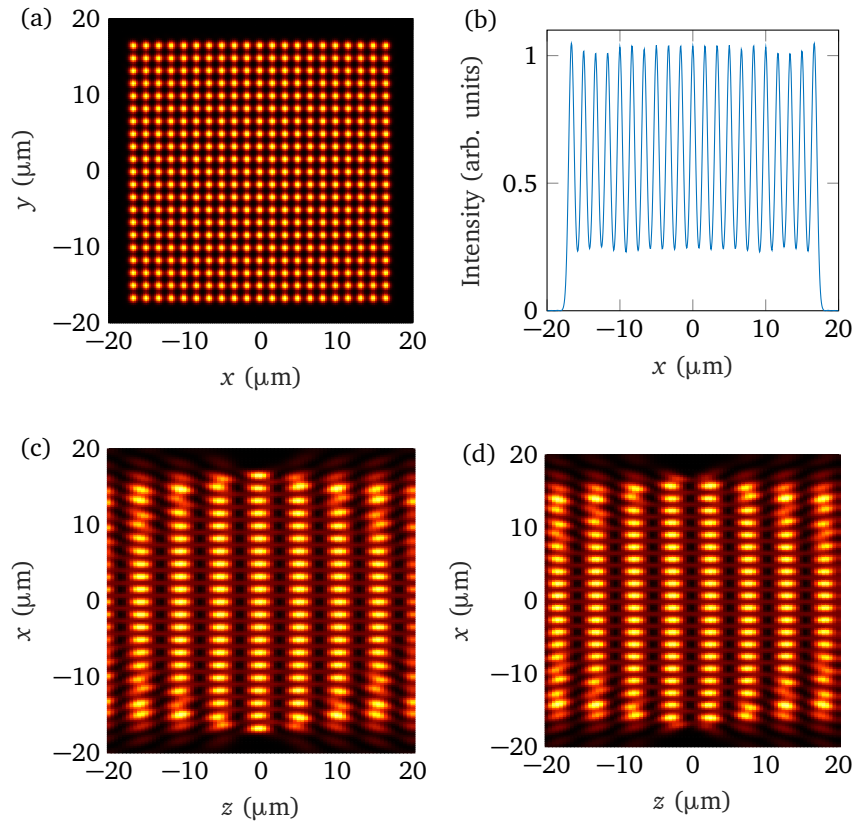


Figure 4.6: Intensity distributions for $\lambda = 1064$ nm and a thin ideal objective, (a) shows the intensity distribution in the image plane, (b) depicts a cut along the $y = 0$ line in (a). The intensity distribution in the $y = 0$ plane and the $y = d/2$ plane are shown in (c) and (d) respectively.

the $y = 0$ line of the intensity distribution. The intensity distribution in the $y = 0$ and the $y = d/2$ plane are shown in figure 4.6 (c) and (d) respectively. From these figures, the structure of the Talbot planes can be determined.

4.3.4 Polarization effects

In this subsection, vector diffraction theory is used to verify the validity of the calculations presented in the preceding subsections for which scalar diffraction theory is used. As discussed in subsection 4.2.3, this is necessary due to the high NA of the used objective. In the following, it is assumed that the objective is aberration free and obeys the sine condition. The light field incident on the objective's entrance pupil is linearly polarized in x -direction.

As a first step, polarization effects are studied for the simple case of homogeneous illumination of the objective's entrance pupil by a plane wave. The resulting intensity distribution in the focal plane is shown in figure 4.7 (a) for $\lambda = 1064$ nm, $D = 4.22$ mm, $\text{NA} = 0.68$, $f = 3.1$ mm, and linear polarization. In contrast to the result from scalar diffraction theory, the intensity distribution is not rotationally symmetric. The Cartesian polarization components of the intensity distribution are plotted in figure 4.7 (b) to (d).

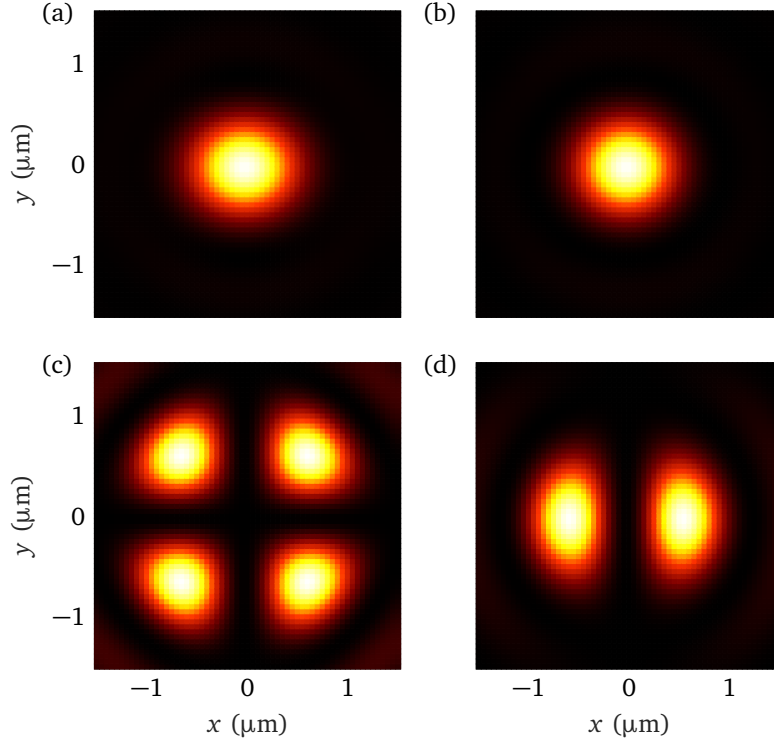


Figure 4.7: Intensity distribution in the focal plane of a homogeneously illuminated aberration free objective with $f = 3.1$ mm and $D = 4.22$ mm. The light used for illumination has a wavelength of $\lambda = 1064$ nm and is linearly polarized in x -direction. The total intensity is shown in (a) whereas the polarization components S_x , S_y , and S_z are shown in (b), (c), and (d) respectively. The color scales range from 0 to 1 (a,b), 0 to 9.6×10^{-4} (c), and 0 to 7.1×10^{-2} (d).

To give a qualitative measure for the strength of polarization effects, the relative magnitude of the polarization components are introduced

$$S_j = \frac{\max_r |e_j \cdot \mathcal{E}(\mathbf{r})|^2}{\max_r |\mathcal{E}(\mathbf{r})|^2}, \quad j \in \{x, y, z\}. \quad (4.14)$$

If the incident light on the objective's entrance pupil is linearly polarized in x -direction, then $S_y \ll 1$ and $S_z \ll 1$ can be used as conditions for the validity of the scalar diffraction theory. Figure 4.8 shows the dependence of S_y and S_z on the objectives NA. This plot shows that for the optical setup considered in the preceding subsections the polarization effects on the intensity distribution can be expected to have a magnitude of a few percents of the peak intensity.

The next step is to compute the intensity distribution in the image plane of the optical setup including the MLA, the achromatic lens, and the objective. The lenslets of the MLA and the achromatic lens are modeled as ideal thin lenses. Whereas, the objective is implemented as described above. The propagation of the light field from the MLA to the entrance pupil of the objective is computed using scalar diffraction theory in combination with the Fresnel approximation. The propagation from the entrance pupil to the image plane is calculated using vector diffraction theory. For an array of 11×11 lenslets and $\lambda = 1064$ nm the resulting intensity distribution is shown in figure 4.9 (a). The intensity distributions of the polarization components are shown in figure 4.9 (b) to (d).

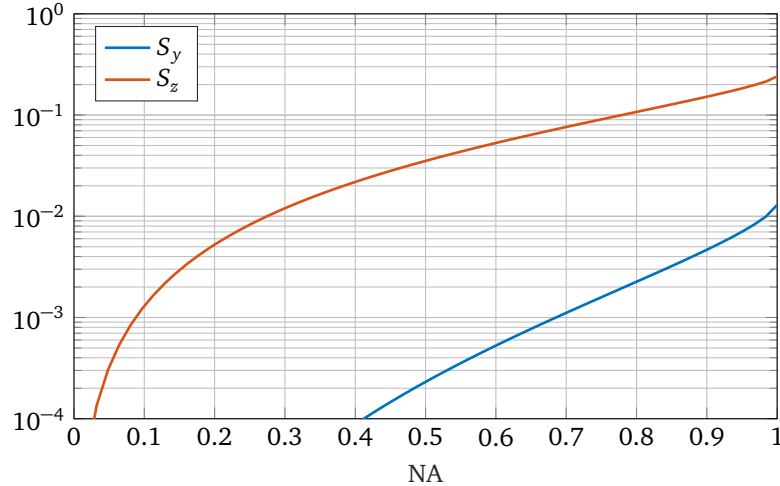


Figure 4.8: Relative intensity of polarization components S_y and S_z versus numerical aperture for an aberration free objective obeying the sine condition (cf. equation (4.7)). The lens is homogeneously illuminated by a plane wave, which is linearly polarized in x -direction. For comparison, $S_x = 1$.

Analogous to the case of homogeneous illumination, the spots are asymmetric. This can be seen from figure 4.9 (e) where the cuts through the intensity distribution along the $x = 0$ and the $y = 0$ line are shown.

The asymmetry of the focal spots is an obstacle for the implementation of an isotropic two-dimensional Bose-Hubbard model since it results in anisotropic tunneling strengths. This effect can be compensated in three different ways. First, the shape of the traps can be shaped by controlling the illumination of the lenslets with the SLM. Second, for a square lattice, isotropic tunneling rates can be achieved by choosing an angle of 45° between the lattice and the polarization axis. Third, circularly polarized light can be used for the generation of the optical microtraps.

It is worth noting that the polarization state of the light field is a function of position. In particular, the light is not linearly polarized everywhere. This affects the optical potential which becomes dependent on the prepared m_F state [36, 172–174]. The importance of this effect can be estimated from the relative strength of the z polarization component which is small, i. e. $S_z \leq 0.04$. In addition, the deviation from linear polarization is strongest between the traps, where the atomic wave functions are smallest. Therefore, this effect is negligible for the chosen parameters.

4.4 Parametrization of the intensity distribution

In this section, the simulated intensity distribution is parametrized. This serves two purposes: First, an approximate closed-form expression for the intensity provides quantitative insight into the structure of the light field. Second, this expression is used for the calculation of the parameters of the Bose-Hubbard model in the next chapter.

The intensity distribution that is considered for parametrization is the one simulated in section 4.3.3, because the use of a diffraction-limited objective and light with a wavelength of $\lambda = 1064$ nm seems to be reasonable for an experimental realization. In addition, the investigation of polarization effects in section 4.3.4 shows, that the only relevant deviation from the results of scalar diffraction theory is the asymmetry of traps which can be compensated.

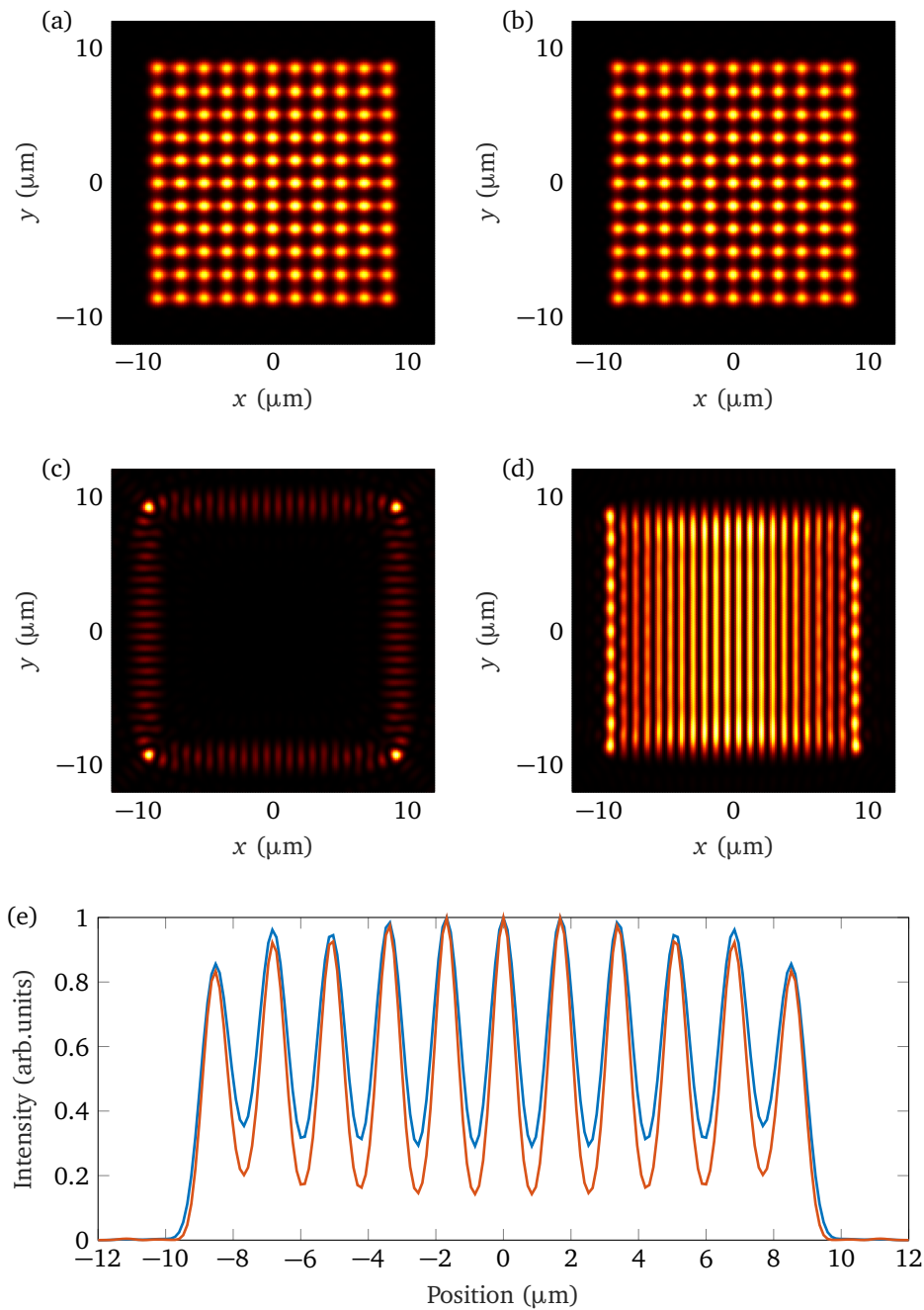


Figure 4.9: Intensity distribution in the image plane of an optical setup consisting of a 11×11 MLA, a $f = 200$ mm lens, and an objective with $D = 4.22$ mm, $f = 3.1$ mm, and $\text{NA} = 0.68$. (a) shows the total intensity distribution in the image plane. (b), (c), and (d) depict the intensity distributions of the polarization components S_x , S_y , and S_z respectively. The color scales range from 0 to 1 (a,b), 0 to 4×10^{-4} (c), and 0 to 4×10^{-2} (d). (e) shows cuts along the $x = 0$ line (orange) and the $y = 0$ line (blue).

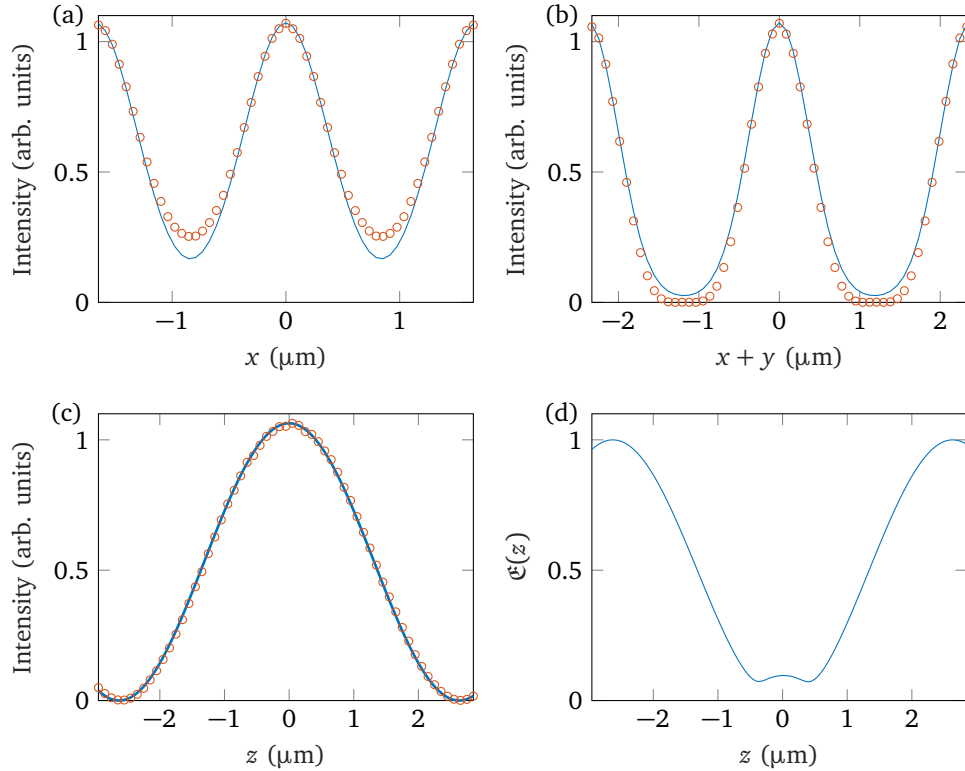


Figure 4.10: Comparison between the simulated intensity distribution I_{sim} and the parametrization I_{fit} given in equation (4.15). Cuts through the intensity distributions along the x -axis, the x - y -diagonal, and the z -axis are shown in (a), (b), and (c) respectively. The error measure $\mathfrak{E}(z)$ is plotted in (d).

The relevant region for atom-trapping is a slice around the image plane excluding the Talbot planes. This part of the intensity distribution can be parametrized using

$$I_{\text{fit}}(x, y, z) = I_0 \frac{1 + \cos(\kappa z)}{2} \sum_{i=1}^M \exp\left(-2 \frac{(x - X_i)^2 + (y - Y_i)^2}{w_0^2}\right). \quad (4.15)$$

The trap waist w_0 , the trap-center coordinates (X_i, Y_i) , and the amplitude I_0 are determined from a fit to the simulated intensity distribution I_{sim} in a part of the image plane with $|x| \leq 1.7 \mu\text{m}$, $|y| \leq 1.7 \mu\text{m}$, and $z = 0$. The parameter κ is determined by a fit to the simulated intensity distribution along the $x = 0$ and $y = 0$ line with $|z| \leq 3 \mu\text{m}$. The fits result in a trap waist of $w_0 = (0.742 \pm 0.002) \mu\text{m}$, a trap distance of $d = (1.68 \pm 0.02) \mu\text{m}$, and $\kappa = (1.195 \pm 0.004) \mu\text{m}^{-1}$. Comparisons between I_{fit} and I_{sim} along the x -axis, the x - y -diagonal, and the z -axis are shown in figure 4.10 (a), (b), and (c) respectively. In order to quantify the deviation of I_{sim} from I_{fit} , the error measure

$$\mathfrak{E}(z) = \frac{\iint |I_{\text{sim}}(x, y, z) - I_{\text{fit}}(x, y, z)| dx dy}{\iint I_{\text{sim}}(x, y, z) dx dy} \quad (4.16)$$

is introduced and plotted in figure 4.10 (d). This shows, that the parametrization given in equation (4.15) is a reasonable approximation of the simulated intensity distribution for $|z| \leq 0.5 \mu\text{m}$.

Chapter 5

Hubbard parameters

In this chapter, techniques for the calculation of the Hubbard parameters (cf. section 3.2) are discussed and applied to the optical potentials derived in the preceding chapter. This is done for periodic optical potentials in section 5.1. Here, the discrete translational symmetry simplifies the calculations. In section 5.2, approximate closed-form expressions for the Hubbard parameters are derived and compared to the numerical results of sections 5.1. To investigate the impact of fluctuations in the trap parameters and to validate the used approximations for the optical potential, the case of non-periodic potentials is considered in section 5.3.

5.1 Periodic potentials

In this section, the calculation of the Hubbard parameters for periodic optical potentials is discussed. It is worth noting that all optical potentials in experiments are non-periodic. This is caused by the finite extent of the light field and by its inhomogeneity. Therefore, the results of this section are based on an idealization, i. e. an infinite, perfectly homogeneous microtrap array. A comparison between the Hubbard parameters for periodic and non-periodic potentials is provided in section 5.3.

5.1.1 MLA-based optical potential

Before the calculation of the Hubbard parameters for periodic potentials can be performed, the shape of the considered optical potentials is discussed in this subsection. The potential is proportional to the light field's intensity which is investigated in chapter 4. Close to the image plane the intensity distribution can be approximated by the expression given in equation (4.15). To prohibit tunneling to neighboring Talbot planes, a light sheet is added. In the following, it is assumed that the light sheet is implemented by an astigmatic Gaussian laser beam propagating in x -direction and linearly polarized in y -direction. The beam waist in y -direction is much larger than the extent of the microtrap array whereas the beam waist in z direction is given by $w_{0\parallel}$. The resulting total optical potential is the sum of the contributions from the light passing through the MLA and that of the light sheet

$$V(x, y, z) = -V_{0\perp} \frac{1 + \cos(\kappa z)}{2} \sum_{i=1}^M \exp\left(-2 \frac{(x - X_i)^2 + (y - Y_i)^2}{w_{0\perp}^2}\right) - \frac{V_{0\parallel}}{\sqrt{1 + x^2/z_R^2}} \exp\left(-2 \frac{z^2}{w_{0\parallel}^2 (1 + x^2/z_R^2)}\right). \quad (5.1)$$

Here, the amplitudes $V_{0\perp}$ and $V_{0\parallel}$ are proportional to the peak intensities of the respective light fields. The parameters $w_{0\perp}$ and κ are derived from the optical simulations in

Quantity	Symbol	Value
Waist of microtraps	$w_{0\perp}$	0.74 μm
Waist of light sheet	$w_{0\parallel}$	2.5 μm
Trap spacing	d	1.7 μm
Wavelength	λ	1064 nm
Rayleigh length	z_R	18.5 μm

Table 5.1: Parameters for the optical potential given in equation (5.1) and (5.2). The values are based on optical simulations discussed in chapter 4.

chapter 4 and are summarized in table 5.1. The Rayleigh range of the light sheet is given by $z_R = \pi w_{0\parallel}^2 / \lambda$. Before the Hubbard parameters are calculated, additional approximations are made, which are based on the following assumptions. First, it is assumed that the extension of the microtrap array is not larger than the Rayleigh range $z_R = 18.5 \mu\text{m}$. Second, it is assumed that the confinement in z -direction is dominated by the light sheet. These assumptions justify the usage of a simplified approximate form of the optical potential $V(x, y, z) = V_{\perp}(x, y) + V_{\parallel}(z)$ with

$$V_{\perp}(x, y) = -V_{0\perp} \sum_{i=1}^M \exp\left(-2 \frac{(x - X_i)^2 + (y - Y_i)^2}{w_{0\perp}^2}\right), \quad V_{\parallel}(z) = -V_{0\parallel} e^{-2z^2/w_{0\parallel}^2}. \quad (5.2)$$

Since V_{\perp} depends only on x and y whereas V_{\parallel} depends only on z , the Bloch functions (cf. equation (3.3)) factorize

$$\Psi_{\mathbf{k}}^{n,m}(x, y, z) = \psi_{\mathbf{k}}^n(x, y) \phi^m(z). \quad (5.3)$$

The wave function ϕ^m is a solution to the one-dimensional time-independent Schrödinger equation

$$\left[-\frac{\hbar^2}{2m} \partial_z^2 + V_{\parallel}(z) \right] \phi^m(z) = \epsilon^m \phi^m(z), \quad (5.4)$$

with m being the associated quantum number. The two-dimensional Bloch functions $\psi_{\mathbf{k}}^n$ of the n^{th} band are solutions to the following equation

$$\left[-\frac{\hbar^2}{2m} (\partial_x^2 + \partial_y^2) + \tilde{V}_{\perp}(x, y) \right] \psi_{\mathbf{k}}^n(x, y) = \epsilon_{\mathbf{k}}^n \psi_{\mathbf{k}}^n(x, y), \quad (5.5)$$

with the periodic continuation \tilde{V}_{\perp} of the potential V_{\perp} . The resulting Wannier functions are given by

$$W_i^{n,m}(x, y, z) = w_i^n(x, y) \phi^m(z), \quad (5.6)$$

with the two-dimensional Wannier functions w_i^n being associated to the Bloch functions $\psi_{\mathbf{k}}^n$ (cf. equation (3.4)). The task of computing Wannier functions and Hubbard parameters can be split into the numerical solution of the one-dimensional Schrödinger equation (5.4) and a two-dimensional band structure calculation solving equation (5.5). In the following subsection, the latter part is discussed.

5.1.2 Band structure

In this subsection, the plane wave expansion method for the calculation of the band structure in periodic potentials is discussed. This method is then applied to the potential specified in equation (5.2) using the parameters given in table 5.1.

For a periodic potential V the eigen wave functions of the single-particle Hamilton operator have the form given in equation (3.3). Inserting this expression into the time-independent Schrödinger equation yields

$$\frac{\hbar^2}{2m}(\mathbf{k} - i\nabla)^2 u_{\mathbf{k}}^n(\mathbf{r}) + V(\mathbf{r})u_{\mathbf{k}}^n(\mathbf{r}) = E_{\mathbf{k}}^n u_{\mathbf{k}}^n(\mathbf{r}). \quad (5.7)$$

One approach to solving the above equation is to expand V and $u_{\mathbf{k}}^n$ in a complete orthogonal system of functions. Due to the periodicity of the problem, it is reasonable to choose plane waves for this expansion. The resulting Fourier series for the potential and the Bloch functions are given by

$$V(\mathbf{r}) = \frac{1}{\sqrt{\Upsilon}} \sum_{\mathbf{q}} v_{\mathbf{q}} e^{i\mathbf{q}\mathbf{r}}, \quad v_{\mathbf{q}} = \frac{1}{\sqrt{\Upsilon}} \int_{\Upsilon} e^{-i\mathbf{q}\mathbf{r}} V(\mathbf{r}) d^D r, \quad (5.8)$$

$$u_{\mathbf{k}}^n(\mathbf{r}) = \frac{1}{\sqrt{\Upsilon}} \sum_{\mathbf{q}} c_{\mathbf{k}\mathbf{q}}^n e^{i\mathbf{q}\mathbf{r}}, \quad c_{\mathbf{k}\mathbf{q}}^n = \frac{1}{\sqrt{\Upsilon}} \int_{\Upsilon} e^{-i\mathbf{q}\mathbf{r}} u_{\mathbf{k}}^n(\mathbf{r}) d^D r. \quad (5.9)$$

with the reciprocal lattice vectors

$$\mathbf{q} \in \left\{ \sum_{i=1}^D z_i \mathbf{b}_i : z_i \in \mathbb{Z} \right\}, \quad \mathbf{a}_i \cdot \mathbf{b}_j = 2\pi \delta_{ij}. \quad (5.10)$$

To allow for numerical calculation, the infinite set of reciprocal lattice vectors needs to be truncated. This is done by introducing a momentum cutoff $|\mathbf{q}| \leq G_{\max}$, which limits the spatial resolution. Inserting equations (5.8) and (5.9) into equation (5.7) yields

$$\frac{\hbar^2}{2m}(\mathbf{k} + \mathbf{q})^2 c_{\mathbf{k}\mathbf{q}}^n + \frac{1}{\sqrt{M}} \sum_{\mathbf{q}'} v_{\mathbf{q}-\mathbf{q}'} c_{\mathbf{k}\mathbf{q}'}^n = E_{\mathbf{k}}^n c_{\mathbf{k}\mathbf{q}}^n. \quad (5.11)$$

The above equation allows to compute the coefficients $c_{\mathbf{k}\mathbf{q}}^n$ and energies $E_{\mathbf{k}}^n$ by solving the corresponding matrix eigenvalue problem for the quasi momentum \mathbf{k} of interest. From this the Bloch functions $u_{\mathbf{k}}^n$ can be computed via equation (5.9).

It is worth noting that the plane wave expansion method discussed above is well known, though not often used in condensed matter physics [56]. The latter is caused by two obstacles. First, the shape of the ionic potentials is not well suited for a plane wave expansion, i. e. for a satisfactory approximation the number of required plane waves is very high omitting efficient calculations. Second, solid-state physics is often dominated by higher bands which again requires many plane waves. However, for optical microtraps, the plane wave expansion method is well-suited because the plane-wave expansion of the potential is efficient and most of the time only the lowest band is relevant.

To apply the plane wave expansion method to the potential specified in the preceding subsection, the lattice geometry needs to be specified. By construction, only 1D and 2D lattices are feasible with the technique discussed in chapter 4. Further, since the lenslets on commercially available MLAs are arranged on square or triangular grids, only lattices based on these geometries are investigated in this section. Therefore, in this work, the one-dimensional lattice, the square lattice, the triangular lattice, and the honeycomb

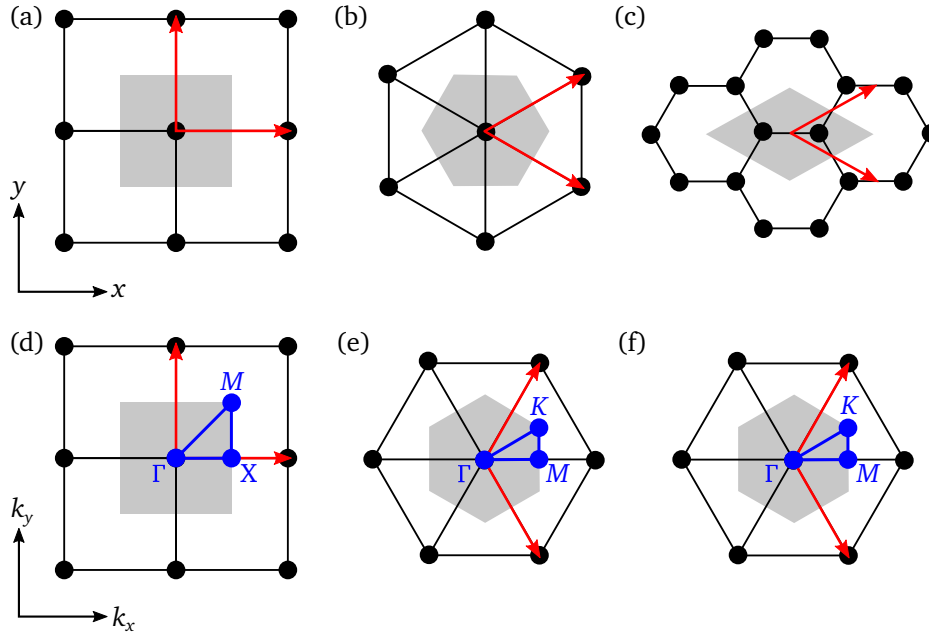


Figure 5.1: Two-dimensional lattices considered in this chapter. The real space arrangements of the square, triangular, and honeycomb lattice are shown in (a), (b), and (c) respectively. The grey areas are the Wigner-Seitz cells, and the red arrows represent the primitive lattice vectors. The corresponding reciprocal lattices are shown in (d), (e), and (f). In these subfigures, the grey areas are the first Brillouin zones and the blue dots are the corresponding symmetry points [175].

lattice are considered. Figure 5.1 shows the geometries of the two-dimensional lattices and the corresponding reciprocal lattices. The calculation of expansion coefficients v_q for these lattices is discussed in appendix C.

The band structure for the lattices mentioned above is calculated with the plane wave expansion method using the software package *Wannier states for optical lattices* [176]. For the parameters given in table 5.1 the results are shown in figure 5.2. The one-dimensional lattice is implemented as a rectangular lattice with non-isotropic trap spacings $d_x = d$ and $d_y = 2.8 \mu\text{m}$. For each geometry, three different lattice depths $V_{0\perp}$ were considered. The lattice depth is measured in the natural energy scale of the lattice $\mathcal{E} = \hbar^2/(2md^2)$. Here, in contrast to the situation in optical lattices, this energy scale is not directly related to the recoil energy $E_r = \hbar^2/(2m\lambda^2)$.

For the one-dimensional, square, and triangular lattice the qualitative features of the band structure are similar, i. e. the lowest band is separated by an energy gap from the higher bands. For the considered lattice depths this energy gap is much larger than the width of the lowest band. Therefore, for sufficiently low temperatures and weak interactions, the one-band approximation is justified. In case of the honeycomb lattice, the situation is qualitatively different, since the lowest and the second lowest band are degenerate at the symmetry point K . This is caused by the fact that the honeycomb lattice is not a Bravais lattice, i. e. its primitive cell contains more than one site.

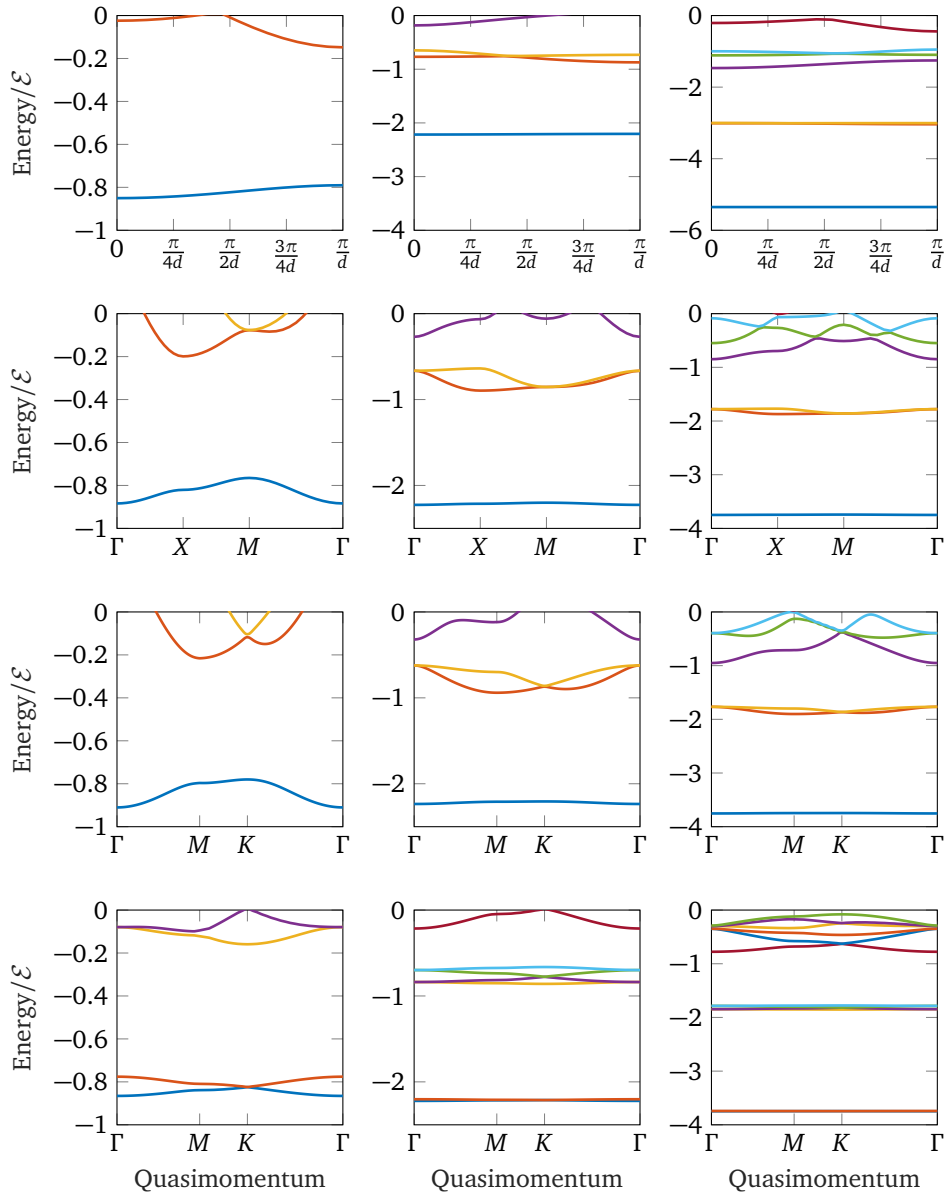


Figure 5.2: Band structure of the potential V_{\perp} . The energies of the lowest bands are plotted versus the quasi momentum \mathbf{k} . The rows correspond to different lattice geometries (from top to bottom): quasi 1D, square, triangular, and honeycomb lattice. The columns correspond to different lattice depths (from left to right): $V_{0\perp} = 2\mathcal{E}$, $V_{0\perp} = 4\mathcal{E}$, and $V_{0\perp} = 6\mathcal{E}$. The remaining parameters are chosen as in table 5.1.

5.1.3 Wannier functions and Hubbard parameters

The band structure calculations performed in the preceding subsection serve as input to the computation of the Wannier functions and finally of the Hubbard parameters. In case of an isolated band, the Wannier functions can be calculated from equation (3.4) or to be more precise from its discrete version

$$w_i^n(\mathbf{r}) = \frac{1}{M} \sum_{\mathbf{k}} e^{-i\mathbf{k}\mathbf{R}_i} \psi_{\mathbf{k}}^n(\mathbf{r}). \quad (5.12)$$

Here, the sum extends over M sampling points in the first Brillouin zone (cf. equation (3.12)).

If the lowest band is connected to a higher band by a degenerate point in the Brillouin zone, then these bands form a composite group. In this case, the above definition does not result in exponentially localized Wannier functions. To restore this property the concept of maximally localized, generalized Wannier functions (MLGWFs) was introduced [59]. These functions are defined by

$$w_i^n(\mathbf{r}) = \frac{1}{M} \sum_{\mathbf{k}} e^{-i\mathbf{k}\mathbf{R}_i} \sum_m U_{nm}^k \psi_{\mathbf{k}}^m(\mathbf{r}). \quad (5.13)$$

In the above equation the index m runs over all energy bands of the composite group. The unitary matrices U^k are found by minimizing the spread functional

$$\Omega = \sum_m (\langle r^2 \rangle_m - \langle \mathbf{r} \rangle_m^2). \quad (5.14)$$

The expectation values $\langle \cdot \rangle_m$ are defined with respect to the Wannier function w_j^m with $\mathbf{R}_j = \mathbf{0}$. In this work, the software package *Wannier states for optical lattices* is used, which implements the calculation of the band structure and the MLGWFs. For details the interested reader is referred to [176].

Figure 5.3 shows a section along the x -axis of lowest-band Wannier functions calculated for a square lattice with the parameters specified in table 5.1. In this figure, a characteristic feature of Wannier functions is visible; a change of sign close to neighboring lattice sites, which is a consequence of orthogonality. Further, it is apparent that for increasing potential depths the Wannier functions become more localized. Both observations are not specific to the considered square lattice but hold for all geometries.

The determination of the two-dimensional Wannier functions w_i^n from the results of the band-structure calculation needs to be complemented by the computation of the functions ϕ^m , to determine the three-dimensional Wannier functions $W_i^{n,m}$. The functions ϕ^m are obtained by solving equation 5.4 numerically.

From the Wannier functions $W_i^{n,m}$ the Hubbard parameters can be calculated. The on-site interaction strength for the lowest band is given by

$$U = U_i = \frac{4\pi a_s \hbar^2}{m} \int [W_i^{0,0}(\mathbf{r})]^4 d^3r. \quad (5.15)$$

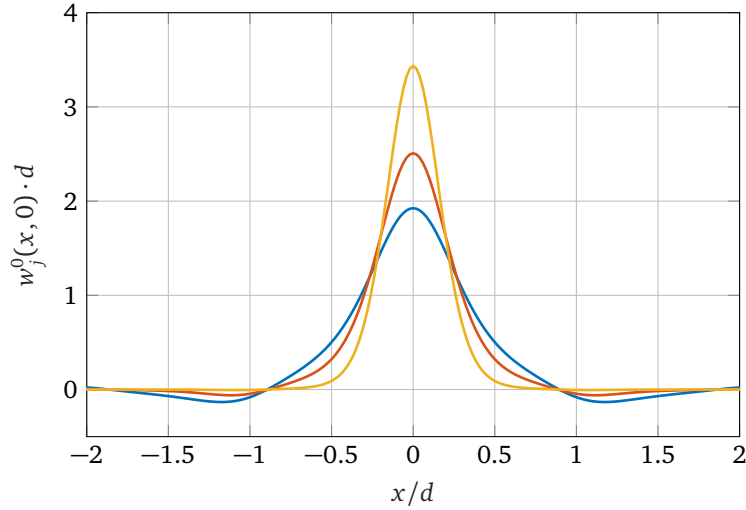


Figure 5.3: Cut along the x -axis of the lowest band Wannier function w_j^0 for a square lattice with the parameters specified in table 5.1 and lattice depth $V_{0\perp} = \mathcal{E}$ (blue), $V_{0\perp} = 2\mathcal{E}$ (red), and $V_{0\perp} = 5\mathcal{E}$ (yellow).

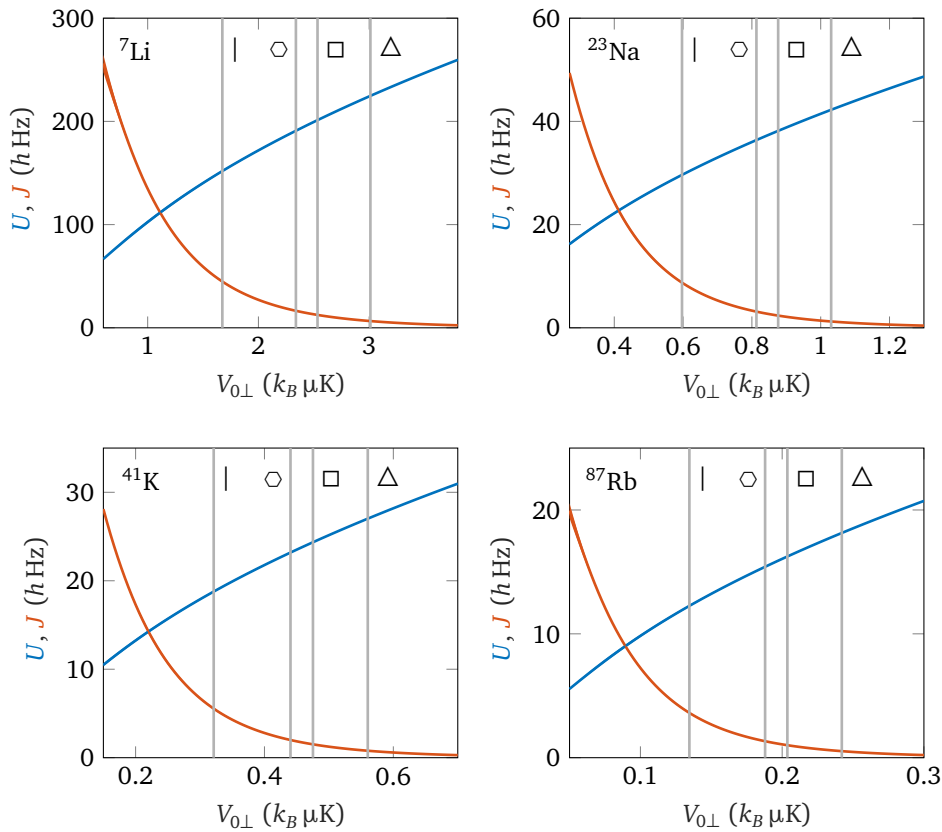


Figure 5.4: Hubbard parameters U (blue) and J (red) plotted versus the lattice depths $V_{0\perp}$ for ${}^7\text{Li}$, ${}^{23}\text{Na}$, ${}^{41}\text{K}$, and ${}^{87}\text{Rb}$. The respective depths of the light sheet are $V_{0\parallel} = 4.97 \text{ k}_B\mu\text{K}$, $V_{0\parallel} = 1.74 \text{ k}_B\mu\text{K}$, $V_{0\parallel} = 0.94 \text{ k}_B\mu\text{K}$, and $V_{0\parallel} = 0.4 \text{ k}_B\mu\text{K}$. The grey vertical lines indicate the superfluid-insulator transition for the lattice geometry indicated by the respective symbol (one-dimensional lattice |, honeycomb lattice \circ , square lattice \square , triangular lattice \triangle). For all these lattices the values for U and J lie within an interval that is smaller or equal to the width of the respective line.

It is worth noting that in contrast to the on-site interaction strength, the lowest band tunneling parameter J does not depend on the potential V_{\parallel}

$$J = J_{ij} = - \int W_i^{0,0}(\mathbf{r}) \left[-\frac{\hbar^2}{2m} \nabla^2 + V(\mathbf{r}) \right] W_j^{0,0}(\mathbf{r}) d^3r \quad (5.16)$$

$$= - \iint w_i^0(x, y) \left[-\frac{\hbar^2}{2m} (\partial_x^2 + \partial_y^2) + V_{\perp}(x, y) \right] w_j^0(x, y) dx dy. \quad (5.17)$$

Figure 5.4 shows the Hubbard parameters as functions of the potential depth $V_{0\perp}$ for the bosonic alkali species ${}^7\text{Li}$, ${}^{23}\text{Na}$, ${}^{41}\text{K}$, and ${}^{87}\text{Rb}$. The relevant properties of these isotopes are summarized in appendix A.

5.2 Closed-form expressions for the Hubbard parameters

In this section, closed-form expressions for the Hubbard parameters are derived. To obtain satisfying results, different approaches are used for the interaction strength U and the tunneling parameter J .

5.2.1 Interaction strength

Since the Wannier function is taken to the power of four in the expression for the interaction strength U (cf. equation (5.15)), the contribution of the part close to the respective potential minimum dominates. Therefore, to obtain an approximate closed-form expression for U , it is reasonable to expand the potential around the respective minimum. To quadratic order this expansion for the potential specified in equation (5.2) yields

$$V(x, y, z) \approx -V_{0\perp} - V_{0\parallel} + \frac{2V_{0\perp}}{w_{0\perp}^2} (x^2 + y^2) + \frac{2V_{0\parallel}}{w_{0\parallel}^2} z^2. \quad (5.18)$$

This potential corresponds to an anisotropic harmonic oscillator with frequencies

$$\omega_x = \omega_y = \sqrt{\frac{4V_{0\perp}}{mw_{0\perp}^2}}, \quad \omega_z = \sqrt{\frac{4V_{0\parallel}}{mw_{0\parallel}^2}}. \quad (5.19)$$

Using the ground state of the harmonic oscillator as an ansatz for the lowest-band Wannier function yields

$$w_i(x, y) = \frac{1}{\sqrt{\pi}a_{\perp}} \exp\left[-\frac{(x - X_i)^2 + (y - Y_i)^2}{2a_{\perp}^2}\right], \quad (5.20)$$

$$\phi(z) = \frac{1}{\sqrt[4]{\pi}\sqrt{a_{\parallel}}} \exp\left[-\frac{z^2}{2a_{\parallel}^2}\right], \quad (5.21)$$

with oscillator lengths $a_{\perp} = \sqrt{\hbar/(m\omega_{x/y})}$ and $a_{\parallel} = \sqrt{\hbar/(m\omega_z)}$. For ϕ this ansatz yields satisfying results, because the considered potential depth $V_{0\parallel}$ is sufficiently large. However, this is not the case for w_i , since the considered range for $V_{0\perp}$ includes small values.

To improve the approximation, a_{\perp} is used as a variational parameter. It is determined by minimizing the expectation value of the energy for a single Gaussian potential well of width $w_{0\perp}$ (cf. appendix G and [177]). Summarizing the results, the widths of the Gaussian functions are expressed in terms of the natural length and energy scale of the

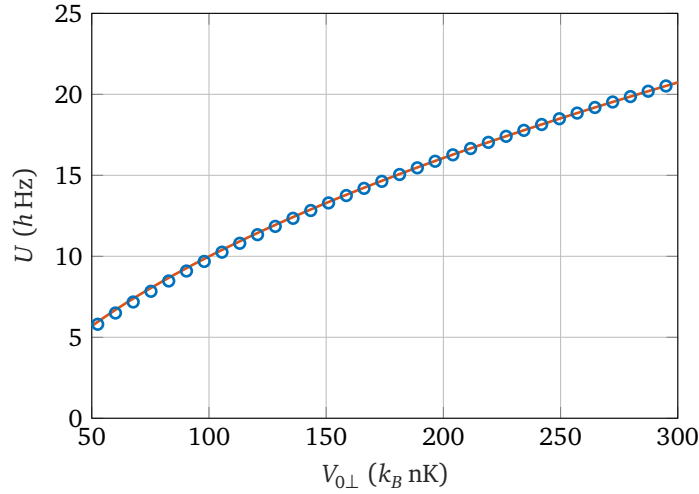


Figure 5.5: The interaction strength U is plotted versus the potential depth $V_{0\perp}$ for ^{87}Rb using the same parameters as in figure 5.4. The blue circles are the numerical results discussed in section 5.1 (cf. equation (5.15)), whereas the orange line is computed using the closed-form expression given in equation (5.23).

lattice d and \mathcal{E}

$$a_{\perp} = \sqrt{\frac{w_{0\perp}^2 d}{2\pi w_{0\perp} \sqrt{2V_{0\perp}/\mathcal{E}} - 2d}}, \quad a_{\parallel} = \sqrt{\frac{w_{0\parallel} d}{2\pi} \sqrt{\frac{\mathcal{E}}{2V_{0\parallel}}}}. \quad (5.22)$$

Substituting the expressions in equations (5.20) and (5.21) into equation (5.15) yields

$$U = \frac{a_s d^2 \mathcal{E}}{\sqrt{2\pi^5} a_{\perp}^2 a_{\parallel}}. \quad (5.23)$$

Figure 5.5 shows that the above expression quantitatively agrees with the numerical results from the preceding section.

5.2.2 Tunneling parameter

The Gaussian wave functions that are used in the preceding subsection are not suitable to calculate the tunneling parameter J . This is because J crucially depends on the slopes of the wave functions, where the difference between the exponentially localized Wannier functions and the Gaussian wave functions is significant. Therefore, a different approach is used in this subsection.

Semiclassical methods have proven to be a valuable tool for the determination of tunneling strengths [178]. For one-dimensional problems, the Wentzel-Kramers-Brillouin (WKB) method is frequently used [179]. However, the application of this method to general, higher-dimensional problems has proven to be problematic [180]. An equivalent alternative approach is to apply the stationary-phase approximation to the path-integral formulation of quantum mechanics [181]. A practical implementation of this technique for tunneling in higher-dimensional systems is based on the concept of instantons [182–188] and was developed by Mil'nikov and Nakamura in [180, 189–191]. This formalism has been applied to determine the tunneling parameter for optical honeycomb lattices [123] and is used in this subsection.

In the following, a brief introduction to the instanton method is given. Starting point is Feynman's formulation of quantum mechanics [181], in which transition matrix elements are expressed in terms of path integrals

$$\langle \mathbf{r}_2 | e^{-i\hat{H}t/\hbar} | \mathbf{r}_1 \rangle = \mathcal{N} \int e^{iS[\gamma]/\hbar} \mathcal{D}\gamma. \quad (5.24)$$

In the above equation \mathbf{r}_1 and \mathbf{r}_2 are position vectors, \hat{H} is the single-particle Hamilton operator, S is the corresponding classical action functional, \mathcal{N} is a normalization constant, and the integration is performed over all curves γ obeying the boundary conditions $\gamma(0) = \mathbf{r}_1$ and $\gamma(t) = \mathbf{r}_2$. The next step is to introduce imaginary time $t \rightarrow -i\tau$. This process is called Wick rotation and leads to

$$\langle \mathbf{r}_2 | e^{-\hat{H}\tau/\hbar} | \mathbf{r}_1 \rangle = \mathcal{N} \int e^{-S_E[\gamma]/\hbar} \mathcal{D}\gamma. \quad (5.25)$$

The functional S_E is called Euclidean action, since the introduction of imaginary time in special relativity transforms Minkowskian to Euclidean geometry. Further, S_E can be viewed as the classical action of a particle moving in a potential with flipped sign. The reason for the introduction of imaginary time is the analogy to statistical physics, i. e. identifying τ/\hbar with the inverse temperature β . In the low-temperature limit $\beta \rightarrow \infty$, the path integral approach allows to determine the ground state energy and wave function of \hat{H} from

$$\langle \mathbf{r}_2 | e^{-\hat{H}\tau/\hbar} | \mathbf{r}_1 \rangle = \mathcal{N} \sum_{n=0}^{\infty} e^{-E_n\tau/\hbar} \langle \mathbf{r}_1 | n \rangle \langle n | \mathbf{r}_2 \rangle, \quad (5.26)$$

with $|n\rangle$ being the eigenstate corresponding to the eigenenergy E_n . Until this point, all relations are exact. However, the evaluation of the path integrals is a complicated task. A successful approximation scheme stems from the observation that only those curves that minimize the action functional S_E are significant for the integral in equation (5.25), because the contributions from all other curves are suppressed exponentially. The former are the trajectories of classical particles moving in the sign-flipped potential. These trajectories are called instantons and are the foundation for a successful semiclassical approximation scheme developed in quantum field theory [182–185, 187, 188].

The aim of this subsection is to determine the tunneling strength between adjacent sites in a trap array of the form given in equation (5.2). To do so, the semiclassical instanton method is applied. This can be done by considering two adjacent traps as a symmetric double-well potential with minima located at \mathbf{r}_+ and \mathbf{r}_- . For sufficiently deep traps, the two lowest eigenenergies E_0 and E_1 are well separated from the remaining part of the spectrum and the corresponding wave functions are the symmetric and antisymmetric combination of functions localized around the potential minima. The energy difference $\Delta = E_1 - E_0$ is called tunneling splitting and is connected to the tunneling parameter $\Delta = 2J$. To apply the instanton method, the tunneling splitting needs to be expressed in terms of path integrals of the form given in equation (5.25). This can be done using the following observations. First, for large τ the summation in equation (5.26) can be truncated at $n = 1$. Second, the potential and the ground state $|0\rangle$ are symmetric under the parity transformation with respect to the point $(\mathbf{r}_+ + \mathbf{r}_-)/2$, whereas $|1\rangle$ is antisymmetric under this transformation. This implies the following relations

$$|\langle \mathbf{r}_\pm | 0 \rangle|^2 = |\langle \mathbf{r}_\pm | 1 \rangle|^2 = \langle \mathbf{r}_+ | 0 \rangle \langle 0 | \mathbf{r}_- \rangle = -\langle \mathbf{r}_+ | 1 \rangle \langle 1 | \mathbf{r}_- \rangle. \quad (5.27)$$

A straight forward calculation starting from equation (5.26) results in

$$\Delta = \lim_{\tau \rightarrow \infty} \frac{\hbar}{\tau} \ln \left(\frac{\langle \mathbf{r}_- | e^{-\hat{H}\tau/\hbar} | \mathbf{r}_- \rangle + \langle \mathbf{r}_- | e^{-\hat{H}\tau/\hbar} | \mathbf{r}_+ \rangle}{\langle \mathbf{r}_- | e^{-\hat{H}\tau/\hbar} | \mathbf{r}_- \rangle - \langle \mathbf{r}_- | e^{-\hat{H}\tau/\hbar} | \mathbf{r}_+ \rangle} \right). \quad (5.28)$$

The computation of the transition matrix elements $\langle \mathbf{r}_\pm | e^{-\hat{H}\tau/\hbar} | \mathbf{r}_- \rangle$ using the instanton method (cf. [191] and appendix E) yields

$$\Delta = \sqrt{\hbar} \mathcal{A} e^{-S_0/\hbar}. \quad (5.29)$$

The exponent S_0 is the Euclidean action of the instanton connecting \mathbf{r}_- and \mathbf{r}_+ whereas the pre-exponential factor \mathcal{A} is connected to the fluctuations around the instanton. Its calculation is technically demanding and is discussed in appendix E.

Having established the required formalism, the tunneling between Gaussian wells in 2D can be analyzed. The considered geometry is that of a square lattice. However, the results of section 5.1 show that the obtained values are transferable to other lattice geometries. The in-plane part of the potential is given by (cf. appendix C)

$$V_\perp(x, y) = -V_{0\perp} \xi \vartheta_3 \left(-\frac{\pi x}{d}, e^{-\pi \xi} \right) \vartheta_3 \left(-\frac{\pi y}{d}, e^{-\pi \xi} \right), \quad (5.30)$$

with the Jacobi theta function ϑ_3 [47] and $\xi = \pi w_{0\perp}^2 / (2d^2)$. For the following discussion it is convenient to introduce dimensionless coordinates

$$\tilde{x} = \frac{2\pi x}{d}, \quad \tilde{y} = \frac{2\pi y}{d}, \quad \tilde{t} = 2\pi \sqrt{\frac{V_{0\perp}}{md^2}} t. \quad (5.31)$$

Using these coordinates the two-dimensional time-dependent Schrödinger equation can be rewritten to

$$i\hbar_e \partial_{\tilde{t}} \psi(\tilde{x}, \tilde{y}, \tilde{t}) = -\frac{\hbar_e^2}{2} (\partial_{\tilde{x}}^2 + \partial_{\tilde{y}}^2) \psi(\tilde{x}, \tilde{y}, \tilde{t}) + \tilde{V}(\tilde{x}, \tilde{y}) \psi(\tilde{x}, \tilde{y}, \tilde{t}), \quad (5.32)$$

with the shifted dimensionless potential

$$\tilde{V}(\tilde{x}, \tilde{y}) = -\xi \vartheta_3 \left(-\frac{\tilde{x}}{2}, e^{-\pi \xi} \right) \vartheta_3 \left(-\frac{\tilde{y}}{2}, e^{-\pi \xi} \right) + \xi \vartheta_3(0, e^{-\pi \xi}) \vartheta_3(0, e^{-\pi \xi}) \quad (5.33)$$

and an effective dimensionless Planck constant $\hbar_e = \sqrt{2\mathcal{E}/V_{0\perp}}$. From equation (5.32) it follows that the semiclassical limit $\hbar_e \rightarrow 0$ is realized for deep potentials, i. e. $V_{0\perp} \gg \mathcal{E}$. This is compatible with the condition for the validity of the Bose-Hubbard model $V_{0\perp} \gtrsim \mathcal{E}$ (cf. section 3.2.1 and references therein). Here, traps centered at $\mathbf{r}_+ = (2\pi, 0)$ and $\mathbf{r}_- = (0, 0)$ are considered. From the symmetry of the potential it is clear that the instanton is a straight line connecting \mathbf{r}_- and \mathbf{r}_+ . Using energy conservation in the sign-flipped potential it is straightforward to express the instanton's dimensionless action in the following way

$$\tilde{S}_0 = \int_0^{2\pi} \sqrt{2\tilde{V}(\tilde{x}, 0) - 2\tilde{V}(0, 0)} d\tilde{x}. \quad (5.34)$$

The integral in the above equation cannot be calculated analytically. However, the numerical evaluation is straightforward. The computation of the pre-exponential factor $\tilde{\mathcal{A}}$ is presented in appendix E. In figure 5.6, the parameters \tilde{S}_0 and $\tilde{\mathcal{A}}$ are plotted versus the ratio $w_{0\perp}/d$.

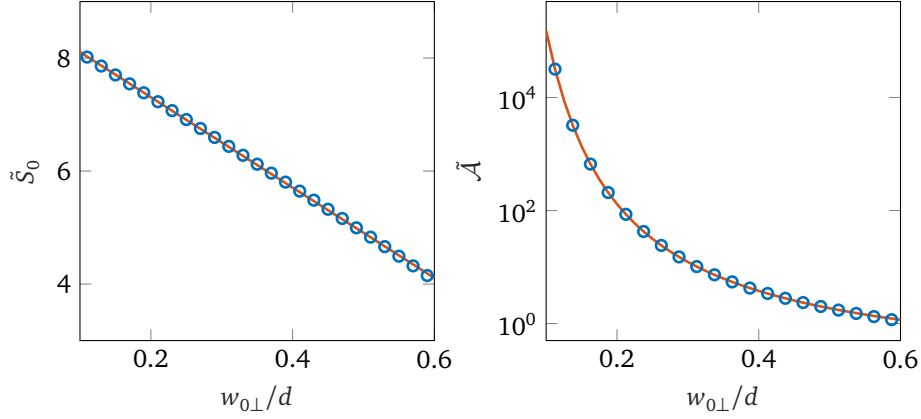


Figure 5.6: Parameters of the instanton approach. The left figure shows the instanton's Euclidean action \tilde{S}_0 as a function of the ratio $w_{0\perp}/d$ (blue circles). The orange line is a linear fit to this data with a slope of -8.00 and a y -axis intercept of 8.91 . The right figure shows the pre-exponential factor \tilde{A} versus $w_{0\perp}/d$ (blue circles). The orange line is a fitted function with $x \mapsto 0.11 \cdot e^{1.41/x}$.

Summarizing the results of the preceding paragraphs, the instanton approximation for tunneling parameter is given by

$$J_{\text{inst}}/\mathcal{E} = 2\tilde{A}\left(\frac{V_{0\perp}}{2\mathcal{E}}\right)^{3/4} \exp\left(-\tilde{S}_0\sqrt{\frac{V_{0\perp}}{2\mathcal{E}}}\right). \quad (5.35)$$

It is worth noting that the above expression is universal in the sense that different atomic species and trap distances can be incorporated by scaling the energy \mathcal{E} . The parameters \tilde{S}_0 and \tilde{A} need to be recalculated only if the ratio $w_{0\perp}/d$ changes.

For the parameters given in table 6.3 the calculations yield $\tilde{S}_0 = 5.44$ and $\tilde{A} = 2.85$. In figure 5.7, the instanton approximation is compared to the result of the numerical band structure calculations. For shallow potentials the instanton method significantly overestimates the tunneling parameter. However, as expected the quality of the approximation increases for deeper potentials.

To find a closed-form expression that provides a satisfactory approximation for the entire relevant parameter regime, equation (5.35) is generalized in the following way [192]

$$J_{\text{fit}}/\mathcal{E} = A\left(\frac{V_{0\perp}}{\mathcal{E}}\right)^B \exp\left(-C\sqrt{\frac{V_{0\perp}}{\mathcal{E}}}\right). \quad (5.36)$$

The parameters A , B , and C are determined from a fit to the results of the band structure calculation yielding $A = 2.82$, $B = 1.56$, and $C = 4.47$. The comparison between the results of the band structure calculation and the expression given in equation (5.36) is shown in figure 5.8 revealing quantitative agreement on the percent level.

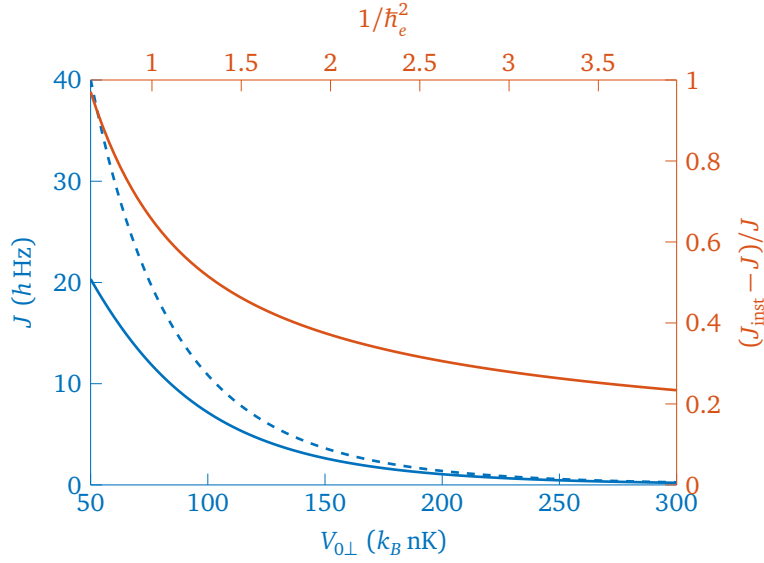


Figure 5.7: Tunneling parameter J versus potential depth $V_{0\perp}$ for ^{87}Rb using the same parameters as in figure 5.4. The solid blue line is the result of a band structure calculation (cf. section 5.1) and the dashed blue line is the instanton approximation (cf. equation (5.35)). In addition, the relative error of the instanton method $(J_{\text{inst}} - J)/J$ (orange line) is plotted versus the inverse square of the effective Planck constant \hbar_e .

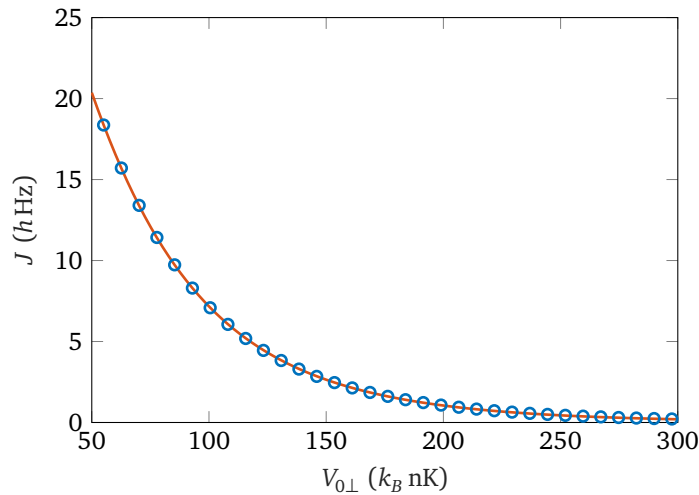


Figure 5.8: The tunneling parameter J is plotted versus the potential depth $V_{0\perp}$ for ^{87}Rb atoms in a square lattice using the same parameters as in figure 5.4. The blue circles are the results of band structure calculations, whereas the orange line is a fitted function of the form given in equation (5.36).

5.3 Non-periodic potentials

In section 5.1, Hubbard parameters for periodic potentials are derived. However, as stated earlier, arrays of optical microtraps are non-periodic due to their finite size and inhomogeneity. Therefore, it is reasonable to transfer the concept of Wannier functions to non-periodic arrays of traps. This is discussed in section 5.3.1. Using this concept, effects of fluctuations in the optical potential are investigated in section 5.3.2. In section 5.3.3, the validity of the approximation for the optical potential given in equation (5.2) is verified by comparing the resulting Hubbard parameters to those obtained from a three-dimensional calculation performed using the simulated optical potential.

5.3.1 Maximally localized low-energy functions

Consider a particle of mass m in a potential V with M pronounced local minima $\{\mathbf{R}_m\}$. The corresponding time-independent Schrödinger equation is given by

$$\left[-\frac{\hbar^2}{2m}\Delta + V(\mathbf{r}) \right] \psi_n(\mathbf{r}) = E_n \psi_n(\mathbf{r}), \quad (5.37)$$

with energy eigenvalues E_n and corresponding wave functions ψ_n . If all M local minima are of sufficient and similar depth, then the M lowest eigenenergies are well separated from the remaining spectrum. This situation is analogous to an isolated band in case of a periodic potential. This analogy can be used to construct a set of localized functions $\{\mathcal{W}_m\}$ that correspond to Wannier functions in the periodic case. In the remainder of this work, these functions are denoted maximally localized low-energy functions (MLLEFs). Their definition in terms of the solutions of the single-particle Schrödinger equation is given by

$$\mathcal{W}_m(\mathbf{r}) = \sum_{n=1}^M A_{mn} \psi_n(\mathbf{r}). \quad (5.38)$$

The matrix A is obtained by minimizing the spread functional

$$\Omega = \sum_{m=1}^M \int \mathcal{W}_m(\mathbf{r}) (\mathbf{r} - \mathbf{R}_m)^2 \mathcal{W}_m(\mathbf{r}) d^D r, \quad (5.39)$$

which is the analog to the spread functional given in equation (5.14). It is worth noting that the functions ψ_n and \mathcal{W}_m can be chosen to be real. If orthogonality and normalization of the MLLEFs is demanded, i. e.

$$\int \mathcal{W}_m(\mathbf{r}) \mathcal{W}_n(\mathbf{r}) d^D r = \delta_{mn}, \quad (5.40)$$

then A is an orthogonal matrix.

To compute the MLLEFs for a given potential, the M energetically lowest wave functions ψ_n need to be calculated. This is approached in the following way. First, the single particle Hamilton operator is represented by a sparse matrix using finite differences for the kinetic part. Second, the eigenvectors corresponding to the lowest eigenvalues of this sparse matrix are computed using the implicitly restarted Lanczos algorithm [193–195]. The next step is to compute the matrix A by minimizing the spread functional. Since A is required to be orthogonal, its matrix elements cannot be varied independently. Therefore, they are not a suitable set of optimization variables. It is preferable to parametrize A with a set of independent variables. Such a parametrization is provided by generalized

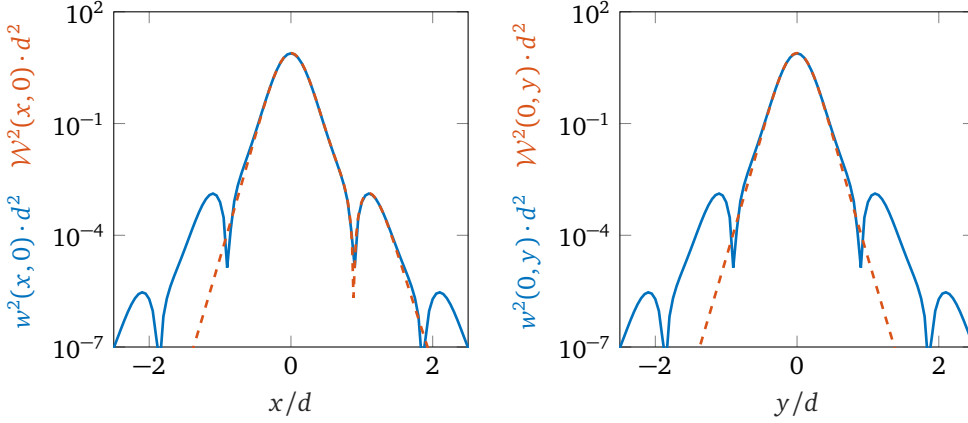


Figure 5.9: Comparison between the MLEF for a two-dimensional Gaussian double-well potential (orange dotted line) and the Wannier function of a two-dimensional Gaussian square lattice (solid blue line). The chosen parameters are those given in table 5.1 with $V_{0\perp}/k_B = 100$ nK and $V_{0\parallel}/k_B = 400$ nK.

Euler angles [196]. Using the set of wave functions $\{\psi_n\}$ and the matrix A the MLEFs \mathcal{W}_m can be determined from equation (5.38). The parameters U and J then follow from inserting the \mathcal{W}_m into the respective expressions given in equations (5.15) and (5.16).

As a first example, a two-dimensional Gaussian double-well potential of the form given in equation (5.2) is considered. The potential minima are located at $\mathbf{R}_1 = (0, 0)$ and $\mathbf{R}_2 = (d, 0)$. In figure 5.9, the MLEF corresponding to the left potential well is shown. This function is compared to the Wannier function of the square lattice with the same trap parameters. In the region of the two potential wells, both functions agree on a quantitative level. However, outside this region, they differ significantly.

The derived Hubbard parameters are plotted versus the potential depth $V_{0\perp}$ in figure 5.10 and are compared to the results for the square lattice revealing quantitative agreement on the percent level. The difference in the Hubbard parameters decreases with increasing potential depth because the MLEFs are more and more localized in the region for which the double-well potential and the square lattice potential coincide.

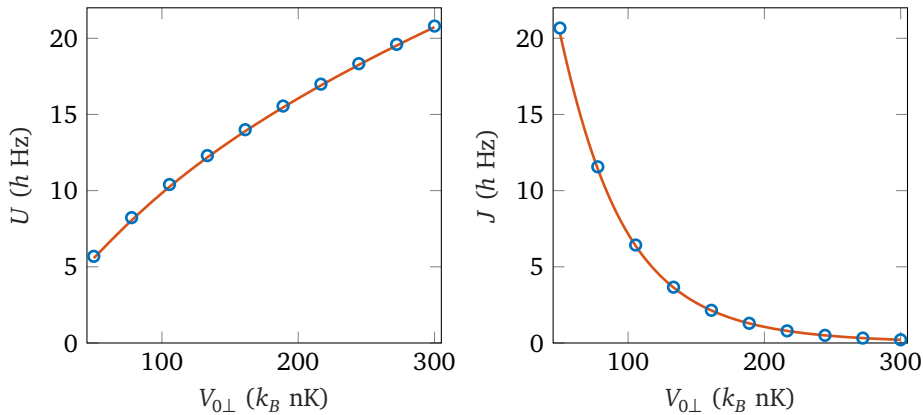


Figure 5.10: Hubbard parameters for a two-dimensional Gaussian double-well potential (blue circles) and a two-dimensional Gaussian square lattice (orange line) are plotted versus the potential depth $V_{0\perp}$. The remaining parameters are the same as in figure 5.9.

5.3.2 Effects from fluctuations of the optical potential

In this part, the method described in the preceding subsection is used to compute the impact of fluctuations in the optical potential on the Hubbard parameters. This problem is of interest because it determines the required amount of control over the light field that is needed to adjust the Hubbard parameters.

Before calculations are performed, it is reasonable to discuss sources and strengths of fluctuations in the optical potential for the experimental setup discussed in chapter 4. The optical potential is proportional to the light field's intensity distribution and is described with the parameters $V_{0\perp}$, $V_{0\parallel}$, $w_{0\perp}$, $w_{0\parallel}$, and d . All these parameters can be subject to temporal fluctuations. In addition, the parameters $V_{0\perp}$, $w_{0\perp}$, and d can differ from trap to trap. Due to the robustness of the experimental setup, temporal fluctuations in the geometrical parameters $w_{0\perp}$, $w_{0\parallel}$, and d are expected to be negligible. The main contribution to temporal fluctuations in the potential depth $V_{0\perp}$ and $V_{0\parallel}$ are expected to arise from fluctuations in the laser power. These fluctuations affect all traps in the same way since all lenses are illuminated by the same laser beam. State-of-the-art laser systems allow for relative power stability on the 10^{-3} level. Spatial fluctuations of the parameters $w_{0\perp}$, $w_{0\parallel}$, and d can be caused by an inhomogeneous laser beam profile, production tolerances of the MLA, and aberrations of the demagnification optics.

For a sufficiently small fluctuation ΔX of the parameter $X \in \{V_{0\perp}, V_{0\parallel}, w_{0\perp}, w_{0\parallel}, d\}$ the relation to the fluctuation ΔY of the Hubbard parameter $Y \in \{U, J, \epsilon\}$ is linear

$$\frac{\Delta Y}{Y} \approx C(X, Y) \frac{\Delta X}{X}. \quad (5.41)$$

The susceptibility $C(X, Y)$ can be determined in the following way. First, the parameter X is sampled from a normal distribution with mean \bar{X} and standard deviation ΔX . Second, using this random potential parameter the resulting Hubbard parameter Y is computed using the method presented in subsection 5.3.1. The preceding steps are repeated $N_{\text{sample}} = 100$ times. From this sample, the standard deviation ΔY is estimated. All preceding steps are performed for several ΔX up to a cutoff ΔX_{max} . A linear fit to this data set then yields an estimate for $C(X, Y)$. It is worth noting that in general the value of $C(X, Y)$ depends on the working point $V_{0\perp}$. However, for $X \in \{V_{0\parallel}, w_{0\parallel}\}$ this is not the case because the problem factorizes into an in-plane and an out-of-plane part. These susceptibilities are given in table 5.2 whereas the remaining susceptibilities are plotted versus $V_{0\perp}$ in figure 5.11.

An alternative approach to determine the susceptibilities $C(X, Y)$ is to use the closed-form expressions given in section 5.2 for error propagation. The results of this calculation are shown in figure 5.11 and agree quantitatively with the numerical results. However,

	MLLEF calculation	Error propagation
$C(V_{0\parallel}, U)$	0.27 ± 0.01	0.25
$C(V_{0\parallel}, \epsilon_{\parallel})$	0.97 ± 0.06	1.02
$C(w_{0\parallel}, U)$	0.45 ± 0.03	0.50
$C(w_{0\parallel}, \epsilon_{\parallel})$	0.046 ± 0.002	0.048

Table 5.2: Fluctuation susceptibilities connected to the out-of-plane confining potential V_{\parallel} . In the left column, the results from the MLLEF based calculation are given, whereas for the right column error propagation for the closed-form expression given in section 5.2 is used.

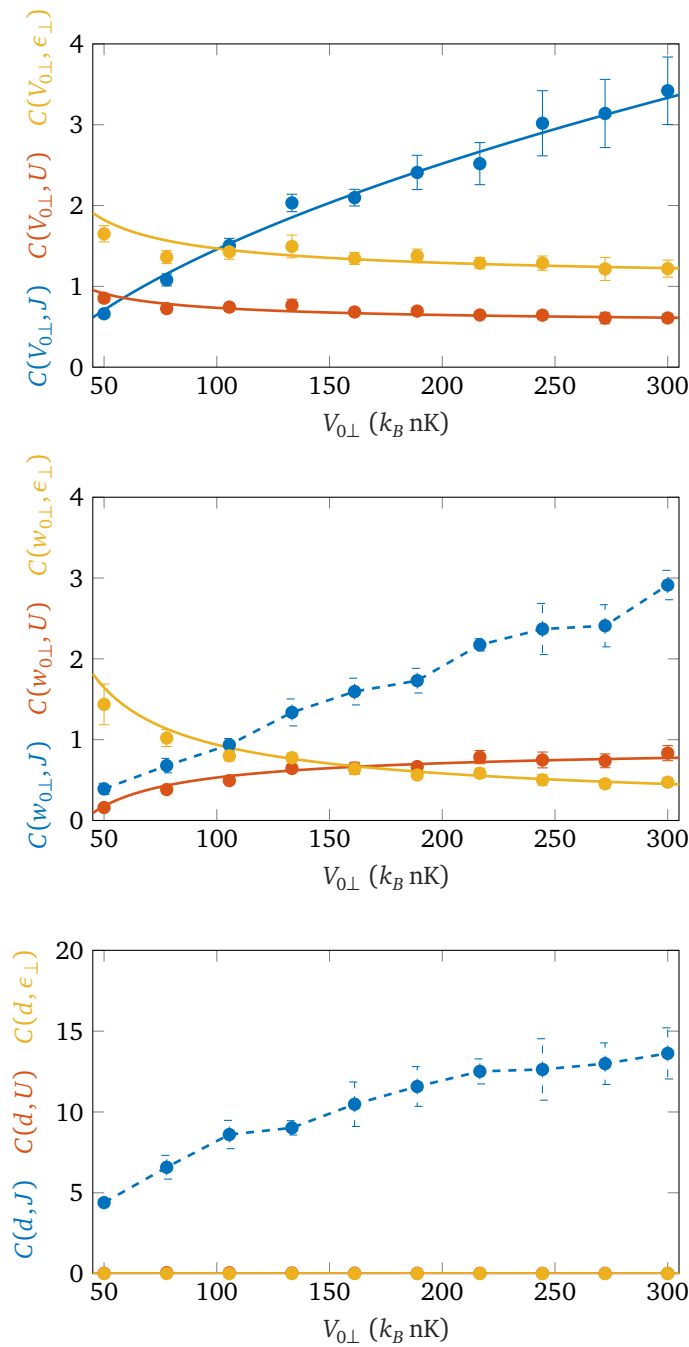


Figure 5.11: Fluctuation susceptibilities $C(X, Y)$ versus potential depth $V_{0\perp}$ for $X = V_{0\perp}$ (top), $X = w_{0\perp}$ (mid), and $X = d$ (bottom). The circles are the results from the calculation based on MLEFs whereas the solid lines are based on the linearization of the closed-form expressions given in section 5.2. The dashed lines are guides to the eye for cases in which no quantitatively satisfying closed-form expression is known.

this approach does not allow for the computation of $C(w_{0\perp}, J)$ and $C(w_{0\perp}, J)$, since no reliable closed form expression for the dependency of J on $w_{0\perp}$ and d has been found.

In tunneling experiments with cold atoms in double-well potentials, which were generated by optical tweezers [152, 153], it was found that the biggest challenge in terms of the control over the light field is posed by the requirement for unobstructed tunneling $\Delta\epsilon < J$. This condition refers to spatial fluctuations of the local single-particle energies. Therefore, only spatial fluctuations in the parameters $V_{0\perp}$, $w_{0\perp}$, and d need to be considered. Further, the effect of these fluctuations on $\Delta\epsilon$ can be compensated by adjusting the local trap depths $V_{0\perp}$ using the SLM. Assuming that a liquid-crystal based SLM with 768×768 pixel is used to control the illumination of a square array of 25×25 lenses with circular aperture, then 741 pixel per lens are available. Since the transmission of each pixel can be controlled in 256 steps [197] static imperfections can be compensated on the $\Delta V_{0\perp}/V_{0\perp} = (741 \cdot 256)^{-1} = 5.3 \cdot 10^{-6}$ level. From the results for $C(V_{0\perp}, \epsilon)$ and the values for J and ϵ it follows that $\Delta\epsilon/J \leq 1\%$ for $V_{0\perp} \leq k_B 180$ nK ($U/J \leq 10$) and $\Delta\epsilon/J \leq 5\%$ for $V_{0\perp} \leq k_B 250$ nK ($U/J \leq 40$).

5.3.3 Validity of approximations for the optical potential

In this part, the method presented in subsection 5.3.1 is used to compute the Hubbard parameters for the three-dimensional optical potential which is obtained from the optical simulations performed in chapter 4. For this purpose, the light field is computed for the case of two adjacent microlenses resulting in a double-well potential. This is combined with the light-sheet potential V_{\parallel} for out-of-plane confinement (cf. equation 5.1). In figure 5.12, the resulting Hubbard parameters are compared to those computed for a square lattice potential of the form given in equation 5.2 for ^{87}Rb . For the relevant parameter regime, the relative deviations are below 20% for both U and J . The approximation given in equation 5.2 underestimates both U and J . For J the relative deviation is approximately constant, whereas for U it rises for increasing $V_{0\perp}$. This stems from the influence of V_{\perp} on the out-of-plane confinement which is neglected in equation 5.2.

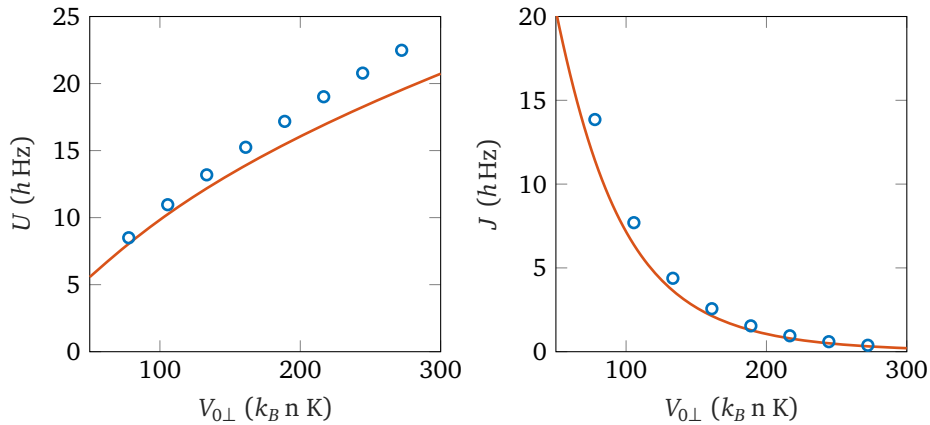


Figure 5.12: Hubbard parameters U (left) and J (right) are plotted versus the potential depth $V_{0\perp}$ for ^{87}Rb . The blue circles are obtained by applying the MLLEF method to the 3D double-well potential directly obtained from an optical simulation, whereas the orange lines correspond to the approximation given in equation 5.2 with the parameters specified in table 5.1.

Chapter 6

State preparation

In this chapter, the preparation of ultracold atoms in optical microtrap arrays is investigated. The challenge is to prepare states of sufficiently low entropy, to reach the quantum many-body regime of the Bose-Hubbard model, i. e. its superfluid or Mott-insulator phase.

In optical lattice experiments, state preparation is done in the following way. First, a degenerate quantum gas is prepared in a wide trap using standard techniques, i. e. a combination of laser cooling and evaporative cooling [34]. Subsequently, the depth of the optical lattice is ramped up adiabatically preserving the system's low entropy. In section 6.1, it is investigated whether this approach can be transferred to the case of optical microtrap arrays discussed in chapter 4.

An alternative approach is to start from arrays of deep optical microtraps. The deterministic preparation of one atom per trap in 1D and 2D arrays has been demonstrated recently [155, 198–200]. Using Raman side-band cooling, the atoms can be prepared in the motional ground state [174, 201]. Thereafter, to reach an itinerant many-body system, the trap depths are reduced significantly. This process needs to be adiabatic to preserve the system's low entropy and is analyzed in section 6.2.

6.1 Loading from a Bose-Einstein condensate

In this section, the transfer process from a BEC in a wide trap to a many-body state in the Bose-Hubbard regime is investigated. First, in subsection 6.1.1 the initial state, i. e. the BEC, is specified using state-of-the-art experiments as references. Second, the loading sequence is discussed in section 6.1.2 based on a comparison to optical lattice experiments. Third, in section 6.1.3 entropy and temperature of the final state are estimated and discussed in terms of the phase diagram of the Bose-Hubbard model.

6.1.1 Initial state

For this section, it is assumed that standard techniques are used to prepare a degenerate quantum gas of bosonic atoms. The relevant information about this initial configuration is the geometry of the trap and the entropy of the quantum gas. This is discussed in the following.

To obtain a large spatial overlap of the initial BEC and the final many-body state in a 2D trap array, it is necessary to prepare the BEC in an oblate ellipsoidal trap also known as pancake trap. In 2D optical lattice experiments with single-site resolution [94–96], this is done by using a single slice of a 1D optical lattice. Details about the experimental procedure to prepare the BEC are given in [202, 203]. An analogous approach appears to be feasible for the experimental scheme discussed in this thesis.

To reach the superfluid or Mott-insulator phase of the Bose-Hubbard model, low entropies are required. If the transfer to the trap array is adiabatic, then the entropies of the initial and final state are identical. Therefore, attainable entropies in state-of-the-art BEC

Trap depth $V_{0\perp}/\mathcal{E}$	Tunneling strength J/h	
	computed	rescaled from [95]
1.25	21 Hz	13 Hz
2.5	7.9 Hz	3.8 Hz
3.75	3.0 Hz	1.3 Hz
3.75	1.3 Hz	0.5 Hz

Table 6.1: Comparison between the tunneling strength J of ^{87}Rb atoms in the MLA-based optical potential (cf. chapter 5) and a 2D optical lattice experiment [95]. The latter are rescaled according to equation 6.1 to compensate for the different trap distances.

experiments are highly relevant. Until recently, the measured entropy per particle S/N in these experiments had a lower bound of about $0.1 k_B$ [204]. However, due to advances in thermometry and cooling, a quantum gas with $S/N \approx 10^{-3} k_B$ was reported [205].

6.1.2 Loading sequence

As stated earlier, the transfer of atoms from the pancake trap to the microtrap array needs to be adiabatic. Therefore, a slow transfer is advantageous. However, its length is limited by heating and loss processes as well as by the desire for short experimental cycles. Thus, it is important to determine the shortest transfer time τ for which the non-adiabatic excitations are negligible. For optical lattice experiments this has been studied extensively [206–214]. Therefore, it is reasonable to transfer these results to the situation investigated in this thesis. This is approached by rescaling the ramp duration τ' found for an optical lattice setup with a trap spacing d' and an atomic mass m' using the formula

$$\tau \approx \frac{md^2}{m'd'^2} \tau'. \quad (6.1)$$

This relation is derived by assuming that all relevant time durations scale inversely to the fundamental energy scale of a lattice system $\mathcal{E} = h^2/(2md^2)$. Apparently, this is not true if the trap geometry differs significantly between experiments. Therefore, it is reasonable to test the relation given in equation (6.1) by applying it to known quantities. An evident choice are the Hubbard parameters U and J because they are known in optical lattice experiments and are calculated in chapter 5. In contrast to U , J does not depend on the out-of-plane confinement, which can be chosen independently of the in-plane potential. Therefore, it is the preferred quantity to test equation (6.1).

Table 6.1 shows a comparison between the values computed in this thesis and rescaled results from [95]. This experiment is chosen for the following reasons. First, like in the MLA-based setup, the lattice geometry is two-dimensional. Second, the Hubbard parameters are tabulated for several potential depths. Third, the used ramp duration is stated explicitly. The tunneling parameters computed in this thesis are about a factor of two larger than the ones rescaled from [95]. This discrepancy can be attributed to the different trap geometries, i. e. an array of Gaussian traps versus a sinusoidal lattice. However, since the rescaled tunneling parameters systematically underestimate the actual tunneling parameters, the resulting estimates for τ given in table 6.2 are conservative.

It is worth noting that the ramp speed in optical lattice experiments is limited by the inhomogeneous envelope of the lattice potential stemming from the profiles of the used laser beams [209, 213]. Since the MLA-based setup allows for individual control of the

Species	Rescaled from [95]		Rescaled from [213]	
	τ	N_{sc}	τ	N_{sc}
^7Li	62 ms	$0.5 \cdot 10^{-3}$	4 ms	$3.2 \cdot 10^{-5}$
^{23}Na	202 ms	$0.6 \cdot 10^{-3}$	13 ms	$3.9 \cdot 10^{-5}$
^{41}K	361 ms	$1.3 \cdot 10^{-3}$	24 ms	$8.6 \cdot 10^{-5}$
^{87}Rb	766 ms	$1.4 \cdot 10^{-3}$	51 ms	$9.3 \cdot 10^{-5}$

Table 6.2: Rescaled ramp duration τ and resulting average number of photon-scattering events N_{sc} per atom.

local trap depth using an SLM, it is possible to provide a homogeneous lattice potential. This should allow for significantly faster loading sequences by omitting atom transport through Mott-insulator regions. To estimate this effect, the result from a continuum-model simulation for a 1D lattice [213] is rescaled according to equation (6.1). The result is given in table 6.2 revealing a speed-up by more than an order of magnitude compared to the values obtained from [95].

The ramp durations that are given in table 6.2 can be put into perspective by comparison with timescales for atom loss and heating processes. In typical experiments, the atom-loss limited lifetime of BECs is well above 10 s. Therefore, the ramp duration should not be problematic. In optical lattice experiments, light scattering has been identified as the dominant heating source [204]. To assess the impact of this process, the average number of scattering events per atom N_{sc} (cf. section 2.1.2) during the ramp duration is given in table 6.2. For this calculation, it is assumed that $V_{0\perp}$ is linearly increased from zero to its final value at $U/J = 10$ within the duration τ and that $V_{0\parallel}$ is constant with the value used in chapter 5.

6.1.3 Final state

In this part, the properties of the system's state after the transfer process is discussed. The main question is whether the strongly correlated, low-temperature regime of the Bose-Hubbard model, i. e. the Mott-insulator phase, can be reached. It is assumed that the ramp durations discussed in the preceding subsection are sufficiently long to render ramp-induced excitations negligible. If no external heating mechanisms exist, then the system's entropy is conserved. In this case, the temperature of the final state can be computed from the initial entropy S_i of the BEC by solving the equation $S(T) = S_i$ for T . The calculation of $S(T)$ for the Mott-insulator phase is discussed in appendix F. The blue line in figure 6.1 shows the final temperature in the Mott-insulator phase as a function of the initial entropy S_i for a square lattice geometry.

As discussed in the preceding subsection, the dominant external heating process is light scattering. Its impact on the system's temperature can be estimated by considering the corresponding energy increase during the ramp duration. This can be estimated from $\Delta E \approx 2E_r N N_{\text{sc}}$ [30, 31, 36]. Assuming that this excess energy fully thermalizes, the corresponding temperature increase ΔT can be determined from $E(T + \Delta T) = E(T) + \Delta E$. The calculation of the thermodynamic relation $E(T)$ is discussed in appendix F for the Mott-insulator phase. The resulting temperature is shown by the orange line in figure 6.1. For this result the estimated ramp duration obtained from [213] is used, i. e. $\tau = 51$ ms.

It is worth noting that optical lattice experiments [215, 216] and theoretical studies [217, 218] have shown that the actual heating rate is lower than the one predicted by

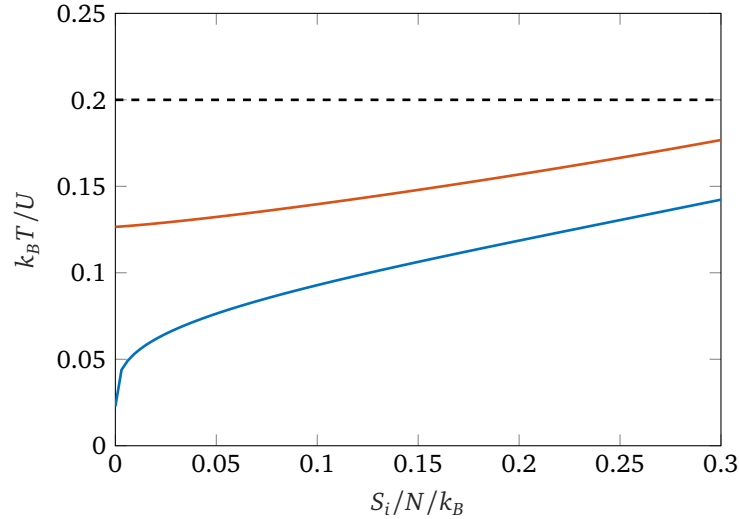


Figure 6.1: The final temperature in the Mott-insulator phase of the Bose-Hubbard model is plotted versus the entropy of the cold Bose gas from which the loading sequence starts. The case of ^{87}Rb on a square lattice with unit filling is considered. For the blue line, it is assumed that the loading sequence is adiabatic and no additional heating occurs. The orange line results from assuming that the excess energy from light scattering during a linear ramp with $\tau = 51$ ms (cf. table 6.2) fully thermalizes. The dashed black line indicates the melting temperature of the Mott insulator [75].

assuming full thermalization of ΔE . Therefore, the orange line in figure 6.1 can be considered as an upper bound for the final temperature as long as ramp-induced excitation and additional heating sources, e. g. technical noise [219], are negligible.

To put the results for the attainable temperatures shown in figure 6.1 into perspective, it is necessary to briefly discuss the phase diagram of the Bose-Hubbard model at finite temperature [82, 88, 220]. Strictly speaking, the Mott-insulating phase exists only at $T = 0$ and $U/J > (U/J)_c$. However, the characteristic features of the Mott-insulator survive up to the so-called melting temperature $T_m = 0.2 U/k_B$ [75]. This temperature is indicated by the dashed line in figure 6.1. Since the expected temperatures lie below T_m , the relevant low-temperature regime of the Bose-Hubbard model appears to be accessible with the considered loading scheme.

It is worth noting that the average number of scattering events per atom during the ramp $N_{\text{sc}} \ll 1$ (cf. table 6.2). Therefore, the assumption that in each experimental run the energy increases by approximately $2E_r N N_{\text{sc}}$ is only valid for large atom numbers N . For lower atom numbers, no scattering event occurs in most experimental runs. However, for those runs in which a photon is scattered the energy increase per particle is large. Therefore, it would be advantageous if these experimental runs could be identified and excluded from data analysis.

6.2 Loading from the atomic limit

Deterministic loading of cold atoms into optical microtrap arrays [155, 198, 199, 221] combined with Raman sideband cooling [174, 201] constitutes a promising source for low-entropy many-body states [222, 223]. This approach assembles quantum many-body systems atom-by-atom, contrasting the loading schemes used in optical lattice experiments (cf. section 6.1), which start from the bulk, i. e. Bose-Einstein condensates or degenerated Fermi gases [15, 16]. The deterministic preparation of atomic arrays with unit filling and the Raman sideband cooling of the atoms to the respective motional ground state require tight, isolated traps, which prohibit inter-site tunneling. Therefore, after the cooling process, the trap depth or the trap spacing needs to be reduced significantly, to explore the itinerant physics of the Hubbard model. This was demonstrated for atom pairs in double-wells [152].

In this section, the time-dependent transfer of bosonic atoms from an array of isolated traps to a tunnel-coupled lattice is investigated. Reducing the trap depth instead of the trap spacing is preferred because the latter results in a large overlap of the optical microtraps prohibiting cross-talk free single-site control [224]. Clearly, the time-dependent transfer has to be "as fast as possible, but as slow as necessary," to avoid ramp-induced excitations on the one hand, and to suppress external heating mechanisms or loss processes, on the other hand. To satisfy these conflicting conditions, optimal ramp shapes are derived.

The section is organized as follows: In subsection 6.2.1, an adiabatic variational procedure for optimal time-dependent parameter ramps is formulated. In subsection 6.2.2, the model for ultracold atoms in optical microtraps is formulated, the regimes traversed during the transfer process are discussed, and the formalism developed in subsection 6.2.1 is applied. Current experiments with optically trapped atoms are used as benchmarks to obtain realistic system parameters in subsection 6.2.3. Employing these results, an optimal adiabatic ramp is computed in subsection 6.2.4. For this ramp, the impact of heating due to light scattering is estimated, and the transfer fidelity is computed by solving the time-dependent Schrödinger equation for the one-dimensional Bose-Hubbard model. The particle number scaling behavior of the procedure is discussed in subsection 6.2.5. Finally, in subsection 6.2.6 the transfer to a BEC is discussed.

6.2.1 Rapid adiabatic parameter ramps

Time-dependent manipulations of atom traps have to be sufficiently slow to avoid excitations. Therefore, one has to specify the conditions of adiabaticity and define error measures for time-dependent transfer processes.

Consider a quantum system with Hamilton operator $\hat{H}(\gamma)$, which is controlled by a ℓ -dimensional time-dependent parameter $\gamma(t)$ within the time interval $[0, \tau]$. Its instantaneous energies $E_i(\gamma)$ and eigenstates $|i(\gamma)\rangle$ are obtained from the stationary Schrödinger equation

$$\hat{H}(\gamma)|i(\gamma)\rangle = E_i(\gamma)|i(\gamma)\rangle. \quad (6.2)$$

The adiabatic theorem [39, 225] states that systems prepared initially in the energy eigenstate $|i(\gamma(0))\rangle$ will remain in $|i(\gamma(t))\rangle$, if the change of the parameter γ is sufficiently slow and the energy levels $E_i(\gamma)$ are well separated. In absence of induced resonant transitions,

a sufficient criterion [226, 227] for adiabaticity is given by

$$\max_{0 \leq t \leq \tau} \left| \frac{\alpha_{ij}(\gamma, \dot{\gamma})}{\hbar \omega_{ij}^2(\gamma)} \right|^2 \ll 1, \quad \forall j \neq i. \quad (6.3)$$

Here, the transition frequencies

$$\omega_{ij}(\gamma) = \frac{E_j(\gamma) - E_i(\gamma)}{\hbar}, \quad (6.4)$$

and the transition matrix elements

$$\alpha_{ij}(\gamma, \dot{\gamma}) = \langle j | \partial_t \hat{H} | i \rangle = \sum_{l=1}^{\ell} \dot{\gamma}_l \langle j | \partial_{\gamma_l} \hat{H} | i \rangle, \quad (6.5)$$

are introduced. Based on measuring the instantaneous loss out of the state $|i\rangle$ into any other state $|j\rangle$ by

$$\mathcal{L}(\gamma, \dot{\gamma}) = \sum_{j \neq i} \left| \frac{\alpha_{ij}(\gamma, \dot{\gamma})}{\hbar \omega_{ij}^2(\gamma)} \right|^2, \quad (6.6)$$

one can express the cumulative adiabatic error as

$$\mathbb{E}_{\infty}[\gamma, \dot{\gamma}] = \max_{0 \leq t \leq \tau} \mathcal{L}(\gamma(t), \dot{\gamma}(t)). \quad (6.7)$$

The smallness of the functional \mathbb{E}_{∞} defines an optimality criterion for the adiabaticity (cf. equation (6.3)) of a time-dependent process $\gamma(t)$, starting from $\gamma(0)$ and reaching $\gamma(\tau)$ within the duration τ .

Alternatively, the time-averaged functional

$$\mathbb{E}_1[\gamma, \dot{\gamma}] = \frac{1}{\tau} \int_0^{\tau} \mathcal{L}(\gamma(t), \dot{\gamma}(t)) dt, \quad (6.8)$$

is also a cumulative measure for the non-adiabaticity of the process. Clearly, the definition of equation (6.8) is more amenable to extremization using variational analysis than the definition of equation (6.7). In Appendix G, it is shown that for the one-dimensional case considered in this manuscript a parameter curve which minimizes \mathbb{E}_1 also minimizes \mathbb{E}_{∞} .

By considering the structure of \mathcal{L} in equations (6.5) and (6.6), a quadratic form in terms of the velocities $\dot{\gamma}$ can be obtained,

$$\mathcal{L}(\gamma, \dot{\gamma}) = \sum_{k,l=1}^{\ell} \frac{1}{2} \dot{\gamma}_k \mathcal{M}_{kl}(\gamma) \dot{\gamma}_l \quad (6.9)$$

with a symmetric, parameter-dependent mass matrix $\mathcal{M}(\gamma)$ in close analogy to Lagrangian mechanics. Optimal trajectories γ are obtained from the Euler-Lagrange equations

$$\frac{d}{dt} \partial_{\dot{\gamma}_l} \mathcal{L} = \partial_{\gamma_l} \mathcal{L}. \quad (6.10)$$

Clearly, a canonical momentum $\pi_i = \partial_{\dot{\gamma}_i} \mathcal{L} = (\mathcal{M}\dot{\gamma})_i$ can be introduced which yields the Hamiltonian function

$$\mathcal{H}(\gamma, \pi) = \sum_{l=1}^{\ell} \pi_l \dot{\gamma}_l - \mathcal{L} = \sum_{k,l=1}^{\ell} \frac{1}{2} \pi_k \mathcal{M}_{kl}^{-1}(\gamma) \pi_l, \quad (6.11)$$

via a Legendre transformation. From equation (6.11) Hamilton's equation of motion can be derived as

$$\dot{\gamma}_l = \partial_{\pi_l} \mathcal{H} = (\mathcal{M}^{-1}(\gamma)\pi)_l, \quad \dot{\pi}_l = -\partial_{\gamma_l} \mathcal{H}. \quad (6.12)$$

If the system is not subject to any external time dependence, then the Hamiltonian function is constant

$$\mathcal{H}(\gamma(t), \pi(t)) = \mathcal{H}_0. \quad (6.13)$$

In the special case of one-dimensional parameter processes $\ell = 1$, which is considered in section 6.2.4, this leads to completely integrable dynamics

$$\int_{\gamma(0)}^{\gamma(t)} d\gamma \sqrt{\mathcal{M}(\gamma)} = \pm \sqrt{2\mathcal{H}_0} t \quad (6.14)$$

for the optimal adiabatic process $\gamma(t)$.

The approach discussed here is equivalent to the concept of the 'quantum adiabatic brachistochrone' [228] and strongly related to constant adiabaticity pulses used in nuclear magnetic resonance [229].

6.2.2 Cold atoms in optical microtraps

In section 3.2, it is shown that the physics of ultracold bosonic atoms in optical microtraps is described by the multi-band Bose-Hubbard Hamilton operator [230]

$$\hat{H}(\gamma) = \sum_{n,i} \epsilon_i^n(\gamma) \hat{a}_i^{n\dagger} \hat{a}_i^n - \sum_{n,i \neq j} J_{ij}^n(\gamma) \hat{a}_i^{n\dagger} \hat{a}_j^n + \frac{1}{2} \sum_{nopq} \sum_{ijkl} U_{ijkl}^{nopq}(\gamma) \hat{a}_i^{n\dagger} \hat{a}_j^{o\dagger} \hat{a}_k^p \hat{a}_l^q. \quad (6.15)$$

Here, γ is the control parameter of the optical potential $V(\mathbf{r}, \gamma)$. Since the Wannier functions are determined by V , both the Bose-Hubbard parameters and the annihilation operators \hat{a}_i^n depend on γ . However, to have a compact notation, the parameter dependency is suppressed if the resulting expression is unambiguous.

Atomic limit

The transfer process starts from an array of tight isolated traps with one atom per site prepared in the respective motional ground state. The corresponding many-body state is given by the Fock state $|g_{\text{al}}\rangle = |\mathbf{n}\rangle$ with the occupation numbers $n_i^n = \delta_{0n}$ (cf. section 3.2.3). In this regime, the *atomic limit*, inter-site tunneling is strongly suppressed. Therefore, the only possible reaction of the system to time-dependent modulations of the trap depth are local inter-band excitations (cf. figure 6.2) resulting in states of the form $\hat{a}_i^{n\dagger} \hat{a}_i^0 |g_{\text{al}}\rangle$.

Due to the tight confinement of the atoms around the respective potential minima, each trap can be described by a harmonic oscillator. The corresponding frequencies

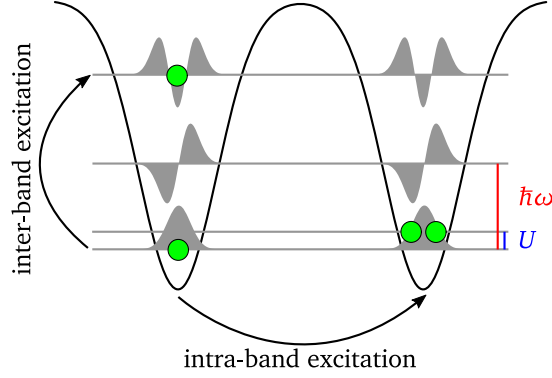


Figure 6.2: Excitation pathways in a microtrap array: inter-band excitations dominate in deep traps since intra-band tunneling is exponentially suppressed. However, for shallower potentials intra-band tunneling prevails, as long as the two-particle interaction energy $U = U_{iiii}^{0000}$ remains smaller than the band gap $\hbar\omega$.

$(\Omega_x(t), \Omega_y(t), \Omega_z(t)) = \gamma(t)$ are the control parameters for the adiabatic loading procedure. The multi-band Bose-Hubbard Hamiltonian operator of equation (6.15) reduces to the sum of local harmonic oscillators

$$\hat{H}_{\text{al}}(\gamma) = \sum_{n,i} \epsilon_i^n(\gamma) \hat{a}_i^{n\dagger} \hat{a}_i^n, \quad \epsilon_i^n(\gamma) = \hbar \sum_{l=x,y,z} (n_l + \frac{1}{2}) \Omega_l. \quad (6.16)$$

If local Cartesian coordinates $\xi = \mathbf{r} - \mathbf{R}_i$ around the trap minimum \mathbf{R}_i of the i^{th} site are introduced, then the Wannier function

$$w_i^n(\mathbf{r}) = w^n(\xi) = (\xi | n_x n_y n_z), \quad (6.17)$$

factorizes into one-dimensional harmonic oscillator states

$$(\xi_l | n_l) = \frac{e^{-\frac{\xi_l^2}{2a_l^2}}}{\sqrt{\pi(2^{n_l} n_l! a_l)^2}} H_{n_l} \left(\frac{\xi_l}{a_l} \right). \quad (6.18)$$

Here, $a_l = \sqrt{\hbar/(m\Omega_l)}$ denote the three oscillator lengths, $n = (n_x, n_y, n_z) \in \mathbb{N}_0^3$ are the motional quantum numbers, and H_m is the m^{th} Hermite polynomial.

To determine the adiabatic Lagrangian function $\mathcal{L}_{\text{al}}(\gamma, \dot{\gamma})$ from equation (6.6), parameter derivatives of the form

$$\frac{\partial \hat{H}_{\text{al}}}{\partial \gamma_l} = \sum_{n,i} \frac{\partial \epsilon_i^n}{\partial \gamma_l} \hat{a}_i^{n\dagger} \hat{a}_i^n + \epsilon_i^n \left(\frac{\partial \hat{a}_i^{n\dagger}}{\partial \gamma_l} \hat{a}_i^n + \hat{a}_i^{n\dagger} \frac{\partial \hat{a}_i^n}{\partial \gamma_l} \right) \quad (6.19)$$

need to be calculated. The derivatives of the operators \hat{a}_i^n can be found from equation (3.5) [219, 231]

$$\frac{\partial \hat{a}_i^n}{\partial \gamma_l} = \sum_{p,j} C_{ij;l}^{np} \hat{a}_j^p, \quad C_{ij;l}^{np} = \int \frac{\partial w_i^n(\mathbf{r})}{\partial \gamma_l} w_j^p(\mathbf{r}) d^3r. \quad (6.20)$$

The coefficients $C_{ij;l}^{np}$ can be interpreted geometrically as the generators of a basis-rotation and satisfy the relation $C_{ij;l}^{np} = -C_{ji;l}^{pn}$. Using the harmonic approximation for the Wannier

functions given in equation (6.18), one obtains

$$C_{ii;l}^{n0} = \frac{\delta_{n_l 2}}{\sqrt{8}\gamma_l} \prod_{l' \neq l}^{\ell} \delta_{n_{l'} 0}. \quad (6.21)$$

The calculation of the transition amplitudes defined in equation (6.5) requires the evaluation of matrix-element between ground and excited state. Using equations (6.19) and (6.20) one finds

$$\langle g_{\text{al}} | \hat{a}_i^{0\dagger} \hat{a}_i^n \partial_{\gamma_l} \hat{H}_{\text{al}} | g_{\text{al}} \rangle = (\epsilon_i^n - \epsilon_i^0) C_{ii;l}^{n0}, \quad (6.22)$$

yielding

$$\alpha_{ii}^{0n} = \sum_{l=1}^3 \dot{\gamma}_l (\epsilon_i^n - \epsilon_i^0) C_{ii;l}^{n0}. \quad (6.23)$$

The energies of inter-band excitations

$$\hbar\omega_i^n(\gamma) = \epsilon_i^n - \epsilon_i^0 = \hbar \sum_{l=1}^3 n_l \gamma_l, \quad (6.24)$$

can be inferred from the harmonic oscillator level spacing. Finally, by summing over all excited states, the adiabatic error Lagrangian function in the atomic limit can be determined

$$\mathcal{L}_{\text{al}}(\gamma, \dot{\gamma}) = \sum_{l=1}^3 \frac{1}{2} \mathcal{M}_{\text{al}}(\gamma_l) \dot{\gamma}_l^2, \quad (6.25)$$

with the extensive mass-function $\mathcal{M}_{\text{al}}(\gamma_l) = M(2\gamma_l)^{-4}$ and the number of sites M .

Fortunately, \mathcal{L}_{al} is separable. From the integrability condition of equation (6.14), the optimal adiabatic ramp with the well-known hyperbolic shape [232] is obtained

$$\gamma_l^{-1}(t) = \Omega_{l0}^{-1} + (\Omega_{l\tau}^{-1} - \Omega_{l0}^{-1}) \frac{t}{\tau}, \quad (6.26)$$

for the transfer of trapped particles from an initial trap with $\gamma(0) = (\Omega_{x0}, \Omega_{y0}, \Omega_{z0})$ to a final trap with $\gamma(\tau) = (\Omega_{x\tau}, \Omega_{y\tau}, \Omega_{z\tau})$. The quantitative measure for residual excitations

$$\mathbb{E}_{\infty}^{\text{al}}[\gamma, \dot{\gamma}] = \frac{M}{32\tau^2} \sum_{l=x,y,z} (\Omega_{l\tau}^{-1} - \Omega_{l0}^{-1})^2 \quad (6.27)$$

is inversely proportional to the square of the ramp duration τ .

In an experiment, the trap frequencies are determined by the optical potential. Therefore, the actual control parameter is the trap depth. In section 6.2.3, the relations between the trap frequencies and the trap depth are derived for realistic system parameters obtained from experiments.

Mott insulator

For shallower traps, one obtains an itinerant many-body state. In this regime, intra-band excitations due to tunneling between adjacent traps (cf. figure 6.2) are energetically favored over inter-band excitations. It is assumed that the initial cooling process was

efficient and the preceding adiabatic transfer has not populated higher bands. Therefore, the following analysis is restricted to the lowest band. Further, a sufficiently deep and homogeneous trap array is assumed such that only nearest-neighbor tunneling and on-site interactions need to be considered and $\epsilon \equiv \epsilon_i^0$, $J \equiv J_{i,i+1}^0$, $U \equiv U_{iii}^{0000}$. In this case, the single-band Bose-Hubbard model [13, 15, 16, 55, 61]

$$\hat{H}_{\text{bh}}(\gamma) = \epsilon N - J \sum_{\langle i,j \rangle} \hat{a}_i^{0\dagger} \hat{a}_j^0 + \frac{U}{2} \sum_i \hat{a}_i^{0\dagger} \hat{a}_i^{0\dagger} \hat{a}_i^0 \hat{a}_i^0 \quad (6.28)$$

emerges from equation (6.15). The notation $\langle i, j \rangle$ indicates a summation over nearest-neighbor pairs of traps. The relevant control parameter is $\gamma = (J, U)$, since the on-site single-particle energy ϵ results only in a constant energy offset.

To evaluate the adiabatic Lagrangian function from equation (6.6), one needs to find the energy eigenstates of \hat{H}_{bh} . For $U \gg J$, this can be done perturbatively starting from the ground state in the atomic limit $|g_{\text{al}}\rangle$ (cf. section 3.2.3 and [71]). In the Mott-insulator phase, low-lying excited states $|p, q\rangle = \hat{a}_p^{0\dagger} \hat{a}_q^0 |g_{\text{al}}\rangle / \sqrt{2}$, transport an atom from site q to site $p \neq q$. These transitions are called particle-hole or intra-band excitations (cf. figure 6.2). To first order in perturbation theory, the ground state reads

$$|g_{\text{bh}}\rangle = |g_{\text{al}}\rangle + \frac{\sqrt{2}J}{U} \sum_{\langle p,q \rangle} |p, q\rangle + \mathcal{O}\left(\frac{J^2}{U^2}\right). \quad (6.29)$$

The energy corresponding to a particle-hole excitation is given by

$$\hbar\omega_{pq} = \langle p, q | \hat{H}_{\text{bh}} | p, q \rangle - \langle g_{\text{bh}} | \hat{H}_{\text{bh}} | g_{\text{bh}} \rangle = U + \mathcal{O}\left(\frac{J^2}{U^2}\right). \quad (6.30)$$

The transition matrix elements can be calculated from equation (6.5) yielding

$$\alpha_{pq} = \dot{U} \langle p, q | \partial_U \hat{H}_{\text{bh}} | g_{\text{bh}} \rangle + J \langle p, q | \partial_J \hat{H}_{\text{bh}} | g_{\text{bh}} \rangle = -\sqrt{2}U \partial_t \left(\frac{J}{U} \right) + \mathcal{O}\left(\frac{J^2}{U^2}\right). \quad (6.31)$$

It is worth noting that a change in the parameters U and J is connected to a change in the Wannier functions. Therefore, the derivative of the operators \hat{a}_i with respect to U and J need to be considered. However, terms connected to these derivatives are neglected in equation (6.31) since they do not induce intra-band excitations [219, 233].

From equations (6.30) and (6.31) the adiabatic functional on a two-dimensional parameter space $\gamma = (J, U)$ can be derived

$$\mathcal{L}_{\text{bh}}(\gamma, \dot{\gamma}) = \frac{1}{2} \sum_{k,l=1}^2 \dot{\gamma}_k \mathcal{M}_{kl}(\gamma) \dot{\gamma}_l + \mathcal{O}\left(\frac{J^3}{U^3}\right), \quad \mathcal{M} = \frac{4Mz\hbar^2}{U^6} \begin{pmatrix} U^2 & -JU \\ -JU & J^2 \end{pmatrix}, \quad (6.32)$$

with z being the average number of nearest-neighbor sites, commonly called coordination number.

In experiments [15] the on-site interaction strength $U(t) = U(V_0(t))$ and the tunneling parameter $J(t) = J(V_0(t))$ are not independent variables but functionally depend on the depth of the optical potential $V_0(t)$. This is described in section 6.2.3. Therefore, a one-dimensional parameter curve $\gamma(t) = V_0(t)$ and an adiabatic Lagrangian function

$$\mathcal{L}_{\text{bh}}(\gamma, \dot{\gamma}) = \frac{1}{2} \mathcal{M}_{\text{bh}}(\gamma) \dot{\gamma}^2, \quad \mathcal{M}_{\text{bh}}(\gamma) = \frac{4Mz\hbar^2}{U^2(\gamma)} \left[\partial_\gamma \left(\frac{J(\gamma)}{U(\gamma)} \right) \right]^2 \quad (6.33)$$

are obtained, with a well-defined positive mass function $\mathcal{M}_{\text{bh}}(\gamma) > 0$.

6.2.3 Realistic experimental setting

In this section, details of an implementation based on recent experiments are discussed. From this, a realistic set of experimental parameters is determined, which deviates from the one used in the remainder of this thesis. However, the differences are small. Therefore, the conclusions drawn from the following investigations can be transferred to the setup considered in section 4.

Optical potential

There are multiple techniques to generate arrays of optical microtraps (cf. section 4.1). Among these are acousto-optic deflectors (AOD) [152, 154, 155], spatial light modulators (SLM) [157, 198], and microlens arrays (MLA) [147, 148, 224]. Here, no assumptions about the used approach are made. However, it is presumed that the microtraps have an approximately Gaussian shape with a waist of $w_0 = 0.71 \mu\text{m}$ and are generated by linearly polarized light with a wavelength of $\lambda_{\perp} = 852 \text{ nm}$ as in [152]. Further, the species ^{87}Rb is considered, which is the workhorse for the field of ultracold atoms and has been used in most of the experiments relevant for this work [152, 154, 155, 198, 201]. It is assumed that the atoms are prepared in the state $|5^2S_{1/2}, F = 2, m_F = 2\rangle$ as they were in [152, 201]. In [154], the setup from [152] has been used to generate a 2×2 optical tweezer array with one atom per trap. The minimal trap spacing that allows for a high preparation efficiency of 90% has been determined to $d = 1.7 \mu\text{m}$. For this trap spacing, the overlap of adjacent traps is negligible, which facilitates cross-talk free single-site control over the optical potential [224].

For the experiments [152, 174, 201], the cooling efficiency in the axial direction was considerably lower than in the transverse direction. This results from weaker confinement in the axial direction. The effect can be compensated by additional axial confinement. Further, this prevents atoms to tunnel to diffraction patterns along the optical axis that exist if the trap array is generated by an MLA or an SLM (cf. Talbot effect). Therefore, axial confinement implemented by a standing wave is considered, which is produced by two laser beams with a wavelength $\lambda_{\parallel} = 1064 \text{ nm}$ that enclose an angle of $\theta = 24.6^\circ$. This results in a spacing of $2.5 \mu\text{m}$ between the antinodes of the optical potential which is large enough to prohibit tunneling in the out-of-plane direction for the considered potential depths. The total optical potential reads

$$V(\mathbf{r}, t) = V_{\perp}(\mathbf{r}, t) + V_{\parallel}(\mathbf{r}, t) \quad (6.34)$$

with the optical microtrap array potential

$$V_{\perp}(\mathbf{r}, t) \approx -V_{0\perp}(t) \sum_{i=1}^N e^{-2 \frac{(x-X_i)^2 + (y-Y_i)^2}{w_0^2}} \quad (6.35)$$

and the standing wave potential for out-of-plane confinement

$$V_{\parallel}(\mathbf{r}, t) \approx -V_{0\parallel}(t) \cos^2(\kappa z). \quad (6.36)$$

Here, the potential depths $V_{0\perp}$ and $V_{0\parallel}$ as well as the i^{th} site's coordinates X_i and Y_i are introduced. The projection of the wave vector onto the lattice direction $\kappa = \sin(\theta/2) 2\pi/\lambda_{\parallel}$ determines the periodicity of the 1D optical lattice used for out-of-plane confinement. For equations (6.35) and (6.36) it is assumed that the out-of-plane confinement from V_{\perp} is weak in comparison to that from V_{\parallel} and that the laser beams generating V_{\parallel} have a waist that is larger than the extent of the microtrap array. During the cooling process it is

Quantity	Symbol	Value
Atomic mass of ^{87}Rb	m	86.9 u
Scattering length	a_s	5.24 nm
Energy scale	\mathcal{E}	38.1 nK $\cdot k_B$
Wavelength for V_{\perp}	λ_{\perp}	852 nm
Wavelength for V_{\parallel}	λ_{\parallel}	1064 nm
Trap spacing	d	1700 nm
Trap waist	w_0	710 nm
Inclination angle	θ	24.6°
Initial depth of V_{\perp}	$V_{0\perp}(0)$	1 mK $\cdot k_B$
Final depth of V_{\perp}	$V_{0\perp}(\tau)$	158 nK $\cdot k_B$
Initial depth of V_{\parallel}	$V_{0\parallel}(0)$	2.5 mK $\cdot k_B$
Final depth of V_{\parallel}	$V_{0\parallel}(\tau)$	395 nK $\cdot k_B$

Table 6.3: Experimental parameters used for obtaining realistic estimates for the adiabatic loading procedure.

assumed that $V_{0\perp}/k_B = 1$ mK, which is consistent with the values used in experiments [152, 174, 201]. To have an equally strong confinement in the out-of-plane direction, $V_{0\parallel}/k_B = 2.5$ mK is chosen. The used parameters are summarized in table 6.3.

Trap frequencies and Bose-Hubbard parameters

To evaluate the expressions for the adiabatic Lagrangian functions derived in section 6.2.1, the trap frequencies and the Hubbard parameters need to be expressed as functions of the optical potential depths $V_{0\perp}$ and $V_{0\parallel}$. This is done in the present subsection. The harmonic trapping frequencies can be computed from the curvature of the potentials given in equations (6.35) and (6.36) yielding

$$\Omega_x = \Omega_y = \sqrt{\frac{4V_{0\perp}}{mw_0^2}}, \quad \Omega_z = \sqrt{\frac{2\kappa^2 V_{0\parallel}}{m}}. \quad (6.37)$$

In combination with equation (6.25) these expressions allow to estimate the adiabaticity of the transfer process in the atomic limit.

To obtain the Hubbard parameters for tunneling J and on-site interaction U , the Wannier functions w_i need to be computed. Since the optical potential is a sum of the in-plane part V_{\perp} and the out-of-plane part V_{\parallel} , the Wannier functions factorize

$$w_i^0(\mathbf{r}) = \varphi_i(x, y)\phi(z). \quad (6.38)$$

In out-of-plane direction, the tunneling is strongly suppressed at all times. Therefore, a natural choice for ϕ is the ground state of one slice of the standing wave potential given in equation (6.36). ϕ is calculated by solving the corresponding 1D time-independent Schrödinger equation numerically. For the potential in the x - y plane, a regular square lattice of 20×20 sites and periodic boundary conditions are assumed. φ_i is the lowest band Wannier function for this potential obtained from a numerical band structure calculation (cf. section 5.1 and [176]). The Hubbard parameters for tunneling J between adjacent sites i and j and the on-site interaction U can be calculated from equations (3.8) and (3.9) respectively. It is worth noting that the results for U and J can be adopted for

different lattice geometries like one-dimensional, triangular, and hexagonal lattices since the relative deviations are small.

For convenience in later computations simple expressions for the Hubbard parameters are advantageous. The on-site interaction strength can be reliably approximated by using Gaussian wave functions for ϕ and φ_i (cf. section 5.2.1). For the out-of-plane direction the harmonic oscillator length can be used as $1/\sqrt{e}$ width for the Gaussian wave function

$$a_{\parallel} = \sqrt[4]{\frac{d^2 \mathcal{E}}{4\pi^2 \kappa^2 V_{0\parallel}}}. \quad (6.39)$$

To obtain a satisfying approximation for the Wannier function φ_i , a variational calculation is performed to find the wave function's width that minimizes the energy in a Gaussian potential well (cf. appendix D). This yields

$$a_{\perp} = \sqrt{\frac{w_0^2 d}{2\pi w_0 \sqrt{2V_{0\perp}/\mathcal{E}} - 2d}}. \quad (6.40)$$

Using the above expressions, the on-site interaction can be calculated

$$U = g \mathcal{U}_{\perp} \mathcal{U}_{\parallel}, \quad (6.41)$$

with the in-plane and out-of-plane part

$$\mathcal{U}_{\perp} = \iint \varphi_i^4(x, y) dx dy \approx \sqrt{\frac{2V_{0\perp}}{w_0^2 d^2 \mathcal{E}}} - \frac{1}{\pi w_0^2}, \quad (6.42)$$

$$\mathcal{U}_{\parallel} = \int \phi^4(z) dz \approx \sqrt[4]{\frac{\kappa^2 V_{0\parallel}}{d^2 \mathcal{E}}}. \quad (6.43)$$

The tunneling parameter J cannot be well approximated using the Gaussian wave function ansatz because it significantly underestimates the Wannier function's value at the position of neighboring sites. Instead, J is parametrized using a semiclassical ansatz (cf. section 5.2.2 and [123, 192])

$$J = A \left(\frac{V_{0\perp}}{\mathcal{E}}\right)^C e^{-B \sqrt{V_{0\perp}/\mathcal{E}}} \mathcal{E}. \quad (6.44)$$

A fit to the numerical calculations yields $A = 2.26 \pm 0.05$, $B = 4.02 \pm 0.01$, $C = 1.00 \pm 0.03$. Figure 6.3 shows the comparison between the discussed approximations and the results from the numerical band structure calculations revealing quantitative agreement.

6.2.4 Rapid adiabatic loading of a Mott insulator

In this section, the transfer from the atomic limit to a Mott insulator close to the quantum phase transition is investigated. The challenge is to find ramps $V_{0\perp}(t)$ and $V_{0\parallel}(t)$ that minimize excitations during this process. In section 6.2.2, the instantaneous measures \mathcal{L}_{al} and \mathcal{L}_{bh} are derived for the regimes dominated by intra-band and inter-band excitations respectively. However, it is apparent that the system will traverse an intermediate regime where both excitation pathways are of similar importance. Therefore, a reasonable approximate measure for the instantaneous adiabaticity of the transfer process is given by the sum

$$\mathcal{L}(\gamma, \dot{\gamma}) = \mathcal{L}_{\text{al}}(\gamma, \dot{\gamma}) + \mathcal{L}_{\text{bh}}(\gamma, \dot{\gamma}). \quad (6.45)$$

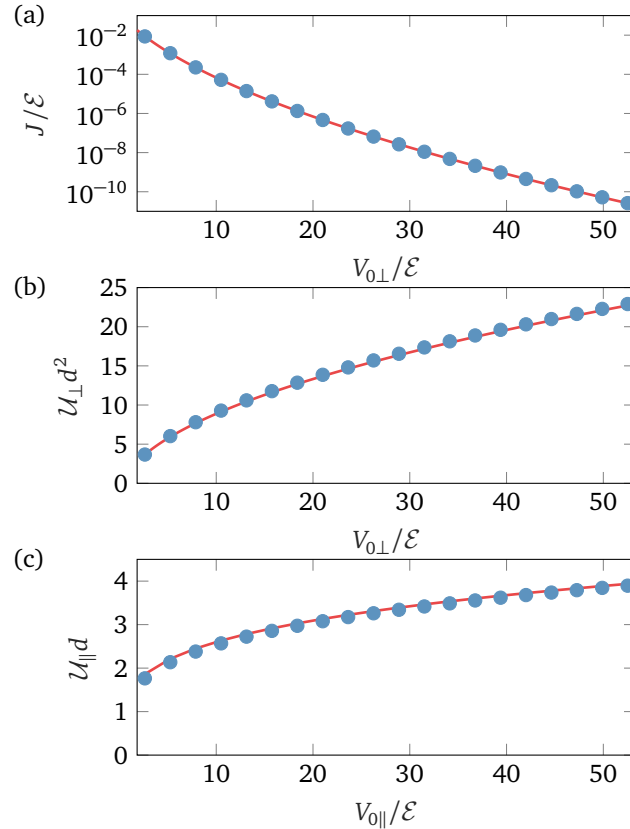


Figure 6.3: Comparison between results from the numerical solution of the single-particle Schrödinger equation (circles) and the approximate closed-form expressions (lines) for the Hubbard parameters. (a) Tunneling parameter J as a function of the potential depth $V_{0\perp}$ for ^{87}Rb atoms in a square lattice of Gaussian dipole traps with waist $w_0 = 0.71 \mu\text{m}$ and trap spacing $d = 1.7 \mu\text{m}$. (b) The in-plane part U_{\perp} of the on-site interaction parameter versus $V_{0\perp}$ for the same parameters as in (a). (c) The out-of-plane part U_{\parallel} of the on-site interaction parameter versus $V_{0\parallel}$ for the same parameters as in (a).

From this, global error measures defined in equations (6.7) and (6.8) are obtained. Before optimal ramp shapes can be computed, the initial and final values for the potential depth need to be determined. The initial values are fixed by the requirement of efficient sideband cooling and given in section 6.2.3. Whereas, the final values are determined by the targeted many-body regime. Here, this is the Mott-Insulator phase close to the phase transition, occurring at $U/J = 3.4$ for a 1D lattice. Therefore, a final value of $U/J = 10$ is chosen.

To obtain equal trap frequencies in all directions $\Omega_x = \Omega_y = \Omega_z$, a constant ratio

$$\frac{V_{0\perp}(t)}{V_{0\parallel}(t)} = \frac{\kappa^2 w_{0\perp}^2}{2} \quad (6.46)$$

is chosen. This determines the final values of the potential depths $V_{0\perp}(\tau)/k_B = 158 \text{ nK}$ and $V_{0\parallel}(\tau)/k_B = 395 \text{ nK}$ yielding $U/h = 22 \text{ Hz}$ and $J/h = 2.2 \text{ Hz}$. Due to the constant ratio between the potential depths the instantaneous adiabatic Lagrangian function \mathcal{L} can be expressed as a function of $V_{0\perp}$ and $\dot{V}_{0\perp}$ only.

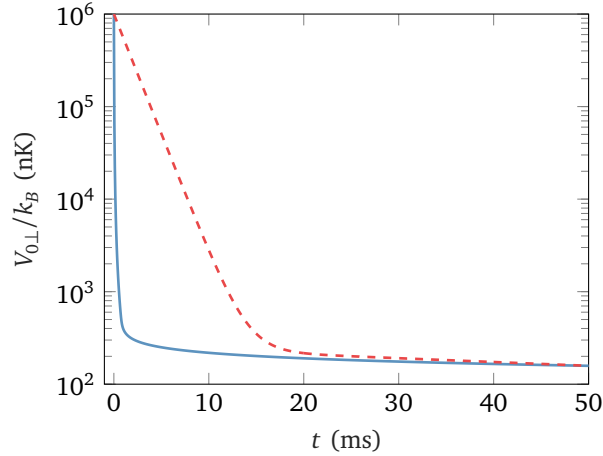


Figure 6.4: Potential depth $V_{0\perp}(t)$ versus time t . The red dashed line shows the ramp resulting from the bi-exponential ansatz whereas the blue solid line is the optimal adiabatic ramp.

Optimal ramps for the potential depth

A simple approach for finding an optimal ramp $V_{0\perp}(t)$ is to use a suitable, parametrized test function as an ansatz and optimize its parameters. Since the system traverses two different regimes, which are associated with two different time scales for an adiabatic transfer (cf. section 6.2.1), a bi-exponential ansatz of the form

$$V_{0\perp}(t) = V_a e^{-t/\tau_a} + V_b e^{-t/\tau_b} \quad (6.47)$$

is chosen, with decay times τ_a , τ_b and amplitudes V_a , V_b . The amplitudes are fixed by imposing the boundary values at $t = 0$ and $t = \tau$. The time constants are computed by numerically minimizing the quantity \mathbb{E}_∞ , i. e. calculating

$$\min_{\tau_a, \tau_b} \mathbb{E}_\infty(V_{0\perp}, \dot{V}_{0\perp}). \quad (6.48)$$

The red line in figure 6.4 shows the resulting ramp $V_{0\perp}(t)$ for the given parameters and $\tau = 50$ ms. For this ramp the time dependencies of \mathcal{L}_{al} and \mathcal{L}_{bh} are shown in figure 6.5 (dotted and solid red line respectively). The fact that during the first 15 ms both \mathcal{L}_{al} and \mathcal{L}_{bh} are much smaller than \mathbb{E}_∞ indicates that a better ramp can be realized with a faster decrease during this time interval.

The variational approach proposed in this article follows from solving the Euler-Lagrange equation

$$\frac{d}{dt} \frac{\partial \mathcal{L}}{\partial \dot{V}_{0\perp}} = \frac{\partial \mathcal{L}}{\partial V_{0\perp}}, \quad (6.49)$$

as discussed in section 6.2.1. The explicit form of the above equation can be obtained by using equations (6.25), (6.33), (6.37), and (6.39) to (6.45). In general, a solution $V_{0\perp}(t)$ to the above equation makes the functional \mathbb{E}_1 stationary. However, in appendix G it is shown that in this particular case it also minimizes \mathbb{E}_1 and \mathbb{E}_∞ . Therefore, a solution to equation (6.49) can be considered as an optimal adiabatic ramp. It is worth noting that \mathcal{L} is a constant of motion. Therefore, the optimal adiabatic ramp is equivalent to constant adiabaticity pulses used in nuclear magnetic resonance [229]. For a ramp duration of $\tau = 50$ ms, this ramp is shown in figure 6.4 (blue line). As expected from the discussion of the bi-exponential ramp function the optimal ramp shape shows a much

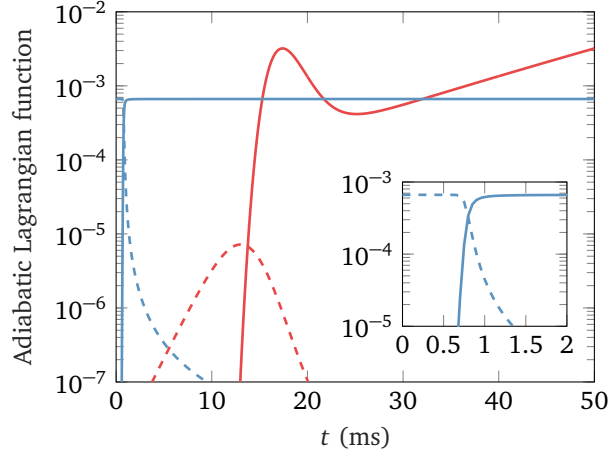


Figure 6.5: The adiabatic Lagrangian functions per site $\mathcal{L}_{\text{al}}/M$ (dashed) and $\mathcal{L}_{\text{bh}}/M$ (solid) are plotted versus time t for a bi-exponential (red) and an optimal adiabatic (blue) transfer sequence of duration $\tau = 50$ ms.

faster decrease for $t < 15$ ms. The dashed and solid blue lines in figure 6.5 show the time dependence of the components \mathcal{L}_{al} and \mathcal{L}_{bh} respectively. This demonstrates that inter-band excitations are only relevant during the first millisecond. Thereafter, intra-band excitations dominate.

In the following, analytic expressions for the optimal adiabatic ramp shape are derived. It is straight forward to obtain the ramp shape for the initial time interval, in which inter-band excitation dominate, using equations (6.26) and (6.37)

$$V_{0\perp}(t) = \frac{\mathcal{V}_i \mathcal{V}_f}{\left[\sqrt{\mathcal{V}_f} + \left(\sqrt{\mathcal{V}_i} - \sqrt{\mathcal{V}_2} \right) \frac{t}{\tau} \right]^2}, \quad \forall t < \tau_1. \quad (6.50)$$

Here, $\mathcal{V}_1 = V_{0\perp}(0)$, $\mathcal{V}_2 = V_{0\perp}(\tau_1)$, and $\tau_1 = 0.7$ ms, which marks the end of the first time interval (cf. inset of figure 6.5), are introduced.

For the second time interval intra-band transitions dominate. The corresponding mass function \mathcal{M}_{bh} can be determined from equations (6.33), (6.41), (6.42), (6.43), and (6.44). This complicated expression prohibits an analytic calculation of the integral in equation (6.14). However, for the relevant parameter regime one finds that

$$\mathcal{M}_{\text{bh}}(V_{0\perp}) \approx \frac{M\hbar^2}{\mathcal{E}^3 V_{0\perp}} \exp(a - b\sqrt{V_{0\perp}}), \quad (6.51)$$

with fit parameters $a = 24.4$ and $b = 9.66 \mathcal{E}^{-1/2}$. The above approximation is compared to the full expression for \mathcal{M}_{bh} in figure 6.6. Using equations (6.51) and (6.14) an approximate expression for the optimal adiabatic ramp can be derived

$$V_{0\perp}(t) = \mathcal{V}_0 \ln^2 \left(\frac{t-t_0}{\tau_2} \right), \quad \forall t > 1 \text{ ms}. \quad (6.52)$$

with $\tau_2 = 651$ s, $\mathcal{V}_0/k_B = 1.75$ nK, and $t_0 = 0.83$ ms. In figure 6.7, the closed form expressions for the optimal adiabatic ramp are compared to the numeric result showing excellent agreement in the respective time intervals.

In the following, the dependency of \mathbb{E}_∞ on the ramp duration τ is investigated. This is shown in figure 6.8 (a) for the bi-exponential and the optimal ramp shape. In both cases the data agrees very well with a $k \tau^{-2}$ dependency, with k being a constant. Least

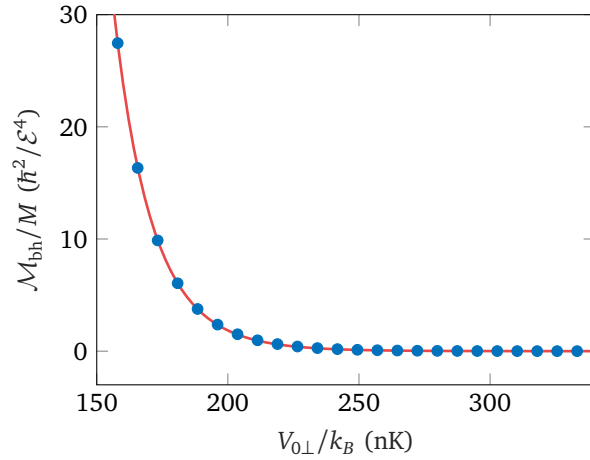


Figure 6.6: The mass function per site $\mathcal{M}_{\text{bh}}/M$ is plotted versus the potential depth $V_{0\perp}$. The blue points represent the full mass function obtained from equations (6.33), (6.41), (6.42), (6.43), and (6.44), whereas the orange line corresponds to the approximation given in equation (6.51).

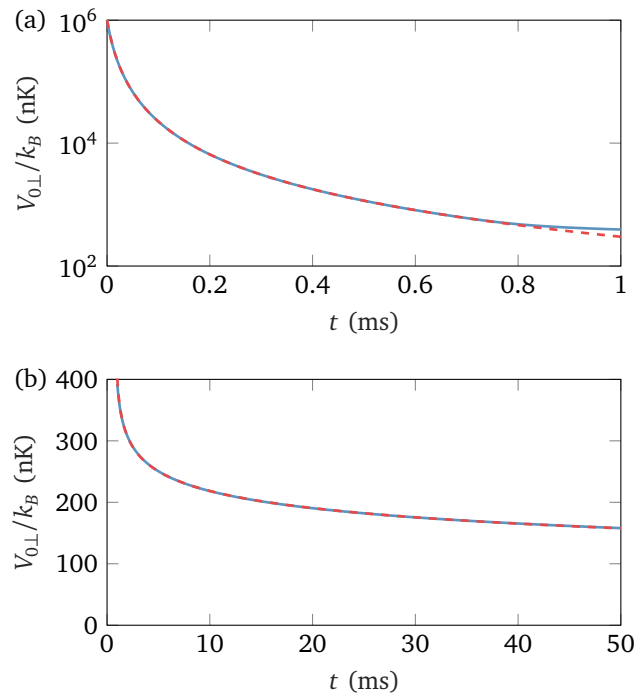


Figure 6.7: Optimal adiabatic potential ramp $V_{0\perp}(t)$ versus time t : comparison between the numerical solution of the Euler-Lagrange equation (blue solid lines) and the analytic approximation (dashed red lines) given in equations (6.50) and (6.52). For $t < 0.7$ ms (a) inter-band excitations dominate, whereas for $t > 1$ ms (b) intra-band excitations are the most relevant.

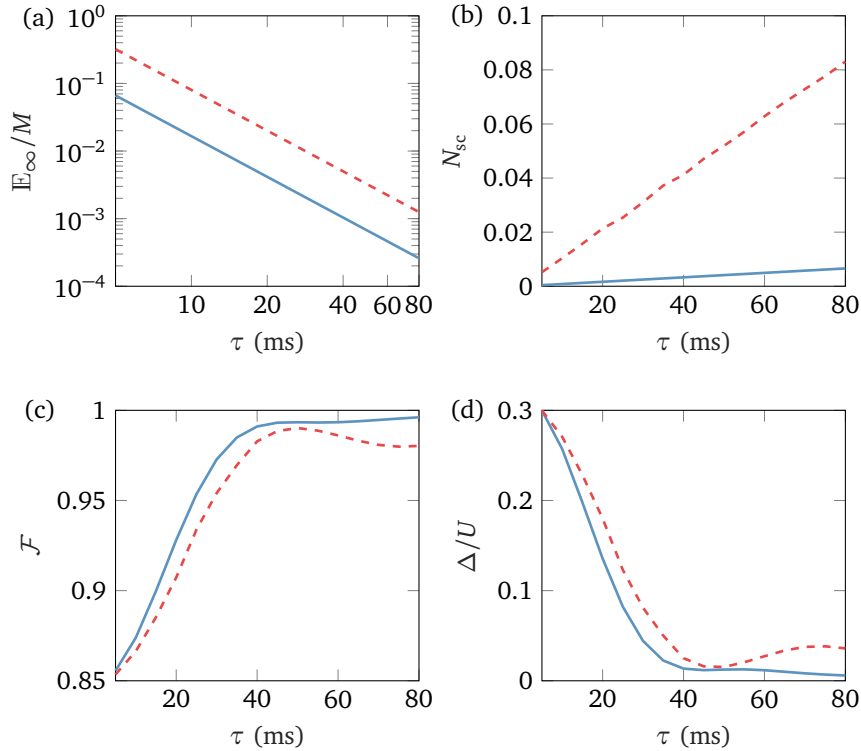


Figure 6.8: Figures of merit for the bi-exponential (dashed red line) and the optimal adiabatic (solid blue line) ramp versus the ramp duration τ : (a) maximal value \mathbb{E}_∞/M of the adiabatic Lagrangian function per site during the ramp, (b) number of scattering events per atom N_{sc} during the ramp, (c) transfer fidelity \mathcal{F} , (d) excess energy Δ of the final state in units of the interaction energy U at $t = \tau$. The results shown in (c) and (d) are obtained from a many-body calculation for a 1D lattice with periodic boundary conditions and $M = N = 8$ particles.

square fits yield $k = 8.01 \text{ ms}^2$ and $k = 1.66 \text{ ms}^2$ for the bi-exponential and the optimal ramp respectively. This dependency can be explained from $\mathbb{E}_\infty \propto (\partial_t V_{0\perp})^2 \propto \tau^{-2}$, which also coincides with the result for the atomic limit given in equation (6.27).

Impact of light scattering

The physical process that limits the usage of long ramp durations is heating due to light scattering. This effect has been studied in [30, 31] and recently, with regard to optical lattices, in [217, 218, 234]. To estimate the impact of this process, the number of scattering events per atom N_{sc} during the transfer process is calculated (cf. section 2.1.2). Figure 6.8 (b) shows the dependency of N_{sc} on the ramp duration τ for both the bi-exponential and the optimal ramp. The relation is linear with slopes of 1.04 s^{-1} and 0.08 s^{-1} for the bi-exponential and the optimal ramp respectively. Again, this can be explained using the time scale argument. The number of scattering events per atom can be reduced further by using light with a larger detuning, e.g. $\lambda_\perp = 1064 \text{ nm}$. However, already for the parameters used in this work an adiabatic transfer processes with negligible scattering can be realized.

Fidelity of the transfer process

To validate the adiabaticity of the transfer process, simulations of the many-body system are performed using the calculated ramps. For this purpose, the 1D single-band Bose-Hubbard model with periodic boundary conditions is used. This disregards possible excitations to higher bands. However, figure 6.5 shows that these excitations are negligible for the majority of the ramp duration.

The time-dependent Schrödinger equation

$$i\hbar\partial_t |\psi(t)\rangle = \hat{H}(t) |\psi(t)\rangle, \quad (6.53)$$

is solved for the Hamilton operator $\hat{H}(J(t), U(t))$ given in equation (6.28). The time dependence of the parameters U and J is determined by the ramp $\gamma(t) = V_{0\perp}(t)$ computed in section 6.2.4. To solve equation (6.53), the system's state is expanded using the Fock basis (cf. section (B.1)). This results in a system of ordinary differential equations (cf. section H.3)

$$i\hbar\dot{\psi}_{\mathbf{n}}(t) = \sum_{|\mathbf{n}'|=N} A_{\mathbf{n}\mathbf{n}'}(t) \psi_{\mathbf{n}'}(t), \quad (6.54)$$

$$A_{\mathbf{n}\mathbf{n}'}(t) = \langle \mathbf{n} | \hat{H}(t) + \hat{W}(t) | \mathbf{n}' \rangle. \quad (6.55)$$

The operator $\hat{W}(t)$ stems from the temporal change in the Wannier functions and is given by

$$\hat{W}(t) = i\hbar\dot{V}_{0\perp}(t) \sum_{np} \sum_{ij} C_{ij;1}^{np}(V_{0\perp}(t)) \hat{a}_i^{n\dagger} \hat{a}_j^p, \quad (6.56)$$

However, as stated earlier, this term does not induce intra-band excitation, i. e. $C_{ij;1}^{nn} = 0$ [219, 233]. Therefore, it is neglected for the single-band simulation.

The initial state $|\psi(0)\rangle$ is the ground state of $\hat{H}(0)$. From the final state $|\psi(\tau)\rangle$ two figures of merit are obtained

$$\mathcal{F} = |\langle \phi | \psi(\tau) \rangle|, \quad (6.57)$$

$$\Delta = \langle \psi(\tau) | \hat{H}(\tau) | \psi(\tau) \rangle - \langle \phi | \hat{H}(\tau) | \phi \rangle. \quad (6.58)$$

Here, $|\phi\rangle$ is the ground state of the final Hamilton operator $\hat{H}(\tau)$, \mathcal{F} is the transfer fidelity, and Δ is the energy difference between $|\phi\rangle$ and $|\psi(\tau)\rangle$. Figure 6.8 (c) and (d) show the dependency of \mathcal{F} and Δ on τ for the bi-exponential and the optimal adiabatic ramp. As expected, the transfer fidelity increases and the excess energy decreases for increasing ramp durations. This indicates a reduction of ramp-induced excitations. At $\tau \approx 40$ ms the slopes change significantly and saturation can be observed. In case of the bi-exponential ramp, this is accompanied by small amplitude oscillations.

The calculations are performed with particle numbers up to $M = N = 8$. For ramp durations $\tau > 40$ ms, both transfer fidelity and the excess energy are size independent.

The results of this section show that a high transfer fidelity $\mathcal{F} > 98\%$ can be achieved with ramp durations below 50 ms and negligible photon scattering $N_{\text{sc}} < 0.01$. It is worth noting that the ramp shape might be further improved by finding shortcuts to adiabaticity using optimal control [235]. However, the presented approach has the advantage to result in simple and robust ramps.

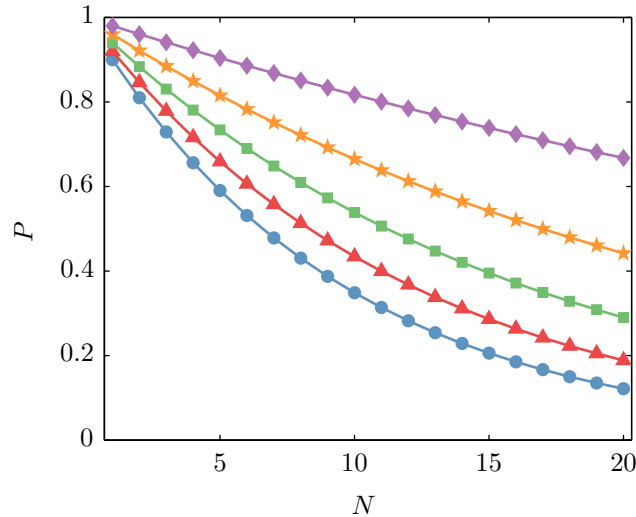


Figure 6.9: Joint probability $P = p_0^N$ to prepare N atoms in the motional ground state of N isolated traps versus particle number N , for various single site success probabilities $p_0 = 0.9$ (blue circles), $p_0 = 0.92$ (red triangles), $p_0 = 0.94$ (green squares), $p_0 = 0.96$ (orange stars), and $p_0 = 0.98$ (violet diamonds).

6.2.5 Limits on scalability

Clearly, there are limitations for the maximum number of atoms that can be prepared. One limitation arises from the necessity to provide an array of many, sufficiently deep optical microtraps. With AODs, SLMs, or MLAs, and laser powers of a few Watts, it is possible to produce arrays of a few hundred traps [148, 157, 198].

The next challenge is to prepare exactly one atom per trap. For arrays of up to 50 microtraps, unit filling is experimentally feasible [155, 198]. According to Ref. [198], this could be extended to a few hundred traps using state-of-the-art technology.

Another prerequisite of the discussed scheme is the preparation of atoms in the motional ground-state with high fidelity. Using Raman sideband cooling, an occupation probability of $p_0 = 90\%$ has been achieved [201]. This value was limited by weak confinement in axial direction. Application of additional axial confinement, as considered in this work, should enhance the probability. However, if the technique is applied in parallel to an N -trap array, then the joint success probability $P = p_0^N$ to cool all atoms to the motional ground state decreases exponentially. This trend is shown in figure 6.9 for several values of p_0 and constitutes the biggest challenge on the path to large atom numbers.

6.2.6 Transfer to a Bose-Einstein condensate

If the depth of the microtrap array is reduced beyond the point discussed in this work, then first the superfluid phase of the Bose-Hubbard model and finally a BEC can be prepared. Here, the analysis of the loading process based on the adiabatic theorem breaks down, because the energy gap between the ground state and the lowest excited state vanishes. However, this process corresponds to the time-reversed loading scheme used in optical lattices. The feasibility of this approach for microtrap arrays with similar parameters as discussed in this section is shown in section 6.1. This opens an alternative route for the preparation of BECs by direct laser cooling [236], which is especially appealing for the investigation of atomic and molecular species that cannot be cooled evaporatively.

Part III

Applications

Chapter 7

Tunneling dynamics between coupled ring lattices

In this chapter, the tunneling dynamics of atoms between two weakly coupled ring lattices (cf. figure 7.1) is investigated. This configuration can be regarded as an extension of a double-well, where the structure of the Bose-Hubbard model is added to each site. This is an example of a system which can be implemented utilizing the versatility of the setup investigated in the preceding chapters.

The chapter is organized as follows: In section 7.1, the system's Hamilton operator is discussed, and an effective two-mode approximation is introduced. The tunneling dynamics of atoms, which are initially prepared in the ground state of one of the ring lattices, is analyzed in section 7.2 for different interaction regimes. Finally, in section 7.3 it is investigated how the phenomena described in 7.2 can be observed experimentally using the setup discussed in the preceding chapters.

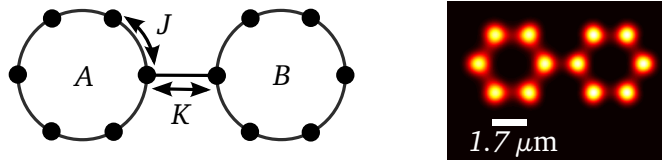


Figure 7.1: Sketch of the coupled Bose Hubbard rings for $M = 6$ (left) and the corresponding simulated intensity distribution (right) for the optical setup discussed in chapter 4.

7.1 Hamilton operator and two-mode approximation

The system's Hamilton operator consists of three parts. The first two parts correspond to the M -sited ring lattices which are denoted with A and B. The part associated with ring A is given by the one-dimensional Bose-Hubbard Hamilton operator (cf. equation (3.10)) with periodic boundary conditions

$$\hat{H}_A = -J \sum_{\langle ij \rangle} (\hat{a}_i^\dagger \hat{a}_j + \hat{a}_j^\dagger \hat{a}_i) + \frac{U}{2} \sum_{i=0}^{M-1} \hat{a}_i^\dagger \hat{a}_i^\dagger \hat{a}_i \hat{a}_i. \quad (7.1)$$

For ring B, the Hamilton operator \hat{H}_B is obtained by the substitution $\hat{a}_i \rightarrow \hat{b}_i$. Both rings are coupled via tunneling of strength K between the sites with $i = 0$. For the remainder of this chapter, it is assumed that the rings are weakly coupled, i. e. $K \ll J$. The resulting total Hamilton operator is given by

$$\hat{H} = \hat{H}_A + \hat{H}_B - K(\hat{a}_0^\dagger \hat{b}_0 + \hat{b}_0^\dagger \hat{a}_0). \quad (7.2)$$

For weak interactions, an effective description of the system can be constructed by using the ground state manifold \mathcal{G}_0 of non-interacting atoms $U = 0$ in uncoupled rings $K = 0$. This manifold consists of $N + 1$ degenerate states that are given by

$$|n\rangle = \frac{\hat{\alpha}_0^{\dagger n} \hat{\beta}_0^{\dagger N-n}}{\sqrt{n!(N-n)!}} |\text{vac}\rangle, \quad (7.3)$$

with $0 \leq n \leq N$ indicating the distribution of N atoms between the two rings. In order to avoid ambiguity, the vacuum state is denoted $|\text{vac}\rangle$ in this chapter. The quantized amplitudes of the Bloch waves

$$\hat{\alpha}_\ell = \sum_{m=0}^{M-1} \frac{e^{-ik_\ell md}}{\sqrt{M}} \hat{a}_m, \quad \hat{\beta}_\ell = \sum_{m=0}^{M-1} \frac{e^{-ik_\ell md}}{\sqrt{M}} \hat{b}_m. \quad (7.4)$$

correspond to the lattice momenta

$$k_\ell = \frac{2\pi\ell}{Md}, \quad -M/2 < \ell \leq M/2. \quad (7.5)$$

The energies associated to the single-particle Bloch states are given in equation 3.14.

For $K, U \ll J$, the lowest energetic eigenstates of \hat{H} approximately lie within \mathcal{G}_0 , i. e. $1 - \langle \psi | \hat{\mathcal{P}} | \psi \rangle \ll 1$, with the projection operator

$$\hat{\mathcal{P}} = \sum_{n=0}^N |n\rangle \langle n|. \quad (7.6)$$

Therefore, it is convenient to consider the Hamilton operator restricted to \mathcal{G}_0

$$\hat{H}_0 = \hat{\mathcal{P}} \hat{H} \hat{\mathcal{P}} = -k(\hat{\alpha}_0^\dagger \hat{\beta}_0 + \hat{\beta}_0^\dagger \hat{\alpha}_0) + \frac{u}{2}(\hat{\alpha}_0^\dagger \hat{\alpha}_0^\dagger \hat{\alpha}_0 \hat{\alpha}_0 + \hat{\beta}_0^\dagger \hat{\beta}_0^\dagger \hat{\beta}_0 \hat{\beta}_0) - 2JN. \quad (7.7)$$

describing a two-sited Bose-Hubbard model with tunneling parameter $k = K/M$ and interaction strength $u = U/M$. A derivation of \hat{H}_0 is given in appendix I.

7.2 Tunneling dynamics

In this section, the tunneling dynamics between the rings is analyzed for the case that all atoms are prepared initially in the ground state of ring A. The observable of interest is the normalized population imbalance between the rings

$$\zeta = \frac{N_A - N_B}{N}. \quad (7.8)$$

The expectation value of the atom number for the individual rings are

$$N_A = \sum_{i=0}^{M-1} \langle \hat{a}_i^\dagger \hat{a}_i \rangle, \quad N_B = \sum_{i=0}^{M-1} \langle \hat{b}_i^\dagger \hat{b}_i \rangle. \quad (7.9)$$

In the following subsections, the time dependence of ζ is analyzed for different interaction strengths.

7.2.1 Josephson oscillations

For the non-interacting case, i. e. $U = 0$, the Hamilton operator given in equation (7.7) can be diagonalized

$$\hat{H}_0|_{U=0} = k\hat{c}_-^\dagger\hat{c}_- - k\hat{c}_+^\dagger\hat{c}_+ \quad (7.10)$$

by introducing the operators

$$\hat{c}_\pm = \frac{\hat{\alpha}_0 \pm \hat{\beta}_0}{\sqrt{2}}. \quad (7.11)$$

The corresponding eigenstates and eigenenergies are given by

$$|n\rangle = \frac{\hat{c}_-^{\dagger n}\hat{c}_+^{\dagger N-n}}{\sqrt{n!(N-n)!}}|\text{vac}\rangle, \quad E_n = k(2n - N) - 2JN. \quad (7.12)$$

Since all atoms are prepared initially in the ground state of ring A, the system's initial state is given by $|\psi(0)\rangle = |N\rangle$. Using equation (7.12) and

$$(n|N\rangle = (n|\frac{\hat{\alpha}_0^{\dagger N}}{\sqrt{N!}}|\text{vac}\rangle = (n|\frac{(\hat{c}_+^\dagger + \hat{c}_-^\dagger)^N}{\sqrt{2^N N!}}|\text{vac}\rangle = \sum_{k=0}^N \binom{N}{k} (n|\frac{\hat{c}_+^{\dagger N-k}\hat{c}_-^{\dagger k}}{\sqrt{2^N N!}}|\text{vac}\rangle \quad (7.13)$$

$$= \sum_{k=0}^N \sqrt{\frac{k!(N-k)!}{2^N N!}} (n|k\rangle \binom{N}{k} = \frac{1}{\sqrt{2^N}} \binom{N}{n}^{1/2} \quad (7.14)$$

the system's time evolution can be calculated

$$|\psi(t)\rangle = \frac{1}{\sqrt{2^N}} \sum_{n=0}^N \binom{N}{n}^{1/2} e^{-iE_n t/\hbar} |n\rangle \quad (7.15)$$

using the binomial coefficient

$$\binom{N}{n} = \frac{N!}{n!(N-n)!}. \quad (7.16)$$

From equation (7.15) the population inversion ζ can be computed

$$\zeta(t) = \frac{1}{N} \sum_{i=0}^{M-1} \langle \psi(t) | \hat{a}_i^\dagger \hat{a}_i - \hat{b}_i^\dagger \hat{b}_i | \psi(t) \rangle \quad (7.17)$$

$$= \frac{1}{2^N N} \sum_{i=0}^{M-1} \sum_{m,n=0}^N \binom{N}{m}^{1/2} \binom{N}{n}^{1/2} (m|\hat{a}_i^\dagger \hat{a}_i - \hat{b}_i^\dagger \hat{b}_i|n\rangle e^{i(E_m - E_n)t/\hbar} \quad (7.18)$$

$$= \frac{1}{2^N N} \sum_{n=0}^{N-1} \binom{N}{n+1}^{1/2} \binom{N}{n}^{1/2} \sqrt{(n+1)(N-n)} e^{2ikt/\hbar} \quad (7.19)$$

$$+ \frac{1}{2^N N} \sum_{n=1}^N \binom{N}{n-1}^{1/2} \binom{N}{n}^{1/2} \sqrt{n(N-n+1)} e^{-2ikt/\hbar} \quad (7.20)$$

$$= \frac{1}{2^{N-1}} \sum_{n=0}^{N-1} \binom{N-1}{n} \cos\left(\frac{2k}{\hbar}t\right) = \cos(2\pi t/\tau_j), \quad (7.21)$$

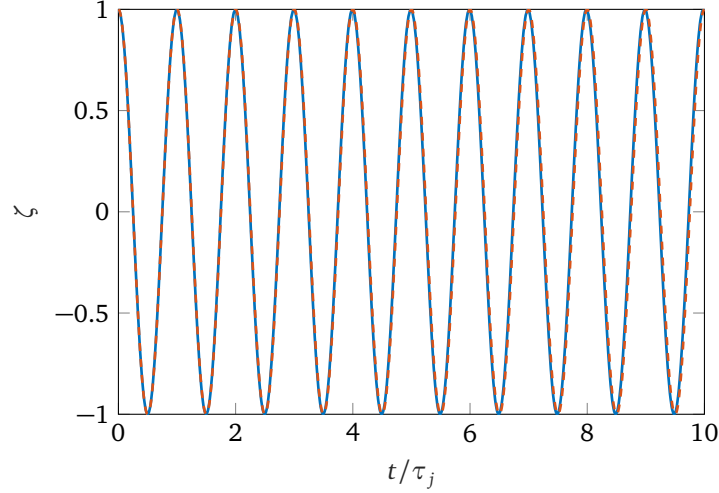


Figure 7.2: The time evolution of the population inversion ζ is shown for $U = 0$, $K/J = 0.1$, $M = 6$, and $N = 4$. The solid blue line is the numerical solution obtained from the full Hamilton operator given in equation (7.1). The red dashed line is the two-mode approximation given in equation (7.21).

revealing sinusoidal Josephson oscillations with the period $\tau_j = h/(2k)$. For the above calculation the following results are used

$$(m|\hat{a}_i^\dagger \hat{a}_i - \hat{b}_i^\dagger \hat{b}_i|n) = \langle \text{vac} | \frac{\hat{c}_-^m \hat{c}_+^{N-m}}{\sqrt{m!(N-m)!}} (\hat{a}_i^\dagger \hat{a}_i - \hat{b}_i^\dagger \hat{b}_i) \frac{\hat{c}_-^{\dagger n} \hat{c}_+^{\dagger N-n}}{\sqrt{n!(N-n)!}} | \text{vac} \rangle \quad (7.22)$$

$$= \frac{\delta_{m,n+1}}{M} \sqrt{(n+1)(N-n)} + \frac{\delta_{m,n-1}}{M} \sqrt{n(N-n+1)}, \quad (7.23)$$

$$[\hat{a}_i, \hat{c}_\pm^{\dagger n}] = \frac{n}{\sqrt{2M}} \hat{c}_\pm^{\dagger n-1}, \quad [\hat{b}_i, \hat{c}_\pm^{\dagger n}] = \pm \frac{n}{\sqrt{2M}} \hat{c}_\pm^{\dagger n-1}, \quad \sum_{n=0}^N \binom{N}{n} = 2^N. \quad (7.24)$$

In figure 7.2, the two-mode approximation given in equation (7.21) is compared to the numerical solution of the time dependent Schrödinger equation using the full Hamilton operator given in equation (7.2) (cf. appendix H). The quantitative agreement between the graphs shows the validity of the two-mode approximation for the chosen parameters.

7.2.2 Collapse and revival

For $0 < u < k$, the system's time evolution can be computed by considering perturbative correction to the energies E_n from the on-site interaction. In order to compute these corrections, the commutator relations

$$[\hat{\alpha}_0, \hat{c}_\pm^\dagger] = \frac{1}{\sqrt{2}}, \quad [\hat{\beta}_0, \hat{c}_\pm^\dagger] = \pm \frac{1}{\sqrt{2}}, \quad (7.25)$$

and the action of the operators $\hat{\alpha}_0$ and $\hat{\beta}_0$ on the state $|n\rangle$

$$\hat{\alpha}_0|n\rangle = \frac{1}{\sqrt{n!(N-n)!}} \hat{\alpha}_0 \hat{c}_+^{\dagger N-n} \hat{c}_-^{\dagger n} |\text{vac}\rangle \quad (7.26)$$

$$= \frac{1}{\sqrt{n!(N-n)!}} \left(\frac{N-n}{\sqrt{2}} \hat{c}_+^{\dagger N-n-1} \hat{c}_-^{\dagger n} + \frac{n}{\sqrt{2}} \hat{c}_+^{\dagger N-n} \hat{c}_-^{\dagger n-1} \right) |\text{vac}\rangle, \quad (7.27)$$

$$\hat{\beta}_0|n\rangle = \frac{1}{\sqrt{n!(N-n)!}} \left(\frac{N-n}{\sqrt{2}} \hat{c}_+^{\dagger N-n-1} \hat{c}_-^{\dagger n} - \frac{n}{\sqrt{2}} \hat{c}_+^{\dagger N-n} \hat{c}_-^{\dagger n-1} \right) |\text{vac}\rangle, \quad (7.28)$$

are helpful. From these equations the following expectation values can be obtained

$$\langle n | \hat{\alpha}_0^\dagger \hat{\alpha}_0^\dagger \hat{\alpha}_0 \hat{\alpha}_0 | n \rangle = \frac{1}{4} (N-n)(N-n-1) + \frac{1}{2} (N-n)n + \frac{1}{4} n(n-1), \quad (7.29)$$

$$\langle n | \hat{\beta}_0^\dagger \hat{\beta}_0^\dagger \hat{\beta}_0 \hat{\beta}_0 | n \rangle = \frac{1}{4} (N-n)(N-n-1) - \frac{1}{2} (N-n)n + \frac{1}{4} n(n-1). \quad (7.30)$$

In combination with equation (7.7) and (7.12) this yields the energy correction to first order in the interaction strength u

$$E_n^{(1)} = \langle n | \hat{H}_0 | n \rangle = k(2n-N) - 2JN + \frac{u}{4} [N(N-1) + 2n(n-N)]. \quad (7.31)$$

Using the above result in combination with

$$\sum_{n=0}^N \binom{N}{n} \cos(a+bn) = \text{Re} \sum_{n=0}^N \binom{N}{n} e^{i(a+bn)} \quad (7.32)$$

$$= \text{Re} [e^{ia} (1 + e^{ib})^N] \quad (7.33)$$

$$= 2^N \text{Re} [e^{i(a+bN/2)} \cos(b/2)^N] \quad (7.34)$$

$$= 2^N \cos(b/2)^N \cos(a + bN/2), \quad (7.35)$$

a calculation analogous to equations (7.17) to (7.21) yields

$$\zeta(t) = \frac{1}{2^{N-1}} \sum_{n=0}^{N-1} \binom{N-1}{n} \cos\left(\frac{E_{n+1}^{(1)} - E_n^{(1)}}{\hbar} t\right) \quad (7.36)$$

$$= \cos(2\pi t/\tau_j) \cos(\pi t/\tau_r)^{N-1}, \quad (7.37)$$

with $\tau_r = h/u$. For $N \gg 1$ and $t \ll \tau_r$, the following approximate expression can be derived

$$\zeta(t) \approx \cos(2\pi t/\tau_j) \left(1 - \frac{\pi^2 t^2}{2\tau_r^2}\right)^{N-1} \approx \cos(2\pi t/\tau_j) e^{-t^2/\tau_c^2}. \quad (7.38)$$

Thus, the population oscillations exhibit an approximately Gaussian collapse on a time scale of $\tau_c = \tau_r \sqrt{2/[\pi^2(N-1)]}$ and a revival at $\tau_r = h/u$. A similar result is derived in [237] for the two-site Bose-Hubbard model with $N \gg 1$. Figure 7.3 shows a comparison between the numerical solution of the time-dependent Schrödinger equation using the full Hamilton operator and the approximation given in equation (7.37).

At $u \approx k$ the time scales of the population oscillations and the collapse and revival dynamics are similar, i.e. $\tau_j \approx \tau_r$. In this regime, the inversion ζ exhibits a complex oscillatory behavior (cf. blue line in figure 7.4) which is not accurately described by the perturbative approach used in this subsection.

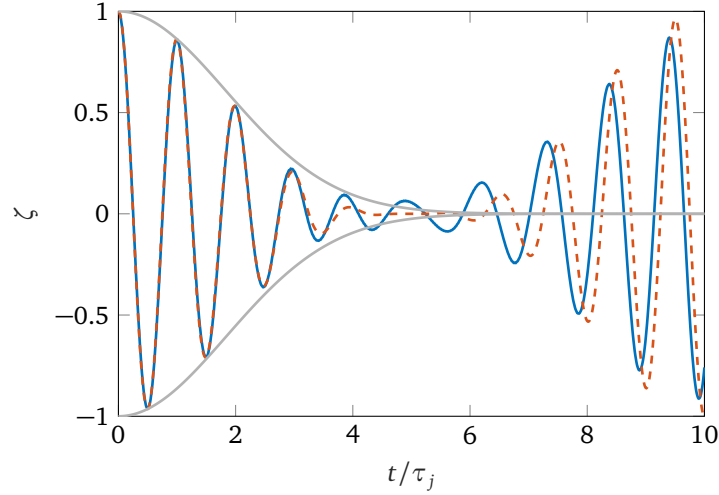


Figure 7.3: The time evolution of the population inversion ζ is shown for $U/J = 0.02$, $K/J = 0.1$, $M = 6$, and $N = 4$. The solid blue line is the numerical solution obtained from the full Hamilton operator and the red dashed line is the perturbative result given in equation (7.37). The gray lines indicate the Gaussian envelope (cf. equation (7.38)).

7.2.3 High-order tunneling and self-trapping

For $u > k$, all transitions from the initial state $|N\rangle$ to other states $|n\rangle$ are energetically forbidden except for $n = 0$. Therefore, the system's dynamics can be described by Josephson oscillations between the states of an effective two-level model. The tunneling strength for this model can be deduced from the matrix representation of the Hamilton operator

$$H_{\mathcal{B}} = \begin{pmatrix} a_0 & b_1 & & & \\ b_1 & a_1 & b_2 & & \\ & b_2 & a_2 & \ddots & \\ & & & \ddots & \ddots \\ & & & & & \ddots \end{pmatrix} \quad (7.39)$$

with respect to the basis $\mathcal{B} = \{|0\rangle, |1\rangle, \dots, |N\rangle\}$ of the low-energy manifold \mathcal{G}_0 . The matrix elements are given by

$$a_n = \langle n | \hat{H} | n \rangle - \langle N | \hat{H} | N \rangle = -Un(N - n) \quad (7.40)$$

$$b_n = -J\sqrt{(N - n + 1)n}. \quad (7.41)$$

Note that the constant $\langle N | \hat{H} | N \rangle$ is subtracted from the diagonal elements which corresponds to an interaction picture in which a_0 and a_N are zero. In order to obtain the effective two-level model, the amplitudes corresponding to the states $|n\rangle$ with $0 < n < N$ need to be eliminated from the time-dependent Schrödinger equation. This can be achieved by setting $\partial_t \psi_n = 0$ and solving the respective equation for ψ_n

$$0 = b_n \psi_{n-1} + a_n \psi_n + b_{n+1} \psi_{n+1} \quad \implies \quad \psi_n = -\frac{b_n}{a_n} \psi_{n-1} - \frac{b_{n+1}}{a_n} \psi_{n+1}. \quad (7.42)$$

This procedure is called adiabatic elimination and is frequently applied for the description of multi-photon processes in atomic physics [238, 239]. The quality of this approximation depends on the chosen interaction picture [238, 239], which is the reason for the

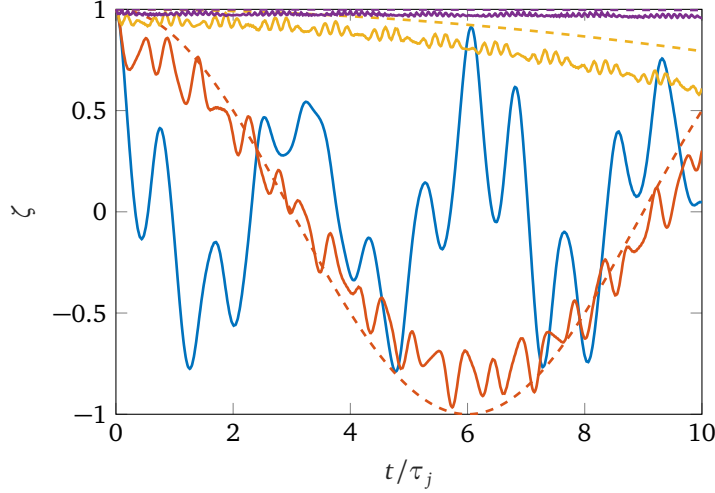


Figure 7.4: The time evolution of the population inversion ζ is shown for $U/J = 0.1$ (blue line), $U/J = 0.2$ (orange line), $U/J = 0.4$ (yellow line), $U/J = 0.8$ (purple line), $K/J = 0.1$, $M = 6$, and $N = 4$. The dashed lines are sinusoidal oscillations with a period of $h/(2k_{\text{eff}})$.

subtraction of the constant energy $\langle N | \hat{H} | N \rangle$ from the Hamiltonian matrix. From equation (7.42), it is clear that the effective tunneling strength between the states $|0\rangle$ and $|N\rangle$ is given to lowest non-vanishing order in k/u by

$$k_{\text{eff}} = \prod_{n=1}^N -\frac{b_n}{a_n} = (-1)^N \frac{Nk^N}{(N-1)!u^{N-1}}. \quad (7.43)$$

This expression agrees for the case of $N = 2$ with the results from investigations on tunneling of repulsively bound pairs in the Bose-Hubbard model [240–242]. Equation (7.43) shows that the oscillation frequency quickly decreases with increasing u and N . Thus, for sufficiently large u and N the atoms are trapped in ring A for experimentally accessible time scales. This corresponds to the self-trapping effect which was studied for BECs in double-well potentials [243–245].

In figure 7.4, the time dependence of the inversion ζ is shown for different interaction strength $u > k$. The curves show slow large-amplitude oscillations which are modulated by fast small-amplitude oscillation. The frequencies of the former are in qualitative agreement with the expression given in equation (7.43) (dashed lines) whereas the latter arise from contributions of off-resonant states.

7.2.4 Many-body resonances

The effective two-sided Bose-Hubbard model given in equation (7.7) is able to explain the tunneling dynamics in the regimes discussed in the preceding subsections. For large u and N it predicts increasingly slow population oscillations that effectively result in population trapping on experimentally accessible time scales. However, it can be expected that the effective description using equation (7.7) breaks down at some point. This is investigated using the quantity

$$\zeta_m = \min_{t \in [0, 10\tau_j]} \zeta(t), \quad (7.44)$$

which measures the maximal amount of population transfer between the rings during the time interval $[0, 10\tau_j]$. The case $\zeta_m = 1$ corresponds to no population transfer whereas

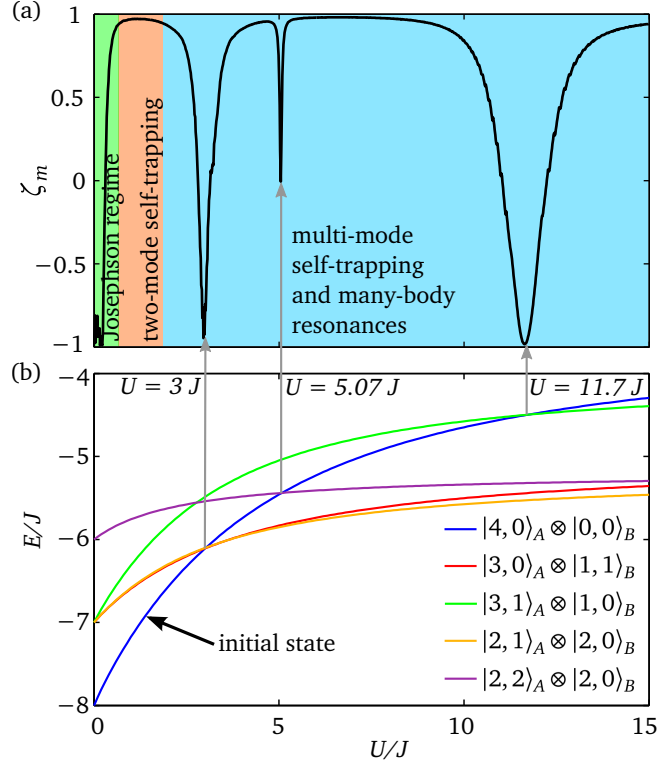


Figure 7.5: Self-trapping and many-body resonances. (a) shows the quantity ζ_m as a function of the ratio U/J for $K/J = 0.1$, $M = 6$, and $N = 4$. (b) shows the energies $\mathcal{E}_n(N_A, U) + \mathcal{E}_{n'}(N_B, U)$ versus the ratio U/J for the same parameters.

$\zeta_m = -1$ corresponds to full population transfer. Figure 7.5 shows ζ_m as a function of the interaction strength U . For $U < J$ full population transfer occurs in the regimes discussed in the subsections 7.2.1 and 7.2.2. For $U > J$ self-trapping occurs resulting in $\zeta_m \approx 1$. However, for $U/J = 3$, $U/J = 5.07$, and $U/J = 11.7$ distinct peaks in ζ_m signal considerable population transfer.

The peaks can be explained by considering the energy spectra of the uncoupled Bose-Hubbard rings. Without loss of generality ring A is considered in the following. The corresponding expressions for ring B can be obtained by substituting $\hat{a}_i \rightarrow \hat{b}_i$. For $U = 0$ and $K = 0$, the eigenstates of \hat{H}_A and the corresponding energies

$$|\{n_\ell\}\rangle = \prod_\ell \frac{\hat{\alpha}_\ell^{\dagger n_\ell}}{\sqrt{n_\ell!}} |\text{vac}\rangle, \quad \mathcal{E}_{\{n_\ell\}} = -2J \sum_\ell n_\ell \cos(k_\ell d), \quad (7.45)$$

are obtained by distributing $N_A = \sum_\ell n_\ell$ atoms over M Bloch states (cf. equations 7.4 and 7.5). It is worth noting that states with the same $|\ell|$ are degenerate.

Though for $U > 0$ the eigenstates and energies of $\hat{H}_A + \hat{H}_B$ change, the quasimomentum k_ℓ remains a good quantum number since the discrete translation symmetry persists. For $K \ll J$ the eigenstates of \hat{H} are approximately given by

$$|\{n_\ell\}\rangle_A \otimes |\{n'_\ell\}\rangle_B. \quad (7.46)$$

Due to the system's symmetry, the initial state with all atoms in the $\ell = 0$ state of ring A only couples to superpositions of $+\ell$ and $-\ell$ that result in standing waves.

In order to explain the peaks in figure 7.5, only Bloch states with $|\ell| = 0$ and $|\ell| = 1$ are

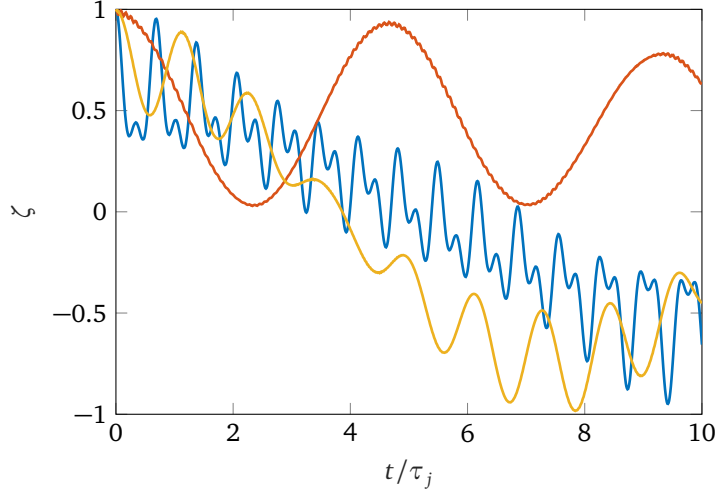


Figure 7.6: The time evolution of the population inversion ζ is shown for $U/J = 3$ (blue line), $U/J = 5.07$ (orange line), $U/J = 11.7$ (yellow line), $K/J = 0.1$, $M = 6$, and $N = 4$.

required. Thus, the following shorthand notation for the eigenstates and corresponding energies is introduced

$$|N_A, n\rangle_A \otimes |N_B, n'\rangle_B, \quad \mathcal{E}_n(N_A, U) + \mathcal{E}_{n'}(N_B, U), \quad (7.47)$$

with n and n' being the number of atoms in the standing wave Bloch state superposition with $|l| = 1$ in ring A and B respectively. The corresponding eigenvalue relations are

$$\hat{H}_A |N_A, n\rangle_A = \mathcal{E}_n(N_A, U) |N_A, n\rangle_A, \quad \hat{H}_B |N_B, n'\rangle_B = \mathcal{E}_{n'}(N_B, U) |N_B, n'\rangle_B. \quad (7.48)$$

The condition for resonant population transfer out of the initial state $|N, 0\rangle_A \otimes |0, 0\rangle_B$ can be stated as

$$\mathcal{E}_0(N, U) + \mathcal{E}_0(0, U) = \mathcal{E}_n(N_A, U) + \mathcal{E}_{n'}(N_B, U). \quad (7.49)$$

The lower subplot in figure 7.5 shows the energies of multiple states as a function of U/J . The crossings of these lines with that of the initial state represent points at which the condition in equation (7.49) is satisfied. The vertical grey arrows show that these points can be mapped onto the resonances depicted in the upper subplot of figure 7.5. In figure 7.6, the time evolution of ζ at these points is shown.

It is worth noting that comparable effects have been predicted and observed in other systems. In [246], enhanced tunneling at large interaction strengths due to resonant coupling to higher motional states is predicted for a BEC in a double-well potential using the Gross-Pitaevskii equation. Further, interaction induced tunneling in tilted optical lattices has been observed in [247].

7.3 Experimental considerations

In this section, the feasibility of an experimental implementation of the model considered in the preceding section is investigated using the setup described in chapter 4. The first question in this context is whether the relevant tunneling dynamics happens on experimentally accessible time scales. The intra-ring tunneling strength J can be determined from the results obtained in chapter 5. For the case considered in the preceding section, this also determines the inter-ring tunneling strength $K = 0.1J$. The fastest tunneling dynamics is attainable with ${}^7\text{Li}$ at $V_{0\perp} = \mathcal{E}$ yielding $J/h = 318$ Hz at $U/J = 0.17$. The condition $V_{0\perp} \geq \mathcal{E}$ is required for the single-band Bose-Hubbard model to be valid (cf. subsection 3.2.1). The resulting inter-ring tunneling period is given by $\tau_j = 32$ ms. Therefore, the considered tunneling dynamics occurs during a time interval with a length of 320 ms that is experimentally accessible (cf. section 6.1.2). The ratio U/J can be tuned by either varying the potential depth $V_{0\perp}$ or by using controlling the s -wave scattering length via Feshbach resonance. The former approach has the disadvantage that in order to obtain a large value for the ratio U/J the tunneling strength needs to be reduced significantly which leads to slow dynamics. In addition, the non-interacting regime $U = 0$ is not accessible due to the condition $V_{0\perp} \geq \mathcal{E}$. Therefore, the latter approach appears to be more promising.

The inter-ring tunneling strength needs to be controlled in order to obtain the desired ratio K/J . This can be done by either changing the spacing or the barrier depth between the sites with the index $i = 0$. The former can be achieved by illuminating the MLA with two beams with different incident angles [149] whereas the latter can be implemented using a strongly focused, blue-detuned beam.

For state preparation, the techniques discussed in chapter 6 can be applied. The approach starting from a BEC does not grant a fixed particle number, however since the particle number is measured this can be compensated by post-selection. The approach starting from the atomic limit only provides states with unit filling. States with lower fillings can be prepared by starting with fewer traps and switching on the remaining traps of the ring adiabatically.

Chapter 8

Quantum computing with continuous-time quantum walks

In this chapter, a scheme for universal quantum computing based on continuous-time quantum walks of interacting particles is investigated, and its implementation using ultracold atoms in adjustable optical microtrap arrays is analyzed. Quantum walks [248–250] have recently attracted considerable interest. This is triggered by two developments. On the one hand, quantum walks have been identified as a powerful model for quantum computation [20, 251]. On the other hand, they have been realized experimentally in many platforms, e.g. photons, trapped ions, and neutral atoms [252]. In [242], continuous-time quantum walks of interacting indistinguishable particles have been implemented using ultracold atoms in an optical lattice. In addition, significant advances in the generation of configurable optical microtrap arrays [151, 156–158, 224], the deterministic preparation of trap arrays with unit filling [155, 198, 199], and the ground-state cooling in optical tweezers [174, 201] have been reported recently. This raises the question whether ultracold atoms in arrays of optical microtraps can be used as a platform for universal quantum computing based on the continuous-time quantum walk approach described in [20]. In this chapter, the results of a theoretical study investigating this question are presented.

The chapter is organized in the following way. In section 8.1, the original proposal for quantum computation with continuous-time quantum walks of interacting particles by Childs, Gosset, and Webb [20] is reviewed. Further, an implementation of this approach with ultracold atoms in arrays of optical microtraps is sketched, and the resulting challenges are discussed. Based on this, a modified scheme utilizing time-dependent control over the optical potential depths is developed in section 8.2. In section 8.3, the implementation of computational basis states with Gaussian wave packets is discussed, and techniques for wave packet preparation and compression are investigated. In section 8.4, the fidelity of the basic subgraphs is calculated taking into account the finite momentum width of the used wave packets and fluctuations in the optical potential. Practical limits for the scalability of the proposed setup are discussed in section 8.5.

8.1 Childs-Gosset-Webb scheme

The basic idea for the implementation of universal quantum computing using continuous-time quantum walks [20] is to represent qubits by the position of particles moving on graphs. This can be done in the following way. Consider a simple graph consisting of two disconnected one-dimensional lattices L_1 and L_2 . The computational basis states of a qubit $|0\rangle$ and $|1\rangle$ can be implemented by preparing a single particle as a wave packet with momentum k on L_1 or L_2 respectively. The measurement of the particle's position implements a projective measurement with respect to the basis $\{|0\rangle, |1\rangle\}$. A one-qubit

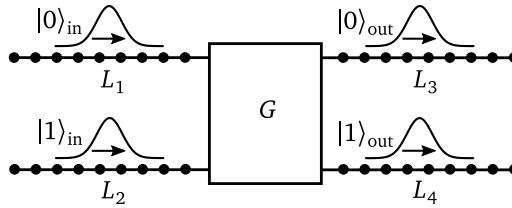


Figure 8.1: Schematic representation of a one-qubit gate implemented by the Graph G in the Childs-Gosset-Webb scheme.

gate can be implemented by connecting L_1 and L_2 with two further lattices L_3 and L_4 via a graph G . This situation is shown in figure 8.1. The particle is prepared as a wave packet that moves towards G with momentum k . Subsequently, the particle scatters from G into L_3 and L_4 . The position of the particle after this scattering process represents the qubit after the application of the gate that is implemented by G . It is worth noting that G is constructed so that the particle is not reflected back into L_1 or L_2 .

This scheme can be extended to arbitrary n -qubit circuits by using $2n - 1$ qubits. Each qubit is implemented as described in the preceding paragraph by an atom moving on a pair of parallel one-dimensional lattices. The latter are aligned vertically as shown figure 8.2. n of the qubits are used as computational qubits while the remaining $n - 1$ qubits are used as mediator qubits. The mediator qubits are placed in between the computational qubits and are used to implement two-qubit gates between adjacent computational qubits by utilizing on-site interaction. The desired circuit is implemented by a graph connecting all incoming and outgoing lattices. This graph can be built from a set of basic subgraphs shown in figure 8.3. In [20], it is proven that this construction allows implementing any n -qubit g -gate circuit using a planar, time-independent graph. The size of this graph is bounded by a polynomial in n and g .

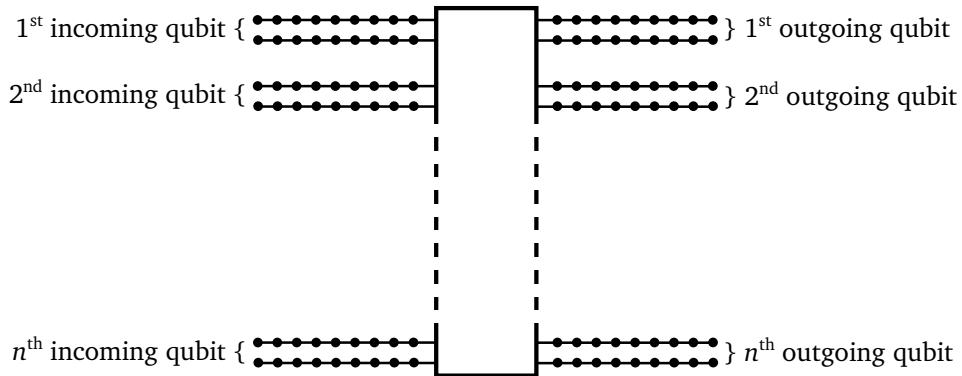


Figure 8.2: Schematic representation of an n -qubit gate in the Childs-Gosset-Webb scheme.

A physical implementation of this scheme can be built from ultracold bosonic atoms in two-dimensional arrays of optical dipole traps. Each trap represents a vertex of the graph, and the connections (edges) of the graph are realized by tunneling between adjacent traps. The required interaction is the on-site repulsion of the atoms. A first experimental step in this direction is the implementation of continuous-time quantum walks of one and two atoms in an optical lattice [242]. However, to implement universal quantum computing, two major challenges need to be addressed: First, trap arrays which implement all subgraphs shown in figure 8.3 and sufficiently large combinations thereof need

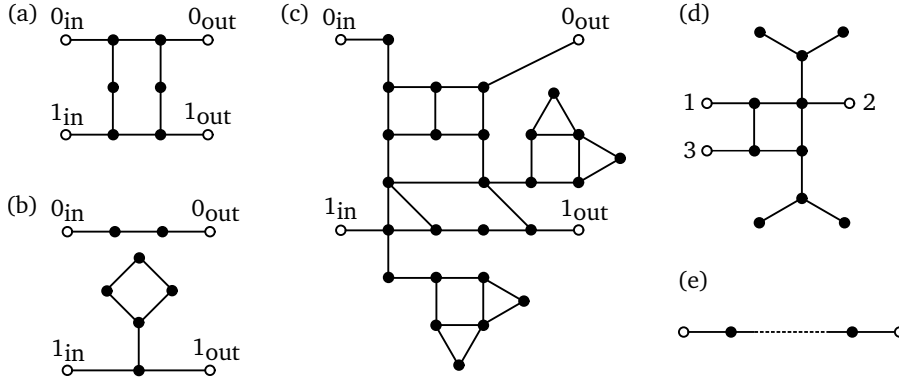


Figure 8.3: Elementary subgraphs: (a) basis changing gate at $k = \pi/(4a)$, (b) phase gate at $k = \pi/(4a)$, (c) Hadamard gate at $k = \pi/(2a)$, (d) momentum switch at $k = \pi/(2a)$ and $k = \pi/(4a)$, (e) line segment. The white circles represent the connections to the adjacent subgraphs. For (a), (b), and (c) these are labeled by the computational basis states (0 and 1) for the incoming (in) and outgoing (out) qubit. The momentum switch shown in (d) routes wave packets with $k = \pi/(4a)$ between the connections 1 and 3 and wave packets with $k = \pi/(2a)$ between the connections 2 and 3.

to be generated. This can be achieved with spatial light modulators [156–158], acousto-optical deflectors [151], or microlens arrays [224]. Second, for state preparation wave packets with a well-defined quasimomentum need to be produced. An approach to this task is discussed in section 8.3.

8.2 Modified scheme with time-dependent control

In this section, a modification of the Childs-Gosset-Webb scheme is presented that utilizes time-dependent control over local trap depths. On the one hand, this allows routing the wave packets through the graph which eliminates the need for mediator qubits. A fact that reduces the set of basic subgraphs to the ones shown in (a), (b), and (e) of figure 8.3. On the other hand, the time-dependent control can be used to reconfigure parts of the graph after the wave packets passed through it. This part can then be reused by reflecting the wave packets at the end of line segments. This allows reducing the physical extent of graphs for multi-gate circuits significantly. The required time-dependent control can be implemented experimentally with spatial light modulators [224].

The structure of a graph for the discussed scheme is shown in figure 8.4 (a). Here, the black lines represent line segments (cf. figure 8.3 (e)) which are long enough to support the atomic wave packets. The gray boxes are adjustable subgraphs that can implement the identity gate, the basis changing gate, and the phase gate. A geometry which allows for this by switching traps on and off is shown in figure 8.4 (b). The horizontal, parallel lines in figure 8.4 (a) implement qubits in the way shown in figure 8.1. At the ends of these lines, the wave packets are reflected and run through the setup again. During this process, the graph can be adjusted to implement a different set of gates. A two-qubit gate between adjacent qubits can be applied by routing the wave packet on the $|1\rangle$ -line of the upper qubit and the wave packet on the $|0\rangle$ -line of the lower qubit in such a way that they interact on a vertical line segment. This procedure is shown schematically in figure 8.4 (c). For $\kappa = \pi/(4a)$ and an on-site interaction strength of $U = 2\sqrt{2}J$ this induces a relative phase of $e^{-i\pi/2}$ between the counterpropagating wave packets (cf. appendix J).

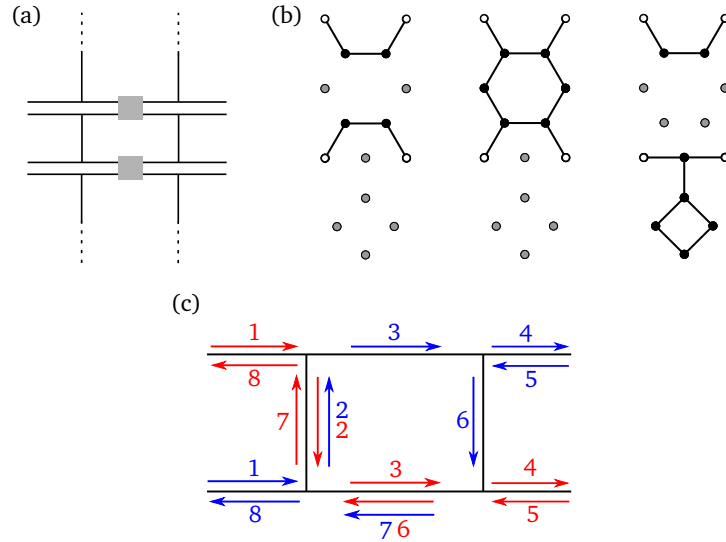


Figure 8.4: Modified scheme for quantum computing with continuous-time quantum walks (cf. section 8.2). (a) Structure of the graph implementing a circuit. The black lines represent line segments as shown in figure 8.3 (e) and the gray boxes are adjustable graphs shown in (b). These graphs can implement the identity gate (left), the basis changing gate (middle), and the phase gate (right). Here, the white circles are connections to adjacent subgraphs, whereas the black and gray circles represent active and inactive vertices respectively. (c) Scheme for the routing of wave packets in the implementation of a two-qubit gate between adjacent qubits. The red and blue arrows represent the propagation steps of the wave packets representing the state $|1\rangle$ of the upper qubit and the state $|0\rangle$ of the lower qubit respectively. The numbers indicate the temporal order. At the second propagation step the atoms interact on the left vertical line.

The controlled phase gate described in [20] can be implemented by applying an X gate to the lower qubit before and after the two-qubit gate discussed above.

Though the scheme discussed in the preceding paragraphs utilizes time-dependent control, the motion of the particles still has the character of a quantum walk. The reason for this is that changes only occur in parts of the graph in which the wave functions vanish.

8.3 Computational basis states

The graphs shown in figure 8.3 implement the desired gates for specific momenta only. Therefore, plane waves would be ideal states for the computational basis. However, plane waves have an infinite spatial extension. Therefore, they cannot be prepared experimentally. Consequently, wave packets with a finite momentum width need to be used. In this section, the choice of suitable wave packets and a scheme for their preparation is discussed.

8.3.1 Gaussian wave packets

In the following, the physics of a particle moving on a one-dimensional lattice with nearest-neighbor tunneling is reviewed. The corresponding Hamilton operator is given by

$$\hat{H}_l = -J \sum_{j \in \mathbb{Z}} (|j\rangle\langle j+1| + |j+1\rangle\langle j|). \quad (8.1)$$

Here, $|j\rangle$ is the state for which the atom is localized at site j , i. e. occupies the respective Wannier function, and J is the tunneling energy. The eigenstates of \hat{H}_l are Bloch waves (cf. section 3.2.2) of the form

$$|k\rangle = \frac{1}{\sqrt{2\pi}} \sum_{j \in \mathbb{Z}} e^{ikaj} |j\rangle, \quad (8.2)$$

with the lattice constant a and the quasimomentum k which lies in the first Brillouin zone $\text{BZ} = [-\pi/a, \pi/a)$. The associated eigenenergies are given by

$$\hbar\omega(k) = -2J \cos(ka). \quad (8.3)$$

An arbitrary time-dependent state $|\psi(t)\rangle$, e.g. a wave packet, can be decomposed in the position or momentum basis

$$|\psi(t)\rangle = \sum_{j \in \mathbb{Z}} \psi_j(t) |j\rangle = \int_{\text{BZ}} \tilde{\psi}_k(t) |k\rangle dk. \quad (8.4)$$

The amplitudes ψ_j and $\tilde{\psi}_k$ are connected via

$$\tilde{\psi}_k(t) = \frac{1}{\sqrt{2\pi}} \sum_{j \in \mathbb{Z}} \psi_j(t) e^{-ikaj}, \quad (8.5)$$

$$\psi_j(t) = \frac{1}{\sqrt{2\pi}} \int_{\text{BZ}} \tilde{\psi}_k(t) e^{ikaj} dk. \quad (8.6)$$

A natural choice for the computational basis states are Gaussian wave packets, which are defined via their initial spatial amplitudes

$$\psi_j(0) = \frac{\sqrt{a} e^{i\kappa j}}{(2\pi\sigma_0^2)^{1/4}} \exp\left(-\frac{(ja - x_0)^2}{4\sigma_0^2}\right), \quad (8.7)$$

with the average quasimomentum κ , the initial position x_0 , and the initial width σ_0 . The time evolution of the corresponding probability distributions in position and momentum can be determined using equations (8.3), (8.5), and (8.6). For this it is assumed that the wave packet is sufficiently wide, i. e. $\sigma_0 > a$, such that it is well localized in momentum space. This allows for an expansion of the eigenenergies to second order in $(k - \kappa)$

$$\omega(k) \approx \omega_0 + v(k - \kappa) + \beta(k - \kappa)^2. \quad (8.8)$$

Using the above approximation one obtains

$$|\tilde{\psi}_k(t)|^2 \approx \frac{1}{\sqrt{2\pi\tilde{\sigma}^2}} \exp\left(-\frac{(k-\kappa)^2}{2\tilde{\sigma}^2}\right), \quad (8.9)$$

$$|\psi_j(t)|^2 \approx \frac{a}{\sqrt{2\pi\sigma^2(t)}} \exp\left(-\frac{(ja-x(t))^2}{2\sigma^2(t)}\right), \quad (8.10)$$

with the momentum width $\tilde{\sigma} = 1/(2\sigma_0)$, the time-dependent center of mass

$$x(t) = x_0 + vt, \quad (8.11)$$

and the time-dependent position width

$$\sigma(t) = \sqrt{\sigma_0^2 + \frac{\beta^2 t^2}{\sigma_0^2}}. \quad (8.12)$$

The wave packet's velocity v and spread coefficient β are given by

$$v = \frac{2Ja}{\hbar} \sin(\kappa a), \quad \beta = \frac{Ja^2}{\hbar} \cos(\kappa a). \quad (8.13)$$

The above relations reveal two advantages of Gaussian wave packets. First, the shape is approximately preserved during time evolution. Second, the product of initial position and momentum width is minimal, i. e. $\tilde{\sigma}\sigma_0 = 1/2$.

8.3.2 Wave packet preparation

In this subsection, the preparation of Gaussian wave packets is discussed. In cold atom experiments, it is possible to prepare exactly one atom in the motional ground state of a trap. This can be achieved with high success probability either from the Mott insulator phase in an optical lattice [242] or from atoms in optical tweezers [152, 154, 174, 201]. Therefore, the following considerations start from a state with a single atom localized in a trap. From equation (8.5), it follows that this state contains all momenta to an equal amount. In [251], it is proposed to filter out all unwanted momenta using additional subgraphs. However, this procedure implies that only in a small fraction of experimental runs the computational basis state is prepared successfully. Here, an alternative approach is discussed.

In the following, a finite chain of M traps with controllable, time-depended energy offsets $\epsilon_j(t)$ is considered. The corresponding Hamilton operator is given by

$$\hat{H}_c(t) = \sum_{j=1}^M \epsilon_j(t) |j\rangle\langle j| - J \sum_{j=1}^{M-1} (|j\rangle\langle j+1| + |j+1\rangle\langle j|). \quad (8.14)$$

The energy offsets ϵ_j can be controlled by locally varying the intensity of the light field that generates the optical potential. It is assumed that the atom is prepared in $|j=1\rangle$ at $t=0$ and that the ϵ_j are sufficiently small, such that the tunneling parameter J remains undisturbed. The goal is to prepare the atom in a Gaussian wave packet at $t=\tau$. This is a typical problem in optimal control theory [235, 253–255]. The following ansatz for

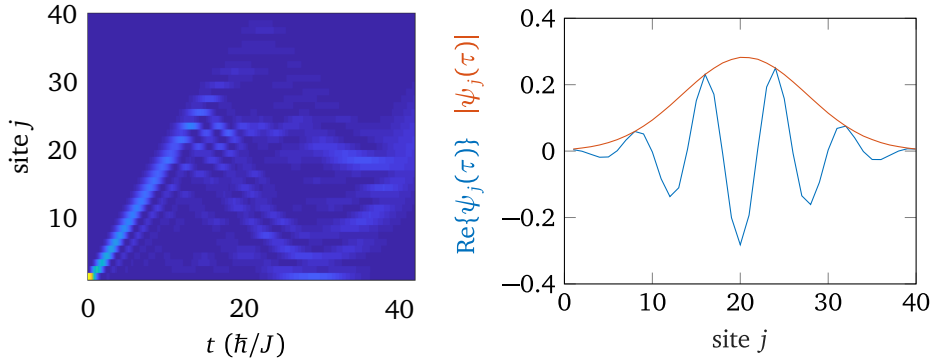


Figure 8.5: Wave packet preparation using optimal control. The left subfigure shows the time evolution of the atomic density $|\psi_j(t)|^2$ during the wave packet preparation. The right subfigure shows the final wave packet. The parameters are: $M = 40$, $\tau = 41.9 \hbar/J$, $\kappa = \pi/(4a)$, $\sigma_0 = 5a$, and $L = 3$.

the energy offsets is chosen

$$\epsilon_j(t) = J \sum_{l=1}^L c_{jl} \sin(l\pi t/\tau), \quad (8.15)$$

with parameters c_{jl} . Using this expression the final state of the system $|\psi(\tau)\rangle$ is computed by solving the time dependent Schrödinger equation

$$i\hbar\partial_t |\psi(t)\rangle = \hat{H}_c(t) |\psi(t)\rangle. \quad (8.16)$$

This allows to compute the fidelity \mathcal{F} , i. e. the overlap between the final state $|\psi(\tau)\rangle$ and the targeted Gaussian wave packet. The parameters c_{jl} and the time duration τ are obtained by numerically maximizing \mathcal{F} . Figure 8.5 shows the resulting time evolution of the amplitudes ψ_j and the final wave packet for $L = 3$, $\sigma_0 = 5a$, $x_0 = M/2$ and $M = 40$. The resulting infidelity $1 - \mathcal{F} = 2.3 \cdot 10^{-6}$ is very low.

In an experiment, the trap depth ϵ_j cannot be controlled with arbitrary precision. To determine the sensitivity of the state preparation scheme on errors in the local energies, the coefficients c_{jl} are sampled from a normal distribution with means given by the optimization procedure and identical variances Δc^2 . From a sample of 100 realizations, the average fidelity is estimated. The result is shown in figure 8.6 for the parameters used in figure 8.5. This reveals that the local energies need to be controlled on the level of $10^{-2}J$. For most experiments, the ratio of potential depth to tunneling energy is $\sim 10^2$. Thus, the potential depths need to be controlled with a relative accuracy of 10^{-4} . Though experimentally challenging, this amount of control is feasible (cf. section 5.3.2 and [153, 224]).

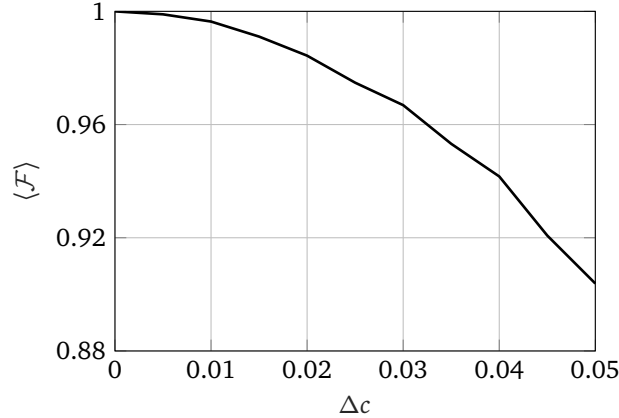


Figure 8.6: Average fidelity $\langle \mathcal{F} \rangle$ of the prepared wave packet versus the fluctuation strength Δc in the control parameters c_{jl} . The same parameters as in figure 8.5 are used.

8.3.3 Wave packet compression

The spreading of the wave packet (cf. equation (8.12)) leads to the following problem. The line segments connecting the gates need to be long enough to support the entire wave packet. However, due to its continuous spreading this condition is violated at some point which limits the propagation time and therefore the number of gates that can be applied. Using the equations (8.11), (8.12), (8.13) and demanding $\sigma(t) \leq \sqrt{2}\sigma_0$ the following relation for the distance covered by the wave packet is obtained

$$x(t) - x_0 \leq \frac{2\sigma_0^2}{a} \tan(\kappa a). \quad (8.17)$$

To fully traverse N line segments, which are large enough to support the entire wave packet, the propagation distance needs to be at least $8N\sigma_0$. This leads to the condition

$$\sigma_0 \geq \frac{4\sqrt{2}}{\tan(\kappa a)} Na. \quad (8.18)$$

For a circuit the above relation leads to a quadratic scaling of the propagation distance with the number of gates. One way to overcome this problem is to use a momentum for which $\beta(\kappa) = 0$, i. e. $\kappa = \pi/(2a)$. However, there are no simple planar graphs that implement a complete set of one-qubit gates for this momentum [256].

An alternative approach is to use dynamical control over the local energy offsets to compress the wave packets at regular intervals. This can be done analogously to the procedure of wave packet preparation by applying the concept of optimal control. Consider a wave packet with initial width σ_0 which propagated for a time τ , after which its width increased to $\sigma(\tau)$. To restore its initial width, the local energy offsets of several sites on the path of the wave packets are modulated according to equation (8.15). Again, the coefficients are determined by maximizing the overlap of the time evolved state with the targeted Gaussian wave packet of reduced spatial width.

In figure 8.7 (a), the situation is shown for $\sigma_0 = 5a$ and $\sigma(\tau) = \sqrt{25}a$. Here, the probability distributions $|\psi_j|^2$ for the widened (blue line), time-evolved (orange line), and targeted (dashed black line) wave packet are plotted. Again a high fidelity is achieved $\mathcal{F} = 99.86\%$. In analogy to the case of wave packet preparation (cf. figure 8.6), the impact of fluctuations in the trap parameters is investigated by varying the coefficients

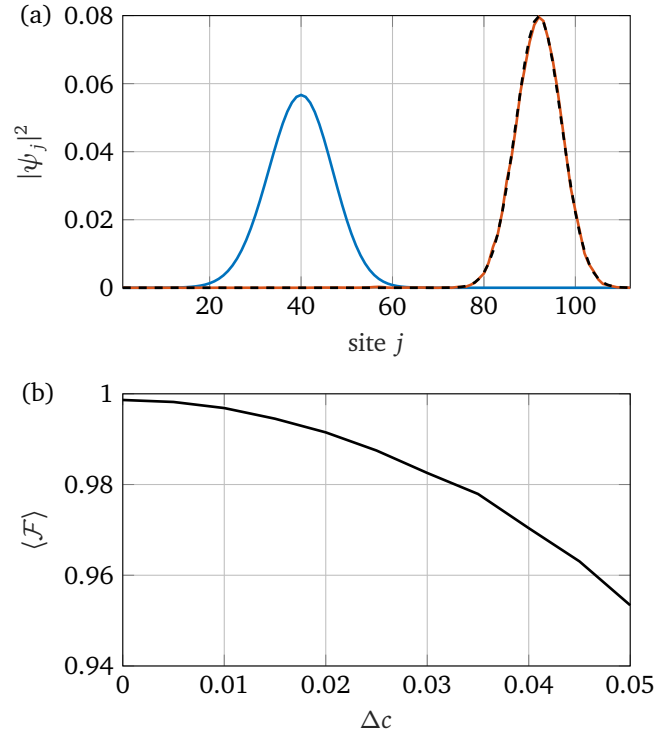


Figure 8.7: Wave packet compression: (a) shows the probability distribution of the widened wave packet with a width if $\sigma(\tau) = \sqrt{2}\sigma_0$ (blue line), of the final wave packet after compression at $t = \tau + 54.2 \hbar/J$ (orange line), and of the targeted Gaussian wave packet (black dashed line). The wave packet's initial width and average momentum are $\sigma_0 = 5a$ and $\kappa = \pi/(4a)$ respectively. For the applied compression the energy offsets of the sites with $58 \leq j \leq 72$ are used. (b) The averaged fidelity $\langle \mathcal{F} \rangle$ of the final wave packet is plotted versus the fluctuation strength Δc .

c_{jl} stochastically. The results of the corresponding calculations, shown figure 8.7 (b), reveal that the required amount of control is similar to that for wave packet preparation.

8.4 Gate fidelity

In this section, the fidelities of the basic gates (cf. figure 8.3) are calculated, considering wave packets with finite momentum spread and fluctuations in the trap parameters. In comparison to these effects, additional influences like light scattering and atom loss are negligible on the time scale of a gate operation. Since interactions with environments are not considered, the fidelity of a gate can be defined using pure states

$$\mathcal{F} = |\langle \psi_f | \psi_t \rangle|. \quad (8.19)$$

Here, $|\psi_t\rangle = \hat{U} |\psi_i\rangle$ is the targeted state which is obtained by applying the unitary operator \hat{U} of the ideal gate to the initial state $|\psi_i\rangle$. In contrast, $|\psi_f\rangle$ is the actual state of the system after the application of the gate considering its physical implementation. Using the minimal fidelity,

$$\mathcal{F}_{\min} = \min_{|\psi_i\rangle} \mathcal{F}, \quad (8.20)$$

the performance of a gate can be estimated for all initial states. To determine this quantity, the initial state needs to be parameterized, and the final state must be calculated.

Single-qubit gates

For one-qubit gates, the initial state can be written as

$$|\psi_i\rangle = \int \psi(k) (c_0 |0, k\rangle + c_1 |1, k\rangle) dk. \quad (8.21)$$

Here, $|n, k\rangle$ is the momentum state on the line segment corresponding to the basis state $|n\rangle$. The complex coefficients c_0 and c_1 obey the normalization condition $|c_0|^2 + |c_1|^2 = 1$. After the scattering process, the system's state is given by

$$|\psi_f\rangle = \int \psi(k) \hat{U}(k) (c_0 |0, k\rangle + c_1 |1, k\rangle) dk. \quad (8.22)$$

The operator $\hat{U}(k)$ can be computed from a scattering analysis of the respective graph (cf. appendix J and [251, 256, 257]). It is worth noting, that due to reflection into the incoming line segments the operator $\hat{U}(k)$ is in general non-unitary. This is a consequence of disregarding the corresponding scattering channels in the chosen state description.

Two-qubit gates

For the two-qubit gate, the initial state can be parametrized in the following way

$$|\psi_i\rangle = \iint \psi(k) \psi(k') \left(\sum_{m,n=0}^1 c_{mn} |m, k\rangle |n, k'\rangle \right) dk dk', \quad (8.23)$$

with complex coefficients obeying

$$\sum_{m,n=0}^1 |c_{mn}|^2 = 1. \quad (8.24)$$

The final state after the application of the two-qubit gate is given by

$$|\psi_f\rangle = \iint \psi(k) \psi(k') \hat{U}(k, k') \left(\sum_{m,n=0}^1 c_{mn} |m, k\rangle |n, k'\rangle \right) dk dk', \quad (8.25)$$

The operator $\hat{U}(k, k')$ can be determined by analyzing the scattering process of two counterpropagating wave packets on an infinite line segment (cf. appendix J and [20]).

8.4.1 Effects from finite momentum widths

As discussed in section 8.3.3, the finite extent of any experimental apparatus enforces the usage of finite-size wave packets which results in a momentum spread. Due to the momentum dependence of the operators $\hat{U}(k)$ and $\hat{U}(k, k')$, the fidelity for these wave packets is reduced. In figure 8.8, the minimal fidelity \mathcal{F}_{\min} is plotted versus the initial wave packet size σ_0 for the basic gates. All curves show the expected behavior, for increasing σ_0 the momentum width decreases resulting in a rising fidelity. For comparison, the same dependency is also shown for the Hadamard gate at $\kappa = \pi/(2a)$ which is required for the Childs-Gosset-Webb scheme. The fidelity of this gate is significantly smaller

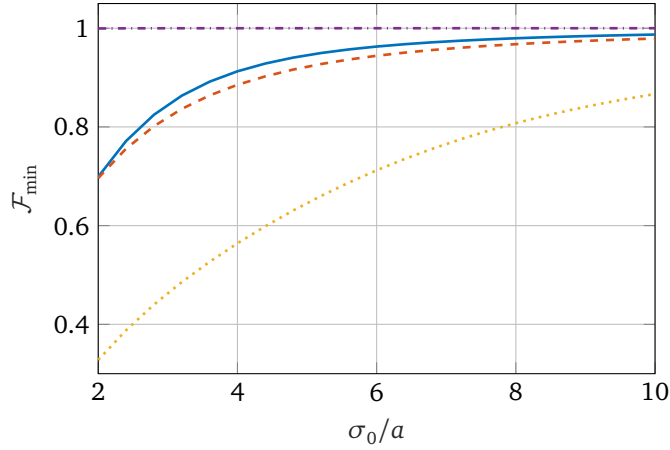


Figure 8.8: The minimal fidelity \mathcal{F}_{\min} is plotted as a function of the wave packet size σ_0 for the phase gate (solid blue line), the basis changing gate (orange dashed line), the planar Hadamard gate (yellow dotted line), and the controlled phase gate (purple dash-dotted line).

than for the other gates. This is due to the complexity of the corresponding graph (cf. figure 8.3) which results in a strong momentum dependence of the operator $\hat{U}(k)$.

8.4.2 Effects from parameter fluctuations

The optical microtraps cannot be generated with arbitrary precision. Therefore, the trap parameters fluctuate which decreases the fidelity. This effect is investigated for single-qubit gates and the propagation through line segments in the following way. First, the local energy offsets ϵ_i and the tunneling strength J_{ij} are sampled from normal distributions with averages 0, J and variances $\Delta\epsilon$, ΔJ . Second, the scattering problem is solved for the resulting graph (cf. appendix J). Third, the average minimal fidelity $\langle \mathcal{F}_{\min} \rangle$ is estimated from a sample of 100 repetitions. The results of these calculations are shown in figure 8.9 for the basis changing gate, the phase gate, and a line segment of length $40a$ which is used for the connection of gates. From these curves, it can be determined that the trap parameters need to be controlled on the $10^{-2}J$ level. These requirements are consistent with those arising from the analysis of wave packet preparation and compression (cf. section 8.3).

The impact of fluctuations in the trap parameters on the two-qubit gate's fidelity can be divided into two parts. On the one hand, fluctuations in the local energy offsets and tunneling parameters which affect the wave packet propagation through the line segments (cf. figure 8.9). On the other hand, fluctuations in the ratio U/J of the interaction strength to the tunneling parameter result in a change of the acquired relative phase which reduces the fidelity (cf. appendix J). The dependency of the minimal fidelity on U/J is shown in figure 8.10.

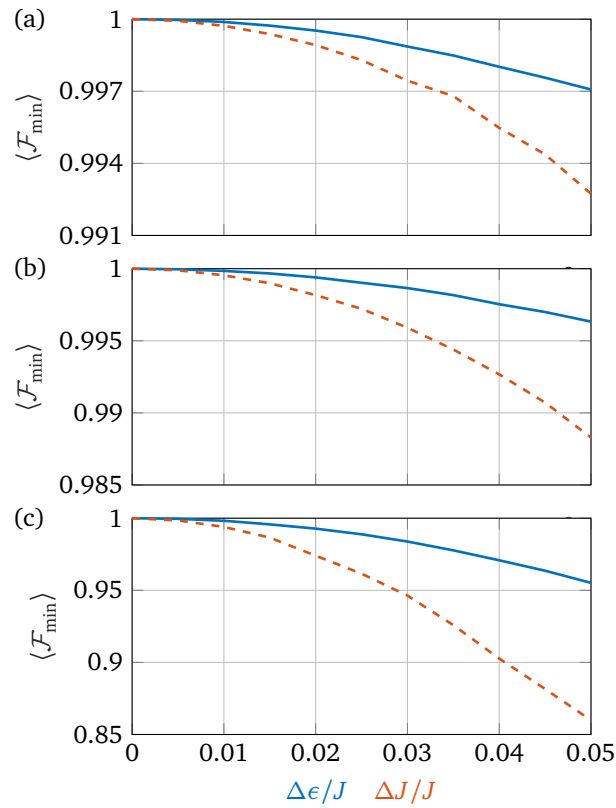


Figure 8.9: The minimal fidelity $\langle \mathcal{F}_{\min} \rangle$ is plotted versus the fluctuation strengths $\Delta\epsilon$ (blue) and ΔJ (orange) for the phase gate (a), the basis changing gate (b), and a line segment of 40 sites (c). Plane waves with momentum $\kappa = \pi/(4a)$ were used for the calculations.

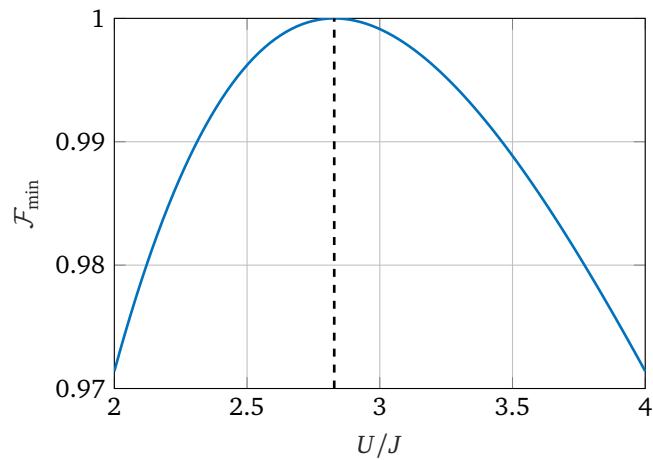


Figure 8.10: The minimal fidelity \mathcal{F}_{\min} of the controlled phase gate is plotted versus the ratio U/J for a plane wave with momentum $\kappa = \pi/(4a)$.

8.5 Scalability

In this section, practical limitations for the scalability of the proposed setup are discussed. One question in this context is how many microtraps can be generated. This depends on the technical implementation of the microtraps, e.g. microlens arrays [147, 148, 224], holographic trap arrays [157], or optical lattices with single-site control [158, 242]. However, certain considerations should apply to all of these. First, the available laser power limits the number of traps. With realistic powers of several Watts, the generation of a few hundred traps is possible [198]. Second, the field of view of the microscope objective that is needed to generate the required structures on a micrometer scale in combination with a finite trap size given on the scale of the light's wavelength limits the number of traps. Recently, a high NA objective for ultracold atom experiments has been characterized to have a field of view with a diameter of $76 \mu\text{m}$ [200]. Assuming a trap spacing of $d = 1.5 \mu\text{m}$ this results in 50×50 traps. Third, the number of pixel that a spatial light modulator provides per trap limits the precision of the control over the trap depths. For a setup using a combination of a microlens array together with a liquid-crystal-based spatial light modulator the local energy offsets can be controlled with a relative precision of 10^{-5} (cf. section 5.3.2 and [224]). This allows for the required control of the Hubbard parameters on the $10^{-2}J$ level. Further, the time of experimental runs is limited by processes like light scattering and atom loss. Considering typical photon scattering rates and lifetimes of Bose-Einstein condensates, accessible durations for experimental runs are of the order of 1 s. The atomic wave packets at momentum $\pi/(4a)$ propagate at a velocity of $aJ/(\sqrt{2}\hbar)$ (cf. equation (8.11) and equation (8.13)). For typical tunneling parameters of $J/\hbar = 100$ Hz, this results in maximum traversed distances of several hundred sites. The preceding considerations suggest that circuits with about ten qubits and a similar number of gate operations are feasible with state-of-the-art technology. In addition, it is worth noting that none of the limitations discussed above are fundamental.

Chapter 9

Conclusion and outlook

In this thesis, an experimental platform based on ultracold atoms in adjustable arrays of optical microtraps is investigated. This setup offers a new approach to the experimental study of itinerant quantum many-body systems in two-dimensional trap arrays with full single-site control over the trap parameters.

In part II, the feasibility of an experimental implementation is investigated. As a first step, the light field generating the microtraps is simulated using a detailed model of the optical setup. These calculations provide the intensity distribution which is proportional to the potential for the atoms. The simulation results are validated by a comparison to measurements performed in the research group of Gerhard Birkl. In these measurements, light with a wavelength of 780 nm is used. This is not suitable for trapping ^{87}Rb atoms. In addition, the optical simulations reveal that aberrations caused by the objective lens hinder the implementation of a homogeneous trap array. Therefore, to obtain trap parameters for a promising scenario, simulations using a wavelength of 1064 nm and a diffraction-limited objective are performed. In the image plane, this yields approximately Gaussian spots with waists of $0.74\ \mu\text{m}$ and separations of $1.7\ \mu\text{m}$. Along the optical axis, a Talbot structure can be observed with periodic reoccurrences of the light field's structure every $7\ \mu\text{m}$. To prevent tunneling to neighboring Talbot planes, the usage of a light sheet is proposed. As an additional feature, cross-talk-free single-site control over the trap depth can be added by using a spatial light modulator that controls the illumination of the microlens array.

Based on the optical simulations discussed above, the parameters of the Bose-Hubbard model for the lightest bosonic alkalis are obtained from numerical band structure calculations. Despite the large trap separations compared to optical lattices, the results show that the superfluid to Mott insulator transition can be reached with sufficiently fast tunneling rates. In addition, approximate closed-form expressions are provided using a variational Gaussian wave function ansatz for the interaction strength U and the instanton technique for the tunneling parameter J . For non-periodic potentials, an analog to Wannier functions is introduced. This concept is used to determine the impact of fluctuations in the optical potential on the Bose-Hubbard parameters.

For the preparation of low-entropy states, two alternatives are investigated. On the one hand, an analog to the loading scheme used in optical lattice experiments is considered. Here, the starting point is a BEC prepared in a wide trap. The system is transferred to an array of microtraps by increasing the depth of the corresponding potential adiabatically. Realistic timescales for this process are estimated by rescaling theoretical and experimental results for optical lattices. The obtained ramp durations are compared to typical lifetimes in cold atom experiments, and the effect of heating due to light scattering is investigated. The results of these considerations render the implementation of this approach feasible. On the other hand, a loading scheme is considered which starts from an array of isolated tight traps. Recently developed experimental techniques can be used for the deterministic preparation of one atom per site [155, 198, 199] and efficient cooling

to the motional ground state [174, 201]. To access the regime of itinerant many-body physics, the trap depths need to be reduced significantly. The conditions for the adiabaticity of this process are derived, and optimal adiabatic ramp shapes are computed. For the latter, the transfer fidelity is calculated, and the impact of external heating due to light scattering is discussed. The results of these considerations show the feasibility of the considered loading scheme, which has the advantage of being applicable to species that cannot be cooled evaporatively.

In part III, two applications for the considered setup are investigated. First, the tunneling dynamics of ultracold atoms between a pair of weakly coupled ring lattices is analyzed. This system extends the concept of a double-well by adding the structure of the Bose-Hubbard model to each well. Depending on the interaction strength, multiple regimes are identified and explained on a quantitative level: sinusoidal oscillations exhibiting collapse and revival, self-trapping, and tunneling resonances. Second, the implementation of universal quantum computing based on continuous-time quantum walks of interacting particles is investigated. To simplify the experimental implementation, the original scheme [20] is modified by adding time-dependent control over the local trap depths. In addition, the impact of finite size effects and fluctuations in the optical potential are considered, and the scalability of the approach is analyzed. These considerations render an implementation using the discussed experimental platform feasible.

In addition to the examples investigated in part III of this thesis, further applications can be envisioned. The capability to adjust the trap depth of each site individually can be used to implement controlled disorder. This allows for a systematic experimental study of the connection between disorder and localization in interacting many-body systems. Though this topic has attracted considerable interest [258], the difficulty of a theoretical treatment has prevented a comprehensive understanding [137, 138].

Solid state systems are considered as the prime target for quantum simulators in the field of cold atoms. However, the setup discussed in this thesis also allows implementing the potential landscapes of planar molecules. If a controlled number of fermionic atoms is adiabatically loaded into this structure, then the atoms fill the lowest orbitals. The atomic density can be imaged with a recently proposed technique [259].

Atomtronics [260, 261] is an emerging field in which neutral atoms in external potentials mimic electronic circuits. Due to its flexibility in generating 2D structures of optical microtraps, the setup discussed in this thesis can be used as a pinboard for atomtronic circuits. Implementations of basic components such as diodes and transistors have been proposed [262, 263].

Using fast, periodic, external driving of quantum many-body systems the effective Hamilton operator for long-time dynamics can be altered [125, 264, 265]. This technique is referred to as Floquet engineering and has been applied successfully to optical lattice experiments [247, 266–273]. The setup investigated in this thesis allows applying fully adjustable periodic modulations of up to 10 kHz with single-site addressability by using a spatial light modulator.

Part IV

Appendices

Appendix A

Properties of relevant isotopes

In this appendix, the properties of several alkali metal isotopes are summarized. The considered isotopes are ${}^7\text{Li}$, ${}^{23}\text{Na}$, ${}^{41}\text{K}$, and ${}^{87}\text{Rb}$. These are the lightest stable bosonic alkalis. The isotopes ${}^{39}\text{K}$ and ${}^{85}\text{Rb}$ are not considered because of their negative scattering length.

In table A.1 the relevant properties of the considered isotopes are summarized. The given scattering lengths a_s of ${}^{23}\text{Na}$, ${}^{41}\text{K}$, and ${}^{87}\text{Rb}$ in the $|F = 1, m_F = -1\rangle$ state are taken from [274], [275], and [276] respectively. For ${}^7\text{Li}$ it is assumed that the scattering length is tuned to the given value via a Feshbach resonance. The wavelength λ and decay rates Γ for the $D1$ and $D2$ lines are taken from [42].

Quantity	${}^7\text{Li}$	${}^{23}\text{Na}$	${}^{41}\text{K}$	${}^{87}\text{Rb}$
m	7.02 u	22.99 u	40.96 u	86.91 u
a_s	5.31 nm	2.93 nm	3.44 nm	5.31 nm
λ_{D1}	671 nm	590 nm	770 nm	795 nm
λ_{D2}	671 nm	589 nm	767 nm	780 nm
Γ_{D1}	$3.69 \cdot 10^7 \text{ s}^{-1}$	$6.14 \cdot 10^7 \text{ s}^{-1}$	$3.74 \cdot 10^7 \text{ s}^{-1}$	$3.61 \cdot 10^7 \text{ s}^{-1}$
Γ_{D2}	$3.69 \cdot 10^7 \text{ s}^{-1}$	$6.15 \cdot 10^7 \text{ s}^{-1}$	$3.79 \cdot 10^7 \text{ s}^{-1}$	$3.81 \cdot 10^7 \text{ s}^{-1}$

Table A.1: Properties of the considered alkali isotopes. Provided are the atomic mass m , the scattering length for the $|F = 1, m_F = -1\rangle$ state, and the wavelengths λ and decay rates of the $D1$ and $D2$ lines. In case of ${}^7\text{Li}$ it is assumed that the scattering length is tuned via a Feshbach resonance.

Appendix B

Representations of the many-body state

In this appendix, representations of the many-body state for the Bose-Hubbard model are discussed. First, in section B.1 the number state representation is discussed and used to visualize states of few-well Bose-Hubbard models. Second, in section B.2 phase states are introduced. For sufficiently large occupation numbers this state representation leads to the quantum rotor model. Finally, in section B.3 phase coherent states are introduced to derive an exact generalized quantum rotor model.

B.1 Number-state representation

The number states defined in equation (3.32) constitute an orthonormal basis for the Hilbert space of the Bose-Hubbard model. Therefore, an arbitrary state can be expanded in the following way

$$|\psi\rangle = \sum_{\mathbf{n} \in \mathcal{N}} \psi_{\mathbf{n}} |\mathbf{n}\rangle. \quad (\text{B.1})$$

It is worth noting, that the condition $\sum_i n_i = N$ constraints the relevant \mathbf{n} to an $(M - 1)$ -dimensional simplex. The corresponding energy functional $\langle \psi | \hat{H} | \psi \rangle$ for the Bose-Hubbard Hamilton operator given in equation (3.10) can be calculated from the matrix elements

$$\langle \psi | \hat{a}_i^\dagger \hat{a}_j | \psi \rangle = \sum_{\mathbf{n} \in \mathcal{N}} \psi_{\mathbf{n}}^* \psi_{\mathbf{n}_{ij}} \sqrt{n_i(n_j + 1)}, \quad (\text{B.2})$$

$$\langle \psi | \hat{a}_i^\dagger \hat{a}_i^\dagger \hat{a}_i \hat{a}_i | \psi \rangle = \sum_{\mathbf{n} \in \mathcal{N}} |\psi_{\mathbf{n}}|^2 n_i(n_i - 1). \quad (\text{B.3})$$

Here, the following notation is introduced

$$\mathbf{n}_{ij} = (n_1 \dots n_i + 1 \dots n_j - 1 \dots n_M). \quad (\text{B.4})$$

Using the identity

$$\psi^*(\mathbf{n})\psi(\mathbf{n}_{ij}) + \psi(\mathbf{n})\psi^*(\mathbf{n}_{ij}) = |\psi(\mathbf{n})|^2 + |\psi(\mathbf{n}_{ij})|^2 - |\psi(\mathbf{n}) - \psi(\mathbf{n}_{ij})|^2, \quad (\text{B.5})$$

the energy functional

$$E[|\psi\rangle] = \langle \psi | \hat{H} | \psi \rangle = T[|\psi\rangle] + V[|\psi\rangle], \quad (\text{B.6})$$

can be split into a kinetic

$$T[|\psi\rangle] = J \sum_{\langle i,j \rangle} \sum_{\mathbf{n} \in \mathcal{N}} |\psi(\mathbf{n}) - \psi(\mathbf{n}_{ij})|^2 \sqrt{n_i(n_j + 1)}, \quad (\text{B.7})$$

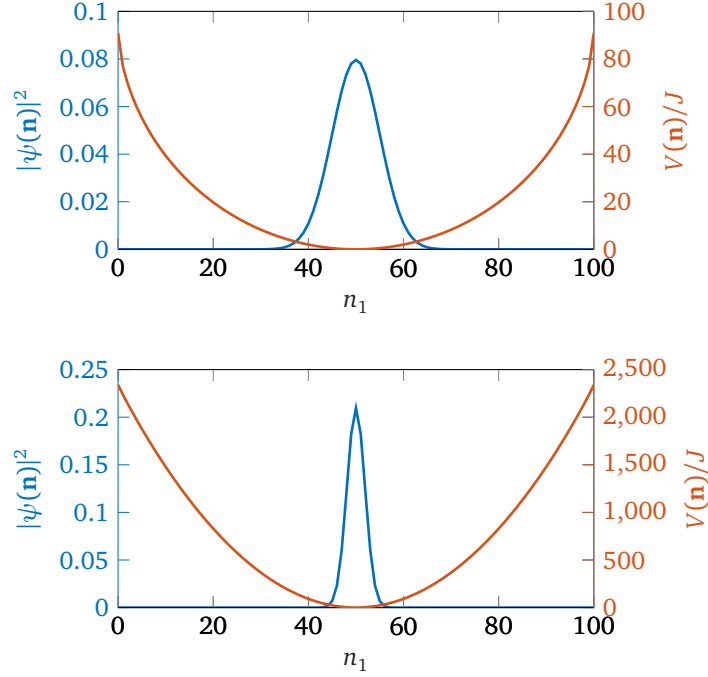


Figure B.1: The ground state $\psi(\mathbf{n})$ (blue line) and the effective potential $V(\mathbf{n})$ (orange line) are shown for a double well with $N = 100$ particles and $U/J = 0$ (upper subfigure) and $U/J = 0.9$ (lower subfigure).

and a potential part

$$\begin{aligned}
 V[|\psi\rangle] = & \frac{U}{2} \sum_{i=1}^M \sum_{\mathbf{n} \in \mathcal{N}} |\psi(\mathbf{n})|^2 n_i (n_i - 1) \\
 & - J \sum_{\langle i,j \rangle} \sum_{\mathbf{n} \in \mathcal{N}} (|\psi(\mathbf{n})|^2 + |\psi(\mathbf{n}_{ij})|^2) \sqrt{n_i (n_j + 1)}.
 \end{aligned} \tag{B.8}$$

For $N \gg M$ the occupation numbers \mathbf{n} can be interpreted as continuous variables and the term $|\psi(\mathbf{n}) - \psi(\mathbf{n}_{ij})|$ becomes a derivative. Due to the factor $\sqrt{n_i (n_j + 1)}$ in equation B.7 the resulting Schrödinger equation in Fock space has a position dependent mass term. The ground-state wave function $\psi(\mathbf{n})$ is peaked around $n_i = N/M$. For increasing interaction strengths $\psi(\mathbf{n})$ gets more localized around this minimum because the effective potential gets tighter. This picture explains the decrease in occupation number fluctuations for increasing interaction strength that results in the superfluid to Mott-insulator phase transition.

Figure B.1 shows the Fock-space potential V and the wave function ψ for a double well ($M = 2$) with $N = 100$. The comparison of the cases $U/J = 0$ and $U/J = 0.9$ demonstrates the Fock space localization caused by repulsive interaction. In figures B.2 and B.3 the cases of three-well and four-well configurations are shown.

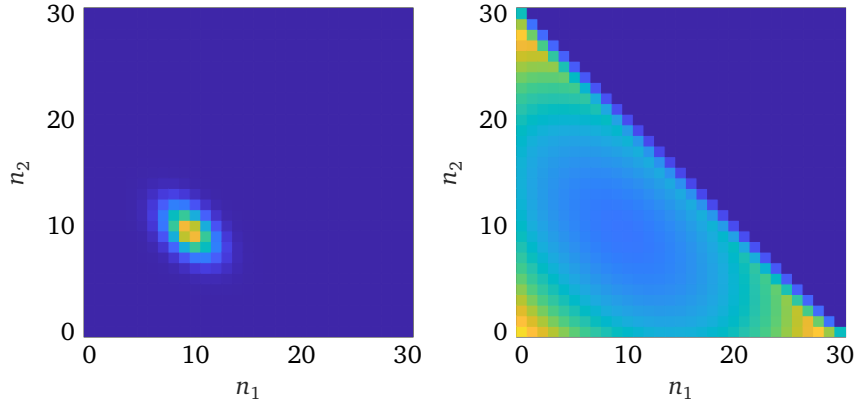


Figure B.2: The ground state $|\psi(\mathbf{n})|^2$ (left subplot) and the effective potential $V(\mathbf{n})$ (right subplot) are shown for $M = 3$, $N = 30$, and $U/J = 1$. The color scale goes from blue for small values to yellow for large values.

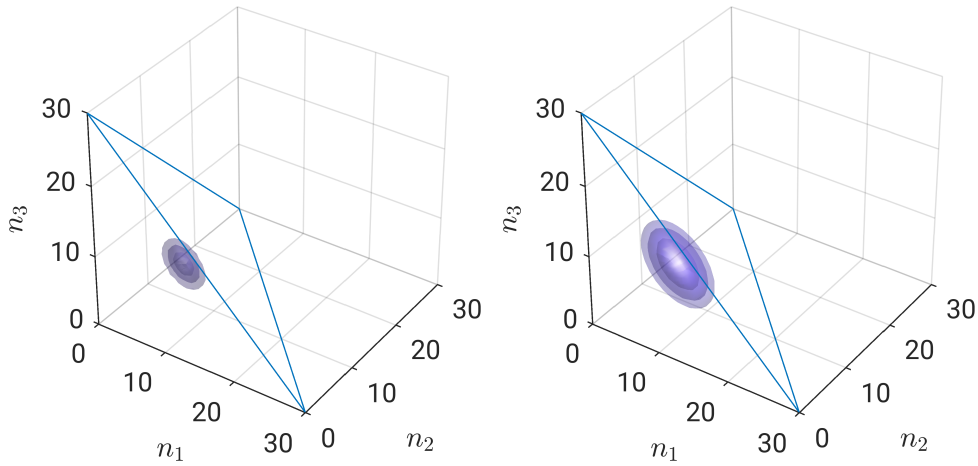


Figure B.3: Isosurfaces of the ground state $|\psi(\mathbf{n})|^2$ (left subplot) and the effective potential $V(\mathbf{n})$ (right subplot) are shown for $M = 4$, $N = 30$, and $U/J = 1$. The blue lines indicate the edges of the simplex in which the condition $\sum_i n_i = N$ is satisfied.

B.2 Phase-state representation

Complementary to the number states, the so-called phase states also constitute a basis of the many-body Hilbert space. These states are defined by

$$\langle \mathbf{n} | \boldsymbol{\phi} \rangle = \frac{e^{i\mathbf{n}\boldsymbol{\phi}}}{\sqrt{2\pi^M}}. \quad (\text{B.9})$$

An arbitrary state can be represented in the following way

$$|\psi\rangle = \frac{1}{\sqrt{2\pi^M}} \int_{\Omega} e^{-i\tilde{\mathbf{n}}\sum_k \phi_k} \tilde{\psi}(\boldsymbol{\phi}) |\boldsymbol{\phi}\rangle d^M \boldsymbol{\phi} \quad (\text{B.10})$$

Here, the average particle number per site $\bar{n} = N/M$ and $\Omega = [-\pi, \pi]^M$ are introduced. The amplitudes ψ_n and $\tilde{\psi}(\boldsymbol{\phi})$ are connected via

$$\tilde{\psi}(\boldsymbol{\phi}) = \sum_{\mathbf{n}} \psi_{\mathbf{n}} e^{-i\mathbf{n}\boldsymbol{\phi}}, \quad \psi_{\mathbf{n}} = \frac{1}{(2\pi)^M} \int_{\Omega} e^{-i\bar{n}\sum\phi_k} \tilde{\psi}(\boldsymbol{\phi}) e^{i\mathbf{n}\boldsymbol{\phi}} d\boldsymbol{\phi}. \quad (\text{B.11})$$

The factor $e^{i\bar{n}\sum\phi_k}$ ensures that the condition $\sum_i n_i = N$ is satisfied. Using the above equations the energy functional in phase-state representation can be calculated. For the interaction terms one obtains

$$\langle \hat{a}_i^\dagger \hat{a}_i^\dagger \hat{a}_i \hat{a}_i \rangle = \sum_{\mathbf{n}} \frac{n_i(n_i-1)}{(2\pi)^{2M}} \iint e^{i\bar{n}\sum(\phi'_k - \phi_k)} \tilde{\psi}^*(\boldsymbol{\phi}') \tilde{\psi}(\boldsymbol{\phi}) e^{i\mathbf{n}(\boldsymbol{\phi} - \boldsymbol{\phi}')} d^M \boldsymbol{\phi} d^M \boldsymbol{\phi}' \quad (\text{B.12})$$

$$= \iint \frac{e^{i\bar{n}\sum(\phi'_k - \phi_k)}}{(2\pi)^{2M}} \tilde{\psi}^*(\boldsymbol{\phi}') \tilde{\psi}(\boldsymbol{\phi}) \left[\sum_{\mathbf{n}} n_i(n_i-1) e^{i\mathbf{n}(\boldsymbol{\phi} - \boldsymbol{\phi}')} \right] d^M \boldsymbol{\phi} d^M \boldsymbol{\phi}' \quad (\text{B.13})$$

$$= \iint \frac{e^{i\bar{n}\sum(\phi'_k - \phi_k)}}{(2\pi)^{2M}} \tilde{\psi}^*(\boldsymbol{\phi}') \tilde{\psi}(\boldsymbol{\phi}) \left[(i\partial_{\phi_i} - \partial_{\phi_i}^2) \sum_{\mathbf{n}} e^{i\mathbf{n}(\boldsymbol{\phi} - \boldsymbol{\phi}')} \right] d^M \boldsymbol{\phi} d^M \boldsymbol{\phi}' \quad (\text{B.14})$$

$$= \iint \frac{e^{i\bar{n}\sum(\phi'_k - \phi_k)}}{(2\pi)^M} \tilde{\psi}^*(\boldsymbol{\phi}') \tilde{\psi}(\boldsymbol{\phi}) \left[(i\partial_{\phi_i} - \partial_{\phi_i}^2) \delta(\boldsymbol{\phi} - \boldsymbol{\phi}') \right] d^M \boldsymbol{\phi} d^M \boldsymbol{\phi}'. \quad (\text{B.15})$$

Using integration by parts the derivatives can be applied to the functions $\tilde{\psi}$ as shown in the following calculation

$$\int e^{-i\bar{n}\sum\phi_k} \tilde{\psi}(\boldsymbol{\phi}) e^{i\mathbf{n}\boldsymbol{\phi}} \partial_{\phi_i} \delta(\boldsymbol{\phi} - \boldsymbol{\phi}') d^M \boldsymbol{\phi} = - \int \partial_{\phi_i} \left[e^{-i\bar{n}\sum\phi_k} \tilde{\psi}(\boldsymbol{\phi}) \right] \delta(\boldsymbol{\phi} - \boldsymbol{\phi}') d^M \boldsymbol{\phi} \quad (\text{B.16})$$

Note that there is no boundary term since Ω is a M -dimensional torus. Applying integration by parts to all derivatives and performing the integration over $\boldsymbol{\phi}'$ yields

$$\langle \hat{a}_i^\dagger \hat{a}_i^\dagger \hat{a}_i \hat{a}_i \rangle = \int \left[\bar{n}(\bar{n}-1) |\tilde{\psi}|^2 + (2\bar{n}+1) i \tilde{\psi}^* \frac{\partial}{\partial \phi_i} \tilde{\psi} - \tilde{\psi}^* \frac{\partial^2}{\partial \phi_i^2} \tilde{\psi} \right] \frac{d^M \boldsymbol{\phi}}{(2\pi)^M}. \quad (\text{B.17})$$

The first term in the square brackets is a constant and therefore irrelevant and the second term vanishes as a result of the continuity equation. It remains to compute the hopping terms

$$\langle \hat{a}_i^\dagger \hat{a}_j \rangle = \iint \frac{e^{i\bar{n}\sum(\phi'_k - \phi_k)}}{(2\pi)^{2M}} \tilde{\psi}^*(\boldsymbol{\phi}') \tilde{\psi}(\boldsymbol{\phi}) \left[\sum_{\mathbf{n}} \sqrt{n_j(n_j+1)} e^{i\mathbf{n}(\boldsymbol{\phi} - \boldsymbol{\phi}')} \right] e^{i(\phi_j - \phi_i)} d^M \boldsymbol{\phi} d^M \boldsymbol{\phi}'. \quad (\text{B.18})$$

The sum over \mathbf{n} cannot be evaluated. However, for large fillings the factor $\sqrt{n_j(n_j+1)}$ can be approximated by \bar{n} . This yields

$$\langle \hat{a}_i^\dagger \hat{a}_j \rangle = \frac{\bar{n}}{(2\pi)^M} \int \tilde{\psi}^*(\boldsymbol{\phi}) e^{i(\phi_j - \phi_i)} \tilde{\psi}(\boldsymbol{\phi}) d^M \boldsymbol{\phi}. \quad (\text{B.19})$$

From the equations (3.10), (B.17), and (B.19) the phase state representation of the Hamilton operator can be derived

$$H_\phi = -2J\bar{n} \sum_{\langle i,j \rangle} \cos(\phi_i - \phi_j) - \frac{U}{2} \sum_{i=1}^M \partial_{\phi_i}^2. \quad (\text{B.20})$$

This is the Hamilton operator of the quantum phase model [277–279]. For $\bar{n}J \gg U$ the second term can be neglected and the Hamilton function of the classical XY-model is obtained. In two dimensions this model exhibits a Berezinskii–Kosterlitz–Thouless-type phase transition [280]. This regime has been studied with cold atoms in optical lattices at high fillings [281, 282].

B.3 Phase-coherent-state representation

In the preceding section the phase-state representation of the Bose-Hubbard Hamilton operator was derived for large \bar{n} . In this section a different set of states is introduced to find an exact representation of the Hamilton operator in terms of phases. This was first investigated for double-wells [283] and later generalized to lattices [284]. The required states are called phase coherent states and are defined by

$$\langle \mathbf{n} | \varphi \rangle = \frac{e^{i\mathbf{n}\varphi}}{\sqrt{n_1! \dots n_M!}}, \quad |\psi\rangle = \frac{1}{\sqrt{2\pi^M}} \int_{\Omega} e^{-i\bar{n} \sum_k \varphi_k} \psi(\varphi) |\varphi\rangle d\varphi. \quad (\text{B.21})$$

The advantage of this representation is that the action of the operators \hat{a}_i and \hat{a}_i^\dagger on the basis states can be computed directly

$$\hat{a}_i |\varphi\rangle = \hat{a}_i \sum_{\mathbf{n}} |\mathbf{n}\rangle \langle \mathbf{n} | \varphi \rangle \quad (\text{B.22})$$

$$= \sum_{\mathbf{n}} \frac{e^{i\mathbf{n}\varphi}}{\sqrt{n_1! \dots n_M!}} \sqrt{n_i} |n_1 \dots n_i - 1 \dots n_M\rangle \quad (\text{B.23})$$

$$= \sum_{\mathbf{n}'} e^{i\varphi_i} \frac{e^{i\mathbf{n}'\varphi}}{\sqrt{n_1'! \dots n_M'!}} |\mathbf{n}'\rangle \quad (\text{B.24})$$

$$= e^{i\varphi_i} |\varphi\rangle \quad (\text{B.25})$$

$$\hat{a}_i^\dagger |\varphi\rangle = \hat{a}_i^\dagger \sum_{\mathbf{n}} |\mathbf{n}\rangle \langle \mathbf{n} | \varphi \rangle \quad (\text{B.26})$$

$$= \sum_{\mathbf{n}} \frac{e^{i\mathbf{n}\varphi}}{\sqrt{n_1! \dots n_M!}} \sqrt{n_i + 1} |n_1 \dots n_i + 1 \dots n_M\rangle \quad (\text{B.27})$$

$$= \sum_{\mathbf{n}'} e^{-i\varphi_i} n_i' \frac{e^{i\mathbf{n}'\varphi}}{\sqrt{n_1'! \dots n_M'!}} |\mathbf{n}'\rangle \quad (\text{B.28})$$

$$= -ie^{-i\varphi_i} \frac{\partial}{\partial \varphi_i} |\varphi\rangle. \quad (\text{B.29})$$

Using the above equations the tunneling terms

$$\hat{a}_i^\dagger \hat{a}_j |\psi\rangle = -\frac{i}{\sqrt{2\pi}^M} \int_{\Omega} e^{-i\bar{n}\sum_k \varphi_k} \psi(\varphi) e^{i(\varphi_j - \varphi_i)} \frac{\partial}{\partial \varphi_i} |\varphi\rangle d\varphi \quad (\text{B.30})$$

$$= \frac{1}{\sqrt{2\pi}^M} \int_{\Omega} e^{-i\bar{n}\sum_k \varphi_k} e^{i(\varphi_j - \varphi_i)} \left[(\bar{n} + 1)\psi(\varphi) + i \frac{\partial}{\partial \varphi_i} \psi(\varphi) \right] |\varphi\rangle d\varphi \quad (\text{B.31})$$

and the interaction terms can be computed

$$\hat{a}_i^\dagger \hat{a}_i^\dagger \hat{a}_i \hat{a}_i |\psi\rangle = -\frac{1}{\sqrt{2\pi}^M} \int_{\Omega} e^{-i\bar{n}\sum_k \varphi_k} \psi(\varphi) \left(\frac{\partial^2}{\partial \varphi_i^2} + i \frac{\partial}{\partial \varphi_i} \right) |\varphi\rangle d\varphi \quad (\text{B.32})$$

$$= -\frac{1}{\sqrt{2\pi}^M} \int_{\Omega} \frac{\partial^2}{\partial \varphi_i^2} \left(e^{-i\bar{n}\sum_k \varphi_k} \psi(\varphi) \right) |\varphi\rangle d\varphi \quad (\text{B.33})$$

$$+ \frac{i}{\sqrt{2\pi}^M} \int_{\Omega} \frac{\partial}{\partial \varphi_i} \left(e^{-i\bar{n}\sum_k \varphi_k} \psi(\varphi) \right) |\varphi\rangle d\varphi$$

$$= -\frac{1}{\sqrt{2\pi}^M} \int_{\Omega} e^{-i\bar{n}\sum_k \varphi_k} \left(\frac{\partial^2}{\partial \varphi_i^2} \psi(\varphi) \right) |\varphi\rangle d\varphi \quad (\text{B.34})$$

$$+ \frac{i(2\bar{n} - 1)}{\sqrt{2\pi}^M} \int_{\Omega} e^{-i\bar{n}\sum_k \varphi_k} \left(\frac{\partial}{\partial \varphi_i} \psi(\varphi) \right) |\varphi\rangle d\varphi$$

$$+ \frac{\bar{n}(\bar{n} - 1)}{\sqrt{2\pi}^M} \int_{\Omega} e^{-i\bar{n}\sum_k \varphi_k} \psi(\varphi) |\varphi\rangle d\varphi.$$

Thus, the effective Hamilton operator H_φ , which is defined by

$$\hat{H} |\psi\rangle = \frac{1}{\sqrt{2\pi}^M} \int_{\Omega} e^{-i\bar{n}\sum_k \varphi_k} [H_\varphi \psi(\varphi)] |\varphi\rangle d\varphi, \quad (\text{B.35})$$

can be calculated

$$H_\varphi = -J \sum_{\langle i,j \rangle} \left[2(\bar{n} + 1) \cos(\varphi_i - \varphi_j) + i e^{i(\varphi_i - \varphi_j)} \frac{\partial}{\partial \varphi_j} + i e^{i(\varphi_j - \varphi_i)} \frac{\partial}{\partial \varphi_i} \right] \quad (\text{B.36})$$

$$- \frac{U}{2} \sum_{i=1}^M \frac{\partial^2}{\partial \varphi_i^2} + UM \frac{\bar{n}(\bar{n} - 1)}{2}.$$

It is worth noting that H_φ is not Hermitian. However, Hermiticity is restored by the projection onto the set of states with a fixed particle number N due to the factor $e^{-i\bar{n}\sum_k \varphi_k}$ [283].

Appendix C

Two-dimensional Gaussian lattices

In this appendix, the plane wave expansion coefficients for two-dimensional Gaussian lattices with different geometries are given. These are required for the band-structure calculations discussed in section 5.1. The general form of the considered potentials (cf. subsection 5.1.1) is given by

$$V_{\perp}(x, y) = -V_{0\perp} \sum_i \exp\left(-2\frac{(x - X_i)^2 + (y - Y_i)^2}{w_{0\perp}^2}\right), \quad (\text{C.1})$$

with the coordinates of the lattice sites X_i and Y_i determining the geometry. In the following square, triangular, and honeycomb lattices are discussed.

C.1 Square lattice

The square lattice potential is given by

$$V_{\perp}(x, y) = -V_{0\perp} \sum_{m, n \in \mathbb{Z}} \exp\left(-2\frac{(x - md)^2}{w_{0\perp}^2}\right) \exp\left(-2\frac{(y - nd)^2}{w_{0\perp}^2}\right) \quad (\text{C.2})$$

$$= -V_{0\perp} \frac{\pi w_{0\perp}^2}{2d^2} \vartheta_3\left(-\frac{\pi x}{d}, e^{-\frac{\pi^2 w_{0\perp}^2}{2d^2}}\right) \vartheta_3\left(-\frac{\pi y}{d}, e^{-\frac{\pi^2 w_{0\perp}^2}{2d^2}}\right). \quad (\text{C.3})$$

In the above equation, $\vartheta_3(z, q)$ is the third Jacobian theta function [47] which is defined by

$$\vartheta_3(z, q) = 1 + 2 \sum_{n=1}^{\infty} q^{n^2} \cos(2nz) = \sum_{n \in \mathbb{Z}} q^{n^2} e^{2inz}. \quad (\text{C.4})$$

This identity allows to express the potential in the following form

$$V_{\perp}(x, y) = -V_{0\perp} \frac{\pi w_{0\perp}^2}{2d^2} \sum_{m, n \in \mathbb{Z}} e^{-\frac{w_{0\perp}^2 \kappa^2}{8}(m^2 + n^2)} e^{-iq_{mn}r}, \quad (\text{C.5})$$

from which the plane wave expansion coefficients can be obtained

$$v_{\mathbf{q}_{mn}} = -V_{0\perp} \frac{\pi w_{0\perp}^2}{2d^2} e^{-\frac{w_{0\perp}^2 \kappa^2}{8}(m^2 + n^2)} \quad (\text{C.6})$$

for the reciprocal lattice vector

$$\mathbf{q}_{mn} = m\mathbf{b}_1 + n\mathbf{b}_2, \quad \mathbf{b}_1 = \begin{pmatrix} \kappa \\ 0 \end{pmatrix}, \quad \mathbf{b}_2 = \begin{pmatrix} 0 \\ \kappa \end{pmatrix}. \quad (\text{C.7})$$

The vectors \mathbf{b}_1 and \mathbf{b}_2 are the reciprocal basis vectors corresponding to the primitive lattice vectors

$$\mathbf{a}_1 = \begin{pmatrix} d \\ 0 \end{pmatrix}, \quad \mathbf{a}_2 = \begin{pmatrix} 0 \\ d \end{pmatrix}, \quad (\text{C.8})$$

with $\mathbf{a}_i \mathbf{b}_j = 2\pi \delta_{ij}$. In contrast to optical lattice potentials there is an infinite number of non-zero plane wave expansion coefficients. However, the coefficients corresponding to large lattice momenta are strongly suppressed due to the Gaussian factor in equation (C.6). This allows to truncate the sum in equation (C.5).

C.2 Triangular lattice

The triangular lattice potential is given by

$$V_{\perp}(x, y) = -V_{0\perp} \sum_{m, n \in \mathbb{Z}} \exp\left(-2 \frac{(x - \sqrt{3}md/2)^2}{w_{0\perp}^2}\right) \exp\left(-2 \frac{(y - nd + md/2)^2}{w_{0\perp}^2}\right) \quad (\text{C.9})$$

$$\begin{aligned} &= -V_{0\perp} \frac{\pi w_{0\perp}^2}{2\sqrt{3}d^2} \left[\vartheta_3\left(-\frac{\pi x}{d}, e^{-\frac{\pi^2 w_{0\perp}^2}{2d^2}}\right) \vartheta_3\left(-\frac{\pi y}{\sqrt{3}d}, e^{-\frac{\pi^2 w_{0\perp}^2}{6d^2}}\right) \right. \\ &\quad \left. + \vartheta_3\left(\frac{\pi(d-2x)}{2d}, e^{-\frac{\pi^2 w_{0\perp}^2}{2d^2}}\right) \vartheta_3\left(\frac{\pi(\sqrt{3}d-2y)}{2\sqrt{3}d}, e^{-\frac{\pi^2 w_{0\perp}^2}{6d^2}}\right) \right] \quad (\text{C.10}) \end{aligned}$$

$$= -V_{0\perp} \frac{\pi w_{0\perp}^2}{2\sqrt{3}d^2} \sum_{m, n \in \mathbb{Z}} e^{-\frac{w_{0\perp}^2 \kappa^2}{8}(m^2/3+n^2)} e^{i\kappa x m/\sqrt{3}} e^{i\kappa y n} (1 + e^{i\pi(m+n)}) \quad (\text{C.11})$$

$$= -V_{0\perp} \frac{\pi w_{0\perp}^2}{\sqrt{3}d^2} \sum_{l, n \in \mathbb{Z}} e^{-\frac{w_{0\perp}^2 \kappa^2}{6}(l^2+n^2+ln)} e^{i\mathbf{q}_{ln} \mathbf{r}}. \quad (\text{C.12})$$

For the step from equation (C.9) to (C.10) the fact that a triangular lattice can be constructed from two rectangular lattices is used. In equation (C.12) the summation was reorganized by introducing the index l with $m = 2l + n$. The plane wave expansion coefficients are given by

$$v_{\mathbf{q}_{ln}} = -V_{0\perp} \frac{\pi w_{0\perp}^2}{\sqrt{3}d^2} e^{-\frac{w_{0\perp}^2 \kappa^2}{6}(l^2+n^2+ln)}. \quad (\text{C.13})$$

The lattice momentum vector is expressed as the sum of multiples of the reciprocal basis vectors

$$\mathbf{q}_{ln} = l\mathbf{b}_1 + n\mathbf{b}_2, \quad \mathbf{b}_1 = \kappa \begin{pmatrix} 2/\sqrt{3} \\ 0 \end{pmatrix}, \quad \mathbf{b}_2 = \kappa \begin{pmatrix} 1/\sqrt{3} \\ 1 \end{pmatrix}. \quad (\text{C.14})$$

The corresponding primitive lattice vectors are

$$\mathbf{a}_1 = \frac{d}{2} \begin{pmatrix} \sqrt{3} \\ -1 \end{pmatrix}, \quad \mathbf{a}_2 = \begin{pmatrix} 0 \\ d \end{pmatrix}. \quad (\text{C.15})$$

C.3 Honeycomb lattice

The honeycomb lattice can be expressed as the sum of two triangular lattices with a $\sqrt{3}$ times larger spacing. One of the triangular lattices needs to be shifted. A possible choice for this shift is $(0, -d)^\top$. Using the results from the preceding subsection the plane wave expansion coefficients can be deduced

$$v_{\mathbf{q}_{ln}} = -V_{0\perp} \frac{\pi w_{0\perp}^2}{3\sqrt{3}d^2} e^{-\frac{w_{0\perp}^2 \kappa^2}{18}(l^2+n^2+ln)} (1 + e^{2\pi i(n-l)/3}). \quad (\text{C.16})$$

Again the lattice momentum vector is expressed as the sum of multiples of the reciprocal basis vectors

$$\mathbf{q}_{ln} = l\mathbf{b}_1 + n\mathbf{b}_2, \quad \mathbf{b}_1 = \kappa \begin{pmatrix} 2/3 \\ 0 \end{pmatrix}, \quad \mathbf{b}_2 = \frac{\kappa}{3} \begin{pmatrix} 1 \\ \sqrt{3} \end{pmatrix}, \quad (\text{C.17})$$

and the corresponding primitive lattice vectors are given by

$$\mathbf{a}_1 = \frac{d}{2} \begin{pmatrix} 3 \\ -\sqrt{3} \end{pmatrix}, \quad \mathbf{a}_2 = d \begin{pmatrix} 0 \\ \sqrt{3} \end{pmatrix}. \quad (\text{C.18})$$

Appendix D

Variational calculation for the two-dimensional Gaussian well

In this appendix, a Gaussian wave function ansatz of the form

$$\varphi(x, y) = \frac{1}{\sqrt{\pi}a_{\perp}} \exp\left(-\frac{x^2 + y^2}{2a_{\perp}^2}\right) \quad (\text{D.1})$$

is used to approximate the ground state wave function of a two-dimensional Gaussian potential well. The position representation of the corresponding single-particle Hamilton operator is given by

$$H_{2D} = -\frac{\hbar^2}{2m}(\partial_x^2 + \partial_y^2) + V_{0\perp} \exp\left(-2\frac{x^2 + y^2}{w_{0\perp}^2}\right). \quad (\text{D.2})$$

Using equations (D.1) and (D.2) the energy functional can be evaluated

$$E[\varphi] = \iint \varphi(x, y) H_{2D} \varphi(x, y) dx dy = \frac{\hbar^2}{2ma_{\perp}^2} - V_{0\perp} \frac{w_{0\perp}^2}{w_{0\perp}^2 + 2a_{\perp}^2}. \quad (\text{D.3})$$

Minimizing the above expression with respect to the Gaussian width a_{\perp} yields

$$E[\varphi^{\min}] = -V_{0\perp} + \mathcal{E} \left(2\sqrt{\frac{V_{0\perp}}{\mathcal{E}}} - 1\right), \quad a_{\perp}^{\min} = \frac{w_{0\perp}}{\sqrt{2}} \left(\sqrt{\frac{V_{0\perp}}{\mathcal{E}}} - 1\right)^{-1/2} \quad (\text{D.4})$$

Here, the energy scale $\mathcal{E} = \hbar^2/(mw_{0\perp}^2)$ of the Gaussian well is introduced. A similar calculation for a one-dimensional Gaussian well is presented in [177]. Using the relation $\mathcal{E}/\mathcal{E} = 2\pi^2w_{0\perp}^2/d^2$, the equation (5.22) is obtained. The above results can be compared to the harmonic oscillator approximation with

$$E^{\text{ho}} = -V_{0\perp} + 2\mathcal{E}\sqrt{\frac{V_{0\perp}}{\mathcal{E}}}, \quad a_{\perp}^{\text{ho}} = \frac{w_{0\perp}}{\sqrt{2}} \left(\frac{V_{0\perp}}{\mathcal{E}}\right)^{-1/4}. \quad (\text{D.5})$$

Appendix E

Details of the instanton calculation

The aim of this appendix is to provide details about the calculation of the transition matrix elements appearing in equation (5.28) using the instanton method. Starting point is the path integral given by

$$\langle \mathbf{r}_2 | e^{-\hat{H}\mathcal{T}/\hbar} | \mathbf{r}_1 \rangle = \mathcal{N} \int e^{-S_E[\gamma]/\hbar} \mathcal{D}\gamma. \quad (\text{E.1})$$

The Euclidean action for the path γ can be written as

$$S_E(\gamma) = \int_{-\mathcal{T}/2}^{\mathcal{T}/2} \left\{ \frac{m}{2} \dot{\gamma}^2(t) + V[\gamma(t)] \right\} dt, \quad (\text{E.2})$$

with the duration \mathcal{T} , the potential V , and the particle mass m . The next step is to apply the method of steepest decent. Let Γ be the path solving the classical equation of motion

$$m\ddot{\Gamma}(t) = (\nabla V)|_{\Gamma(t)} \quad (\text{E.3})$$

in the sign-flipped potential with $\Gamma(-\mathcal{T}/2) = \mathbf{r}_1$ and $\Gamma(\mathcal{T}/2) = \mathbf{r}_2$. Then in the semiclassical limit, only paths in the neighborhood of Γ contribute to the path integral. Writing $\gamma = \Gamma + \delta\gamma$ and expanding $S_E(\gamma)$ to second order in $\delta\gamma$ yields [191]

$$S_E(\Gamma + \delta\gamma) = S_E(\Gamma) + \frac{1}{2} \int_{-\mathcal{T}/2}^{\mathcal{T}/2} \left[-m\partial_\tau^2 \delta\gamma + \text{Hess}V \delta\gamma \right] \delta\gamma d\tau + \mathcal{O}(\delta\gamma^3). \quad (\text{E.4})$$

To improve readability, the function arguments in the above integrand have been suppressed. The paths Γ and $\delta\gamma$ are evaluated at τ , whereas the Hessian matrix $\text{Hess}V$ of the potential V is evaluated at $\Gamma(\tau)$. It is worth noting that the linear contribution in $\delta\gamma$ vanishes since Γ is a solution to the Euler-Lagrange equation. Using equations (E.1) and (E.4) and carrying out the resulting Gaussian path integral yields

$$\langle \mathbf{r}_2 | e^{-\hat{H}\mathcal{T}/\hbar} | \mathbf{r}_1 \rangle = \frac{\mathcal{N} e^{-S_0/\hbar}}{\sqrt{\det(-m\partial_\tau^2 + \text{Hess}V)}}. \quad (\text{E.5})$$

To compute the tunneling splitting using equation (5.28), the cases $\mathbf{r}_1 = \mathbf{r}_-$ and $\mathbf{r}_2 = \mathbf{r}_\pm$ need to be considered. In addition, the limit $\mathcal{T} \rightarrow \infty$ needs to be performed. This induces two complications. First, there are multiple paths solving the classical equation of motion and obeying $\Gamma(-\infty) = \mathbf{r}_-$ and $\Gamma(\infty) = \mathbf{r}_\pm$. These paths can be constructed by concatenating instantons and anti-instantons. To compute the path integral, the contributions of all these paths need to be summed. Second, due to the time-translation invariance

the operator $-m\partial_\tau^2 + \text{Hess}V$ has an eigenvalue equal to zero which results in a diverging expression in equation (E.5). A detailed analysis of these technical challenges is beyond the scope of this appendix. Therefore, the interested reader is referred to [191], where it is shown that the pre-exponential factor of the tunneling splitting (cf. equation (5.28)) can be expressed as the product $\mathcal{A} = \mathcal{A}_1\mathcal{A}_2$ with

$$\mathcal{A}_1 = \sqrt{\frac{2S_0}{\pi}} \sqrt{\frac{\det(-\partial_\tau^2 + \omega_0^2)}{\det'(-\partial_\tau^2 + \omega^2(\tau))}}, \quad \mathcal{A}_2 = \sqrt{\frac{\det(-\partial_\tau^2 + \Omega_0^2)}{\det(-\partial_\tau^2 + \Omega^2(\tau))}}. \quad (\text{E.6})$$

In the above equations, $\omega(\tau)$ is the frequency associated to the curvature of the potential in the direction of the instanton's tangential vector and ω_0 is the respective frequency at the \mathbf{r}_\pm . The matrix $\Omega(\tau)$ quantifies the frequencies for the directions orthogonal to the instanton's tangential vector and Ω_0 is the respective matrix at \mathbf{r}_\pm . The prime at the determinant in the expression for \mathcal{A}_1 indicates that the lowest eigenvalue is excluded. The procedure for the calculation of the determinants in equation (E.6) is based on their connection to Jacobi fields [186, 285] and is described in detail in [191]. Here it shall suffice to provide the result of these considerations, i. e. the expressions used for the actual calculation

$$\mathcal{A}_1 = \sqrt{\frac{\omega_0 p_0^2}{\pi}} \exp \left[\int_{-\infty}^0 \left(\omega_0 - \frac{\partial_s p}{m} \Big|_\tau \right) d\tau \right], \quad (\text{E.7})$$

$$\mathcal{A}_2 = \sqrt{\frac{\det \Omega_0}{\det \Xi(0)}} \exp \left[\int_{-\infty}^0 \text{Tr} \{ \Omega_0 - \Xi(\tau) \} d\tau \right]. \quad (\text{E.8})$$

In the equations above ∂_s is the spatial derivative along the instanton, $p = \sqrt{-2mV}$ is the semiclassical momentum and p_0 is this momentum at $\tau = 0$. The instanton \mathcal{I} is chosen to obey $\mathcal{I}(0) = (\mathbf{r}_+ + \mathbf{r}_-)/2$ and $\mathcal{I}(\pm\infty) = \mathbf{r}_\pm$. Further, the matrix Ξ obeys the differential equation

$$\dot{\Xi}(\tau) + \Xi^2(\tau) = \Omega^2(\tau), \quad (\text{E.9})$$

with $\Xi(-\infty) = \Omega_0$. The required steps for a computation of the pre-exponential factor \mathcal{A} can be summarized in the following way:

- (I) Calculate the instanton \mathcal{I} , i. e. the solution of the classical equation of motion in the sign-flipped potential (cf. equation (E.3)) obeying $\mathcal{I}(0) = (\mathbf{r}_+ + \mathbf{r}_-)/2$ and $\mathcal{I}(\pm\mathcal{T}/2) = \mathbf{r}_\pm$ for $\mathcal{T} \rightarrow \infty$.
- (II) Calculate \mathcal{A}_1 with equation (E.7) using the instanton \mathcal{I} , the definition of the semiclassical momentum p and the oscillator frequency ω_0 in the direction of the instanton's tangential vector at \mathbf{r}_\pm .
- (III) Determine the transverse part of the potential's oscillator frequency matrix $\Omega(\tau)$ along the instanton trajectory to obtain $\Xi(\tau)$ by solving equation (E.9).
- (IV) Use the expression for $\Xi(\tau)$ to calculate \mathcal{A}_2 using equation (E.8).

In the following, this formalism is used to determine the tunneling parameter between adjacent sites, $\mathbf{r}_- = (0, 0)$ and $\mathbf{r}_+ = (2\pi, 0)$, in a square array of 2D Gaussian wells (cf. section 5.2.2). For this task the dimensionless coordinates defined in equation (5.31) are used. The calculation of \tilde{S}_0 is already discussed in subsection 5.2.2. It remains to determine the pre-exponential factor $\tilde{\mathcal{A}}$.

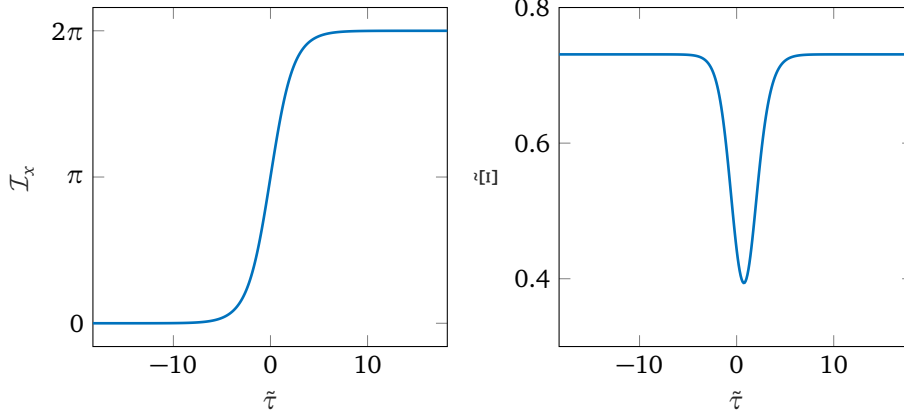


Figure E.1: The dimensionless x -component of the instanton \mathcal{I}_x (left) and the quantity $\tilde{\Xi}$ (right) are plotted versus the dimensionless imaginary time $\tilde{\tau}$ for $\xi = 0.298$ and $\tilde{T} = 16.6$.

Step (I), i. e. the numerical calculation of the instanton $\mathcal{I} = (\mathcal{I}_x, \mathcal{I}_y)$, is straight forward. From the symmetry of the potential \tilde{V} (cf. equation (5.33)) follows $\mathcal{I}_y(\tilde{\tau}) = 0$. The x -component can be determined by solving

$$\partial_{\tilde{\tau}}^2 \mathcal{I}_x(\tilde{\tau}) = -\frac{\xi}{2} \vartheta_3' \left(-\frac{\mathcal{I}_x(\tilde{\tau})}{2}, e^{-\pi\xi} \right) \vartheta_3(0, e^{-\pi\xi}), \quad (\text{E.10})$$

with $\mathcal{I}_x(-\tilde{T}/2) = 0$ and $\mathcal{I}_x(0) = \pi$. ϑ_3' denotes the derivative of ϑ_3 with respect to its first argument. To approximate the infinite time limit, the constant \tilde{T} needs to be chosen sufficiently large.

To perform step (II), i. e. the computation of $\tilde{\mathcal{A}}_1$, explicit expressions for $\tilde{p}(\tilde{x})$ and $\tilde{\omega}_0$ are required. These can be obtained by using the expression for \tilde{V} given in equation (5.33) yielding

$$\tilde{p}(\tilde{x}) = \sqrt{2\xi \vartheta_3 \left(-\frac{\tilde{x}}{2}, e^{-\pi\xi} \right) \vartheta_3(0, e^{-\pi\xi}) - 2\xi \vartheta_3^2(0, e^{-\pi\xi})}, \quad (\text{E.11})$$

$$\tilde{\omega}_0 = \frac{1}{2} \sqrt{-\xi \vartheta_3''(0, e^{-\pi\xi}) \vartheta_3(0, e^{-\pi\xi})}. \quad (\text{E.12})$$

The above expressions in combination with the instanton \mathcal{I} allow to compute the right hand side of equation (E.7).

For step (III) $\tilde{\Omega}$ needs to be determined. Because the considered problem is two-dimensional, there is only one direction transverse to the instanton's tangential vector, the y -direction. Therefore, $\tilde{\Omega}(\tilde{\tau})$ and $\tilde{\Xi}(\tilde{\tau})$ are scalar functions. The latter can be determined from

$$\dot{\tilde{\Xi}}(\tilde{\tau}) + \tilde{\Xi}^2(\tilde{\tau}) = \frac{1}{2} \sqrt{-\xi \vartheta_3''(0, e^{-\pi\xi}) \vartheta_3 \left(\frac{\mathcal{I}(\tilde{\tau})}{2}, e^{-\pi\xi} \right)}, \quad (\text{E.13})$$

$$\tilde{\Xi}(-\tilde{T}/2) = \frac{1}{2} \sqrt{-\xi \vartheta_3''(0, e^{-\pi\xi}) \vartheta_3(0, e^{-\pi\xi})}. \quad (\text{E.14})$$

For the final step (IV) the integral in equation (E.8) is computed numerically using the solution of the above equations. The parameters considered in chapter 5 (cf. table 5.1) result in $\xi = 0.298$. For this case the functions \mathcal{I} and $\tilde{\Xi}$ are shown in figure E.1 and the following parameters are obtained $\tilde{S}_0 = 5.44$ and $\tilde{\mathcal{A}} = 2.85$.

Appendix F

Thermodynamics of the Mott insulator

In this appendix, expressions for the energy $E(T)$ and the entropy $S(T)$ of the Bose-Hubbard model in the Mott-insulator phase are derived. The results are used in section 6.1.3 to estimate the temperature and entropy after state preparation.

In the Mott-insulator phase the lowest energetic excitations are particle-hole pairs (cf. section 3.2.3). For sufficiently low temperatures, these can be treated as an ideal gas of bosonic quasi particles. This allows to compute the grand canonical partition function

$$\mathcal{Z} = \sum_m e^{-\beta(E_m - \mu N_m)}. \quad (\text{F.1})$$

Here, the index m labels the eigenstates of the Hamilton operator, whereas E_m and N_m are the corresponding energies and particle numbers. The partition function is directly related to the grand canonical potential

$$\Omega = -k_B T \ln \mathcal{Z}, \quad (\text{F.2})$$

from which all thermodynamic quantities can be derived. This approach was used in [75] and is summarized in the following.

It is advantageous to split Ω into contributions from local excitations Ω_0 as well as propagating quasi particles $\Delta\Omega_p$ and holes $\Delta\Omega_h$. For the calculation of Ω_0 the eigenstates and energies of \hat{H}_U need to be considered. The former are products of local number states (cf. section 3.2.3). By restricting the Hilbert space to local occupation numbers of $n-1$, n , and $n+1$, Ω_0 can be calculated [286]

$$\Omega_0 = -\frac{M}{\beta} \ln \left(e^{-\beta[\frac{U}{2}n(n-1)/2 - \mu n]} + e^{-\beta[\frac{U}{2}(n+1)n - \mu(n+1)]} + e^{-\beta[\frac{U}{2}(n-1)(n-2) - \mu(n-1)]} \right) \quad (\text{F.3})$$

$$= M \left[\frac{U}{2}n(n-1) - \mu n \right] - \frac{M}{\beta} \ln \left(1 + e^{\beta(\mu - Un)} + e^{\beta[U(n-1) - \mu]} \right). \quad (\text{F.4})$$

In order to calculate $\Delta\Omega_p$ and $\Delta\Omega_h$, quasi particles and holes are treated as ideal Bose gases which is valid for low temperatures, i. e. $k_B T \ll U$. This yields

$$\Delta\Omega_p = \frac{1}{\beta} \sum_k \left[\ln \left(1 - e^{-\beta(E_k^p - \mu)} \right) - \ln \left(1 - e^{-\beta(U(n-\mu))} \right) \right] \quad (\text{F.5})$$

$$\Delta\Omega_h = \frac{1}{\beta} \sum_k \left[\ln \left(1 - e^{-\beta(\mu - E_k^h)} \right) - \ln \left(1 - e^{-\beta(\mu - U(n-1))} \right) \right] \quad (\text{F.6})$$

with $E_k^{p/h}$ being the dispersion relations for quasi particles and holes respectively. The second terms are subtracted because they are already included in Ω_0 . The dispersion

relation for quasi particles and holes was derived in [70, 287]. For finite temperatures and to first order in J/U one arrives at

$$E_k^p = Un + (n+1)\frac{1-b_+}{z_0}\epsilon_k, \quad E_k^h = U(n-1) - n\frac{1-b_-}{z_0}\epsilon_k \quad (\text{F.7})$$

with

$$z_0 = 1 + b_+ + b_-, \quad b_+ = e^{\beta(\mu - Un)}, \quad b_- = e^{\beta[U(n-1) - \mu]}, \quad (\text{F.8})$$

and the single particle dispersion relation ϵ_k . For D -dimensional cubic lattices in the tight-binding regime ϵ_k is given in equation (3.14). Using this expression and expanding the logarithm according to $\ln(1-x) = -\sum_{m=1}^{\infty} x^m/m$, the quasi particle contribution to the grand canonical potential can be calculated

$$\Delta\Omega_p = -\frac{1}{\beta} \sum_k \sum_{m=1}^{\infty} \frac{e^{-m\beta(Un-\mu)}}{m} \left[\exp\left(-2m\beta J \frac{1-b_+}{z_0} \sum_{i=1}^D \cos(k_i d)\right) - 1 \right] \quad (\text{F.9})$$

$$= -\frac{M}{\beta} \sum_{m=1}^{\infty} \frac{e^{-m\beta(Un-\mu)} d^D}{m(2\pi)^D} \int \left[\exp\left(-2m\beta J \frac{1-b_+}{z_0} \sum_{i=1}^D \cos(k_i d)\right) - 1 \right] d^D k \quad (\text{F.10})$$

$$= -\frac{M}{\beta} \sum_{m=1}^{\infty} \frac{e^{-m\beta(Un-\mu)}}{m} \left[\prod_{i=1}^D \int_{-\pi}^{\pi} \exp\left(-2m\beta J \frac{1-b_+}{z_0} \cos q_i\right) \frac{dq_i}{2\pi} - 1 \right] \quad (\text{F.11})$$

$$= -\frac{M}{\beta} \sum_{m=1}^{\infty} \frac{e^{-m\beta(Un-\mu)}}{m} \left[I_0^D\left(2m\beta J \frac{1-b_+}{z_0}\right) - 1 \right]. \quad (\text{F.12})$$

Here the modified Bessel function I_0 has been used [47]. An analogous calculation yields

$$\Delta\Omega_h = -\frac{M}{\beta} \sum_{m=1}^{\infty} \frac{e^{-m\beta(\mu - U(n-1))}}{m} \left[I_0^D\left(2m\beta J \frac{1-b_-}{z_0}\right) - 1 \right]. \quad (\text{F.13})$$

From equations (F.4), (F.12), and (F.13) particle number, entropy and energy can be derived using the thermodynamic relation

$$N = -\frac{\partial\Omega}{\partial\mu}, \quad S = -\frac{\partial\Omega}{\partial T}, \quad E = \Omega + N\mu + TS. \quad (\text{F.14})$$

It is worth noting that μ is fixed by demanding $N = nM$. Figure F.1 shows the energy and entropy for $n = 1$, $U/J = 40$, and a cubic lattice. The fact that both entropy and energy are approximately constant for low temperatures is caused by the energy gap between the ground state and the lowest-energetic excited states.

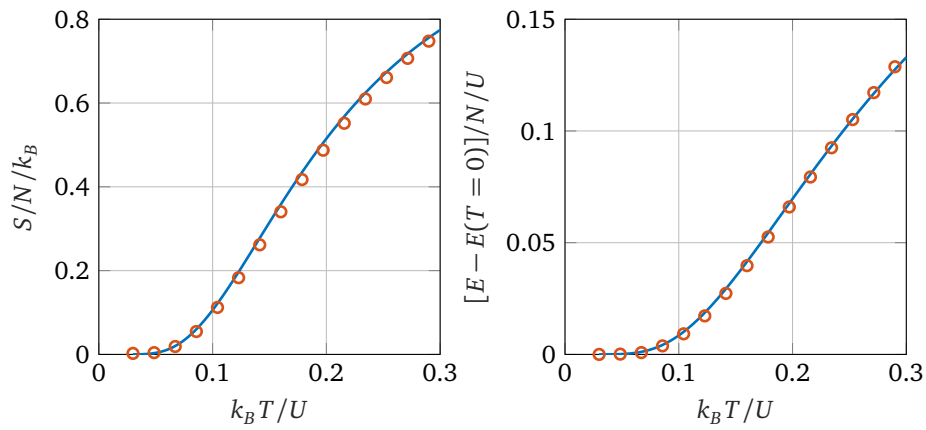


Figure F.1: Entropy (left subfigure) and Energy (right subfigure) per particle are plotted versus temperature for the Bose-Hubbard model on a cubic lattice with unit filling $N/M = 1$ and $U/J = 40$. The blue lines are obtained using equations (F.4), (F.12), (F.13), and (F.14). The orange circles are the result of a quantum Monte Carlo calculation taken from [86].

Appendix G

Minimization of the adiabatic error measures

In this appendix, it is shown that for the situation considered in section 6.2.4, the solution to the Euler-Lagrange equation minimizes the adiabatic error measures \mathbb{E}_1 and \mathbb{E}_∞ . The considered situation can be summarized in the following way. In the time interval $[0, \tau]$ the system is controlled by a one-dimensional and monotonically decreasing parameter curve $\gamma(t)$ with $\gamma(0) = \gamma_i$ and $\gamma(\tau) = \gamma_f$. The Lagrange function

$$\mathcal{L}(\gamma, \dot{\gamma}) = \frac{1}{2} \mathcal{M}(\gamma) \dot{\gamma}^2 \quad (\text{G.1})$$

is convex and the mass function $\mathcal{M}(\gamma)$ is sufficiently smooth, monotonically decreasing, and positive. Under these conditions the following proposition can be stated.

Proposition. The parameter curve $\gamma_0(t)$ is a minimum of the functionals $\mathbb{E}_1[\gamma, \dot{\gamma}]$ and $\mathbb{E}_\infty[\gamma, \dot{\gamma}]$, if $\gamma_0(t)$ satisfies the corresponding Euler-Lagrange equation.

Proof. The fact that $\gamma_0(t)$ is a minimum of $\mathbb{E}_1[\gamma, \dot{\gamma}]$ follows from the convexity of the Lagrange function [288]. In order to proof that $\gamma_0(t)$ is a minimum of $\mathbb{E}_\infty[\gamma, \dot{\gamma}]$ the following intermediate steps are used.

- I $\mathcal{L}(\gamma_0(t), \dot{\gamma}_0(t))$ is constant for $t \in [0, \tau]$.
- II $\gamma_0(t)$ minimizes the functional $\max_t \sqrt{\mathcal{L}(\gamma, \dot{\gamma})}$.

Using the fact that γ_0 satisfies the Euler-Lagrange equation, it is straight forward to show I,

$$\frac{d}{dt} \mathcal{L}(\gamma_0(t), \dot{\gamma}_0(t)) = \mathcal{M}(\gamma_0) \dot{\gamma}_0 \ddot{\gamma}_0 + \frac{\dot{\gamma}_0^3}{2} \frac{\partial \mathcal{M}}{\partial \gamma} \Big|_{\gamma=\gamma_0} = \dot{\gamma}_0 \left(\frac{d}{dt} \frac{\partial \mathcal{L}}{\partial \dot{\gamma}} - \frac{\partial \mathcal{L}}{\partial \gamma} \right) \Big|_{\gamma=\gamma_0} = 0. \quad (\text{G.2})$$

In order to prove the implication I \Rightarrow II the following observation is helpful. The integral $\int_0^\tau \sqrt{\mathcal{L}} dt$ is the same for all admissible parameter curves. This is shown in the following calculation

$$\int_0^\tau \sqrt{\mathcal{L}(\gamma(t), \dot{\gamma}(t))} dt = - \int_0^\tau \dot{\gamma}(t) \sqrt{\frac{1}{2} \mathcal{M}(\gamma(t))} dt = - \int_{\gamma_i}^{\gamma_f} \sqrt{\frac{1}{2} \mathcal{M}(\gamma)} d\gamma. \quad (\text{G.3})$$

Therefore, the parameter curve that provides a constant $\sqrt{\mathcal{L}}$ or equivalently a constant \mathcal{L} , i. e. γ_0 , minimizes the functional $\max_t \sqrt{\mathcal{L}(\gamma, \dot{\gamma})}$. This proofs the implication I \Rightarrow II. It is apparent that II implies that $\gamma_0(t)$ is a minimum of $\mathbb{E}_\infty[\gamma, \dot{\gamma}]$ since the function $x \mapsto x^2$ is monotonically increasing for $x > 0$. \square

Appendix H

Solving the Bose-Hubbard model numerically

In this appendix, an exact numerical approach to the solution of the Bose-Hubbard model is discussed following the presentations in [105, 289, 290]. This approach is based on the matrix representation of the Hamilton operator with respect to the number state basis (cf. equation (3.32)) and described in section H.1. By diagonalizing the Hamilton matrix the spectrum and the corresponding eigenstates of the Bose-Hubbard model can be computed. This is the topic of section H.2. In section H.3, the numerical solution of the time-dependent Schrödinger equation is discussed.

H.1 Matrix representation of the Hamilton operator

The set of number states defined in equation (3.32) is an orthonormal basis for the Hilbert space \mathcal{H} of the Bose-Hubbard model with M sites and fixed particle number N . Therefore, a state $|\psi\rangle$ can be expanded in the following way

$$|\psi\rangle = \sum_{\mathbf{n} \in \mathcal{N}} \psi_{\mathbf{n}} |\mathbf{n}\rangle, \quad \psi_{\mathbf{n}} = \langle \mathbf{n} | \psi \rangle \in \mathbb{C}. \quad (\text{H.1})$$

This allows to determine the dimension of \mathcal{H} , i. e.

$$\dim(\mathcal{H}) = \binom{N+M-1}{N} = \frac{(N+M-1)!}{N!(M-1)!}, \quad (\text{H.2})$$

since the number of basis vectors is given by the number of ways N identical particles can be distributed among M sites. The above equation reveals a major difficulty in quantum many-body physics, i. e. the fast growth of the Hilbert space's dimension with system size. In figure H.1 the required memory for the storage of a state vector and the full matrix representation of an operator is plotted versus the system size for unit filling $N = M$. If most matrix elements of an operator are zero, then it is more efficient to store only the non-zero matrix elements together with the respective indices. This is called sparse matrix representation and significantly reduces the required memory to store the Hamilton matrix (cf. yellow line in figure H.1). The reason for this is that only on-site interaction and nearest-neighbor hopping are considered in the Bose-Hubbard model.

To compute the matrix representation of the Hamilton operator, the set of number states needs to be ordered. Lexicographical ordering provides an efficient scheme for this purpose. Here, a state $|\mathbf{n}\rangle$ is listed before a different state $|\mathbf{n}'\rangle$ if $n_i > n'_i$, with i being the lowest index for which the components of the two states differ. A procedure to generate all basis states in this order is described in [289]. It remains to compute the matrix elements $\langle \mathbf{n} | \hat{H} | \mathbf{n}' \rangle$. In the following the inhomogeneous Bose-Hubbard model is

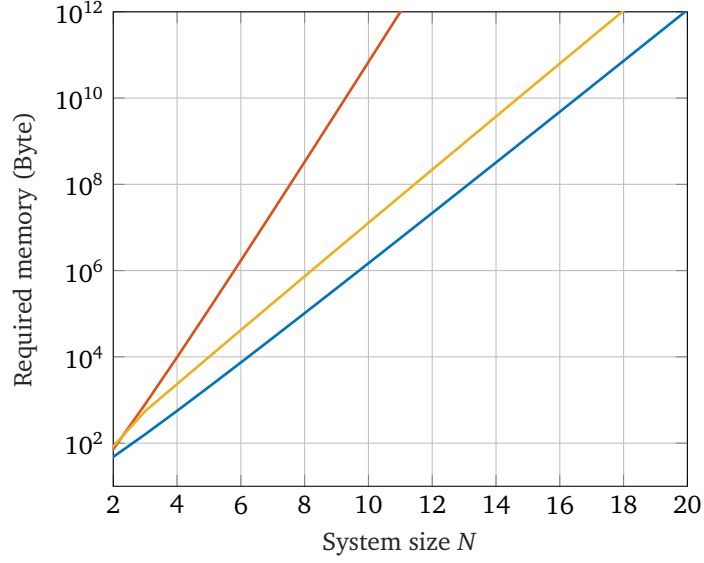


Figure H.1: The memory requirement is plotted versus the system size N for the Bose-Hubbard model with unit filling $N = M$. The blue line corresponds to the storage of a state vector, i. e. the complex coefficients ψ_n , whereas the orange and yellow lines correspond to the storage of the full and sparse matrix representation of the Hamilton operator. Here, a 1D Bose-Hubbard model with periodic boundary conditions is assumed. For all graphs it is assumed that real numbers are stored in the 64 Bit floating-point format. The row and column indices for the sparse matrix are stored as 16 Bit integers.

considered with the Hamilton operator

$$\hat{H} = - \sum_{i,j=1}^M J_{ij} \hat{a}_i^\dagger \hat{a}_j + \frac{1}{2} \sum_{i=1}^M U_i \hat{a}_i^\dagger \hat{a}_i^\dagger \hat{a}_i \hat{a}_i + \sum_{i=1}^M \epsilon_i \hat{a}_i^\dagger \hat{a}_i. \quad (\text{H.3})$$

Here, J is a symmetric $M \times M$ matrix with zeros on its diagonal. The off-diagonal entries encode the tunneling strength between the respective sites. It can be interpreted as the adjacency matrix of the graph which determines the lattice geometry. The components of U and ϵ are the local on-site interaction strengths and energy offsets. The matrix elements associated to the local terms in equation (H.3) lie on the diagonal and can be computed from

$$\frac{U_i}{2} \langle \mathbf{n} | \hat{a}_i^\dagger \hat{a}_i^\dagger \hat{a}_i \hat{a}_i | \mathbf{n}' \rangle = \frac{U_i}{2} n_i (n_i - 1) \delta_{\mathbf{n}\mathbf{n}'}, \quad \epsilon_i \langle \mathbf{n} | \hat{a}_i^\dagger \hat{a}_i | \mathbf{n}' \rangle = \epsilon_i n_i \delta_{\mathbf{n}\mathbf{n}'}. \quad (\text{H.4})$$

The matrix elements corresponding to the tunneling term are given by

$$J_{ij} \langle \mathbf{n} | \hat{a}_i^\dagger \hat{a}_j | \mathbf{n}' \rangle = J_{ij} \sqrt{n_i (n_j + 1)} \delta_{n_i, n'_i + 1} \delta_{n_j, n'_j - 1} \prod_{k \neq i, j} \delta_{n_k, n'_k}. \quad (\text{H.5})$$

To find the non-zero off-diagonal matrix elements efficiently a hashing technique can be used [289]. This allows to determine the position of a state $|\mathbf{n}\rangle$ in the ordered basis without searching the corresponding list.

The structure of the Hamilton operator's matrix representation for a 1D Bose-Hubbard model with periodic boundary conditions is shown in figure H.2. Here, a system size of $M = N = 6$ is considered which results in a Hilbert space dimension of 462.

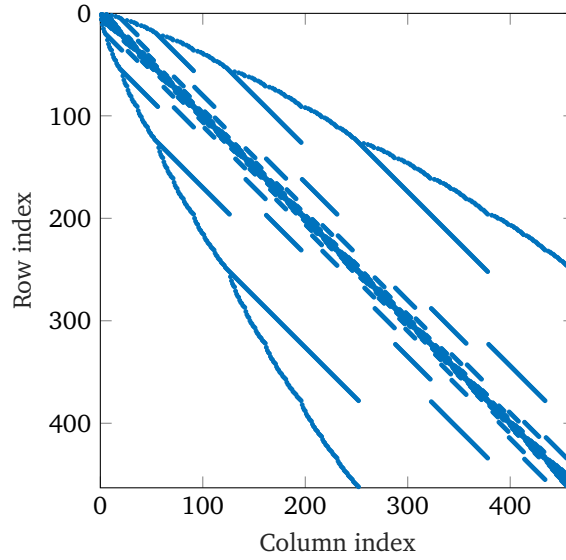


Figure H.2: Structure of the Hamilton operator's matrix representation for a 1D Bose-Hubbard model with periodic boundary conditions and $M = N = 6$. The non-zero matrix elements are indicated with blue dots.

H.2 Diagonalization of the Hamilton matrix

The Hamilton operator's matrix representation can be diagonalized using standard numerical algorithms. This yields all energy eigenvalues and the associated eigenstates. In figure H.3 the spectrum of a 1D Bose-Hubbard model with periodic boundary conditions and $M = N = 6$ is shown for a range of interaction strengths.

For large system sizes, the full diagonalization of the Hamilton matrix becomes computationally expensive, because the Hilbert space dimension gets very large. In addition, most of the time the prime interest is focused on the lowest energetic states. These can be determined efficiently by using the Lanczos algorithm [194] that is based on the concept of Krylov spaces [193, 195]. An implementation of this algorithm is provided by the software library *Lapack* [291].

H.3 Solution of the time-dependent Schrödinger equation

To compute the time evolution of the many-body state $|\psi(t)\rangle$, the time-dependent Schrödinger equation

$$i\hbar \frac{d}{dt} |\psi(t)\rangle = \hat{H}(t) |\psi(t)\rangle \quad (\text{H.6})$$

needs to be solved. If the Hamilton operator is constant in time then the solution of the above equation for an initial state $|\psi(t_0)\rangle$ is given by

$$|\psi(t)\rangle = \exp\left[-\frac{i}{\hbar} \hat{H}(t - t_0)\right] |\psi(t_0)\rangle. \quad (\text{H.7})$$

This can be computed numerically by using the Hamilton operator's matrix representation discussed in section H.1 and standard techniques for the calculation of a matrix exponential. However, similar to the problem of matrix diagonalization this task becomes computationally expensive with increasing system size. Therefore, it is advantageous to use a Krylov space method to compute the product of the matrix exponential and the

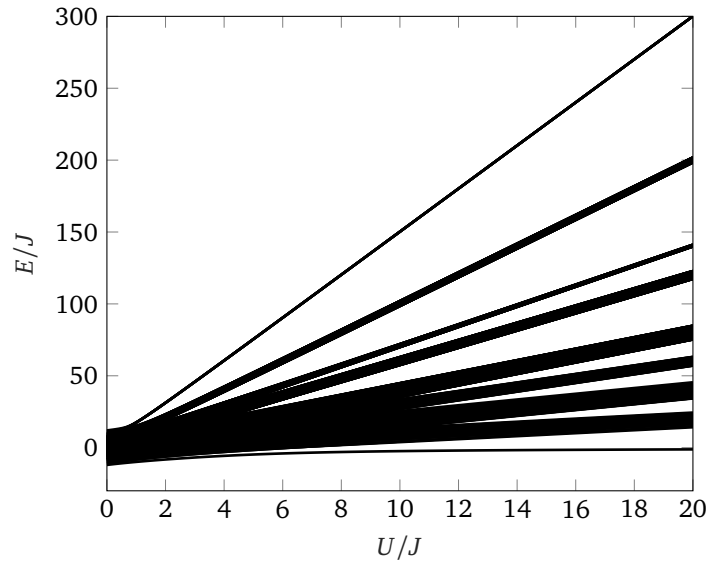


Figure H.3: The energy spectrum of the 1D Bose-Hubbard model with periodic boundary conditions and $M = N = 6$ is plotted versus the ratio U/J .

initial state [292–294]. This approach is implemented in the software package *Expokit* [295] and used for the calculations in chapter 7

For a time-dependent Hamilton operator the Schrödinger equation, given in equation (H.6), can be transformed into a system of coupled, linear, ordinary differential equations for the state's components ψ_n . For the calculations in section 6.2.4, this approach is used. The resulting system of differential equations is solved numerically with the built-in function *ode45* from MATLAB that implements a Runge-Kutta method. It is worth noting that if the Wannier functions are time-dependent, then this is also true for the Fock basis. This causes additional terms in the dynamical equations for the state's components (cf. section 6.2 and [219, 231]).

Appendix I

Two-mode approximation

In this appendix, the effective two-sited Bose-Hubbard Hamilton operator \hat{H}_0 given in equation (7.7) is derived. Using the definition of the projection operator $\hat{\mathcal{P}}$ this task can be reduced to the evaluation of matrix elements of the form $\langle m | \hat{H}_0 | n \rangle$, i. e.

$$\hat{H}_0 = \hat{\mathcal{P}} \hat{H} \hat{\mathcal{P}} = \sum_{m,n=0}^N |m\rangle \langle m| \hat{H} |n\rangle \langle n|. \quad (\text{I.1})$$

For the inter-ring tunneling term this is straight because the state $|n\rangle$ is a product of the corresponding eigenstates

$$-J \sum_{\langle ij \rangle} \langle m | \hat{a}_i^\dagger \hat{a}_j | n \rangle = -2Jn \delta_{mn}, \quad (\text{I.2})$$

$$-J \sum_{\langle ij \rangle} \langle m | \hat{b}_i^\dagger \hat{b}_j | n \rangle = -2J(N-n) \delta_{mn}. \quad (\text{I.3})$$

In order to evaluate the matrix elements of the interaction part of the Hamilton operator the following calculation is helpful

$$\langle n | \hat{a}_i^\dagger \hat{a}_i^\dagger \hat{a}_i \hat{a}_i | n \rangle = \frac{1}{n!(N-n)!} \langle \text{vac} | \hat{\alpha}_0^n \hat{\beta}_0^{N-n} \hat{a}_i^\dagger \hat{a}_i^\dagger \hat{a}_i \hat{a}_i \hat{\alpha}_0^{\dagger n} \hat{\beta}_0^{\dagger N-n} | \text{vac} \rangle \quad (\text{I.4})$$

$$= \frac{1}{n!(N-n)!} \langle \text{vac} | [\hat{\alpha}_0^n, \hat{a}_i^\dagger \hat{a}_i^\dagger] \hat{\beta}_0^{N-n} [\hat{a}_i \hat{a}_i, \hat{\alpha}_0^{\dagger n}] \hat{\beta}_0^{\dagger N-n} | \text{vac} \rangle \quad (\text{I.5})$$

$$= \frac{n^2(n-1)^2}{n!(N-n)!M^2} \langle \text{vac} | \hat{\alpha}_0^{n-2} \hat{\beta}_0^{N-n} \hat{\alpha}_0^{\dagger n-2} \hat{\beta}_0^{\dagger N-n} | \text{vac} \rangle \quad (\text{I.6})$$

$$= \frac{n(n-1)}{M^2}. \quad (\text{I.7})$$

For the above calculation, the definition of $\hat{\alpha}_0$ given in equation (7.4) and the commutator rules

$$[\hat{A}\hat{B}, \hat{C}] = \hat{A}[\hat{B}, \hat{C}] + [\hat{A}, \hat{C}]\hat{B}, \quad [\hat{A}, \hat{B}^n] = n[\hat{A}, \hat{B}]\hat{B}^{n-1}, \quad (\text{I.8})$$

have been used. Here, it is assumed that $[\hat{A}, \hat{B}]$ commutes with \hat{A} and \hat{B} . Using equation (I.7), the analogue expression for ring B, and the fact that the interaction terms do not couple states with different atom distributions between the rings, the interaction matrix

elements can be evaluated to

$$\frac{U}{2} \sum_{i=0}^{M-1} \langle m | \hat{a}_i^\dagger \hat{a}_i^\dagger \hat{a}_i \hat{a}_i | n \rangle = \frac{Un(n-1)}{2M} \delta_{mn}, \quad (\text{I.9})$$

$$\frac{U}{2} \sum_{i=0}^{M-1} \langle m | \hat{b}_i^\dagger \hat{b}_i^\dagger \hat{b}_i \hat{b}_i | n \rangle = \frac{U(N-n)(N-n-1)}{2M} \delta_{mn}. \quad (\text{I.10})$$

With an analogous calculation, the inter-ring tunneling matrix element can be determined

$$-K \langle m | \hat{a}_0^\dagger \hat{b}_0 + \hat{b}_0^\dagger \hat{a}_0 | n \rangle = -\frac{K}{M} \left(\delta_{m-1n} \sqrt{m(N-n)} + \delta_{mn-1} \sqrt{(N-m)n} \right). \quad (\text{I.11})$$

The effective Hamilton operator \hat{H}_0 can be constructed from the set $\{\hat{\alpha}_0, \hat{\alpha}_0^\dagger, \hat{\beta}_0, \hat{\beta}_0^\dagger\}$ by demanding

$$\langle m | \hat{H}_0 | n \rangle = \langle m | \hat{H} | n \rangle \quad \forall m, n. \quad (\text{I.12})$$

Using the results of the preceding calculations and the relations

$$\hat{\alpha}_0^\dagger \hat{\beta}_0 | n \rangle = \sqrt{(n+1)(N-n)} | n+1 \rangle, \quad (\text{I.13})$$

$$\hat{\beta}_0^\dagger \hat{\alpha}_0 | n \rangle = \sqrt{n(N-n-1)} | n-1 \rangle, \quad (\text{I.14})$$

$$\hat{\alpha}_0^\dagger \hat{\alpha}_0^\dagger \hat{\alpha}_0 \hat{\alpha}_0 | n \rangle = n(n-1) | n \rangle, \quad (\text{I.15})$$

$$\hat{\beta}_0^\dagger \hat{\beta}_0^\dagger \hat{\beta}_0 \hat{\beta}_0 | n \rangle = (N-n)(N-n-1) | n \rangle, \quad (\text{I.16})$$

this yields

$$\hat{H}_0 = -k(\hat{\alpha}_0^\dagger \hat{\beta}_0 + \hat{\beta}_0^\dagger \hat{\alpha}_0) + \frac{U}{2}(\hat{\alpha}_0^\dagger \hat{\alpha}_0^\dagger \hat{\alpha}_0 \hat{\alpha}_0 + \hat{\beta}_0^\dagger \hat{\beta}_0^\dagger \hat{\beta}_0 \hat{\beta}_0) - 2JN. \quad (\text{I.17})$$

Appendix J

Scattering on graphs

In this appendix, the operators $\hat{\mathcal{U}}$ are characterized for the basic one-qubit and two-qubit gates of the scheme discussed in section 8.2.

J.1 One-qubit gates

For one-qubit gates, the operators $\hat{\mathcal{U}}$ can be parametrized by

$$\hat{\mathcal{U}}(k) = \sum_{m,n=0}^1 \mathcal{U}_{mn}(k) |m, k\rangle\langle n, k|. \quad (\text{J.1})$$

Here, the coefficients $\mathcal{U}_{mn}(k)$ quantify the transmission from the incoming state $|n, k\rangle$ to the outgoing state $|m, k\rangle$ at quasimomentum k . In this description, reflections back into the lattices carrying the incoming atom are disregarded. Therefore, the operator $\hat{\mathcal{U}}$ is in general non-unitary. The coefficients $\mathcal{U}_{mn}(k)$ are obtained from the analysis of the corresponding scattering problem. A detailed description of this method can be found [257].

For the subgraph shown in figure 8.3 (a), one obtains

$$\mathcal{U}(k) = e^{ika} \begin{pmatrix} 1 & 0 \\ 0 & 1 \end{pmatrix} + \frac{1}{i \sin(ka) + i \sin(3ka) - 2 \cos(ka)} \begin{pmatrix} 1 & 1 \\ 1 & 1 \end{pmatrix}. \quad (\text{J.2})$$

At the momentum $k = \pi/(4a)$, this implements the basis changing gate, i. e.

$$\mathcal{U}\left(\frac{\pi}{4a}\right) = \frac{1}{\sqrt{2}} \begin{pmatrix} i & -1 \\ -1 & i \end{pmatrix}. \quad (\text{J.3})$$

The corresponding expressions for the subgraph shown in figure 8.3 (b) are given by

$$\mathcal{U}(k) = \begin{pmatrix} 1 & 0 \\ 0 & \xi(k) \end{pmatrix}, \quad \xi(k) = \frac{8e^{-ika}}{8 + i \cos(2ka) \csc^3(ka) \sec(ka)}. \quad (\text{J.4})$$

For $k = \pi/(4a)$ this yields $\xi(\pi/(4a)) = e^{-i\pi/4}$, as required for the phase gate.

J.2 Two-qubit gates

Two-qubit gates can be parameterized by

$$\hat{\mathcal{U}}(k, k') = \sum_{m,n,o,p=0}^1 \mathcal{U}_{mn}^{op}(k, k') |m, k\rangle |n, k'\rangle \langle o, k| \langle p, k'|. \quad (\text{J.5})$$

The matrix elements \mathcal{U}_{mn}^{op} are obtained from an analysis of the scattering of two interacting atoms on a lattice.

For the controlled phase gate considered in chapter 8, the two atoms scatter from each other if the upper qubit is in state $|1\rangle$ and the lower qubit is in state $|0\rangle$. Otherwise, the atoms propagate on separated line segments. Therefore, the matrix $\mathcal{U}(k, k')$ has the following form

$$\mathcal{U}(k, k') = \begin{pmatrix} 1 & 0 & 0 & 0 \\ 0 & 1 & 0 & 0 \\ 0 & 0 & f(k, k') & 0 \\ 0 & 0 & 0 & 1 \end{pmatrix}. \quad (\text{J.6})$$

Here, the computational basis states are ordered in the following way $|00\rangle$, $|01\rangle$, $|10\rangle$, $|11\rangle$.

The function $f(k, k')$ is obtained from an analysis of the scattering of two counter-propagating wave packets on a one-dimensional lattice. The corresponding Hamilton operator is given by

$$\hat{H}_2 = \hat{H}_l \otimes \mathbb{1} + \mathbb{1} \otimes \hat{H}_l + U \sum_{j \in \mathbb{Z}} |j\rangle |j\rangle \langle j| \langle j|. \quad (\text{J.7})$$

Here, \hat{H}_l is the single-particle Hamilton operator given in equation (8.1) and U is the on-site interaction strength. In contrast to other parts of this thesis, the formalism of first quantization is used for the above equation. Therefore, the symmetrization of the state for identical bosonic atoms needs to be performed explicitly. In the supplementary material of [20] it is shown that the momenta of the wave packets are conserved by the scattering process and an interaction-induced phase is accumulated

$$f(k, k') = e^{i\phi(k, k')} = \frac{2[\sin(k'a) + \sin(ka)] - iU/J}{2[\sin(k'a) + \sin(ka)] + iU/J}. \quad (\text{J.8})$$

For the considered case of $k = k' = \pi/(4a)$ and $U/J = 2\sqrt{2}$ one obtains $e^{i\phi} = -i$.

Bibliography

- [1] S. Chu, „Nobel lecture: the manipulation of neutral particles“, *Rev. Mod. Phys.* **70**, 685–706 (1998).
- [2] C. N. Cohen-Tannoudji, „Nobel lecture: manipulating atoms with photons“, *Rev. Mod. Phys.* **70**, 707–719 (1998).
- [3] W. D. Phillips, „Nobel lecture: laser cooling and trapping of neutral atoms“, *Rev. Mod. Phys.* **70**, 721–741 (1998).
- [4] M. H. Anderson, J. R. Ensher, M. R. Matthews, C. E. Wieman, and E. A. Cornell, „Observation of Bose-Einstein condensation in a dilute atomic vapor“, *Science* **269**, 198–201 (1995).
- [5] K. B. Davis, M. O. Mewes, M. R. Andrews, N. J. van Druten, D. S. Durfee, D. M. Kurn, and W. Ketterle, „Bose-Einstein condensation in a gas of sodium atoms“, *Phys. Rev. Lett.* **75**, 3969–3973 (1995).
- [6] E. A. Cornell, and C. E. Wieman, „Nobel lecture: Bose-Einstein condensation in a dilute gas, the first 70 years and some recent experiments“, *Rev. Mod. Phys.* **74**, 875–893 (2002).
- [7] W. Ketterle, „Nobel lecture: when atoms behave as waves: Bose-Einstein condensation and the atom laser“, *Rev. Mod. Phys.* **74**, 1131–1151 (2002).
- [8] S. Bose, „Plancks Gesetz und Lichtquantenhypothese“, *Zeitschrift für Physik* **26**, 178–181 (1924).
- [9] A. Einstein, „Quantentheorie des einatomigen idealen Gases.“, *Sitzungsber. K. Preuss. Akad. Wiss., Phys. Math. Kl.* (1924).
- [10] A. Einstein, „Quantentheorie des einatomigen idealen Gases. Zweite Abhandlung.“, *Sitzungsber. K. Preuss. Akad. Wiss., Phys. Math. Kl.* (1925).
- [11] L. D. Carr, D. DeMille, R. V. Krems, and J. Ye, „Cold and ultracold molecules: science, technology and applications“, *New J. Phys.* **11**, 055049 (2009).
- [12] S. Giorgini, L. P. Pitaevskii, and S. Stringari, „Theory of ultracold atomic Fermi gases“, *Rev. Mod. Phys.* **80**, 1215–1274 (2008).
- [13] D. Jaksch, C. Bruder, J. I. Cirac, C. W. Gardiner, and P. Zoller, „Cold bosonic atoms in optical lattices“, *Phys. Rev. Lett.* **81**, 3108–3111 (1998).
- [14] M. Greiner, O. Mandel, T. Esslinger, T. W. Hänsch, and I. Bloch, „Quantum phase transition from a superfluid to a Mott insulator in a gas of ultracold atoms“, *Nature* **415**, 39–44 (2001).
- [15] I. Bloch, J. Dalibard, and W. Zwerger, „Many-body physics with ultracold gases“, *Rev. Mod. Phys.* **80**, 885–964 (2008).
- [16] M. Lewenstein, A. Sanpera, and V. Ahufinger, *Ultracold atoms in optical lattices* (Oxford University Press, 2012).
- [17] R. P. Feynman, „Simulating physics with computers“, *Int. J. Theor. Phys.* **21**, 467–488 (1982).

- [18] I. Bloch, J. Dalibard, and S. Nascimbène, „Quantum simulations with ultracold quantum gases“, *Nature Phys.* **8**, 267–276 (2012).
- [19] B. Josephson, „Possible new effects in superconductive tunnelling“, *Physics Letters* **1**, 251–253 (1962).
- [20] A. M. Childs, D. Gosset, and Z. Webb, „Universal computation by multiparticle quantum walk“, *Science* **339**, 791–794 (2013).
- [21] C. Cohen-Tannoudji, J. Dupont-Roc, and G. Grynberg, *Atom-photon interactions* (Wiley, 1998).
- [22] C. Cohen-Tannoudji, J. Dupont-Roc, and G. Grynberg, *Photons and atoms: introduction to quantum electrodynamics* (Wiley, 1989).
- [23] B. R. Mollow, „Pure-state analysis of resonant light scattering: radiative damping, saturation, and multiphoton effects“, *Phys. Rev. A* **12**, 1919–1943 (1975).
- [24] G. Lindblad, „On the generators of quantum dynamical semigroups“, *Commun. Math. Phys.* **48**, 119–130 (1976).
- [25] S. M. Barnett, and P. M. Radmore, *Methods in theoretical quantum optics* (Clarendon Press, 1997).
- [26] V. Weisskopf, and E. Wigner, „Berechnung der natürlichen Linienbreite auf Grund der Diracschen Lichttheorie“, *Zeitschrift für Physik* **63**, 54–73 (1930).
- [27] W. E. Lamb, and R. C. Retherford, „Fine structure of the hydrogen atom by a microwave method“, *Phys. Rev.* **72**, 241–243 (1947).
- [28] D. A. Steck, *Quantum and atom optics*, (2007) <http://atomoptics-nas.uoregon.edu/~dsteck/teaching/quantum-optics>.
- [29] I. I. Rabi, „Space quantization in a gyrating magnetic field“, *Phys. Rev.* **51**, 652–654 (1937).
- [30] J. Dalibard, and C. Cohen-Tannoudji, „Atomic motion in laser light: connection between semiclassical and quantum descriptions“, *J. Phys. B: At. Mol. Phys.* **18**, 1661 (1985).
- [31] J. P. Gordon, and A. Ashkin, „Motion of atoms in a radiation trap“, *Phys. Rev. A* **21**, 1606–1617 (1980).
- [32] C. Cohen-Tannoudji, „Atomic motion in laser light“, *Fundamental systems in quantum optics*, Les Houches session LIII, 1–164 (1990).
- [33] H. J. Metcalf, and P. Van der Straten, *Laser cooling and trapping* (Springer, 1999).
- [34] C. J. Pethick, and H. Smith, *Bose-Einstein condensation in dilute gases* (Cambridge university press, 2002).
- [35] L. Pitaevskii, and S. Stringari, *Bose-Einstein condensation* (Clarendon press, 2003).
- [36] R. Grimm, M. Weidemüller, and Y. Ovchinnikov, „Optical dipole traps for neutral atoms“, in *Advances in atomic molecular, and optical physics*, Vol. 42 (Elsevier, 2000), 95–170.
- [37] B. W. Shore, *The theory of coherent atomic excitation*, Vol. 1 and 2 (Wiley, 1990).
- [38] H. Friedrich, *Theoretical atomic physics*, second Edition (Springer, 2006).
- [39] A. Messiah, *Quantum mechanics*, Vol. 2 (North-Holland, 1961).
- [40] I. I. Sobelman, *Atomic spectra and radiative transitions*, second edition (1992).
- [41] B. E. King, „Angular momentum coupling and Rabi frequencies for simple atomic transitions“, arXiv, 0804.4528 (2008).

- [42] Y. Ralchenko, *Atomic spectra database*, National Institute for Standards and Technology, <https://www.nist.gov/pml/atomic-spectra-database>.
- [43] N. Proukakis, S. Gardiner, M. Davis, and M. Szymańska, *Quantum gases: finite temperature and non-equilibrium dynamics*, Vol. 1 (World Scientific, 2013).
- [44] J. T. M. Walraven, *Quantum gases - statistics and interactions*, Lecture course at the University of Amsterdam, (2015) <http://www.phlam.univ-lille1.fr/leshouches/cours15/2015-Quantum-Gases.pdf>.
- [45] C. W. Gardiner, and P. Zoller, *The quantum world of ultra-cold atoms and light book iii: ultra-cold atoms* (World Scientific, 2017).
- [46] J. R. Taylor, *Scattering theory* (Wiley, 1972).
- [47] F. W. J. Olver, D. W. Lozier, R. F. Boisvert, and C. W. Clark, *NIST handbook of mathematical functions* (Cambridge University Press, 2010).
- [48] C. Chin, R. Grimm, P. Julienne, and E. Tiesinga, „Feshbach resonances in ultracold gases“, *Rev. Mod. Phys.* **82**, 1225–1286 (2010).
- [49] K. Huang, and C. N. Yang, „Quantum-mechanical many-body problem with hard-sphere interaction“, *Phys. Rev.* **105**, 767–775 (1957).
- [50] T. D. Lee, K. Huang, and C. N. Yang, „Eigenvalues and eigenfunctions of a Bose system of hard spheres and its low-temperature properties“, *Phys. Rev.* **106**, 1135–1145 (1957).
- [51] K. Huang, *Statistical mechanics* (Wiley, 1963).
- [52] E. Fermi, „Motion of neutrons in hydrogenous substances“, *Ric. Scient.* **7**, 13–52 (1936).
- [53] F. Stampfer, and P. Wagner, „Mathematically rigorous formulation of the Fermi pseudopotential for higher-partial-wave scattering in arbitrary dimension“, *Phys. Rev. A* **81**, 052710 (2010).
- [54] O. Penrose, and L. Onsager, „Bose-Einstein condensation and liquid helium“, *Phys. Rev.* **104**, 576–584 (1956).
- [55] J. Hubbard, „Electron correlations in narrow energy bands“, in *Proceedings of the royal society of london a: mathematical, physical and engineering sciences*, Vol. 276, 1365 (The Royal Society, 1963), pp. 238–257.
- [56] J. Callaway, *Quantum theory of the solid state*, Student edition (Academic Press, 1974).
- [57] G. H. Wannier, „The structure of electronic excitation levels in insulating crystals“, *Phys. Rev.* **52**, 191–197 (1937).
- [58] W. Kohn, „Analytic properties of Bloch waves and Wannier functions“, *Phys. Rev.* **115**, 809–821 (1959).
- [59] N. Marzari, and D. Vanderbilt, „Maximally localized generalized Wannier functions for composite energy bands“, *Phys. Rev. B* **56**, 12847–12865 (1997).
- [60] S. Ri, and S. Ri, „Proof that the maximally localized Wannier functions are real“, [arXiv:1407.6824](https://arxiv.org/abs/1407.6824) (2014).
- [61] M. P. A. Fisher, P. B. Weichman, G. Grinstein, and D. S. Fisher, „Boson localization and the superfluid-insulator transition“, *Phys. Rev. B* **40**, 546–570 (1989).
- [62] H. P. Büchler, „Microscopic derivation of Hubbard parameters for cold atomic gases“, *Phys. Rev. Lett.* **104**, 090402 (2010).

- [63] M. J. Mark, E. Haller, K. Lauber, J. G. Danzl, A. J. Daley, and H.-C. Nägerl, „Precision measurements on a tunable Mott insulator of ultracold atoms“, *Phys. Rev. Lett.* **107**, 175301 (2011).
- [64] S. Pilati, and M. Troyer, „Bosonic superfluid-insulator transition in continuous space“, *Phys. Rev. Lett.* **108**, 155301 (2012).
- [65] G. E. Astrakharchik, K. V. Krutitsky, M. Lewenstein, and F. Mazzanti, „One-dimensional Bose gas in optical lattices of arbitrary strength“, *Phys. Rev. A* **93**, 021605 (2016).
- [66] G. Boéris, L. Gori, M. D. Hoogerland, A. Kumar, E. Lucioni, L. Tanzi, M. Inguscio, T. Giamarchi, C. D’Errico, G. Carleo, G. Modugno, and L. Sanchez-Palencia, „Mott transition for strongly interacting one-dimensional bosons in a shallow periodic potential“, *Phys. Rev. A* **93**, 011601 (2016).
- [67] W. Xu, M. Olshanii, and M. Rigol, „Multiband effects and the Bose-Hubbard model in one-dimensional lattices“, *Phys. Rev. A* **94**, 031601 (2016).
- [68] M. Kremer, S. Rashi, A. Benseny, and T. Busch, „Twonniers: interaction-induced effects on Bose–Hubbard parameters“, arXiv, 1707.08355 (2017).
- [69] N. Bogoliubov, „On the theory of superfluidity“, *J. Phys* **11**, 23 (1947).
- [70] D. van Oosten, P. van der Straten, and H. T. C. Stoof, „Quantum phases in an optical lattice“, *Phys. Rev. A* **63**, 053601 (2001).
- [71] J. K. Freericks, and H. Monien, „Phase diagram of the Bose-Hubbard model“, *Europhys. Lett.* **26**, 545 (1994).
- [72] J. K. Freericks, and H. Monien, „Strong-coupling expansions for the pure and disordered Bose-Hubbard model“, *Phys. Rev. B* **53**, 2691–2700 (1996).
- [73] B. Damski, and J. Zakrzewski, „Mott-insulator phase of the one-dimensional bose-hubbard model: a high-order perturbative study“, *Phys. Rev. A* **74**, 043609 (2006).
- [74] N. Teichmann, D. Hinrichs, M. Holthaus, and A. Eckardt, „Process-chain approach to the Bose-Hubbard model: ground-state properties and phase diagram“, *Phys. Rev. B* **79**, 224515 (2009).
- [75] F. Gerbier, „Boson Mott insulators at finite temperatures“, *Phys. Rev. Lett.* **99**, 120405 (2007).
- [76] M. C. Gutzwiller, „Effect of correlation on the ferromagnetism of transition metals“, *Phys. Rev. Lett.* **10**, 159–162 (1963).
- [77] D. S. Rokhsar, and B. G. Kotliar, „Gutzwiller projection for bosons“, *Phys. Rev. B* **44**, 10328–10332 (1991).
- [78] W. Krauth, M. Caffarel, and J.-P. Bouchaud, „Gutzwiller wave function for a model of strongly interacting bosons“, *Phys. Rev. B* **45**, 3137–3140 (1992).
- [79] W. Zwerger, „Mott–Hubbard transition of cold atoms in optical lattices“, *J. Opt. B: Quantum Semiclassical Opt.* **5**, S9 (2003).
- [80] K. Sheshadri, H. R. Krishnamurthy, R. Pandit, and T. V. Ramakrishnan, „Superfluid and insulating phases in an interacting-boson model: mean-field theory and the rpa“, *EPL (Europhysics Letters)* **22**, 257 (1993).
- [81] P. Navez, and R. Schützhold, „Emergence of coherence in the Mott-insulator-superfluid quench of the Bose-Hubbard model“, *Phys. Rev. A* **82**, 063603 (2010).

- [82] P. Navez, F. Queisser, and R. Schützhold, „Large-coordination-number expansion of a lattice Bose gas at finite temperature“, *Phys. Rev. A* **94**, 023629 (2016).
- [83] D.-S. Lühmann, „Cluster Gutzwiller method for bosonic lattice systems“, *Phys. Rev. A* **87**, 043619 (2013).
- [84] D. Jaksch, V. Venturi, J. I. Cirac, C. J. Williams, and P. Zoller, „Creation of a molecular condensate by dynamically melting a Mott insulator“, *Phys. Rev. Lett.* **89**, 040402 (2002).
- [85] J. Zakrzewski, „Mean-field dynamics of the superfluid-insulator phase transition in a gas of ultracold atoms“, *Phys. Rev. A* **71**, 043601 (2005).
- [86] B. Capogrosso-Sansone, N. V. Prokof'ev, and B. V. Svistunov, „Phase diagram and thermodynamics of the three-dimensional Bose-Hubbard model“, *Phys. Rev. B* **75**, 134302 (2007).
- [87] B. Capogrosso-Sansone, G. S. Söyler, N. Prokof'ev, and B. Svistunov, „Monte Carlo study of the two-dimensional Bose-Hubbard model“, *Phys. Rev. A* **77**, 015602 (2008).
- [88] T. P. Polak, and T. K. Kopeć, „Finite-temperature effects on the superfluid Bose–Einstein condensation of confined ultracold atoms in three-dimensional optical lattices“, *J. Phys. B: At., Mol. Opt. Phys.* **42**, 095302 (2009).
- [89] M. Gupta, H. R. Krishnamurthy, and J. K. Freericks, „Strong-coupling expansion for ultracold bosons in an optical lattice at finite temperatures in the presence of superfluidity“, *Phys. Rev. A* **88**, 053636 (2013).
- [90] I. Bloch, „Ultracold quantum gases in optical lattices“, *Nature Phys.* **1**, 23–30 (2005).
- [91] K. V. Krutitsky, „Ultracold bosons with short-range interaction in regular optical lattices“, *Phys. Rep.* **607**, 1–101 (2016).
- [92] C. Gross, and I. Bloch, „Quantum simulations with ultracold atoms in optical lattices“, *Science* **357**, 995 (2017).
- [93] W. Hofstetter, and T. Qin, „Quantum simulation of strongly correlated condensed matter systems“, *Journal of Physics B: Atomic, Molecular and Optical Physics* **51**, 082001 (2018).
- [94] W. S. Bakr, J. I. Gillen, A. Peng, S. Fölling, and M. Greiner, „A quantum gas microscope for detecting single atoms in a Hubbard-regime optical lattice“, *Nature* **462**, 74–77 (2009).
- [95] J. F. Sherson, C. Weitenberg, M. Endres, M. Cheneau, I. Bloch, and S. Kuhr, „Single-atom-resolved fluorescence imaging of an atomic Mott insulator“, *Nature* **467**, 68–72 (2010).
- [96] W. S. Bakr, A. Peng, M. E. Tai, R. Ma, J. Simon, J. I. Gillen, S. Fölling, L. Pollet, and M. Greiner, „Probing the superfluid–to–Mott insulator transition at the single-atom level“, *Science* **329**, 547–550 (2010).
- [97] L. W. Cheuk, M. A. Nichols, M. Okan, T. Gersdorf, V. V. Ramasesh, W. S. Bakr, T. Lompe, and M. W. Zwierlein, „Quantum-gas microscope for fermionic atoms“, *Phys. Rev. Lett.* **114**, 193001 (2015).
- [98] E. Haller, J. Hudson, A. Kelly, D. A. Cotta, B. Peaudecerf, G. D. Bruce, and S. Kuhr, „Single-atom imaging of fermions in a quantum-gas microscope“, *Nature Phys.* **11**, 738–742 (2015).

- [99] M. F. Parsons, F. Huber, A. Mazurenko, C. S. Chiu, W. Setiawan, K. Wooley-Brown, S. Blatt, and M. Greiner, „Site-resolved imaging of fermionic ${}^6\text{Li}$ in an optical lattice“, *Phys. Rev. Lett.* **114**, 213002 (2015).
- [100] G. J. A. Edge, R. Anderson, D. Jervis, D. C. McKay, R. Day, S. Trotzky, and J. H. Thywissen, „Imaging and addressing of individual fermionic atoms in an optical lattice“, *Phys. Rev. A* **92**, 063406 (2015).
- [101] A. Omran, M. Boll, T. A. Hilker, K. Kleinlein, G. Salomon, I. Bloch, and C. Gross, „Microscopic observation of Pauli blocking in degenerate fermionic lattice gases“, *Phys. Rev. Lett.* **115**, 263001 (2015).
- [102] D. Greif, M. F. Parsons, A. Mazurenko, C. S. Chiu, S. Blatt, F. Huber, G. Ji, and M. Greiner, „Site-resolved imaging of a fermionic Mott insulator“, *Science* **351**, 953–957 (2016).
- [103] L. W. Cheuk, M. A. Nichols, K. R. Lawrence, M. Okan, H. Zhang, and M. W. Zwierlein, „Observation of 2D fermionic Mott insulators of ${}^{40}\text{K}$ with single-site resolution“, *Phys. Rev. Lett.* **116**, 235301 (2016).
- [104] S. Peil, J. V. Porto, B. L. Tolra, J. M. Obrecht, B. E. King, M. Subbotin, S. L. Rolston, and W. D. Phillips, „Patterned loading of a Bose-Einstein condensate into an optical lattice“, *Phys. Rev. A* **67**, 051603 (2003).
- [105] R. Roth, and K. Burnett, „Phase diagram of bosonic atoms in two-color superlattices“, *Phys. Rev. A* **68**, 023604 (2003).
- [106] R. Roth, and K. Burnett, „Ultracold bosonic atoms in two-colour superlattices“, *J. Opt. B: Quantum Semiclassical Opt.* **5**, S50 (2003).
- [107] M. Hild, F. Schmitt, and R. Roth, „Response of bose gases in time-dependent optical superlattices“, *J. Phys. B: At., Mol. Opt. Phys.* **39**, 4547 (2006).
- [108] S. Trotzky, P. Cheinet, S. Fölling, M. Feld, U. Schnorrberger, A. M. Rey, A. Polkovnikov, E. Demler, M. Lukin, and I. Bloch, „Time-resolved observation and control of superexchange interactions with ultracold atoms in optical lattices“, *Science* **319**, 295–299 (2008).
- [109] F. Schmitt, M. Hild, and R. Roth, „Phase diagram of bosons in two-color superlattices from experimental parameters“, *Phys. Rev. A* **80**, 023621 (2009).
- [110] F. Schmitt, M. Hild, and R. Roth, „Ab initio phase diagram of ultracold 87 rb in a one-dimensional two-colour superlattice“, *J. Phys. B: At., Mol. Opt. Phys.* **43**, 235301 (2010).
- [111] J. Kangara, C. Cheng, S. Pegahan, I. Arakelyan, and J. E. Thomas, „Atom pairing in optical superlattices“, arXiv, 1709.08484 (2017).
- [112] L. Guidoni, C. Triché, P. Verkerk, and G. Grynberg, „Quasiperiodic optical lattices“, *Phys. Rev. Lett.* **79**, 3363–3366 (1997).
- [113] L. Santos, M. A. Baranov, J. I. Cirac, H.-U. Everts, H. Fehrmann, and M. Lewenstein, „Atomic quantum gases in kagomé lattices“, *Phys. Rev. Lett.* **93**, 030601 (2004).
- [114] G.-B. Jo, J. Guzman, C. K. Thomas, P. Hosur, A. Vishwanath, and D. M. Stamper-Kurn, „Ultracold atoms in a tunable optical kagome lattice“, *Phys. Rev. Lett.* **108**, 045305 (2012).
- [115] J. Sebby-Strabley, M. Anderlini, P. S. Jessen, and J. V. Porto, „Lattice of double wells for manipulating pairs of cold atoms“, *Phys. Rev. A* **73**, 033605 (2006).

- [116] D. Greif, T. Uehlinger, G. Jotzu, L. Tarruell, and T. Esslinger, „Short-range quantum magnetism of ultracold fermions in an optical lattice“, *Science* **340**, 1307–1310 (2013).
- [117] C. Becker, P. Soltan-Panahi, J. Kronjäger, S. Dörscher, K. Bongs, and K. Sengstock, „Ultracold quantum gases in triangular optical lattices“, *New J. Phys.* **12**, 065025 (2010).
- [118] P. Soltan-Panahi, J. Struck, P. Hauke, A. Bick, W. Plenkers, G. Meineke, C. Becker, P. Windpassinger, M. Lewenstein, and K. Sengstock, „Multi-component quantum gases in spin-dependent hexagonal lattices“, *Nature Phys.* **7**, 434–440 (2011).
- [119] L. Tarruell, D. Greif, T. Uehlinger, G. Jotzu, and T. Esslinger, „Creating, moving and merging Dirac points with a Fermi gas in a tunable honeycomb lattice“, *Nature* **483**, 302–305 (2012).
- [120] P. Soltan-Panahi, D.-S. Lühmann, J. Struck, P. Windpassinger, and K. Sengstock, „Quantum phase transition to unconventional multi-orbital superfluidity in optical lattices“, *Nature Phys.* **8**, 71–75 (2012).
- [121] T. Uehlinger, G. Jotzu, M. Messer, D. Greif, W. Hofstetter, U. Bissbort, and T. Esslinger, „Artificial graphene with tunable interactions“, *Phys. Rev. Lett.* **111**, 185307 (2013).
- [122] D.-S. Lühmann, O. Jürgensen, M. Weinberg, J. Simonet, P. Soltan-Panahi, and K. Sengstock, „Quantum phases in tunable state-dependent hexagonal optical lattices“, *Phys. Rev. A* **90**, 013614 (2014).
- [123] K. L. Lee, B. Grémaud, R. Han, B.-G. Englert, and C. Miniatura, „Ultracold fermions in a graphene-type optical lattice“, *Phys. Rev. A* **80**, 043411 (2009).
- [124] J. Dalibard, F. Gerbier, G. Juzeliunas, and P. Öhberg, „Colloquium: artificial gauge potentials for neutral atoms“, *Rev. Mod. Phys.* **83**, 1523–1543 (2011).
- [125] N. Goldman, G. Juzeliunas, P. Öhberg, and I. B. Spielman, „Light-induced gauge fields for ultracold atoms“, *Rep. Prog. Phys.* **77**, 126401 (2014).
- [126] N. Goldman, and J. Dalibard, „Periodically driven quantum systems: effective hamiltonians and engineered gauge fields“, *Phys. Rev. X* **4**, 031027 (2014).
- [127] P. W. Anderson, „Absence of diffusion in certain random lattices“, *Phys. Rev.* **109**, 1492–1505 (1958).
- [128] B. Deissler, M. Zaccanti, G. Roati, C. D’Errico, M. Fattori, M. Modugno, G. Modugno, and M. Inguscio, „Delocalization of a disordered bosonic system by repulsive interactions“, *Nat. Phys.* (2010).
- [129] M. Pasienski, D. McKay, M. White, and B. DeMarco, „A disordered insulator in an optical lattice“, *Nature Phys.* **6**, 677–680 (2010).
- [130] B. Gadway, D. Pertot, J. Reeves, M. Vogt, and D. Schneble, „Glassy behavior in a binary atomic mixture“, *Phys. Rev. Lett.* **107**, 145306 (2011).
- [131] L. Tanzi, E. Lucioni, S. Chaudhuri, L. Gori, A. Kumar, C. D’Errico, M. Inguscio, and G. Modugno, „Transport of a Bose gas in 1D disordered lattices at the fluid-insulator transition“, *Phys. Rev. Lett.* **111**, 115301 (2013).
- [132] C. D’Errico, E. Lucioni, L. Tanzi, L. Gori, G. Roux, I. P. McCulloch, T. Giamarchi, M. Inguscio, and G. Modugno, „Observation of a disordered bosonic insulator from weak to strong interactions“, *Phys. Rev. Lett.* **113**, 095301 (2014).

- [133] M. Schreiber, S. S. Hodgman, P. Bordia, H. P. Lüschen, M. H. Fischer, R. Vosk, E. Altman, U. Schneider, and I. Bloch, „Observation of many-body localization of interacting fermions in a quasirandom optical lattice“, *Science* **349**, 842–845 (2015).
- [134] S. S. Kondov, W. R. McGehee, W. Xu, and B. DeMarco, „Disorder-induced localization in a strongly correlated atomic Hubbard gas“, *Phys. Rev. Lett.* **114**, 083002 (2015).
- [135] C. Meldgin, U. Ray, P. Russ, D. Chen, D. M. Ceperley, and B. DeMarco, „Probing the Bose glass-superfluid transition using quantum quenches of disorder“, *Nat. Phys.* **12**, 646–649 (2016).
- [136] P. Bordia, H. P. Lüschen, S. S. Hodgman, M. Schreiber, I. Bloch, and U. Schneider, „Coupling identical one-dimensional many-body localized systems“, *Phys. Rev. Lett.* **116**, 140401 (2016).
- [137] J.-y. Choi, S. Hild, J. Zeiher, P. Schauß, A. Rubio-Abadal, T. Yefsah, V. Khemani, D. A. Huse, I. Bloch, and C. Gross, „Exploring the many-body localization transition in two dimensions“, *Science* **352**, 1547–1552 (2016).
- [138] P. Bordia, H. Lüschen, S. Scherg, S. Gopalakrishnan, M. Knap, U. Schneider, and I. Bloch, „Probing slow relaxation and many-body localization in two-dimensional quasiperiodic systems“, *Phys. Rev. X* **7**, 041047 (2017).
- [139] P. A. Lee, N. Nagaosa, and X.-G. Wen, „Doping a Mott insulator: physics of high-temperature superconductivity“, *Rev. Mod. Phys.* **78**, 17–85 (2006).
- [140] R. A. Hart, P. M. Duarte, T.-L. Yang, X. Liu, T. Paiva, E. Khatami, R. T. Scalettar, N. Trivedi, D. A. Huse, and R. G. Hulet, „Observation of antiferromagnetic correlations in the Hubbard model with ultracold atoms“, *Nature* **519**, 211–214 (2015).
- [141] L. W. Cheuk, M. A. Nichols, K. R. Lawrence, M. Okan, H. Zhang, E. Khatami, N. Trivedi, T. Paiva, M. Rigol, and M. W. Zwierlein, „Observation of spatial charge and spin correlations in the 2D Fermi-Hubbard model“, *Science* **353**, 1260–1264 (2016).
- [142] M. F. Parsons, A. Mazurenko, C. S. Chiu, G. Ji, D. Greif, and M. Greiner, „Site-resolved measurement of the spin-correlation function in the Fermi-Hubbard model“, *Science* **353**, 1253–1256 (2016).
- [143] M. Boll, T. A. Hilker, G. Salomon, A. Omran, J. Nespolo, L. Pollet, I. Bloch, and C. Gross, „Spin- and density-resolved microscopy of antiferromagnetic correlations in Fermi-Hubbard chains“, *Science* **353**, 1257–1260 (2016).
- [144] J. H. Drewes, L. A. Miller, E. Cocchi, C. F. Chan, N. Wurz, M. Gall, D. Pertot, F. Brennecke, and M. Köhl, „Antiferromagnetic correlations in two-dimensional fermionic mott-insulating and metallic phases“, *Phys. Rev. Lett.* **118**, 170401 (2017).
- [145] A. Mazurenko, C. S. Chiu, G. Ji, M. F. Parsons, M. Kanász-Nagy, R. Schmidt, F. Grusdt, E. Demler, D. Greif, and M. Greiner, „A cold-atom Fermi-Hubbard antiferromagnet“, *Nature* **545**, 462–466 (2017).
- [146] P. T. Brown, D. Mitra, E. Guardado-Sanchez, P. Schauß, S. S. Kondov, E. Khatami, T. Paiva, N. Trivedi, D. A. Huse, and W. S. Bakr, „Spin-imbalance in a 2D Fermi-Hubbard system“, *Science* **357**, 1385–1388 (2017).
- [147] G. Birkel, F. B. J. Buchkremer, R. Dumke, and W. Ertmer, „Atom optics with micro-fabricated optical elements“, *Opt. Commun.* **191**, 67–81 (2001).

- [148] M. Schlosser, S. Tichelmann, J. Kruse, and G. Birkel, „Scalable architecture for quantum information processing with atoms in optical micro-structures“, *Quantum Inf. Process.* **10**, 907–924 (2011).
- [149] M. Schlosser, J. Kruse, C. Gierl, S. Teichmann, S. Tichelmann, and G. Birkel, „Fast transport, atom sample splitting and single-atom qubit supply in two-dimensional arrays of optical microtraps“, *New J. Phys.* **14**, 123034 (2012).
- [150] K. Henderson, C. Ryu, C. MacCormick, and M. G. Boshier, „Experimental demonstration of painting arbitrary and dynamic potentials for Bose–Einstein condensates“, *New J. Phys.* **11**, 043030 (2009).
- [151] B. Zimmermann, T. Müller, J. Meineke, T. Esslinger, and H. Moritz, „High-resolution imaging of ultracold fermions in microscopically tailored optical potentials“, *New J. Phys.* **13**, 043007 (2011).
- [152] A. Kaufman, B. Lester, C. Reynolds, M. Wall, M. Foss-Feig, K. Hazzard, A. Rey, and C. Regal, „Two-particle quantum interference in tunnel-coupled optical tweezers“, *Science* **345**, 306–309 (2014).
- [153] S. Murmann, A. Bergschneider, V. M. Klinkhamer, G. Zürn, T. Lompe, and S. Jochim, „Two fermions in a double well: exploring a fundamental building block of the Hubbard model“, *Phys. Rev. Lett.* **114**, 080402 (2015).
- [154] B. J. Lester, N. Luick, A. M. Kaufman, C. M. Reynolds, and C. A. Regal, „Rapid production of uniformly filled arrays of neutral atoms“, *Phys. Rev. Lett.* **115**, 073003 (2015).
- [155] M. Endres, H. Bernien, A. Keesling, H. Levine, E. R. Anschuetz, A. Krajenbrink, C. Senko, V. Vuletić, M. Greiner, and M. D. Lukin, „Atom-by-atom assembly of defect-free one-dimensional cold atom arrays“, *Science* **354**, 1024 (2016).
- [156] G. Gauthier, I. Lenton, N. M. Parry, M. Baker, M. J. Davis, H. Rubinsztein-Dunlop, and T. W. Neely, „Direct imaging of a digital-micromirror device for configurable microscopic optical potentials“, *Optica* **3**, 1136–1143 (2016).
- [157] F. Nogrette, H. Labuhn, S. Ravets, D. Barredo, L. Béguin, A. Vernier, T. Lahaye, and A. Browaeys, „Single-atom trapping in holographic 2D arrays of microtraps with arbitrary geometries“, *Phys. Rev. X* **4**, 021034 (2014).
- [158] P. Zupancic, P. M. Preiss, R. Ma, A. Lukin, M. E. Tai, M. Rispoli, R. Islam, and M. Greiner, „Ultra-precise holographic beam shaping for microscopic quantum control“, *Opt. Express* **24**, 13881–13893 (2016).
- [159] H. Römer, *Theoretical optics* (John Wiley & Sons, 2006).
- [160] M. Born, and E. Wolf, *Principles of Optics*, 7th (Cambridge University Press, 1999).
- [161] J. W. Goodman, *Introduction to Fourier optics* (Roberts and Company Publishers, 2005).
- [162] D. Mendlovic, Z. Zalevsky, and N. Konforti, „Computation considerations and fast algorithms for calculating the diffraction integral“, *J. Mod. Opt.* **44**, 407–414 (1997).
- [163] E. Wolf, „Electromagnetic diffraction in optical systems. I. An integral representation of the image field“, *P. Phys. Soc. A* **253**, 349–357 (1959).
- [164] P. Debye, „Das Verhalten von Lichtwellen in der Nähe eines Brennpunktes oder einer Brennlinie“, *Ann. Phys.* **335**, 755–776 (1909).

- [165] B. Richards, and E. Wolf, „Electromagnetic diffraction in optical systems. II. Structure of the image field in an aplanatic system“, *P. Phys. Soc. A* **253**, 358–379 (1959).
- [166] M. Leutenegger, R. Rao, R. A. Leitgeb, and T. Lasser, „Fast focus field calculations“, *Opt. Express* **14**, 11277–11291 (2006).
- [167] J.-N. Schmidt, „Generation of artificial optical lattices with direct single-site control“, Bachelor thesis (TU Darmstadt, Germany, 2014).
- [168] Zemax LLC, *Zemax Optical Studio*, <https://www.zemax.com/products/opticstudio>.
- [169] H. F. Talbot, „Facts relating to optical science“, *Philos. Mag.* **9**, 401 (1836).
- [170] L. Rayleigh, „On copying diffraction-gratings, and on some phenomena connected therewith“, *Philos. Mag.* **11**, 196 (1881).
- [171] M. V. Berry, and S. Klein, „Integer, fractional and fractal Talbot effects“, *J. Mod. Opt.* **43**, 2139–2164 (1996).
- [172] I. H. Deutsch, and P. S. Jessen, „Quantum-state control in optical lattices“, *Phys. Rev. A* **57**, 1972–1986 (1998).
- [173] K. L. Corwin, S. J. M. Kuppens, D. Cho, and C. E. Wieman, „Spin-polarized atoms in a circularly polarized optical dipole trap“, *Phys. Rev. Lett.* **83**, 1311–1314 (1999).
- [174] J. D. Thompson, T. G. Tiecke, A. S. Zibrov, V. Vuletić, and M. D. Lukin, „Coherence and Raman sideband cooling of a single atom in an optical tweezer“, *Phys. Rev. Lett.* **110**, 133001 (2013).
- [175] E. N. Economou, *The physics of solids* (Springer, 2010).
- [176] R. Walters, G. Cotugno, T. H. Johnson, S. R. Clark, and D. Jaksch, „Ab initio derivation of Hubbard models for cold atoms in optical lattices“, *Phys. Rev. A* **87**, 043613 (2013).
- [177] S. Nandi, „The quantum Gaussian well“, *Am. J. Phys.* **78**, 1341–1345 (2010).
- [178] J. Ankerhold, *Quantum tunneling in complex systems* (Springer, 2007).
- [179] D. J. Griffiths, *Introduction to quantum mechanics*, second edition (Pearson Prentice Hall, 2004).
- [180] G. V. Mil’nikov, and H. Nakamura, „Practical implementation of the instanton theory for the ground-state tunneling splitting“, *J. Chem. Phys.* **115**, 6881–6897 (2001).
- [181] R. P. Feynman, and A. R. Hibbs, *Quantum mechanics and path integrals* (McGraw-Hill, 1965).
- [182] A. Polyakov, „Compact gauge fields and the infrared catastrophe“, *Phys. Lett. B* **59**, 82–84 (1975).
- [183] A. Belavin, A. Polyakov, A. Schwartz, and Y. Tyupkin, „Pseudoparticle solutions of the Yang-Mills equations“, *Phys. Lett. B* **59**, 85–87 (1975).
- [184] G. ’t Hooft, „Computation of the quantum effects due to a four-dimensional pseudoparticle“, *Phys. Rev. D* **14**, 3432–3450 (1976).
- [185] A. Polyakov, „Quark confinement and topology of gauge theories“, *Nucl. Phys. B* **120**, 429–458 (1977).

- [186] S. Coleman, „The uses of instantons“, in *The whys of subnuclear physics*, edited by A. L. Zichichi, (Springer, 1979), pp. 805–941.
- [187] A. I. Vainshtein, V. I. Zakharov, V. A. Novikov, and M. A. Shifman, „ABC of instantons“, *Soviet Physics Uspekhi* **25**, 195 (1982).
- [188] U. Weiss, and W. Haeffner, „Complex-time path integrals beyond the stationary-phase approximation: decay of metastable states and quantum statistical metastability“, *Phys. Rev. D* **27**, 2916–2927 (1983).
- [189] G. V. Mil’nikov, and H. Nakamura, „Practical implementation of the instanton theory. ii. decay of metastable state through tunneling“, *J. Chem. Phys.* **117**, 10081–10087 (2002).
- [190] G. Mil’nikov, and H. Nakamura, „Tunneling splitting and decay of metastable states in polyatomic molecules: invariant instanton theory“, *Phys. Chem. Chem. Phys.* **10**, 1374–1393 (2008).
- [191] H. Nakamura, and G. Mil’nikov, *Quantum mechanical tunneling in chemical physics* (CRC Press, 2013).
- [192] F. Gerbier, A. Widera, S. Fölling, O. Mandel, T. Gericke, and I. Bloch, „Interference pattern and visibility of a Mott insulator“, *Phys. Rev. A* **72**, 053606 (2005).
- [193] G. H. Golub, and C. F. van Loan, *Matrix computations* (The Johns Hopkins University Press, 1996).
- [194] D. C. Sorensen, *Implicitly restarted Arnoldi/Lanczos methods for large scale eigenvalue calculations* (NASA, 1996).
- [195] Y. Saad, *Numerical methods for large eigenvalue problems*, second edition (SIAM, 2011).
- [196] D. K. Hoffman, R. C. Raffanetti, and K. Ruedenberg, „Generalization of Euler angles to N-dimensional orthogonal matrices“, *J. Math. Phys.* **13**, 528–533 (1972).
- [197] J. Kruse, C. Gierl, M. Schlosser, and G. Birkl, „Reconfigurable site-selective manipulation of atomic quantum systems in two-dimensional arrays of dipole traps“, *Phys. Rev. A* **81**, 060308 (2010).
- [198] D. Barredo, S. de Léséleuc, V. Lienhard, T. Lahaye, and A. Browaeys, „An atom-by-atom assembler of defect-free arbitrary two-dimensional atomic arrays“, *Science* **354**, 1021–1023 (2016).
- [199] H. Kim, W. Lee, H.-g. Lee, H. Jo, Y. Song, and J. Ahn, „In situ single-atom array synthesis using dynamic holographic optical tweezers“, *Nat. Commun.* **7**, 13317 (2016).
- [200] C. Robens, S. Brakhane, W. Alt, F. Kleiðler, D. Meschede, G. Moon, G. Ramola, and A. Alberti, „High numerical aperture (NA = 0.92) objective lens for imaging and addressing of cold atoms“, *Opt. Lett.* **42**, 1043–1046 (2017).
- [201] A. M. Kaufman, B. J. Lester, and C. A. Regal, „Cooling a single atom in an optical tweezer to its quantum ground state“, *Phys. Rev. X* **2**, 041014 (2012).
- [202] W. S. Bakr, „Microscopic studies of quantum phase transitions in optical lattices“, PhD thesis (Harvard University, 2011).
- [203] C. Weitenberg, „Single-atom resolved imaging and manipulation in an atomic Mott insulator“, PhD thesis (LMU Munich, 2011).
- [204] D. C. McKay, and B. DeMarco, „Cooling in strongly correlated optical lattices: prospects and challenges“, *Rep. Prog. Phys.* **74**, 054401 (2011).

- [205] R. Olf, F. Fang, G. E. Marti, A. MacRae, and D. M. Stamper-Kurn, „Thermometry and cooling of a Bose gas to 0.02 times the condensation temperature“, *Nat. Phys.* **11**, 720–723 (2015).
- [206] T. Gericke, F. Gerbier, A. Widera, S. Fölling, O. Mandel, and I. Bloch, „Adiabatic loading of a Bose–Einstein condensate in a 3D optical lattice“, *J. Mod. Opt.* **54**, 735–743 (2007).
- [207] J. Zakrzewski, and D. Delande, „Breakdown of adiabaticity when loading ultracold atoms in optical lattices“, *Phys. Rev. A* **80**, 013602 (2009).
- [208] J.-S. Bernier, G. Roux, and C. Kollath, „Slow quench dynamics of a one-dimensional bose gas confined to an optical lattice“, *Phys. Rev. Lett.* **106**, 200601 (2011).
- [209] S. S. Natu, K. R. A. Hazzard, and E. J. Mueller, „Local versus global equilibration near the bosonic Mott-insulator-superfluid transition“, *Phys. Rev. Lett.* **106**, 125301 (2011).
- [210] J.-S. Bernier, D. Poletti, P. Barmettler, G. Roux, and C. Kollath, „Slow quench dynamics of mott-insulating regions in a trapped bose gas“, *Phys. Rev. A* **85**, 033641 (2012).
- [211] M. Haque, and F. E. Zimmer, „Slow interaction ramps in trapped many-particle systems: universal deviations from adiabaticity“, *Phys. Rev. A* **87**, 033613 (2013).
- [212] S. Masuda, K. Nakamura, and A. del Campo, „High-fidelity rapid ground-state loading of an ultracold gas into an optical lattice“, *Phys. Rev. Lett.* **113**, 063003 (2014).
- [213] M. Dolfi, A. Kantian, B. Bauer, and M. Troyer, „Minimizing nonadiabaticities in optical-lattice loading“, *Phys. Rev. A* **91**, 033407 (2015).
- [214] M. Soni, M. Dolfi, and M. Troyer, „Density redistribution effects in fermionic optical lattices“, *Phys. Rev. A* **94**, 063404 (2016).
- [215] S. Wolf, S. J. Oliver, and D. S. Weiss, „Suppression of recoil heating by an optical lattice“, *Phys. Rev. Lett.* **85**, 4249–4252 (2000).
- [216] S. Trotzky, L. Pollet, F. Gerbier, U. Schnorrberger, I. Bloch, N. Prokof'ev, B. Svistunov, and M. Troyer, „Suppression of the critical temperature for superfluidity near the Mott transition“, *Nature Phys.* **6**, 998–1004 (2010).
- [217] H. Pichler, A. J. Daley, and P. Zoller, „Nonequilibrium dynamics of bosonic atoms in optical lattices: decoherence of many-body states due to spontaneous emission“, *Phys. Rev. A* **82**, 063605 (2010).
- [218] F. Gerbier, and Y. Castin, „Heating rates for an atom in a far-detuned optical lattice“, *Phys. Rev. A* **82**, 013615 (2010).
- [219] H. Pichler, J. Schachenmayer, A. J. Daley, and P. Zoller, „Heating dynamics of bosonic atoms in a noisy optical lattice“, *Phys. Rev. A* **87**, 033606 (2013).
- [220] K. W. Mahmud, E. N. Duchon, Y. Kato, N. Kawashima, R. T. Scalettar, and N. Trivedi, „Finite-temperature study of bosons in a two-dimensional optical lattice“, *Phys. Rev. B* **84**, 054302 (2011).
- [221] C. Robens, J. Zopes, W. Alt, S. Brakhane, D. Meschede, and A. Alberti, „Low-entropy states of neutral atoms in polarization-synthesized optical lattices“, *Phys. Rev. Lett.* **118**, 065302 (2017).
- [222] M. Olshanii, and D. Weiss, „Producing Bose-Einstein condensates using optical lattices“, *Phys. Rev. Lett.* **89**, 090404 (2002).

- [223] D. S. Weiss, J. Vala, A. V. Thapliyal, S. Myrgren, U. Vazirani, and K. B. Whaley, „Another way to approach zero entropy for a finite system of atoms“, *Phys. Rev. A* **70**, 040302 (2004).
- [224] M. R. Sturm, M. Schlosser, R. Walser, and G. Birkl, „Quantum simulators by design: many-body physics in reconfigurable arrays of tunnel-coupled traps“, *Phys. Rev. A* **95**, 063625 (2017).
- [225] M. Born, and V. Fock, „Beweis des Adiabatensatzes“, *Zeitschrift für Physik* **51**, 165–180 (1928).
- [226] K.-P. Marzlin, and B. C. Sanders, „Inconsistency in the application of the adiabatic theorem“, *Phys. Rev. Lett.* **93**, 160408 (2004).
- [227] M. H. S. Amin, „Consistency of the adiabatic theorem“, *Phys. Rev. Lett.* **102**, 220401 (2009).
- [228] A. T. Rezakhani, W.-J. Kuo, A. Hama, D. A. Lidar, and P. Zanardi, „Quantum adiabatic brachistochrone“, *Phys. Rev. Lett.* **103**, 080502 (2009).
- [229] J. Baum, R. Tycko, and A. Pines, „Broadband and adiabatic inversion of a two-level system by phase-modulated pulses“, *Phys. Rev. A* **32**, 3435–3447 (1985).
- [230] O. Dutta, M. Gajda, P. Hauke, M. Lewenstein, D.-S. Lühmann, B. A. Malomed, T. Sowiński, and J. Zakrzewski, „Non-standard Hubbard models in optical lattices: a review“, *Rep. Prog. Phys.* **78**, 066001 (2015).
- [231] M. Łacki, D. Delande, and J. Zakrzewski, „Dynamics of cold bosons in optical lattices: effects of higher Bloch bands“, *New J. Phys.* **15**, 013062 (2013).
- [232] X. Chen, A. Ruschhaupt, S. Schmidt, and J. Muga, „Shortcut to adiabaticity in harmonic traps“, *J. At. Mol. Sci.* **1**, 1–17 (2010).
- [233] M. Łacki, and J. Zakrzewski, „Fast dynamics for atoms in optical lattices“, *Phys. Rev. Lett.* **110**, 065301 (2013).
- [234] J. Schachenmayer, L. Pollet, M. Troyer, and A. J. Daley, „Spontaneous emission and thermalization of cold bosons in optical lattices“, *Phys. Rev. A* **89**, 011601 (2014).
- [235] P. Doria, T. Calarco, and S. Montangero, „Optimal control technique for many-body quantum dynamics“, *Phys. Rev. Lett.* **106**, 190501 (2011).
- [236] J. Hu, A. Urvoy, Z. Vendeiro, V. Crépel, W. Chen, and V. Vuletić, „Creation of a Bose-condensed gas of 87Rb by laser cooling“, *Science* **358**, 1078–1080 (2017).
- [237] H. Veksler, and S. Fishman, „Semiclassical analysis of Bose-Hubbard dynamics“, *New J. Phys.* **17**, 053030 (2015).
- [238] E. Brion, L. H. Pedersen, and K. Mølmer, „Adiabatic elimination in a lambda system“, *J. Phys. A: Math. Theor.* **40**, 1033 (2007).
- [239] V. Paulisch, H. Rui, H. K. Ng, and B.-G. Englert, „Beyond adiabatic elimination: a hierarchy of approximations for multi-photon processes“, *The European Physical Journal Plus* **129**, 12 (2014).
- [240] K. Winkler, G. Thalhammer, F. Lang, R. Grimm, J. H. Denschlag, A. Daley, A. Kantian, H. Büchler, and P. Zoller, „Repulsively bound atom pairs in an optical lattice“, *Nature* **441**, 853–856 (2006).
- [241] D. Petrosyan, B. Schmidt, J. R. Anglin, and M. Fleischhauer, „Quantum liquid of repulsively bound pairs of particles in a lattice“, *Phys. Rev. A* **76**, 033606 (2007).

- [242] P. M. Preiss, R. Ma, M. E. Tai, A. Lukin, M. Rispoli, P. Zupancic, Y. Lahini, R. Islam, and M. Greiner, „Strongly correlated quantum walks in optical lattices“, *Science* **347**, 1229–1233 (2015).
- [243] A. Smerzi, S. Fantoni, S. Giovanazzi, and S. R. Shenoy, „Quantum coherent atomic tunneling between two trapped bose-einstein condensates“, *Phys. Rev. Lett.* **79**, 4950–4953 (1997).
- [244] S. Raghavan, A. Smerzi, S. Fantoni, and S. R. Shenoy, „Coherent oscillations between two weakly coupled Bose-Einstein condensates: Josephson effects, π oscillations, and macroscopic quantum self-trapping“, *Phys. Rev. A* **59**, 620–633 (1999).
- [245] M. Albiez, R. Gati, J. Fölling, S. Hunsmann, M. Cristiani, and M. K. Oberthaler, „Direct observation of tunneling and nonlinear self-trapping in a single bosonic Josephson junction“, *Phys. Rev. Lett.* **95**, 010402 (2005).
- [246] B. Juliá-Díaz, J. Martorell, M. Melé-Messeguer, and A. Polls, „Beyond standard two-mode dynamics in bosonic Josephson junctions“, *Phys. Rev. A* **82**, 063626 (2010).
- [247] F. Meinert, M. J. Mark, K. Lauber, A. J. Daley, and H.-C. Nägerl, „Floquet engineering of correlated tunneling in the Bose-Hubbard model with ultracold atoms“, *Phys. Rev. Lett.* **116**, 205301 (2016).
- [248] Y. Aharonov, L. Davidovich, and N. Zagury, „Quantum random walks“, *Phys. Rev. A* **48**, 1687–1690 (1993).
- [249] E. Farhi, and S. Gutmann, „Quantum computation and decision trees“, *Phys. Rev. A* **58**, 915–928 (1998).
- [250] S. E. Venegas-Andraca, „Quantum walks: a comprehensive review“, *Quantum Inf. Process.* **11**, 1015–1106 (2012).
- [251] A. M. Childs, „Universal computation by quantum walk“, *Phys. Rev. Lett.* **102**, 180501 (2009).
- [252] J. Wang, and K. Manouchehri, *Physical implementation of quantum walks* (Springer, 2013).
- [253] C. Brif, R. Chakrabarti, and H. Rabitz, „Control of quantum phenomena: past, present and future“, *New J. Phys.* **12**, 075008 (2010).
- [254] S. Montangero, T. Calarco, and R. Fazio, „Robust optimal quantum gates for Josephson charge qubits“, *Phys. Rev. Lett.* **99**, 170501 (2007).
- [255] P. Rebentrost, I. Serban, T. Schulte-Herbrüggen, and F. K. Wilhelm, „Optimal control of a qubit coupled to a non-Markovian environment“, *Phys. Rev. Lett.* **102**, 090401 (2009).
- [256] B. A. Blumer, M. S. Underwood, and D. L. Feder, „Single-qubit unitary gates by graph scattering“, *Phys. Rev. A* **84**, 062302 (2011).
- [257] M. Varbanov, and T. A. Brun, „Quantum scattering theory on graphs with tails“, *Phys. Rev. A* **80**, 052330 (2009).
- [258] R. Nandkishore, and D. A. Huse, „Many-body localization and thermalization in quantum statistical mechanics“, *Annu. Rev. Condens. Matter Phys.* **6**, 15–38 (2015).
- [259] D.-S. Lühmann, C. Weitenberg, and K. Sengstock, „Emulating molecular orbitals and electronic dynamics with ultracold atoms“, *Phys. Rev. X* **5**, 031016 (2015).

- [260] B. T. Seaman, M. Krämer, D. Z. Anderson, and M. J. Holland, „Atomtronic: ultracold-atom analogs of electronic devices“, *Phys. Rev. A* **75**, 023615 (2007).
- [261] L. Amico, G. Birkel, M. Boshier, and L.-C. Kwek, „Focus on atomtronic-enabled quantum technologies“, *New J. Phys.* **19**, 020201 (2017).
- [262] R. A. Pepino, J. Cooper, D. Z. Anderson, and M. J. Holland, „Atomtronic circuits of diodes and transistors“, *Phys. Rev. Lett.* **103**, 140405 (2009).
- [263] R. A. Pepino, J. Cooper, D. Meiser, D. Z. Anderson, and M. J. Holland, „Open quantum systems approach to atomtronics“, *Phys. Rev. A* **82**, 013640 (2010).
- [264] M. Bukov, L. D’Alessio, and A. Polkovnikov, „Universal high-frequency behavior of periodically driven systems: from dynamical stabilization to floquet engineering“, *Adv. Phys.* **64**, 139–226 (2015).
- [265] M. Holthaus, „Floquet engineering with quasienergy bands of periodically driven optical lattices“, *J. Phys. B: At., Mol. Opt. Phys.* **49**, 013001 (2016).
- [266] A. Eckardt, C. Weiss, and M. Holthaus, „Superfluid-insulator transition in a periodically driven optical lattice“, *Phys. Rev. Lett.* **95**, 260404 (2005).
- [267] H. Lignier, C. Sias, D. Ciampini, Y. Singh, A. Zenesini, O. Morsch, and E. Arimondo, „Dynamical control of matter-wave tunneling in periodic potentials“, *Phys. Rev. Lett.* **99**, 220403 (2007).
- [268] A. Zenesini, H. Lignier, D. Ciampini, O. Morsch, and E. Arimondo, „Coherent control of dressed matter waves“, *Phys. Rev. Lett.* **102**, 100403 (2009).
- [269] J. Struck, C. Ölschläger, R. Le Targat, P. Soltan-Panahi, A. Eckardt, M. Lewenstein, P. Windpassinger, and K. Sengstock, „Quantum simulation of frustrated classical magnetism in triangular optical lattices“, *Science* **333**, 996–999 (2011).
- [270] M. Aidelsburger, M. Atala, M. Lohse, J. T. Barreiro, B. Paredes, and I. Bloch, „Realization of the Hofstadter hamiltonian with ultracold atoms in optical lattices“, *Phys. Rev. Lett.* **111**, 185301 (2013).
- [271] H. Miyake, G. A. Siviloglou, C. J. Kennedy, W. C. Burton, and W. Ketterle, „Realizing the Harper hamiltonian with laser-assisted tunneling in optical lattices“, *Phys. Rev. Lett.* **111**, 185302 (2013).
- [272] J. Struck, M. Weinberg, C. Ölschläger, P. Windpassinger, J. Simonet, K. Sengstock, R. Höppner, P. Hauke, A. Eckardt, M. Lewenstein, et al., „Engineering ising-xy spin-models in a triangular lattice using tunable artificial gauge fields“, *Nat. Phys.* **9**, 738 (2013).
- [273] G. Jotzu, M. Messer, R. Desbuquois, M. Lebrat, T. Uehlinger, D. Greif, and T. Esslinger, „Experimental realization of the topological haldane model with ultracold fermions“, *Nature* **515**, 237 (2014).
- [274] F. A. van Abeelen, and B. J. Verhaar, „Determination of collisional properties of cold Na atoms from analysis of bound-state photoassociation and Feshbach resonance field data“, *Phys. Rev. A* **59**, 578–584 (1999).
- [275] H. Wang, A. N. Nikolov, J. R. Ensher, P. L. Gould, E. E. Eyler, W. C. Stwalley, J. P. Burke, J. L. Bohn, C. H. Greene, E. Tiesinga, C. J. Williams, and P. S. Julienne, „Ground-state scattering lengths for potassium isotopes determined by double-resonance photoassociative spectroscopy of ultracold ^{39}K “, *Phys. Rev. A* **62**, 052704 (2000).

- [276] E. G. M. van Kempen, S. J. J. M. F. Kokkelmans, D. J. Heinzen, and B. J. Verhaar, „Interisotope determination of ultracold rubidium interactions from three high-precision experiments“, *Phys. Rev. Lett.* **88**, 093201 (2002).
- [277] E. Šimánek, „Instability of granular superconductivity“, *Phys. Rev. B* **22**, 459–462 (1980).
- [278] S. Doniach, „Quantum fluctuations in two-dimensional superconductors“, *Phys. Rev. B* **24**, 5063–5070 (1981).
- [279] S. D. Huber, B. Theiler, E. Altman, and G. Blatter, „Amplitude mode in the quantum phase model“, *Phys. Rev. Lett.* **100**, 050404 (2008).
- [280] J. M. Kosterlitz, and D. J. Thouless, „Ordering, metastability and phase transitions in two-dimensional systems“, *J. Phys. C: Solid State Phys.* **6**, 1181 (1973).
- [281] A. Trombettoni, A. Smerzi, and P. Sodano, „Observable signature of the Berezinskii–Kosterlitz–Thouless transition in a planar lattice of Bose–Einstein condensates“, *New J. Phys.* **7**, 57 (2005).
- [282] V. Schweikhard, S. Tung, and E. A. Cornell, „Vortex proliferation in the Berezinskii–Kosterlitz–Thouless regime on a two-dimensional lattice of Bose–Einstein condensates“, *Phys. Rev. Lett.* **99**, 030401 (2007).
- [283] J. R. Anglin, P. Drummond, and A. Smerzi, „Exact quantum phase model for mesoscopic Josephson junctions“, *Phys. Rev. A* **64**, 063605 (2001).
- [284] J. J. García-Ripoll, J. I. Cirac, P. Zoller, C. Kollath, U. Schollwöck, and J. von Delft, „Variational ansatz for the superfluid Mott-insulator transition in optical lattices“, *Opt. Express* **12**, 42–54 (2004).
- [285] L. S. Schulman, *Techniques and applications of path integration* (Wiley, 1981).
- [286] K. P. Schmidt, A. Reischl, and G. S. Uhrig, „Thermodynamics of adiabatically loaded cold bosons in the Mott insulating phase of one-dimensional optical lattices“, *Eur. Phys. J. D* **38**, 343–352 (2006).
- [287] D. B. M. Dickerscheid, D. van Oosten, P. J. H. Denteneer, and H. T. C. Stoof, „Ultracold atoms in optical lattices“, *Phys. Rev. A* **68**, 043623 (2003).
- [288] E. López, A. Molgado, and J. A. Vallejo, „The principle of stationary action in the calculus of variations“, *Communications in Mathematics* **20**, 89–116 (2012).
- [289] J. M. Zhang, and R. X. Dong, „Exact diagonalization: the Bose–Hubbard model as an example“, *Eur. Phys. J.* **31**, 591 (2010).
- [290] D. Raventós, T. Graß, M. Lewenstein, and B. Juliá-Díaz, „Cold bosons in optical lattices: a tutorial for exact diagonalization“, *J. Phys. B: At., Mol. Opt. Phys.* **50**, 113001 (2017).
- [291] E. Anderson, Z. Bai, C. Bischof, S. Blackford, J. Demmel, J. Dongarra, J. Du Croz, A. Greenbaum, S. Hammarling, A. McKenney, and D. Sorensen, *LAPACK users’ guide*, Third edition (SIAM, Philadelphia, 1999).
- [292] T. J. Park, and J. C. Light, „Unitary quantum time evolution by iterative Lanczos reduction“, *J. Chem. Phys.* **85**, 5870–5876 (1986).
- [293] S. R. Manmana, A. Muramatsu, and R. M. Noack, „Time evolution of one-dimensional quantum many body systems“, *AIP Conf. Proc.* **789**, 269–278 (2005).
- [294] C. Kollath, A. M. Läuchli, and E. Altman, „Quench dynamics and nonequilibrium phase diagram of the Bose–Hubbard model“, *Phys. Rev. Lett.* **98**, 180601 (2007).

- [295] R. B. Sidje, „Expokit: a software package for computing matrix exponentials“, ACM Trans. Math. Softw. **24**, 130–156 (1998).

Danksagung

An dieser Stelle möchte ich all jenen danken, die mich beim Anfertigen dieser Doktorarbeit unterstützt und so zum Gelingen derselben beigetragen haben.

An erster Stelle gilt mein Dank meinem Doktorvater Prof. Dr. Reinhold Walser, für die Möglichkeit in seiner Arbeitsgruppe zu promovieren und für die hervorragende Betreuung während dieser Zeit. Insbesondere möchte ich die Diskussionen von physikalischen Zusammenhängen und Fragestellungen hervorheben, die sowohl mein Verständnis erweiterten als auch neue Ideen generierten. Auch die Möglichkeit an zahlreichen nationalen und internationalen wissenschaftlichen Konferenzen teilnehmen zu können hat mich sehr bereichert.

Prof. Dr. Gerhard Birkel und Dr. Malte Schlosser danke ich für die gute und sehr fruchtbare Zusammenarbeit während den letzten viereinhalb Jahren. Weiterhin möchte ich mich bei Prof. Dr. Gerhard Birkel für die Übernahme des Zweitgutachtens bedanken.

Mein Dank gilt den jetzigen und ehemaligen Mitgliedern der Arbeitsgruppe *Theoretische Quantendynamik* sowohl für die gegenseitige Unterstützung und das kollegiale Klima als auch für die vielen Gespräche über Physik und die anderen Dinge im Leben. Insbesondere möchte ich mich bei der Besetzung von Raum 01 für den tollen Zusammenhalt und das kritische Korrekturlesen dieser Arbeit bedanken.

Abschließend danke ich meiner Familie und meinen Freunden für ihre Unterstützung und die vielen schönen Erlebnisse außerhalb der Physik.

Konferenzbeiträge und Veröffentlichungen

Konferenzbeiträge

- **Posterpräsentation (Hannover, 18. bis 22. März 2013):**
DPG-Frühjahrstagung der Sektion AMOP
"Lasing without inversion in the ultra violet regime"
- **Vortrag (Berlin, 17. bis 21. März 2014):**
DPG-Frühjahrstagung der Sektion AMOP
"Feasibility of UV lasing without inversion in mercury vapor"
- **Posterpräsentation (Heidelberg, 23. bis 27. März 2015):**
DPG-Frühjahrstagung der Sektion AMOP
"Towards many body physics with ultracold atoms in optical microtrap arrays"
- **Posterpräsentation (Les Houches, 14. bis 25. September 2015):**
Les Houches predoc school on cold atoms
"Towards many body physics with ultracold atoms in optical microtrap arrays"
- **Vortrag (München, 21. bis 26. Februar 2016):**
Young atom opticians conference
"Bottom-up approach to many-body physics with ultracold atoms in adjustable lattices"
- **Posterpräsentation (Mainz, 6. bis 10. März 2017):**
DPG-Frühjahrstagung der Sektion AMOP
"Bottom-up approach to many-body physics with ultra- cold atoms in adjustable lattices"
- **Posterpräsentation (Benasque, 7. bis 20. Mai 2017):**
Atomtronics conference
"Bottom-up approach to many-body physics with ultra- cold atoms in adjustable lattices"
- **Vortrag (Erlangen, 4. bis 9. März 2018):**
DPG-Frühjahrstagung der Sektion AMOP
"Bottom-up approach to many-body physics with ultra- cold atoms in adjustable lattices"

Artikel in Fachzeitschriften

- **M. R. Sturm**, B. Rein, Th. Walther, and R. Walser
"Feasibility of UV lasing without inversion in mercury vapor"
J. Opt. Soc. Am. B **31**, 8, 1964-1974 (2014)
- B. Rein, **M. R. Sturm**, R. Walser, and Th. Walther
"Towards Lasing Without Inversion in Neutral Mercury"
J. Phys. Conf. Ser. **594**, 012007 (2015)
- **M. R. Sturm**, M. Schlosser, R. Walser, and G. Birkel
"Quantum simulators by design: Many-body physics in reconfigurable arrays of tunnel-coupled traps"
Phys. Rev. A **95**, 063625 (2017)
- **M. R. Sturm**, M. Schlosser, G. Birkel, and R. Walser
"Rapid loading of a Mott insulator from arrays of non-condensed atoms"
Submitted to Phys. Rev. A
- B. Rein, J. Schmidt, **M. R. Sturm**, R. Walser, and Th. Walther
"Doppler-free three-photon coherence effects in mercury vapor"
In preparation
- **M. R. Sturm**, M. Schlosser, R. Walser, and G. Birkel
"Quantum computation with continuous-time quantum walks of ultracold atoms"
In preparation

Lebenslauf

Martin Raphael Sturm

Geboren am 21. Februar 1989 in Berlin

Email: martinrstorm@googlemail.com

Hochschullaufbahn

01.2014 bis heute	Doktorand und wissenschaftlicher Mitarbeiter AG theoretische Quantendynamik (Prof. Dr. R. Walser) Institut für Angewandte Physik, TU Darmstadt
10.2011 bis 11.2013	Masterstudium Physik and der TU Darmstadt Nebenfach Mathematik
04.2009 bis 09.2011	Bachelorstudium Physik and der TU Darmstadt Nebenfach Informatik

Zivildienst

08.2008 bis 03.2009	TuS Griesheim
----------------------------	---------------

Schulbildung

08.2000 bis 05.2008	Gymnasium Eleonorenschule, Darmstadt
08.1996 bis 07.2000	Grundschule Conrad-Grundschule, Berlin
08.1995 bis 06.1996	Grundschule Paul-Eipper-Schule, Berlin

Erklärung gemäß §9 Promotionsordnung

Hiermit versichere ich, dass ich die vorliegende Dissertation selbstständig angefertigt und keine anderen als die angegebenen Quellen und Hilfsmittel verwendet habe. Alle wörtlichen und paraphrasierten Zitate wurden angemessen kenntlich gemacht. Die Arbeit hat bisher noch nicht zu Prüfungszwecken gedient.

Darmstadt, 9. April 2018

(Martin Raphael Sturm)